A Non-Wetting Packed Bed Gas Scrubber

A Thesis submitted by

Boon Fuei Chang

to

The University of Sheffield

for the Degree of Doctor of Philosophy

January 2003

Department of Chemical and Process Engineering

The University of Sheffield

ORIGINAL COPY TIGHTLY

BOUND

THESIS CONTAINS

CD

Summary

Present integrated gasification combined cycle (IGCC) systems demonstrate high system efficiency and impressive environmental performance, giving them an edge over conventional pulverised fuel power stations. A key area in the development of IGCCs is hot fuel gas clean-up (HGCU). Fuel gas cleaning at elevated temperatures reduces thermal efficiency losses associated with gas quenching in conventional cold gas cleaning methods. Current hot gas desulphurisation techniques focus on the use of regenerable metal oxide sorbents, however the long-term sorbent performance issues have yet to be fully addressed. A fresh and radical approach may provide the key to overcoming the inherent limitations associated with metal oxide sorbents. A molten tin irrigated packed bed scrubber adopted in this research project is one such innovative way forward in HGCU. The hot scrubber offers the prospect of a multicomponent clean-up device. High-temperature sulphur removal takes place via absorption of H_2S (and COS) into molten tin whilst discrete molten tin droplets and rivulets on the packing surface act as solid particulate collectors.

The primary aim of this research project was to investigate the workings of a small-scale room-temperature packed bed scrubber operating under non-wetting flow conditions analogous to the molten tin irrigated scrubber. Water irrigation of low surface energy packings simulated the non-wetting flow of liquid metals. The air-water analogue of the liquid metal scrubber provided the platform for hydrodynamics (flow visualisation, flooding and liquid holdup), particulate removal and mass transfer studies under non-wetting flow conditions. The performance of a small air lift for water circulation through the column was also investigated. These cold studies offered insight into the operation and performance of the liquid metal hot scrubber.

Prior to the cold gas scrubber studies, preliminary small-scale gasification tests on petroleum coke samples were performed to investigate the effect of molten tin on H_2S in the product fuel gas. The tests provided actual experimental evidence of the possibility of sulphur removal by molten tin in a gasification environment.

It was shown that the maximum possible size of a liquid droplet hanging from a non-wetting spherical solid surface could be predicted from the liquid surface tension and density based on force balance. The mobility of static holdup in a non-wettable packed bed has been demonstrated, this being due to the tendency for the liquid to form discrete droplets rather than spreading films. Existing flooding and liquid holdup correlations that hold for conventional wettable packed beds were shown to be inadequate where non-wetting systems were concerned,

hence alternative methods applicable to the latter were sought. The introduction of a non-wetting tendency factor based on the ratio of the solid critical surface tension to the liquid surface tension, enabled the flooding capacities of non-wetting systems including those of this study to be predicted using Sherwood *et al.*'s graphical flooding correlation. The total volumetric liquid holdup was well correlated against the bed pressure drop, true gas velocity and gas density, offering the prospects of predicting holdup for systems using the same spherical packing. In general, the water-irrigated packed bed showed good hydrodynamic similarities to liquid metal systems, suggesting a dominating influence of liquid-solid contact angle which overrides striking differences in liquid physical properties.

The performance of the small air lift pump was unaffected by varying the number of gas ports on the injector without any change to the hole size. The operating curve of the air lift pump could be predicted with good accuracy using momentum balance and two phase flow theory, provided that all major pressure losses in the system were accounted for, including notably the downcomer friction losses and accelerative effects.

The non-wetting packed bed scrubber demonstrated impressive dust removal performance. Total separation efficiencies as high as 99.6% and cut sizes approaching submicron were achieved. Dust particles larger than about 6.5 μm can be separated to efficiencies greater than 98%. Complete particle separation was achieved in all cases for dust particles larger than 16 μm.

Particulate removal in a packed bed of spheres under non-wetting flow conditions has also been modelled using computational fluid dynamics (FLUENT). Simulation results showed that particle separation efficiency increases with particle size and density, but is unaffected by particle concentration. The predicted particle size corresponding to 98% efficiency is about 40 μm.

In mass transfer, the height of the gas film transfer unit of various non-wetting spherical packed bed systems including those of this study was correlated successfully against the gas phase Reynolds number, the liquid superficial velocity and the packing diameter.

Results from the cold gas scrubber studies have offered insight and understanding into the workings and development of the liquid metal packed bed gas scrubber. Findings and correlations derived from the water model studies, occasionally complemented by data from other non-wetting systems, have provided the means to predict the hydrodynamics, particulate removal capability and mass transfer performance of the liquid metal based gas scrubber. The pilot unit of the hot gas scrubber has been designed and fully constructed. The high temperature gas cleaning facility is ready for commissioning.

Acknowledgements

∞∞∞∞∞∞∞∞∞∞∞∞∞

To my mum, dad, sisters and brother,
for their continuous love, support and encouragement.

∞∞∞∞∞∞∞∞∞∞∞∞∞

Contents

List of Figures, Tables and Plates

Tables

Plates   **Page**

Nomenclature

Symbol	Description	Unit
a	Cross-sectional area of annular flow	ft^2
a	Interfacial area per unit volume of column	m^2/m^3
a	Empirical constant	-
A	Gas lift pipe cross-sectional area	ft^2
A	Column cross-sectional area	m^2
A'	$0.2\rho_L gM + 2.7F_s M$	kg^2/s^{5}m^2
A, A'	Empirical constants	-
b_{1-3}, B	Empirical constants	-
B'	$1.2W_L + 0.35(gD)^{1/2}$	m/s
c	Concentration in liquid phase	kmol/m^3
c*	Concentration in liquid phase in equilibrium with gas phase	kmol/m^3
C_D	Discharge coefficient	-
C_D	Drag coefficient	-
C_o	Orifice coefficient	-
C_p	Dust concentration	ppmw
C_s	Capacity factor = $u_G\{\rho_G/(\rho_L-\rho_G)\}^{0.5}$	ft/s
C_{1-6}	Empirical constants	-
C'	Cunningham slip correction factor	-
d	Particle diameter; Packing size or characteristic length	m
$d_{contact}$	Contact diameter	m
d_e	Equatorial diameter	m
d_{equiv}	Packing particle equivalent diameter	m
d_o	Orifice diameter	inch
d_s	Diameter measured from distance d_e up from base of drop	m
d_{sv}	Surface-volume diameter or Sauter diameter	m
d_{50}	Median diameter	μm
D	Gas lift riser inside diameter	in, m
D_G	Gas phase diffusion coefficient or diffusivity	m^2/s
D_h	Hydraulic diameter	mm
D_L	Liquid phase diffusion coefficient or diffusivity	m^2/s
D_{col}	Column diameter	m
e	Absolute error	
E_D	Eddy diffusivity	m^2/s
E_T	Total or overall efficiency	-
E_{total}	Overall particle separation efficiency in packed bed model	-
Eö, Eö*	Eötvös number and modified Eötvös number respectively	-
f	Moody friction factor	-
F	Packing factor	m^2/m^3
F	Wall frictional pressure gradient in two-phase flow	Pa/m
F_i	Source term in momentum equation	kg/m^{2}s^2
F_s	Wall frictional pressure gradient in single liquid phase flow	Pa/m
F_x	Source term in force balance	m/s^2
g	Gravitational acceleration	(m/s^2)

G	Gas superficial mass velocity	kg/m²s
G'	Molar gas flowrate per unit cross-sectional area of column	kmol/m²s
G'	Gas mass flowrate to base of air lift pump (Clark and Dabolt's model)	kg/s
G(x)	Grade efficiency	-
ΔG_R	Gibbs free energy change of reaction	kJ/mol
h_{atm}	Liquid head corresponding to atmospheric pressure	m
h_D	Dynamic (operating or moving) liquid holdup	m³/m³
h_E	Effective liquid holdup	m³/m³
h_L	Liquid head	ft
h_S	Static liquid holdup	m³/m³
$\overline{h}_S$	Average static liquid holdup	m³/m³
h_T	Total liquid holdup	m³/m³
H	Shape dependent quantity	-
H_G	Height of a gas film transfer unit	m
H_L	Height of a liquid film transfer unit	m
H_{OG}	Height of an overall gas phase transfer unit	m
H_{OL}	Height of an overall liquid phase transfer unit	m
H_T	Total volumetric liquid holdup	ml
$H_{x1/x2}$	Sharpness index	-
H	Henry's Law constant	Pa, Pa.m³/kmol
I	Turbulent intensity	%
k	Pipe roughness	mm
k	Turbulent kinetic energy	m²/s²
k_G	Gas film mass transfer coefficient	kmol/m²sPa
k'_G	Gas film mass transfer coefficient in terms of mol fraction	kmol/m²s
k'_Ga	Volumetric gas film mass transfer coefficient in terms of mol fraction	kmol/m³s
k_L	Liquid film mass transfer coefficient	m/s
k'_L	Liquid film mass transfer coefficient in terms of mol fraction	kmol/m²s
k'_La	Volumetric liquid film mass transfer coefficient in terms of mol fraction	kmol/m³s
K	Vapour-liquid equilibrium constant	mol/mol
K_c	Sudden contraction loss coefficient = 0.5	-
K_e	Sudden expansion loss coefficient = 1.0	-
K_G	Overall gas phase mass transfer coefficient	kmol/m²sPa
K'_G	Overall gas phase mass transfer coefficient in terms of mol fraction	kmol/m²s
K_Ga	Overall volumetric gas phase mass transfer coefficient	kmol/m³sPa
K'_Ga	Overall volumetric gas phase mass transfer coefficient in terms of mol fraction	kmol/m³s
K_L	Overall liquid phase mass transfer coefficient	m/s
K'_L	Overall liquid phase mass transfer coefficient in terms of mol fraction	kmol/m²s
K_La	Overall volumetric liquid phase mass transfer coefficient	1/s
K'_La	Overall volumetric liquid phase mass transfer coefficient in terms of mol fraction	kmol/m³s
K_p	Equilibrium constant in terms of partial pressure	
K	Vapour-liquid equilibrium constant	-
Kn	Knudsen number	-
l	Bed thickness or bed height	m
L	Length	m
L	Lift	m, ft
L	Liquid superficial mass velocity	kg/m²s

L'	Molar liquid flowrate per unit cross-sectional area of column	$kmol/m^2s$
L_V	Liquid superficial volumetric velocity	$m^3/s.m^2$
L_w	Wetting rate	m^2/s
m	Vapour-liquid equilibrium constant	mol/mol
m	Mass of sample	g
m_{in}	Mass of dust fed into scrubber	g
m_{out}	Mass of unseparated dust in exit air retained on filter	g
M	$W_G P = G'P_{atm}/A\rho_G$	kg/s^3
M	Mass flowrate of a sample	kg/s
$\overline{M}$	Mean mass flowrate	g/s
M_c	Mass flowrate of coarse (separated) dust in underflow	kg/s
M_f	Mass flowrate of fine (unseparated or penetrating) dust in overflow	kg/s
M_G	Mass flowrate of gas phase	kg/s
M_{in}	Mass flowrate of feed (challenging) dust	kg/s
M_x	Mass flowrate of particles of size x in the sample	kg/s
N	Total molar flux (relative to a fixed plane); Molar rate of absorption per unit area	$kmol/m^2s$
N	Number of data sets	-
N_G	Number of gas film transfer units	-
N_L	Number of liquid film transfer units	-
N_o	Number of orifices	-
N_{OG}	Number of overall gas phase transfer units	-
N_{OL}	Number of overall liquid phase transfer units	-
N_t	Number of transfer units	-
o/A	ratio of annular liquid film to pipe cross-sectional area	-
p	Partial pressure in bulk gas phase	Pa
p*	Partial pressure in gas phase in equilibrium with liquid phase	Pa
p^o	Vapour pressure of pure component	Pa
p_i	Partial pressure at interface	Pa
P	Total pressure	Pa
P_{atm}	Atmospheric pressure	Pa
P_g	Gauge pressure	Pa
P_o	Pressure at air injector level	Pa
P_{op}	Operating pressure	Pa
ΔP	Pressure drop	Pa
ΔP_{dry}	Dry bed pressure drop	Pa
ΔP_A	Accelerative pressure loss	Pa
ΔP_D	Downcomer pressure loss	Pa
ΔP_H	Hydrostatic pressure loss across riser	Pa
ΔP_W	Wall friction pressure loss	Pa
$\Delta P/l$	Pressure gradient	Pa/m
Q	Volumetric flowrate	litre/min, gal/min
R	Universal gas constant	J/kmol K
R^2	Coefficient of determination	-
Re	Reynolds number	-
Re_{Dh}	Reynolds number based on hydraulic diameter	-
Re_G	Gas phase Reynolds number	-
Re_L	Liquid phase Reynolds number	-

Re_p	Single particle Reynolds number $= \rho u d / \mu$	-
Re_R	Relative Reynolds number $= \rho_G U_R d / \mu_G$	-
Re_y	Wall-distance-based, turbulent Reynolds number	-
Re^*	Reynolds number for packed bed flow	-
s	Standard deviation	
S	Specific surface area of particle or packing	m^2/m^3
S	Shape dependent quantity	-
S	Submergence	m, ft
S_m	Source term in continuity equation	$kg/m^3 s$
S_p	External area of a packing particle	m^2
S_B	Specific surface area of packed bed	m^2/m^3
S_R	Submergence ratio	-
S_{sl}	Spreading coefficient	N/m
Sc_G	Gas phase Schmidt number $= \mu_G / \rho_G D_G$	-
Sc_L	Liquid phase Schmidt number $= \mu_L / \rho_L D_L$	-
t	Time	s
T	Temperature	K
u	Superficial velocity	m/s
u'	Actual single phase velocity in two-phase flow	m/s
u'	Root-mean-square of velocity fluctuations in turbulent flow	m/s
$\bar{u}$	Mean flow velocity	m/s
U_G	True gas velocity based on irrigated bed porosity $= u_G / \varepsilon_{eff}$	m/s
U_R	Relative velocity of gas and liquid streams	m/s
v	Superficial velocity	m/s
v	Volume of solution	ml
V	Volume	m^3
V_G	Gas volumetric flowrate	m^3/s
V_G	Gas flow at gas lift discharge conditions	ft^3/min
V_L	Dense phase flow in gas lift	gal/min
V_p	Volume of a packing particle	m^3
W	Single phase superficial velocity in 2-phase flow	m/s
x	Mole fraction in liquid phase	mol/mol
x^*	Mole fraction in liquid phase in equilibrium with gas phase	mol/mol
x	Distance	m
x	Dust particle size (particle physical diameter)	μm
x_{ae}	Particle aerodynamic diameter	$\mu m (g/cm^3)^{1/2} = \mu mA$
x_{max}	Limit of separation	μm
x_{50}	Cut size	μm
x_{98}	Approximate limit of separation	μm
y	Mole fraction in gas phase	mol/mol
y	Distance	m
y^*	Mole fraction in gas phase in equilibrium with liquid phase	mol/mol
z_G, z_L	Effective gas film thickness and effective liquid film thickness respectively	m
Z	Packed bed height	m
Z_{end}	Equivalent bed height of end effects	m

Greek Symbols

α	Empirical constant	-
α	Gas voidage fraction in two-phase flow	-
β	Empirical constant	-
Δ	Change in	-
ε	Dry bed voidage or porosity	-
ε	Turbulent dissipation rate	m^2/s^3
ε_{eff}	Effective voidage or porosity	-
η_p	Pumping efficiency	-
φ	Gas density correction factor = $(\rho_G/\rho_{air,\,293K})^{0.5}$	-
λ	Mean free path of gas molecules	μm
μ	Absolute viscosity (in centipoise in GPDC)	kg/ms
μ_s	Ratio of liquid viscosity to water (20°C) viscosity	-
μ_t	Turbulent viscosity	kg/ms
ν	Kinematic viscosity = μ/ρ	cst, m^2/s
θ	Contact angle	degree
ρ	Density	kg/m^3
ρ_p	Particle density	g/cm^3, kg/m^3
ρ_s	Ratio of liquid density to water (20°C) density	-
σ	Surface tension	dynes/cm, N/m
σ_c	Critical surface tension	dynes/cm, N/m
σ_g	Geometric standard deviation	-
σ_s	Ratio of liquid surface tension to water (20°C) surface tension	-
τ_{ij}	Stress tensor	kg/ms^2
ω_x	Mass fraction of particles of size x in the sample	kg/kg
$\omega_{c,\,x}$	Mass fraction of coarse (separated) dust at particle size x	kg/kg
$\omega_{f,\,x}$	Mass fraction of fine (unseparated or penetrating) dust at particle size x	kg/kg
$\omega_{in,\,x}$	Mass fraction of feed dust at particle size x	kg/kg
$\omega_{out,\,x}$	Mass fraction of exit dust at particle size x	kg/kg
ψ	Liquid density correction factor = (ρ_{water}/ρ_L)	-
ψ_s	Sphericity	-

Subscripts

atm	Atmospheric pressure
A	Component A
B	Bottom of packed bed
f	Fluid
G	(Bulk) Gas phase
i	Gas-liquid interface
lm	Logarithmic mean
L	(Bulk) Liquid phase
lv	Liquid-vapour
p	Particle
sl	Solid-liquid
sv	Solid-vapour
T	Top of packed bed

Acronyms and Abbreviations

AARE	average absolute relative error		KHI	Kawasaki Heavy Industries
ABGC	air-blown gasification cycle		KRW	Kellogg-Rust-Westinghouse
ASM	American Society for Metals			
			LDPE	low density polyethylene
BGL	British Gas Lurgi		LRTAP	Long-Range Transboundary Air Pollution
CCGT	combined cycle gas turbine			
CCNG	combined cycle natural gas		MWe	megawatts electrical output
CCRI	China Coal Research Institute		MWth	megawatts thermal output
CCT	cleaner coal technology			
CFD	computational fluid dynamics		PAH	polycyclic aromatic hydrocarbon
CGCU	cold gas clean-up		PCC	pulverised coal combustion
CMP	Contracts Materials Processing		PF	pulverised fuel
CPC	Combustion Power Company		PFBC	pressurised fluidised bed combustion
CRIEPI	Central Research Institute of Electric Power Industry		ppmv	parts per million by volume
			ppmw	parts per million by weight
CVI	chemical vapour infiltration		PTFE	polytetrafluoroethylene
			PVDF	vinylidene polyfluorure
DSRP	direct sulphur recovery process			
			RNG	renormalisation group
EC	European Community		RTI	Research Triangle Institute
EPA	Environmental Protection Agency			
ESP	electrostatic precipitator		s.g.	specific gravity
ETSU	Energy Technology Support Unit		SPOS	single particle optical sensing
			SPPC	Sierra Pacific Power Company
FETC	Federal Energy Technology Center		SUMAC	Sheffield University Materials Analytical Centre
FGD	flue gas desulphurisation			
GE	General Electric		TECO	Tampa Electric Company
GPDC	generalised pressure drop correlation			
			UCI	United Catalysts Incorporated
HGCU	hot gas clean-up		UK DTI	United Kingdom Department of Trade and Industry
HTW	High Temperature Winkler			
			UNECE	United Nations Economic Commission for Europe
ID	internal diameter			
IDI	Intercat Development Incorporated		US DOE	United States Department of Energy
IEA	International Energy Agency			
IF&P	Industrial Filter and Pump		vol	volume
IGCC	integrated gasification combined cycle		VOC	volatile organic compound
IGT	Institute of Gas Technology			
IH	internal height		wt	weight

Chapter One

Introduction

1.1   The Need for Cleaner Coal Technology in Power Generation

As the world's natural gas and oil reserves become progressively depleted, coal remains the main energy source for power generation in the long term as it is the most abundantly available. Shell (2000) reported that current coal reserves are sufficient for about another 210 years based on present consumption rates which way exceeds the number of years predicted for natural gas (about 60 years) and oil (about 40 years). Accordingly, there is a vast and growing international market for cleaner coal technologies notably for electricity generation. Forecasts by IEA (2000) suggest that coal will continue to be the world's largest source of fuel for electricity generation for the next 20 years. About 38% of the world's electricity will be derived from coal by 2020. Cleaner coal technologies for power generation will therefore provide substantial opportunities in containing global greenhouse gas emissions. These technologies improve the efficiency of energy conversion from coal whilst simultaneously facilitating an environmentally satisfactory way of utilising coal, meeting various regulations on emissions, effluents and residues.

1.2   Integrated Gasification Combined Cycle (IGCC) Systems

The best standard for today's power generation technology is set by the combined cycle natural gas (CCNG) system which boasts of high efficiency, low environmental emissions and low cost. Compared to coal, natural gas has low sulphur and nitrogen contents and high hydrogen to carbon ratio, therefore giving low SO_2, NO_x and CO_2 emissions and eliminating the need for expensive gas clean-up equipment. A high energy conversion efficiency is achieved as the exhaust heat from the high temperature gas turbine is used to raise steam to drive the steam turbines in the combined cycles. Coupled with the relatively low cost of natural gas, CCNG offers the most cost-efficient way of generating electricity.

However in view of the abundant coal reserves in the world (IEA, 2000), coal will stay as the major fuel source for power generation in the longer term as the global reserves of natural gas and oil become progressively exhausted. It is therefore desirable to derive energy from coal and at the same time exploit the advantages offered by the efficient combined cycle system

1

with integration between the high efficiency gas turbine cycle with a steam turbine cycle. A coal-based power generation system is therefore needed whereby solid coal is gasified first generating a fuel gas, which after cleaning, can be used to power the gas turbine. The answer herein lies in a clean coal technology combining gasification with a combined cycle system, known as the integrated gasification combined cycle or IGCC technology. A typical IGCC system is shown in Figure 1.1.

Dry coal or coal in slurry is fed into a high temperature and pressure gasifier, either air- or oxygen-blown with steam. Coal gasification takes place in the gasifier which replaces the traditional combustor in conventional pulverised coal-fired power systems. In the reducing (oxygen-deficient) atmosphere, coal undergoes partial oxidation producing a fuel gas mixture containing mainly CO, H_2, CH_4, CO_2, N_2 and steam. The hot fuel gas also contains contaminants including particulates (ash and char fines), sulphur and nitrogen compounds (H_2S, COS,

Figure 1.1 Schematic diagram of a typical gasification combined cycle unit (US DOE, 2000).

NH_3, HCN) and traces of alkali metals, alkaline earth metals, heavy metals, halogens and organic compounds. The hot raw fuel gas (also termed synthesis gas or syngas) exits the gasifier from the top while residual ash is removed from the bottom. Downstream of the gasifier, the raw coal gas enters the gas cleanup unit which removes the pollutants, prior to being fired in the combustion chamber of the gas turbine. The resulting flue gas undergoes expansion producing electricity. Steam is raised from the gas turbine exhaust heat, at times also from combustion of the gasifier residual char in a combustor. The steam produced is used to generate electricity in a conventional steam turbine. This results in a high-efficiency integrated gas and steam turbine electric power generation system with typically 70% power output from the gas turbine cycle and the remaining 30% from the steam cycle.

Towards the end of the 1990s, there were at least 35 gasification power plants worldwide in various development stages ranging from full operation to those which are at the initial

planning and design stage, running on various feedstocks including bituminous coal, petroleum coke, lignite, biomass and wastes (UK DTI, 1998b). The majority incorporates the combined cycle gas turbine (CCGT) system. Among these are the Buggenum plant in Netherlands, the Piñon Pine and Polk plants in the USA and the Puertollano plant in Spain.

There are generally three groups of IGCC systems (Mitchell, 1998). These are the oxygen-blown fixed bed gasifier (Lurgi, British Gas Lurgi) with conventional cold gas cleaning, the oxygen-blown entrained-flow gasifier (Shell, Texaco, Destec, Prenflo) with conventional cold gas cleaning, and the air-blown fluidised bed gasifier (HTW, U-Gas, KRW, British Coal) with hot gas cleaning. The raw fuel gas composition and calorific value for each of the gasification system show considerable variation due to different coal feed particle size, coal-feeding method, type of oxidant, number of stages, gasifier operating conditions and the incorporation of in-situ sulphur absorbents. This variation is detailed in Table 1.1.

Table 1.1 *Properties of raw fuel gas from different gasification systems*
(Williams and McMullan, 1998; ETSU, 1998).

Fuel gas properties*	Shell	Texaco	BGL	ABGC
Analysis, % v/v				
CO	61-63	39-43	53-57	16-18
H_2	29-30	27-29	27-29	18-20
CO_2	~1	12-14	1-2	9-10
N_2	~4	~1	3-4	44-46
CH_4	0	0	5-7	<2
H_2O	~3	16-19	3-5	7-10
Calorific value, MJ/kg				
HHV	12.7-12.9	8.9-9.8	15.3-15.5	4.7-5.0
LHV	12.0-12.2	8.3-9.1	14.3-14.6	4.3-4.6
Impurities, ppmv				
H_2S/COS	1000-10,000	1000-9000	4500-14000	300-2000
NH_3/HCN	1800-2000	1800-2000	5000	1000-1500
HCl	40-600	40-500	50-700	20-300
Na/K (Alkali Metals)	na	na	na	<10
Ca/Mg (Alkali Earth Metals)	300	na	na	na
Dilution factor‡	10	7.4	11.5	4

* fuel gas composition taken from reported values in published literature for bituminous coals

‡ dilution factor - the ratio of the total gas flow through the gas turbine expander to the fuel gas flow
na not available

The major advantages offered by IGCC systems over the conventional pulverised coal-fired power plants are high system efficiency and impressive environmental performance. Efficiencies as high as 55% are expected of IGCC systems compared to about 38% for subcritical steam conditions and 45% for supercritical steam conditions for a steam power

plant (Wilkinson, 2000). Similar to CCNG, IGCCs are able to exploit the rapid advances in gas turbine technology and hence possess the potential for improved thermal efficiency. The good overall system efficiency in turn translates into low cost of electricity. The IGCC cost of electricity is equivalent to that of traditional pulverised coal-fired power plant, and this cost is expected to drop by 25% by the year 2010 (US DOE, 2000). IGCC represents the cleanest available technology for coal (IChemE, 1999), in which more than 99% of the sulphur content in coal is removed prior to combustion in the gas turbine while over 90% NOx reduction is achieved (US DOE, 2000). Overall, IGCC boasts of lower SO_x, NO_x and particulate emission levels than those of a conventional pulverized fuel power plant as shown in Table 1.2. IGCC thereby could become more important relative to other coal technologies with more stringent emission standards. Also with better electricity generation efficiency, less coal is burned per unit of power produced, meaning reduced net emissions of greenhouse gas CO_2.

Table 1.2 *Comparison of emission levels of IGCC with supercritical pulverised fuel, PF plant (UK DTI, 1998b).*

Emissions (mg/Nm^3 @ 6% O_2)	IGCC	PF Boiler with FGD
SO_x	30	100
NO_x	65	150
Particulates	10	20

However the acceptance of current IGCC systems is limited by problems of high capital costs, poor reliability and low operational flexibility (UK DTI, 1998b). The capital costs of IGCC plants are currently about 20 to 30% higher than those of conventional coal- and oil-fired power plants. Current IGCC plants exhibit poor reliability, this being due to the different individual components in an IGCC plant, some with parts which have not been fully optimised for application with IGCC. IGCC's availability is about 75%, lower than the approximately 90% availability for a PF boiler with FGD. IGCC's low operational flexibility is attributed to the plant's very long start up times from cold especially for highly integrated plants.

Current limitations of IGCCs have to be addressed and overcome for this technology to gain wider acceptance and application. There is a wide scope to improve on the first generation plants as well as to develop the second generation and the succeeding systems (Mitchell, 1998). This necessitates improvements in various areas of the IGCC, a major one being hot fuel gas cleaning.

1.3   The Need for Hot Fuel Gas Cleaning

Hot fuel gas cleaning generally refers to the removal of fuel gas impurities at temperatures above 250°C (Mitchell, 1998) before the gas stream enters the gas turbine. The integration of hot gas clean-up (HGCU) technology to remove pollutants from coal-derived fuel gas offers the prospect of increasing thermal efficiency whilst simultaneously reducing the capital and operating costs of IGCC systems without compromising the environmental performance. Research and development in HGCU has been propelled by the desire to make IGCCs more competitive to conventional coal-based power generation technologies. Both the US DOE (2000) and the UK DTI (1998b) have identified HGCU as one of the major areas of technology requiring further research and development to help improve IGCC systems.

1.3.1   Gas Turbine Protection

The raw fuel gas produced in the gasifier typically contains major contaminants comprising solid particulates, sulphur (H_2S, COS) and nitrogen compounds (NH_3, HCN) as well as minor contaminants of alkali metals (Na, K), alkaline earth metals (Ca, Mg), heavy trace metals (Pb, V, Zn, As, Se, Hg, Cd), halogens (Cl, F), and polycyclic aromatic hydrocarbons (PAHs). The particulates, alkali and alkaline earth metals, halogens and the heavy metal species can cause deposition, erosion and corrosion to the gas turbine parts and degradation of downstream equipment. Therefore the chief aim of gas cleaning in combined cycle systems is to protect gas turbine and downstream equipment, thus preventing costly mechanical damage by these contaminants. The safe limits for the contaminants are specified by gas turbine manufacturers based on experience, gas turbine design and materials corrosion data. The figures can vary quite significantly among the various gas turbine designs as shown in Table 1.3:

Table 1.3   Fuel standards for various gas turbines (Williams and McMullan, 1998).

	Siemens	Nuovo Pignone	GEC Alsthom	ABB	United Aircraft	Pratt & Witney	Westing-house	General Electric
Calorific Value		Adiabatic Flame Temperature >1600°C, CO:H_2 <1.7						
Temperature		Present control valve limit 400°C, Auto-oxidation of H_2 ~500°C (if O_2 Present)						
Sulphur (ppmv) (H_2S + COS)	Emission only	5	100	3000	1800	1800	2500	1
N_2 Comps (ppmv) (NH_3 + HCN)	Emission only	n.d	n.d	n.d	n.d	n.d	n.d	n.d
Alkali Metals (ppbv) (Na + K)	35-80	50-80	n.d	500	200-600	100	70-150	100
Alkaline Earth (ppbv) (Ca, Mg)	120-260	340	n.d	2000	100	10	1400	230
Halogens (ppmv) (Cl, F)	1.5	n.d	<dew pt	n.d	n.d	n.d	n.d	n.d
Vanadium (ppbv)	n.d	85	n.d	1000	n.d	n.d	n.d	n.d
Lead (ppbv)	n.d	170	n.d	500	n.d	n.d	n.d	n.d
Zinc (ppbv)	n.d	n.d	n.d	500	n.d	n.d	n.d	n.d
Reference	[*]	[@]	[&]	[#]	[#]	[#]	[#]	[#]

n.d   No data available
N.B.   The limit can depend on the calorific value of the fuel.
        Alkali metals can affect the sulphur limit due to alkali sulphate formation.
*   Haupt, G. *et al.* (1995) Can hot gas clean-up improve IGCC efficiency today? *In: Power-Gen Asia 95*, Singapore 27-29 September 1995.
@   Modi, R. (1996) *Fuel gas requirements for gas turbine applications.* Contract No. JOF3-CT95-0018, Funded in part by the EC in the framework of the Non Nuclear Energy Programme, Joule III.
&   Brown, D. (1994), European Gas Turbines, *private communication.*
#   Gang, P. and Loffler,F. (1993) Cleaning of hot gases from coal gasifiers in a dry combined process. *In: Gas cleaning at high temperatures.* Blackie Academic and Professional.

A slightly more recent specification for a high efficiency gas turbine is given in Table 1.4:

Table 1.4   *Gas turbine specifications (Siemens Model VX4-3A) (Haupt, 1997).*

Contaminant	Chemical formula	Emission limit†	Comment
Particulates		2 ppmw	Grain size: >10 μm: 0; 2-10 μm: 7.5%; 0-2 μm: 92.5%
Sulphur compounds	$H_2S + COS + CS_2$	20 ppmv	Emission only‡. Only corrosive in combination with alkalis
Nitrogen compounds	$NH_3 + HCN$	–	Emission only
Hydrogen halides	$HCl + HF$	1.0 ppmw	
Alkalis	Na + K	0.03 ppmw	
Heavy metals	V	0.05 ppmw	
	Pb	1 ppmw	
Calcium	Ca	1 ppmw	

* specifications for Siemens Model VX4-3A gas turbine
† based on a lower heating value of 4 MJ/kg fuel, typical of fuel gas diluted with nitrogen and steam for NO_x suppression
‡ in order to reach very low SO_2 content in the flue gas of about 25 mg/m³ (6% O_2, STP (0°C (273 K), 101.3 kPa))

Solid particulates smaller than 10 μm entering the gas turbine is tolerable up to about 2 ppmw, but those bigger than 10 μm are limited by more stringent levels. Smaller particulates pose a lower risk of erosion as they follow the gas streamlines around the turbine blades more easily.

Sulphur compounds can combine with alkali species in the fuel gas to form alkali sulphates which can cause high temperature corrosion of the gas turbine. The limits for sulphur compounds are set assuming that there is a sufficiently high concentration of alkali metals in the gas stream of greater than 0.03 ppmw. Alkali species can also be added into the gas stream along with Ca-based desulphurisation sorbents by condensing or attaching to the bed material.

Nitrogen compounds are converted to NO_x in the gas turbine, hence their removal before combustion is desirable to minimise NO_x emissions. The degree of damage due to halogens or hydrogen halides is still unclear but a maximum limit of about 1 to 2 ppmv is often quoted based on gas turbine design and materials corrosion data. Trace heavy metals can condense out in the cooling stages and therefore their removal from the gas stream is desirable both to protect the gas turbine and heat exchanger surfaces.

1.3.2   Environmental Requirements

Another important goal of gas cleaning is to ensure that emission levels from power plants conform to existing environmental standards especially with regards to the three major pollutants i.e. solid particulates or dust, sulphur dioxide (SO_2) and nitrogen oxides (NO_x). Air pollution legislation is either being established or tightened worldwide as concern over air pollution and its local, regional and transboundary effects increase (McConville, 1997). Existing emission standards in the industrialised nations of Western Europe, North America and Japan are being tightened whilst countries in Central and Eastern Europe are putting into place new air pollution legislation, mainly adopted from the EC. Existing and new coal-based power plants in Asia have to conform to increasingly stringent national air pollution regulations, which are very much driven by changes in international legislation.

A number of international standards have been established to control transboundary air pollution (McConville, 1997). These include protocols made under the United Nations Economic Commission for Europe (UNECE) Convention on Long-Range Transboundary Air Pollution (or LRTAP Convention) signed by European countries as well as USA and Canada, the European Community's (EC) environmental legislation which is binding on its 15 member countries and which also influences Central and Eastern European countries, and the World Bank environmental guidelines which are becoming increasingly important in developing countries in which projects are funded by the World Bank.

Table 1.5 lists the emission standards for particulates, SO_2 and NO_x for new coal-based power plants in selected countries as well as several international standards.

The emission standards range from 20 to 3700 mg/m^3 for particulates, 30 to 3400 mg/m^3 for SO_2 and 95 to 1690 mg/m^3 for NO_x. Compared to gas turbine specifications, the emission standards for particulates are less strict, being substantially higher typically by a factor of ten or greater (Mitchell, 1997; 1998). In general, the contaminant limits specified for a gas turbine are notably lower than corresponding environmental emission restrictions for the same contaminant.

Unlike the mandatory restrictions on particulates, SO_2 and NO_x, the available limits on trace emissions like volatile organic compounds (VOCs), other organic compounds (polycyclic aromatic hydrocarbons, furans, dioxins), hydrogen halides, halogens, alkali metals and heavy metal species (Cd, Hg) are mainly just recommendations or guidelines (Mitchell, 1998).

Table 1.5 *Emission standards (mg/m^{3*}) for particulates, SO_2 and NO_x for new coal-fired plant (>100 MWth) (IEA Coal Research, 1998).*

Country	Particulates	SO_2	NO_x
Australia	80-280†	–	535-860†
Austria	50-280	200-550	200-660
Belgium	50	250-2000	200-650
Canada	145†	740†	490-740†
China, mainland	200-500	‡ §	670
China, Taiwan	50-500	570-1430	515-1025
Czech Republic	100-150	500-2500	650-1100
Denmark	55	400-2000	200-650
Finland	380-620	30-540	135-405
France	50-100	400-3400	650-1300
Germany	50-150	400-2000	200-500
India	150-350	–	–
Italy	50	400-2000	200-650
Japan	30-300	‡	205-980
Netherlands	20-50	200-700	100-500
Poland	190-3700	540-1755	95-460
Spain	50-500	400-2000	650-1300
Sweden	35-50†	160-270	135-540†
Switzerland	55-160	430-2145	215-860
Turkey	140-200	430-1875	800-1690
United Kingdom	50 (25**)	400-2000 (200-300**)	650-1300 (60-270**)
USA	37-123	740-1480	220
UNECE		400-2000	
EC	30	200-850†† 200‡‡	300 200‡‡
World Bank¶	50	2000	750

* emission standards are converted to mg/m³ on dry flue gas at 6%O₂ and standard temperature and pressure (0°C (273 K), 101.3 kPa)
† guidelines
‡ plant specific standards set
§ for plants built after 1 July 1997, the following standards also apply: 2100 mg/m³ for plants using <1% sulphur coal: 1200 mg/m³ for plants using >1% sulphur coal
¶ proposed standards
** achievable emission levels to be taken into account for plant built after 1995
†† for plants 100-300 MWth linear decrease (-3.3P + 1175, where P = plant size in MWth)
‡‡ for plants greater than 300 MWth

Table 1.6 compares typical gas turbine and environmental emission limits for the major gas contaminants of solid particulates, sulphur and nitrogen compounds.

Table 1.6 *Typical gas turbine and environmental emission limits for major gas contaminants (adapted from Mitchell, 1998).*

Contaminant	Gas Turbine Limits	Enviromental Emission Limits	Comments
Particulates	2 ppmw	Process goals more stringent	Grain size limitations typically set by turbine specification Higher specification for 'ruggedised' turbines
Sulphur compounds	20 ppmv or emission only	Subject to regulatory control	Only corrosive when combined with alkali metal species Specified limits correspond to low flue gas SO_2 content
Nitrogen compounds	Emission only	Subject to regulatory control	-

1.3.3 Fuel Gas Cleaning versus Flue Gas Cleaning

End-of-pipe commercial flue gas treatment systems such as conventional fabric filters (bag houses), electrostatic precipitators, selective catalytic reduction and flue gas desulphurisation technologies can be used to reduce most coal gas pollutants to levels conforming to current emission standards. However, it is commonly considered more energy- and cost-efficient in combined cycle systems to clean the fuel gas stream at high temperature and pressure prior to being combusted in the gas turbine (Mitchell, 1998). Prospective advantages of fuel gas cleaning includes better thermal efficiency, lower capital and operating costs attributed to cleaning of smaller volume of high-pressure coal gas before expansion in the gas turbine compared to the more voluminous flue gas after the turbine, better system control, the utilisation of a more advanced, high efficiency gas turbine and the reduction or possibly the removal of costly gas and water treatment facilities.

1.3.4 Hot Fuel Gas Cleaning versus Cold Fuel Gas Cleaning

There are two types of approach in purifying the fuel gas exiting from a gasifier. These are generically termed the cold gas clean-up (CGCU) and the hot gas clean-up methods (HGCU) according to the operating fuel gas temperatures.

The conventional way is the cold (or wet) gas clean-up method where the hot fuel gas from the gasifier is first cooled in a heat exchanger to temperatures less than 200°C (Mitchell, 1997) prior to entering the gas cleaning train. In current demonstration units, the syngas is cooled to below 100°C for conventional cleaning (IEA Coal Research, 2002). The cooled fuel gas stream then passes through a cyclone where most of the entrained solid particulates are separated. This is followed by the removal of nitrogen compounds, halides, alkalis, trace elements and any residual particulates or tarry substances in a series of venturi water scrubbers followed finally by the scrubbing of sulphurous gases in an acid gas treatment plant. These cold gas cleaning techniques are proven technologies in removing particulates, sulphur and nitrogen compounds, halides as well the various metal species in the fuel gas.

In hot gas clean-up, the operating conditions of the gas purification train are closer to those of the gasifier and gas turbine (compared to CGCU), typically at temperatures of about 300 to 600°C and at pressures of about 10 to 25 bar to reduce efficiency losses associated with cooling (Fantom, 1997). The technologies involved in HGCU include cyclone separators to remove coarse particulates, ceramic candle filters to remove fine particulates, chemical

processes with or without combination with filters to remove compounds of sulphur, nitrogen, halogens, as well as alkali and heavy metal species.

Although current established cold (wet) fuel-gas clean-up (CGCU) methods are well-proven technologies offering excellent environmental performance, their limitations associated with fuel gas quenching have brought about the need for HGCU systems. The main advantages offered by HGCU over CGCU are superior thermal efficiency and smaller capital and operating costs.

❑ *Improved Thermal Efficiency*

Existing cold gas cleanup technologies have an adverse effect on cycle efficiency. Although the heat transferred from the cooling of the hot fuel gas (to below 200°C) can be used to raise steam, the steam cycle is less efficient than the gas turbine cycle, hence causing a significant loss in efficiency. This cycle efficiency penalty increases with the quantity of the fuel gas and hence is greater for air-blown gasification. Considerable thermal efficiency loss is also associated with liquid scrubbing at or below ambient temperatures. The fuel gas contains a significant amount of steam which is condensed out in the wet system, resulting in large losses in the latent heat of the steam to cooling water. This effect is more pronounced for wet-feed gasifiers which give higher steam content in the fuel gas. In HGCU, gas quenching is reduced, thereby conserving the sensible and latent heat content of the fuel gas and allowing maximum heat transfer to the more efficient gas turbine. Efficiency losses are minimised and hence, higher overall cycle efficiencies are achieved. Efficiency improvements of 1 to 3 % points have been reported for air-blown, fluidised bed gasification utilising hot gas cleaning compared to the same process with cold gas cleaning (Haupt *et al.*, 1995).

❑ *Reduced Capital and Operating Costs*

Systems incorporating CGCU processes require costly heat-recovery equipment to improve overall thermal efficiencies. The wet clean-up method consumes a large quantity of water and produces aqueous effluent necessitating expensive pre-disposal treatment. On the other hand in HGCU, water consumption to run the system is significantly reduced hence cutting down on operating cost. Dry scrubbing eliminates the production of wet slurry, doing away with costly wastewater treatment facilities and the corresponding additional hardware. Heat exchanger

duty is significantly reduced and complex heat-recovery is unnecessary, simplifying plant configuration and reducing the overall capital investment of the IGCC system.

The combined effect of improved efficiencies and reduced capital and operating costs potentially results in lower cost of electricity for IGCC when incorporating HGCU compared to CGCU. However to fully realise the cost and environmental advantages over the cold systems, it is essential that the HGCU systems have the cleaning performance, reliability and availability comparable to, if not better than the current established wet gas cleaning systems.

1.4   The Future of Hot Fuel Gas Cleaning

Mitchell (1997; 1998) reviewed the current technological and commercial status of hot gas cleaning technologies applicable to coal-based combined cycle power generation systems. He concluded that despite some developers view that similar benefits associated with the use of hot gas cleaning can be potentially achieved by other means (for example by combining improved heat transfer with conventional cold gas cleaning or through the development of advanced steam cycles and gas turbine technologies), hot gas cleaning will persist as a major component of coal-based combined cycle power generation systems. Hot gas cleaning will be especially relevant for the air-blown, fluidised bed integrated gasification combined cycle (IGCC) system and circulating pressurised fluidised bed combustion (PFBC) system. Cleaning of coal-derived fuel gas at high temperature and pressure will enhance the competitiveness of IGCC and PFBC systems relative to advanced pulverised coal combustion (PCC) and combined cycle natural gas (CCNG) systems. Further development in hot gas cleaning is necessary to push the operating temperatures to approach those of the gas turbine (typically up to 900°C) such that the advantages of gas purification at elevated temperatures can be fully realised. Substantial prospects have also been identified for the incorporation of hot gas cleaning into fuel cell systems as well as in the energy conversion from biomass and waste which demand more stringent gas cleaning requirements.

Summing up, hot gas cleaning will continue to play a major role in the development of coal-based combined cycle power generation systems in the foreseeable future.

1.5   Objectives of This Investigation

Current hot gas clean-up methods focus on the use of metal oxide sorbents for sulphur removal and the utilisation of ceramic barrier filters for particulate cleaning. In contrast, this research project adopts an unconventional approach to hot fuel gas cleaning technology incorporating molten tin as the scrubbing medium for the removal of H_2S (and COS) and solid particulates, as first put forward by Warner (2000).

In the proposed gas cleaning process, high temperature sulphur removal takes place in a non-wetting, liquid tin irrigated moving packed bed. Sulphur removal occurs via absorption of hydrogen sulphide into molten tin:

$$H_2S + Sn \rightarrow SnS + H_2$$
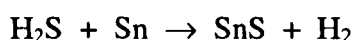
In addition to gas desulphurisation, the packed bed offers the prospect of simultaneous removal of solid particulates from the gas stream, hence acting as a multicomponent clean-up device. Molten tin having high surface energy exhibits non-wetting droplet and rivulet flow on the solid packing surface, potentially giving good inertial capture of solid particulates by the packed bed from the gas stream.

The primary aim of this research project is to perform studies on a room-temperature packed bed scrubber operating under non-wetting conditions analogous to liquid metal flow. The non-wetting characteristic of liquid metals is simulated in the laboratory using water irrigation of a bed of packings having low surface energy. Findings from the investigation would provide insight and understanding into the operation and performance of a packed bed scrubber working under non-wetting flow conditions. Ultimately, this knowledge will contribute towards the development of a geometrically similar, high temperature packed bed gas scrubber irrigated by molten tin for H_2S and particulates removal.

The specific objectives of this PhD programme are as follows:

- To carry out a comprehensive literature search on previous work done in this field.

- To conduct a preliminary investigation into the effect of molten tin on H_2S in the fuel gas derived from small-scale gasification of petroleum coke batch samples.

- To perform studies on the operational hydraulics of a small-scale packed column operating under non-wetting conditions.

- To explore the performance of a small gas lift for liquid circulation through the packed column.

- To investigate particulates removal and gas absorption performance of the packed bed scrubber operating under non-wetting flow conditions.

- To perform computational fluid dynamics modelling using FLUENT on particulate removal in a packed bed under non-wetting conditions.

- To investigate the design of the molten tin based hot gas scrubber, geometrically similar to the air-water model. The dimensions and operating parameters for the hot scrubber to be based on findings from the cold tests.

Following this introductory chapter, Chapter 2 reviews the existing high temperature gas cleaning technologies focussing on sulphur removal and particulate control, including hot gas clean-up using liquid metals. The theory and findings from the literature search on packed column and gas lift operations are outlined in Chapter 3. In Chapter 4, the theoretical background and previous work on gas-solid separation and gas absorption are considered. Details of the experimental programme undertaken in this PhD programme are outlined in Chapter 5 whilst the experimental results are reported and discussed in Chapter 6. The ensuing Chapter 7 covers the computational fluid dynamics simulations performed on particulate removal in a non-wetting packed bed using FLUENT. The design and construction of the hot gas scrubbing system are outlined in the penultimate Chapter 8. Lastly, conclusions are drawn from this investigation and recommendations made for future work in Chapter 9.

Chapter Two

Review of Existing High Temperature Gas Cleaning Technologies

This chapter reviews the available technologies for hot gas desulphurisation and particulate clean-up. Metal oxide sorbents are currently the leading technology for high-temperature sulphur removal. Emphasis is therefore given to the status of disposable and regenerable metal oxide sorbents for the removal of hydrogen sulphide from fuel gas under reducing conditions. This is followed by a review on the various particulate control technologies available and their potential for high temperature gas cleaning. These include ceramic (rigid) barrier filters, the most advanced hot gas particulate control technology to date, and alternative devices including cyclones, electrostatic precipitators, fabric filters, metallic filters and granular bed filters. The final part of this chapter examines previous work on hot gas cleaning using liquid metals which culminates with the proposed molten tin based fuel gas cleaning system that is of interest in this investigation. The research scope is defined at the end of this chapter.

2.1 Hot Gas Desulphurisation

The removal of sulphur compounds (mainly H_2S and COS) from fuel gas is essential to minimise alkali sulphate formation that corrodes gas turbine and heat exchanger parts, to allow deep cooling of flue gases in the waste heat boiler without incurring dew point corrosion, as well as to comply with SO_2 emission standards (see Table 1.5). The gas turbine limits set for sulphur compounds assume that the alkali metal specification is not adhered to (see Table 1.4). Extensive reviews on the technological and commercial status of hot gas desulphurisation technologies were documented by Mitchell (1998) and Williams and McMullan (1998).

Metal oxides possess sulphur removal capability. Since the late 1970s, researchers have tested and developed metal oxide sorbents for hot gas desulphurisation. These metal oxide sorbents can generally be classified into two categories i.e. disposable and regenerable sorbents.

2.1.1 Disposable Sorbents (In-Situ Desulphurisation)

The disposable sorbents are mainly calcium-based materials for instance dolomite ($CaCO_3.MgCO_3$), lime (CaO) and limestone ($CaCO_3$) which are cheap and abundantly

available. They are used in a once-through mode in the fluidised bed gasifier (as well as in fluidised bed combustion systems), removing up to 90% (Mojtahedi *et al.*, 1994) of sulphur in the fuel. The sorbents can be incorporated in-bed, injected into the gas stream, or directly contacted in an external reactor unit. This in-situ high-temperature desulphurisation process is well-proven and involves the following reaction for H_2S removal under reducing conditions:

Sulphidation: $\qquad CaO\ (s) + H_2S\ (g) \rightarrow CaS\ (s) + H_2O\ (g) \qquad\qquad$ (2.1)

Direct sulphidation: $\qquad CaCO_3\ (s) + H_2S\ (g) \rightarrow CaS\ (s) + CO_2\ (g) + H_2O\ (g) \qquad$ (2.2)
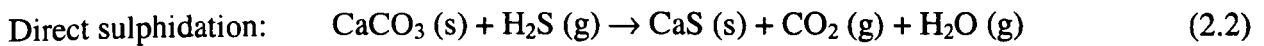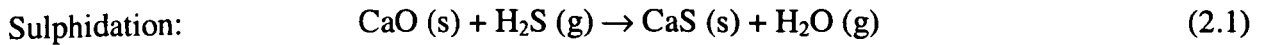
Unstable CaS is formed which is then reacted with air forming the environmentally stable $CaSO_4$ (gypsum) to be disposed off with the gasifier bottom ash. There are several disadvantages associated with the use of these disposable sorbents. Sintering and pore plugging at high temperatures reduce calcium availability, inhibiting CaS stabilisation to $CaSO_4$ and necessitating a secondary oxidiser for complete conversion of CaS to $CaSO_4$. In-bed sulphur retention within the gasifier is limited by thermodynamics at low temperatures. Sulphur removal is 80 to 90% which is lower then the desirable level of 95 to 99% for IGCC (Gangwal *et al.*, 1995), necessitating post-bed H_2S polishing to further reduce the residual H_2S. The resulting $CaSO_4$ has no market value, requiring landfilling which incurs additional removal costs and may pose a problem where land is scarce.

Although H_2S is the main sulphur component in the fuel gas and hence is the focus in the literature regarding gas desulphurisation, similar sorbent sulphidation reactions to those represented by equations 2.1 and 2.2 should apply to COS as well.

2.1.2 Regenerable Sorbents (Post-Bed Desulphurisation/Polishing)

The research focus of hot gas desulphurisation has shifted from once-through disposable calcium-based sorbents to regenerable mixed metal oxides sorbents. This shift is mainly due to the generation of a large amount of sulphur-containing Ca-based solid waste of no commercial value from the former, requiring costly disposal. With the latter, solid wastes are reduced and commercial products such as H_2SO_4 acid and elemental sulphur can be recovered instead.

The metal oxide sorbents are used either to polish the residual H_2S not removed by the in-bed disposable Ca-based sorbents (polishing mode), or to almost completely remove H_2S in the fuel gas from gasifiers that do not incorporate the in-situ desulphurisation (bulk mode). The sulphided sorbent then undergoes regeneration to recover the metal oxide to be reused.

Initial studies concentrated on metal oxides operating at temperatures above 600°C as it was thought that the overall system efficiency improves at higher temperatures. But under long-term high-temperature operation, only a few metal oxide sorbents were able to remove H_2S in the fuel gas to below 20 ppmw to meet gas turbine and emission standards requirements. This drastically limited the choice of sorbent material. More recently, it has been recognised that the thermal efficiency loss associated with lower temperature operation is relatively small, shifting the focus to the use of metal oxide sorbents at a lower temperature range of 350 to 600°C and expanding the choice of potential sorbent material. In addition to lower operating temperature sorbents, there is also now more emphasis on the development of direct sulphur recovery processes (DSRPs) and steam-resistant sorbents, all of which are envisaged to potentially reduce the overall cost of the hot gas clean-up system.

The sulphidation (absorption) and regeneration (desorption) reactions involving metal oxide sorbents can be represented by the following general equations:

Sulphidation: $\qquad M_yO_x \text{ (s)} + xH_2S \text{ (g)} \rightarrow M_yS_x \text{ (s)} + xH_2O \text{ (g)}$ (2.3)

Regeneration: $\qquad M_yS_x \text{ (s)} + (3/2) xO_2 \rightarrow M_yO_x \text{ (s)} + xSO_2 \text{ (g)}$ (2.4)

$\qquad\qquad\quad M_yS_x \text{ (s)} + 2xH_2O \rightarrow M_yO_{2x} \text{ (s)} + xH_2S \text{ (g)} + xH_2 \text{ (g)}$ (2.5)
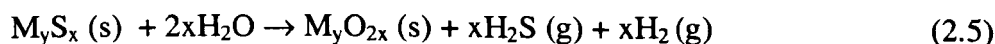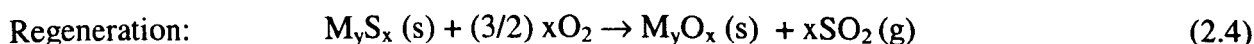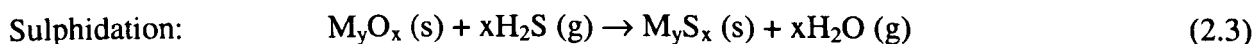
M_yO_x and M_yS_x are the reactive transition metal oxide and the corresponding metal sulphide respectively. The sulphidation reaction should be thermodynamically favourable such that H_2S and COS removal is greater than 99%, while the thermodynamics of metal oxide reduction to metal should be unfavourable to avoid sorbent loss.

Sorbent regeneration is carried out with either air or oxygen, although steam can also be used. Regeneration with air is highly exothermic, requiring a large amount of diluent (nitrogen or steam) in addition to air. Rigid control within a narrow temperature range is necessary to avoid metal sulphate formation at low temperature and sorbent sintering or degradation at high temperature. Air regeneration results in a dilute SO_2 tailgas which in turn must be treated, the final product being either elemental sulphur or H_2SO_4, both having commercial values.

The development and testing of regenerable metal oxide sorbents for hot gas desulphurisation are mainly conducted in the USA with several in Europe, Japan and China (Williams and McMullan, 1998). Various oxides of metals such as copper, cerium, manganese, cobalt, tin, iron and zinc have been researched (Gangwal *et al.*, 1995). These oxides are sometimes mixed with secondary oxides such as silica, alumina, titania and chromia which do not take part in

the sulphidation reaction but instead give additional mechanical support, stabilise the main metal oxides and minimise sorbent losses, as well as aid regeneration. Table 2.1 lists the main metal oxides used as regenerable sorbents and their characteristics.

Table 2.1 Sorbent general characteristics (Williams and McMullan, 1998).

Sorbent	Absorption Temperature (°C)	Regeneration Temperature (°C)	Sorbent Utilisation (%)	H₂S Outlet Concentration (ppmv)
Tin dioxide	350 - 500	400 - 500	85	<100
Copper oxide	350 - 550	650	70	<20
Manganese oxide	350 - 870	900	50	<10
Iron oxide	360 - 500	500 - 650	25 - 45	<100
Zinc oxide	480 - 540	500 - 700	50 - 70	<1
Zinc ferrite	450 - 600	600	20 - 80	<20
Zinc titanate	450 - 750	600 - 750	40 - 60	<10
Copper chromite	650 - 850	No data	40 - 80	<10
Cerium oxide	750 - 1000	600	90	<100

Sorbent reactivity, sulphur retention capacity, chemical resistance, mechanical durability and regeneration efficiency are the main issues addressed in the search for a leading H_2S sorbent. Among the various single and mixed metal oxides evaluated, zinc oxide-based sorbents have commanded the most attention and are currently the leading sorbents for hot gas desulphurisation. This is because zinc oxide demonstrates highly favourable thermodynamics for reaction with H_2S, capable of H_2S removal efficiency of 99% or greater (Gangwal *et al.*, 1995). Extensive research has been carried out on zinc oxide-based sorbents (including Fe and Ti) since the early 1980s and has reached pilot and demonstration scales, whereas sorbent development based on other metal oxides remains at the laboratory scale (Mitchell, 1998).

2.1.2.1 Zinc Ferrite

Earlier work focused on zinc ferrite ($ZnFe_2O_4$), the combination of zinc oxide (ZnO) and iron oxide (Fe_2O_3). On their own, ZnO exhibited better sulphidation thermodynamics than Fe_2O_3, but slower sulphidation kinetics. Combined, zinc ferrite sorbent was found to have higher sulphur absorption capacity than ZnO alone, significantly higher desulphurisation levels (greater than 99%) than Fe_2O_3, as well as showed fast, complete reaction with H_2S. However the use of zinc ferrite is limited to temperatures below 600°C and to moderately reducing coal gas to minimise sorbent loss. Both the ZnO and Fe_2O_3 components are unstable in reducing conditions, being converted to the elementary metals and this is aggravated at higher temperatures. Complete and rapid regeneration is possible at 650°C without significant loss of

sulphidation capability. Strict temperature control is necessary during regeneration due to zinc sulphate formation at lower temperatures and sintering at higher temperatures which reduce the sulphidation reactivity. The main chemical reactions in the desulphurisation cycle involving zinc ferrite are as follows (Mitchell, 1998):

Reduction: $ZnOFe_2O_3 (s) + 1/3H_2 (g) \rightarrow ZnO (s) + 2/3Fe_3O_4 + 1/3H_2O (g)$ (2.6)

Sulphidation: $ZnO(s) + 2/3Fe_3O_4(s) + 3H_2S(g) + 2/3H_2(g) \rightarrow ZnS(s) + 2FeS(s) + 11/3H_2O(g)$ (2.7)

Regeneration: $ZnS (s) + 2FeS (s) + 5O_2 (g) \rightarrow ZnOFe_2O_3 (s) + 3SO_2 (g)$ (2.8)
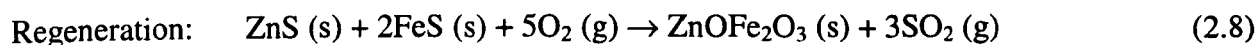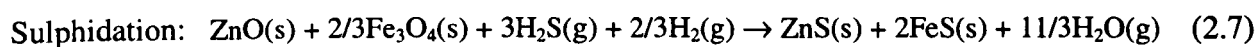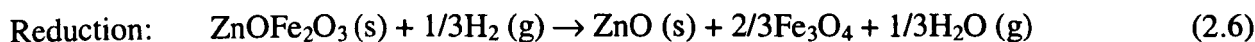
Zinc ferrite sorbents that are being developed in the USA include TNT-MB by TDA Research and Norton as well as the R-5 Series by RTI. At CRIEPI in Japan, a zinc ferrite and silicon dioxide formulation is being tested (Mitchell 1998; Williams and McMullan, 1998).

2.1.2.2 Zinc Titanate

The limitations of zinc ferrite sorbents led to extensive research in zinc titanate (ZnO-TiO_2), currently one of the leading regenerable sorbents for hot gas desulphurisation. Zinc oxide (ZnO) is the active component while titanium oxide (TiO_2) acts as an inert support. TiO_2 also stabilises ZnO, forming mixed metal oxides and preventing ZnO reduction to elemental Zn which can be lost by vaporisation at higher operating temperatures. The chemical reactions in the desulphurisation cycle involving zinc titanate are as follows (Mitchell, 1998):

Sulphidation: $Zn_2TiO_4 (s) + 2H_2S (g) \rightarrow 2ZnS (s) + TiO_2 (s) + 2H_2O (g)$ (2.9)

$Zn_2TiO_3 (s) + H_2S (g) \rightarrow ZnS (s) + TiO_2 (s) + H_2O (g)$ (2.10)

Regeneration: $2ZnS (s) + TiO_2 (s) + 3O_2 (g) \rightarrow Zn_2TiO_4 (s) + 2SO_2 (g)$ (2.11)
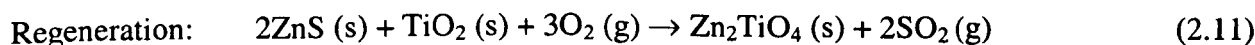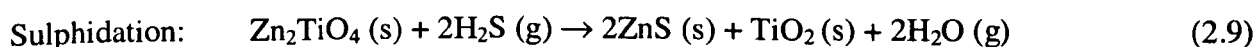
Lew *et al.* (1989) found that zinc titanate sorbent showed lower rate of zinc loss compared to ZnO, but comparable sulphidation kinetics and H_2S removal efficiency in reducing conditions at 650°C. However, zinc titanate has smaller sulphur absorption capacity compared to zinc ferrite because unlike Fe_2O_3 in zinc ferrite, the TiO_2 component in zinc titanate is inert to sulphidation. Rutkowski *et al.* (1993) showed that the overall sorbent cost could be 25 to 35% higher with zinc titanate compared to zinc ferrite as the former is more expensive and possess lower sulphur loadings. However, zinc titanate appeared to have higher mechanical stability.

In general, extensive laboratory-scale tests carried out on fixed beds and fluidised beds have yielded conflicting data about the performance of zinc titanate sorbents (Mitchell, 1998). Such

variations are common, not only to zinc titanate, and are mainly due to different behaviour of sorbents in different reactor systems.

Nearly all the developmental work on zinc titanate sorbents are carried out in the USA (Mitchell, 1998; Williams and McMullan, 1998). This includes the ZT-4, CMP-5 and CMP-107 sorbents by RTI and CMP, the EX-SO3 sorbent by RTI and IDI, the ZVT12LN sorbent by TDA Research and Norton, the MZT Series by GE and UCI, the ICCI-1 and ICCI-2 sorbents by E&A Associates and UCI, and the UCI Series by IGT and UCI. In Europe, zinc titanate sorbents have been tested by Carbona Inc. and Åbo Akademi University in Finland. In China, the China Coal Research Insitute (CCRI) has developed the MC Series sorbents based on zinc titanate-iron titanate formulations.

2.1.2.3 Modified Zinc Oxides

Based on initial experience with zinc ferrite and zinc titanate sorbents, modifiers and additives were used to enhance the performance of the basic zinc oxide material. This leads to new modified zinc oxide formulations, nearly all of which are developed in the USA (Mitchell, 1998; Williams and McMullan, 1998).

Phillips Petroleum's Z-Sorb® (ZnO-NiO formulation) is the most highly developed sorbent available, having undergone extensive testing at temperatures of 315 to 550°C and pressures of 0.5 to 2.0 MPa in various reactor configurations (fluidised bed, moving bed, fixed bed, transport reactor) and at different test levels (bench-, laboratory-, pilot plant-scales). Z-Sorb® sorbents have been supplied for demonstration-scale tests in a General Electric (GE) moving bed reactor at the TECO Polk Power plant and in a MW Kellogg transport reactor at the SPPC Piñon Pine plant. Further sorbent development is still necessary for commercial application.

The METC10 sorbent produced by FETC has been tested on a fixed bed reactor system at FETC, a moving bed reactor at GE and a fixed bed reactor at RTI. In all cases, good attrition resistance and stable reactivity was demonstrated under simulated and actual fuel gas conditions. UCI's METC10-M sorbent, a modified version of METC10 has been evaluated on a fixed bed reactor at RTI. CMP manufactured spray-dried versions of the METC10 sorbent with improved attrition resistance, these were tested at FETC in a fluidised bed reactor.

Other modified zinc oxide formulations developed in the USA include the MCRH Series sorbents jointly by Hampton University, UCI and RTI, as well as the 40ZN and 268-60

sorbents by TDA Research. In Japan, a zinc oxide-based sorbent is being developed by CRIEPI and Hitachi for molten carbonate fuel cell application.

2.1.3   Reactor Designs

There are four types of reactor configurations for sulphidation and regeneration of a sorbent: fixed bed, moving bed, bubbling fluidised bed and circulating fluidised bed (or transport reactor). Fuel gas composition, operating and process requirements dictate the type of reactor to be used. The reactor design in turn affects the physical and mechanical properties requirements of the sorbent. In general, strong, small sorbent particles (100 to 300 μm) with high resistance to spalling are required in fluidised bed reactors (bubbling or circulating), whereas sorbent requirements are less stringent for fixed bed and moving bed reactors in which larger particles (3 to 6 mm) can be used. All four reactor types have undergone significant commercial development such that there is a considerable degree of confidence that scale-up to demonstration units will be successful. Bubbling and circulating fluidised bed (transport reactors) appear to be the most favourable for hot gas desulphurisation application in IGCC (Mitchell, 1998). This is because both utilise small sorbent particle size and have moderate attrition resistance to attain high sulphur removal at temperatures between 350 to 600°C. Also, temperature control during repeated cycling is easier in fluidised bed systems.

2.1.4   Current Limitations

From their reviews of existing hot gas desulphurisation technologies, Mitchell (1998) concluded that no fully commercialised desulphurisation sorbent is available as yet, while Williams and McMullan (1998) documented that "the perfect sorbent is still a long way from commercial reality". There are still issues to be resolved regarding sorbent performance during long-term operation in different reactor systems. In particular, problems related to sorbent mechanical strength, chemical attrition resistance, long-term durability and reactivity have yet to be fully addressed.

2.2   Hot Gas Particulate Cleaning

The technological and commercial status of hot gas particulate cleaning technologies have been extensively reviewed and discussed by Seville (1996; 1997), Seville *et al.* (1996) and

Mitchell (1997). Table 2.2 summarises the particulate control technologies considered for high temperature combined cycle applications and their main performance characteristics:

Table 2.2 Hot gas particulate cleaning technologies (Mitchell, 1997).

Device	Particle Capture Mechanism	Particle Rejection Mechanism	Pressure Drop	Flow capacity	Particle Removal
Cyclones	Inertial concentration	Gravity flow of fly ash (continuous)	High	Moderate	Moderate
Electrostatic Precipitators	Particle charging and migration to plates	Mechanical rapping of plates (intermittent)	Very low	Moderate	Moderate
Bag Filters	Cake formation	Back pulse with clean gas (intermittent)	Low	Moderate	High
Granular Bed Filters	Impact/Diffusion	Gravity flow of granules; granule cleaning (intermittent)	Moderate	Low	High
Metallic Filters	Cake formation	Back pulse with clean gas (intermittent)	Moderate	High	High
Rigid barrier filters	Cake formation	Back pulse with clean gas (intermittent)	Moderate	High	Very high

2.2.1 Ceramic (Rigid) Barrier Filters

Ceramic barrier filters are currently the most advanced and the most optimistic looking technology available in hot gas particulate filtration. They boast of high dust collection efficiencies with only low pressure and temperature drops across the system. The filtration efficiency is "usually extremely close to 100%" (Seville, 1996; 1997) with the exception of substantially submicron dust or large filter medium granule or fibre size. Recent development has also seen the application of ceramic filters for simultaneous removal of particulates and other gaseous contaminants.

2.2.1.1 Ceramic Filter Media

The two available generic types of ceramic filter material are granular and fibrous media. Silicon carbide (SiC) and occasionally alumina (Al_2O_3) or aluminosicilates (Al_2O_3/SiO_2) are used to form granular filter media of high density. In general, siliceous material bonds the granules and it is the nature of this bond that dictates the ultimate tolerable conditions. Fibrous media having low density is typically made up of alumina or aluminosilicate fibres, held together by siliceous bond. Their porosity is notably higher but they are much lower in strength than granular media. The properties of ceramic filter media are summarised in Table 2.3.

Table 2.3 Properties of granular and fibrous media (Peukert, 1995).

Property	Granular Media	Fibrous Media
Porosity (%)	30 - 60	80 – 90
Permeability	Low	High
Weight	High	Low
Pressure drop (kPa)	> 50	> 30
Separation Efficiency	High	High

Novel materials using composite structures of granular and fibrous ceramics are being developed and tested especially in the USA. Examples include vapour-deposited SiC, rigidised fabrics, filament-wound elements and combinations of these materials.

The filter media are used to produce very porous structures with optimal flow capacity (porous enough for minimal pressure drop but sufficiently dense to minimise particle ingress), low thermal expansion and high thermal conductivity (minimise thermal stresses from system fluctuations and back-pulse cleaning), high mechanical strength and resistance to chemical attack.

2.2.1.2 Ceramic Filter Element

There are three major types of ceramic filter element: candle, tube and channel flow (either parallel or cross-flow). The filter element is the basic construction unit of the filtration device. The geometry and flow path of the filter element dictate the filter vessel design and operation. The commercial filter elements are mainly constructed from the same basic materials but vary in the granule or fibre size, binder type and fabrication method. The strength, permeability and durability of the final filter element are dependent on these variables. In power generation applications, high density granular ceramics have been more widely used due to their relatively high mechanical strength.

The principle of operation of each type of ceramic filter element is illustrated in Figure 2.1. The most common filter element is the candle type. It consists of a hollow cylindrical tube with a porous wall, one end is sealed while the other has a flanged collar. A typical size is: 6 cm outside diameter, 1 to 2 cm wall thickness and 1 to 1.5 m total length. The dust-laden gas flows from outside to the inside, depositing the dust cake on the external surface. A pulse of clean, inert gas (nitrogen or process gas) is injected periodically into the interior of the candle to dislodge the dust cake which falls into a hopper at the base of the filter vessel. A large

number of candles in numerous arrays are used in practice, the total number dictated by the gas volume and the required filtration velocity. Air-blown gasification units usually need more candles than oxygen-blown units due to the larger volume of fuel gas to be cleaned. Considerably more candles are required by PFBC due to the significantly larger volumes of nitrogen and excess air in the flue gas. The main suppliers of candle filters based on high density granular media are Schumacher, Coors and Pall. Low density fibrous candle filters are produced by Industrial Filter and Pump (IF&P), Cerel and BWF.
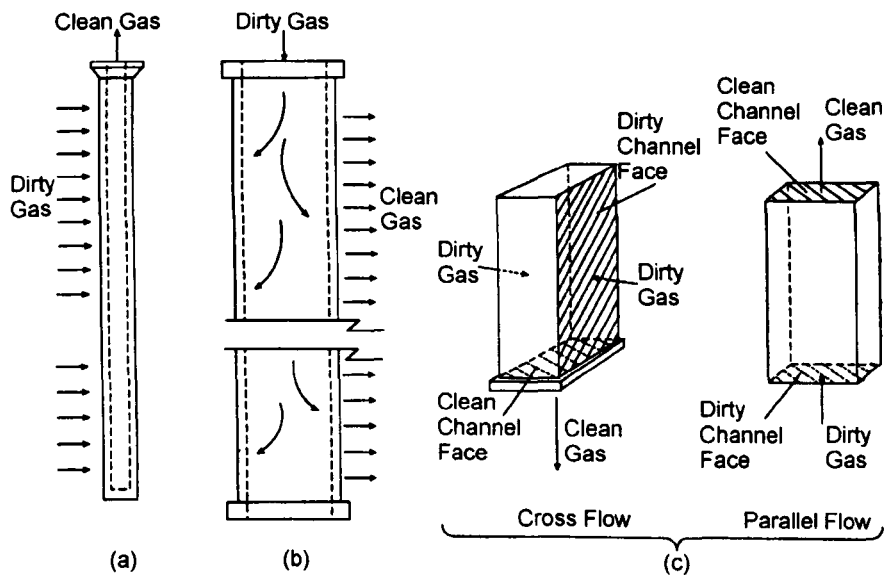
Figure 2.1 *Types of ceramic barrier filter element: (a) candle (b) tube (c) channel-flow (Lippert and Newby, 1995).*

The tube filter element has a cylindrical structure, open at both ends. The dust-laden gas comes in at the top and is directed vertically downwards such that separated dust is carried into the hopper at the bottom. The cleaned gas passes through the ceramic matrix whilst the dust cake deposits on the internal tube surface. Contrary to the candle filter design, the dust cake is removed periodically by reverse pulse to the enclosing chamber rather than to the filter element, improving the durability of the filter. Tube filter elements are of considerably larger diameter and are supported by tube sheets at the top and bottom. Tube filters made from β-cordierite (crystalline compound of $MgO/Al_2O_3/SiO_2$) are manufactured by Asahi Glass Company and Mitsubishi Heavy Industries in Japan.

The channel-flow filter consists of monolithic ceramic blocks with channels for gas flow. Dust-laden gas is filtered through thin, internal, porous ceramic plates or membranes which

are cleaned by applying a reverse pulse of inert gas to the clean side. Channel-flow filter designs have large surface area to volume ratio, up to 4 or 5 times higher than candle filter designs. However the available operating surface area may be significantly reduced due to blocking of some of the internal surfaces. Westinghouse and CeraMem® develop cross-flow and parallel-flow channel-flow filters respectively for coal-based power generation applications. Other channel-flow filter designs include the parallel flow type by NGK, Japan and the cross flow design by Specific Surface Co., USA.

2.2.1.3 Filtration Behaviour and Filter System Design

Ceramic barrier filter systems are generally operated cyclically. During filtration, dust builds up on the filter surface forming a dust cake. After a prescribed time or when the resistance to gas flow reaches a certain level, the filter medium is cleaned usually by applying a reverse pulse of gas to the clean side of the filter while it is online. The cake detaches from the filter surface, falls into a collecting hopper at the bottom of the unit, and the next cycle begins.

Dust capture by ceramic barrier filters resembles surface filtration. The filter element obstructs the dust such that a dust cake builds up on the upstream surface with slight or no dust ingress into the filter medium. Deposition of particles at the barrier surface occurs via mechanisms of Brownian diffusion, gravity settling, inertial impaction and direct interception.

The formed filter cake is detached from the filter surface by applying a gas pulse, typically air, nitrogen or the process gas. The gas pulse provides a pressure drop across the cake which essentially is an added tensile stress acting on the cake. The dust cake detaches from the filter surface when the increase in tensile stress is sufficiently large to overcome either the adhesive force between the cake and the filter medium or the internal cohesive force of the cake.

The filter elements can be mounted in various manifold and support arrangements, but existing filter unit designs are all based on either a single tubesheet or a tiered design. Both designs provide the options of varying filter element packaging efficiency and modular scale-up to larger capacities.

2.2.1.4 Filter Design Problems and Limitations

A number of sub-pilot, pilot and demonstration projects (combustion, gasification and hybrid plant types) have supported the testing and development of ceramic barrier filter systems since

the mid 1980s. As a result, extensive field experience has been gained especially with ceramic candle and tube filter element designs. Material strength, long-term durability and operability with difficult dusts are critical issues concerning filter element design.

First generation ceramic filters suffered thermal fatigue and high temperature corrosion especially in oxidising environments. Factors that limit the life of ceramic filters include reaction of alkali vapour and/or steam with the amorphous binder phase, oxidation of non-oxide based ceramics, as well as degradation due to thermal and mechanical shocks. Typical failures that have occurred during operation include broken filter elements, deformed filters, reduced permeability due to plugging of ceramic matrix pores by ash, and thermal degradation of the ceramic binder phase. Other problems are formation of strongly bonded ash deposits and bridging of ash between candles and hot metal structures.

Mitchell (1997) concluded that individual components of ceramic barrier filters need to undergo long-term assessment under conditions typical of coal-based combined cycle systems in order to gain confidence in commercial application of this technology. Further research and development will be required to provide insight into the influence of operating temperature and gas phase components on dust cake formation and removal behaviour. For IGCC application, there is now evidence that satisfactory operation of ceramic candle filters is possible at temperatures ranging from 250 to 450°C. However, operating temperatures above 500°C and up to 900°C required of advanced combined cycle designs must be the long-term goal such that high system efficiencies can be achieved (Seville *et al.,* 1996; Mitchell, 1997; UK DTI, 1998a).

2.2.2 Alternative Particulate Cleaning Technologies

The potential of other available particulate control devices for high-temperature application in advanced coal-based combined cycle systems are reviewed herein. These include cyclones, electrostatic precipitators (ESPs), fabric filters, metallic filters and granular bed filters.

2.2.2.1 Cyclones

The cyclone is the most common particulate removal device due to its low cost and ease of operation. The dust-laden gas enters the cylindrical vessel tangentially and sets up a rotary motion. The resultant centrifugal force throws the particulates against the walls, separating

them from the gas stream. Cyclones can operate between 0.1 and 10 MPa at temperatures greater than 1000°C. The simple tangential entry designs of Stairmand and Van Tongeren can separate particles down to 5 to 10 μm at high velocities, incurring small pressure loss and low maintenance costs. There has been little progress towards removal of finer particles smaller than 1 μm. The cyclone efficiency increases with particle size, density and gas velocity, but decreases with increasing gas viscosity and cyclone diameter, hence is unlikely to improve at high temperatures and pressures (Mitchell, 1997; Clift, 1997). A number of novel cyclone designs have been developed, however they have not been widely accepted because despite being more costly and complex, their efficiency is not higher than that of a well-designed conventional cyclone (Seville, 1996; Seville *et al.*, 1996). The only way to improve the overall efficiency significantly is by using several smaller cyclones in series or parallel (multicyclones). However, potential drawbacks include increased pressure loss and unstable gas flow distribution through the system. Multicyclones are expensive and are unlikely to find wide use at high temperatures and pressures (Seville, 1996). In gasification combined cycles, cyclones are not efficient enough to protect modern gas turbines, they are used mainly to recycle unreacted char and sorbent back to the gasifier. Even in PFBC combined cycle with a conventional gas turbine, multicyclones could not sufficiently protect the gas turbine from damage by particulates. However, cyclones have been used for final particulate removal with ruggedised gas turbines as well as to remove coarse particulates in combination with ceramic filters in systems with standard gas turbines.

2.2.2.2 Electrostatic Precipitators (ESPs)

Electrostatic precipitators have been widely used for particulate control in coal combustion plants. The gas is ionised when passing between a high-voltage electrode and an earthed electrode. The particulates are charged and attracted to the earthed electrode, separating them from the gas stream. ESPs are typically operated at atmospheric pressure and temperatures ranging from 120 to 450°C, capable of collecting fine particulates (less than 2 μm) with high collection efficiencies in excess of 99.5%. The main difficulty faced by ESPs in high temperature operations is that the voltage difference between the corona onset and sparkover (i.e. when electrical field breaks down) has to be essentially maintained, but this difference decreases with increasing temperatures. However, the voltage difference is increased at higher pressures, indicating the possibility of high-temperature and high-pressure ESP operation. Also, high electric field strengths can be achieved under these conditions meaning that smaller

collecting areas is possible. However at high temperatures, issues concerning corona stability, high energy loss, material durability as well as low-resistivity dust-charging and dust removal difficulties have to be addressed. Research on ESP has mainly centred on its application in PFBC or oxidising conditions, as there are potentially fewer material and fabrication problems encountered than in a reducing gas environment. In the 1980s, it was reported that there was sufficient data to construct a commercial-scale ESP for operation at 15 to 45 bar and 400 to 700°C (Seville, 1996). Higher temperature operation is limited by availability of data on the electric field characteristics and uncertainties concerning the insulator and other materials. There has been very little recent development work on ESPs for modern power generation (Seville, 1996; Seville *et al.*, 1996), suggesting that it is unlikely that ESPs will see much use in current advanced power generation applications.

2.2.2.3 Fabric Filters

Fabric filters (baghouses) consist of flexible, woven or felted fibres that are arranged as a tube or supported by a framework. They are capable of removing fine (down to 1 μm or less) and coarse particulates with high collection efficiencies in excess of 99.5%. They are typically operated below 300°C to remove fly ash in coal-fired power stations. Their flexibility renders them less prone to thermal shock than rigid filters but more susceptible to material degradation by rough handling, high temperature and corrosion. 'Pinholing' with loss in collection efficiency is the most common type of failure. Others include excessive clamping, damage from sharp edges of the clamp, improper tensioning and development of folds. Operation is limited to relatively low filtration velocities of less than 5 cm/s to avoid penetration of particulates into the fabric medium and their re-entrainment. Research into the application of fabric filters in combined cycle power systems has been very limited, with the available ones focusing on pulse jet type of ceramic fabric filters. The main issue is to identify suitable materials to withstand long-term high-temperature operation. Some composite textile materials that are marketed for high temperature duty, quoted to have an average operating temperature of 300°C with surges up to 350°C include 'Tefair' (PTFE/glass fibre) by DuPont and 'Pyrotex' (mineral/ceramic/metal fibres) by BWF. 3M's seamless filter bags woven from aluminium borosilicate ceramic fibre material 'Nextel' are quoted as temperature-resistant up to 1150°C for continuous operation and up to 1370°C for short operating periods. However, the development of a SiC composite rigid candle filter by 3M seems to suggest that the bag filter design is not a serious alternative for high temperature application in combined cycle power

systems. At present, fabric filters do not provide the long-term performance necessary for gas turbine protection in combined cycle applications (Seville *et al.,* 1996; Mitchell, 1997).

2.2.2.4 Metallic Filters

Metallic filters based on stainless steel have been widely rejected for PFBC operations mainly due to their susceptibility to severe hot corrosion in oxidising environments. However, the possibility remains for their application in gasification at temperatures ranging from 350 to 600°C under reducing conditions. The advantages of metallic filters over ceramic filters include their high resistance to thermal and mechanical shock, lower pressure drop resulting in reduced filtration area and lower capital costs, as well as simpler sealing, fabrication, handling and installation. A study to test the long-term corrosion resistance of metal filters in a gasification environment was performed recently by VVT in Finland. Pall's commercial metal filter materials comprising 316 and 310 stainless steels, Inconel 600 and Hastelloy X were tested up to 800 hours in simulated gasification conditions with 300 ppmv H_2S at 400°C and 500°C. All materials showed good durability at 400°C, the slight corrosion being mainly due to oxidation of chromium to chromium oxide (Cr_2O_3). At 500°C, the stainless steel filters notably the 310 demonstrated good resistance, however the nickel-based filters of Inconel and Hastelloy suffered severe sulphidation forming nickel sulphide (Ni_3S_2), blinding the filters. Pall is supplying their sintered stainless steel candle elements for the IGCC project at Polk Power. Pall have developed seamless tube filters using a new corrosion resistant metal alloy of iron aluminide (Fe_3Al) which are claimed to be exceptionally resistant to corrosion in high-temperature, sulphurous environments. The iron aluminide filters will be tested under gasification conditions as well as in oxidising gas streams. However, there continues to be concern over the ability of metallic filters to endure high and low temperature excursions, as well as short-term sulphur level variations (Seville, 1996; Seville *et al.,* 1996).

2.2.2.5 Granular Bed Filters

Granular bed filtration was considered a leading hot gas cleaning technology in power generation applications in the early 1980s before ceramic barrier filters became popular. The filter consists of a bed of granular solids, typically spherical and 1 to 3 mm in size. The main advantage of granular bed filters is their robustness as various mechanically, chemically and thermally resistant (above 1000°C) granular media can be used as collectors. There are three

generic configurations: fixed or slowly moving beds acting as surface filters, fixed or moving beds operating as depth filters and fluidised beds. The main collection mechanisms involved are inertial impaction and agglomeration. Others include diffusion and interception, as well as gravitational, electrostatic, magnetic and acoustic collection mechanisms. In principle, they can operate at relatively high velocities and all the different designs are capable of relatively high collection efficiencies. However in practice, commercial development has been hindered by cake formation and particle retention difficulties as well as severe attrition of the collector medium at high temperatures and high velocities. Commercial granular bed filters are available from the Combustion Power Company (CPC), Westinghouse and Kawasaki Heavy Industries (KHI). In CPC's design, the dust-laden gas travels counter-currently to a downward moving bed consisting of relatively high-value 1 to 3 mm alumina (Al_2O_3) or 6 mm mullite ($Al_2O_2.SiO_2$) spheres. CPC is currently testing an industrial-scale unit in Wilsonville, Alabama. Chemically or catalytically reactive filter media have also been investigated for removal of other gaseous contaminants in addition to dust particulates. These include clay-based sorbents for alkali and heavy metal absorption, sodium-based sorbents for removal of halogen and trace metals, and nickel-based catalysts combined with zinc titanate for NH_3 and H_2S removal. An economic study conducted by CPC with FETC-Morgantown suggested that additional cost savings are expected if the granular bed filter is used for multicontaminant control. Westinghouse' moving granular bed filter employs co-current flow of gas and bed, with pelletised fly ash or an absorbent such as dolomite as the granular medium. The intention is to use cheap collector materials on a once-through basis to keep the cost down as opposed to specialist materials with an added cost of recycling. KHI has two cross-flow granular bed filter designs, one solely for particulate removal using 1 mm mullite granules as collector medium, and the other for combined sulphur and dust clean-up using 1.1 to 1.4 mm mullite beads containing Fe_2O_3 sorbent. Granular beds are unlikely to succeed as a stand-alone particulate filter but may be attractive as a multi-contaminant clean-up device for simultaneous removal of gaseous contaminants and solid particulates (Seville, 1996; Mitchell, 1997).

2.3 Hot Gas Cleaning with Liquid Metals

The concept of using liquid metals for gas desulphurisation dates back to the late 1970s when Meissner (1976) first patented the concept of removing sulphur from hot reducing gases using liquid lead. However since then, only few others have propounded the use of liquid metals for

gas cleaning. They were Meissner and Shora (1981), Schürmann (1984), Reitz (1985), Hedden *et al.,* (1986) and most recently, Warner (1997, 2000, 2001).

2.3.1   Early Work - Gas Desulphurisation with Molten Lead

Meissner (1976) put forward the concept of using molten lead for sulphur removal from hot reducing gases. Lead was selected as the reagent metal due to its relatively low melting point of 327°C. In the proposed process, incoming hot gases containing sulphurous compounds such as hydrogen sulphide are contacted with a slurry or solution mixture of lead sulphide in molten lead in a refractory-lined clean-up chamber. In the clean-up chamber, a rotating wheel that is partially immersed in the melt disperses the mixture into droplets in the gas phase, providing intimate contact with the sulphur compounds in the incoming gases and breaking up the solid lead sulphide skin (if any) on the surface of the melt. The sulphur content in the hot gases reacts with lead forming lead sulphide. The slurry of unreacted molten lead and the formed lead sulphide is withdrawn to a refractory-lined regeneration chamber. Regeneration is carried out by electrolysis on the lead sulphide producing molten lead at the cathode and elemental sulphur at the anode. The regenerated lead together with any unconverted lead sulphide (in solution or slurry form) is recycled back to the clean-up chamber in a volume that is in excess of that required to react with the predetermined sulphur content in the incoming hot gases and to at least form a pumpable mixture of molten lead and solid lead sulphide. The elemental sulphur is removed as a volatilised gas from the regeneration chamber.

Building on the earlier patent by Meissner (1976), Meissner and Shora (1981) proposed a general process for high temperature heat exchange between a gas stream and either a molten metal or a molten salt. This is through generation of liquid droplets in a confined gas passageway giving high interphase contact surface area. The droplet shower can be generated either by impellers or rotating disks partially immersed in a liquid pool, or using submerged gas jets, or with sprayheads and nozzles. If required, simultaneous removal of undesired solid, liquid or gaseous components from the gas stream can also be provided for.

Although Meissner (1976) and Meissner and Shora (1981) patented a system for liquid metal based gas cleaning, there has been no documented evidence to suggest that their idea was explored any further and put into actual practice.

2.3.2 Early Work - Gas Desulphurisation with Molten Tin

In the mid-1980s, the use of molten tin for sulphur removal was investigated by researchers in Germany (Schürmann, 1984; Reitz, 1985; Hedden *et al.*, 1986).

□ *Schürmann (1984)*

Schürmann (1984) showed that it is thermodynamically possible to remove H_2S with molten tin and then demonstrated it experimentally. The possibility of combining sulphur and dust removal in a spray scrubber was also suggested. The desulphurisation reaction is as follows:

$$Sn\,(l)\ +\ H_2S\,(g)\ \rightarrow\ SnS\,(s)\ +\ H_2\,(g) \tag{2.12}$$
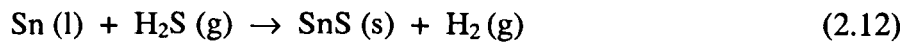
The reaction is an exothermic process. The enthalpy of reaction varies from -90.5 to -82.43 kJ/mol at temperatures 327 to 727°C (600 to 1000 K). The equilibrium constant for the heterogeneous reaction 2.12 is independent of pressure as follows:

$$K_p = p_{H2}\,/\,p_{H2S} \tag{2.13}$$

Figure 2.2 depicts the dependency of the Gibbs free energy change of reaction ΔG_R for reaction 2.12 on temperature T for varying partial pressure ratios $p_{H2}/\,p_{H2S}$.
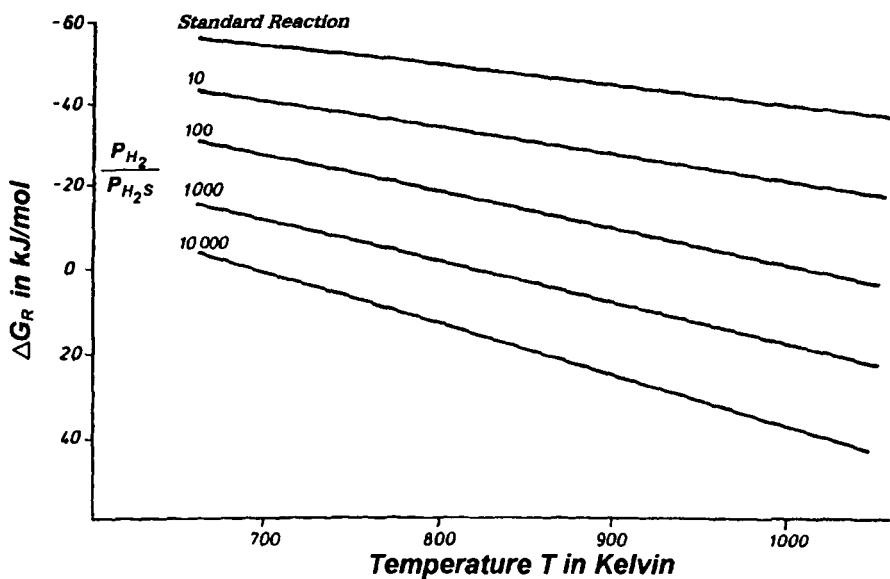
Figure 2.2   Variation of ΔG_R for the reaction Sn (l) + H_2S (g) → SnS (s) + H_2 (g) (Schürmann, 1984).

ΔG_R tends towards a negative value as either the temperature or partial pressure ratio decreases, favouring the forward reaction i.e. H_2S absorption. Conversely as either the temperature or partial pressure ratio increases, ΔG_R tends towards a positive value, favouring

the reverse reaction i.e. SnS decomposition. Therefore either the H_2S absorption or the SnS decomposition is favoured depending on the system temperature and gas composition. For a typical fuel gas composition of 30 vol. % H_2 and 0.5 vol. % H_2S, temperatures of less than 527°C (800 K) have to be kept to achieve H_2S separation of greater than 90%.

A simple test was carried out to investigate the desulphurisation reaction 2.12. 1000 ppmv H_2S in N_2 gas was bubbled through a small amount of molten tin held in a gas washing bottle heated at constant temperature. It was found that as the temperature rose from 400 to 800°C, the degree of H_2S separation increased from approximately 60% to over 90%. According to Schürmann, the temperature dependence of the degree of H_2S separation could only be explained kinetically as complete conversion in all cases could be expected from thermodynamic balance. The kinetic hindrance was probably due to insufficient dispersion of gas bubbles through the molten tin at low temperatures. This problem could be avoided by the dispersion of tin to fine droplets providing a large area for interphase mass transfer.

In addition to sulphur removal, Schürmann also investigated separation of quartz dust and fly ash using liquid tin at a pilot scale batch plant at temperatures of about 400°C. Liquid tin was dispersed into droplets by spraying the melt through nozzles by means of compressed nitrogen. The molten tin spray was directed into the path of the dust-laden gas stream. Approximately 60% dust separation efficiency was reportedly achieved.

□ *University of Karlsruhe*

Researchers at the University of Karlsruhe, Germany (Reitz, 1985; Hedden *et al.*, 1986) proposed the following liquid tin based desulphurisation and tin regeneration process of which reactions 2.14, 2.16 and 2.17 were investigated:

Desulphurisation:	$2\,Sn\,(l) + 2\,H_2S \rightarrow 2\,SnS + 2\,H_2$	(2.14)
Roasting:	$SnS + 2\,O_2 \rightarrow SnO_2 + SO_2$	(2.15)
Sulphur Production:	$SnS + SO_2 \rightarrow SnO_2 + 2\,S$	(2.16)
Reduction:	$2\,SnO_2 + 4\,H_2 \rightarrow 2\,Sn\,(l) + 4\,H_2O$	(2.17)
Overall Reaction:	$2\,H_2S + 2\,H_2 + 2\,O_2 \rightarrow 4\,H_2O + 2\,S$	(2.18)
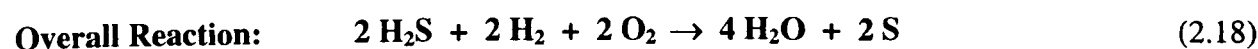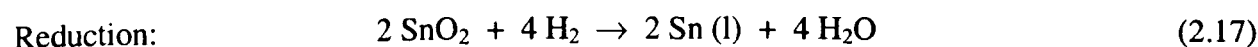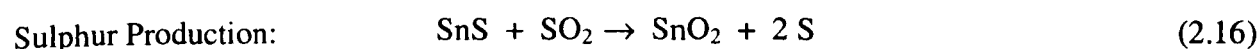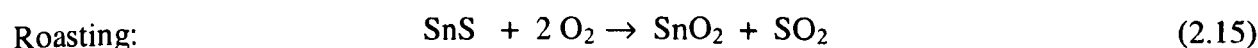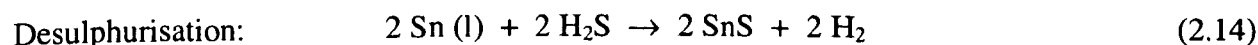
The bulk of the experimental studies (Hedden *et al.*, 1986) focused on the desulphurisation reaction (reaction 2.14) in a bubble column, stirred vessel and double-stirred cell reactors at

temperatures ranging from 400 to 700°C and at pressures higher than atmospheric. It was found that the increase in reaction temperature, surface renewal frequency (i.e. reactor impeller speed) or the residence time improved the degree of H_2S conversion. However, the degree of H_2S conversion dropped slightly with increase in H_2S partial pressure. The presence of other gas components i.e. H_2, H_2O, CO and CO_2 in the gas mixture did not affect the degree of H_2S conversion with tin. The authors concluded that the simple N_2/H_2S gas mixture would suffice as a simulation fuel gas to predict the desulphurisation of gases produced by coal gasification, with the exception of fuel gases with high H_2/H_2S ratios such that the equilibrium conversion of H_2S would be affected.

From their investigation, Hedden *et al.* concluded that the reaction of H_2S with liquid tin in the reactors was first-order with respect to the H_2S concentration at the chemically active interfacial area. The effective interfacial area for reaction was found to be reduced by the formation of solid tin sulphide film on the liquid tin surface, preventing further sulphide formation and hindering desulphurisation. Hence, besides the system temperature and H_2S concentration, the desulphurisation reaction rate was also dependent on the interfacial area surface renewal frequency.

The sulphur production reaction (2.16) was investigated (Hedden *et al.*, 1986) in a fixed bed reactor at 500°C to 800°C. It was found that some of the elemental sulphur produced from the reaction of SnS with SO_2 accumulated on the solid SnS/SnO_2 surface forming polysulphides (SnS_2, SnS_3). Additional heating of the solid to 800°C in a N_2 stream was necessary for complete recovery of the accumulated sulphur. The reduction of SnO_2 (2.17) was effected by H_2 at 480°C and CO at 540°C.

A gas desulphurisation scheme was proposed by Hedden *et al.* (1986) based on the results obtained from the individual reaction steps. After pre-cleaning in a cyclone, simultaneous sulphur and fine dust removal from the hot fuel gas takes place in a molten tin spray scrubber at 500°C and 20 bar. The unreacted molten tin containing solid tin sulphide product and dust particles is removed from the scrubber, the solids scrapped off and the cleaned tin is transported back to the scrubber. The separated solid tin sulphide, SnS is treated with O_2 and SO_2 in a rotary kiln at 800°C to form tin oxide, SnO_2 and elementary sulphur. The tin oxide is reduced by a purified fuel gas (H_2 or CO) in a second rotary kiln, regenerating molten tin. However, there is no reported evidence to suggest that the proposed process has actually been implemented. No subsequent documents were found on the progress of this process.

2.3.3   Gas Desulphurisation with Gaseous Metallic Zinc

At the University of Birmingham, Warner (1997) proposed the removal of sulphur from fuel gases based on interaction between H_2S and COS with gaseous metallic zinc producing saleable, premium grade solid ZnS:

$$Zn \text{ (g)} + H_2S \text{ (g)} \rightarrow ZnS \text{ (s)} + H_2 \text{ (g)} \tag{2.19}$$
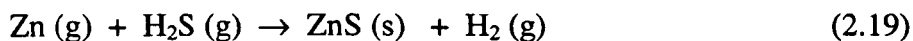
99% or greater H_2S and COS removal was claimed to be possible. The ZnS concentrate can either be treated on-site by direct smelting (i.e. The Warner Zinc Process) to recover the metallic zinc, or it can be sold to a zinc producer. The concentrate has a very small iron content compared to natural ZnS, hence making it an ideal feedstock for the electrolytic Zn industry which are facing heavy environmental pressures regarding the disposal of iron impurities (known as jarosite residues) from Zn concentrates. The leaching of these metal impurities into groundwater and the ecosystem is a matter of serious environmental concern.

Two different processes were identified based on how gaseous Zn can be added to the system:

❑   *Gaseous Zinc Jet Process (External Zinc Gas Generation)*

In this process (Figure 2.3), Zn gas is generated externally and is mixed with an inert diluent. The high-pressure axisymmetric Zn gas stream with diluent is injected into a reaction chamber, well away from the reactor walls. A gas diffusion-controlled heterogeneous reaction between gaseous Zn with H_2S and COS on existing solid ZnS particles results. In theory, very good sulphur removal is achieved with no wall accretions.
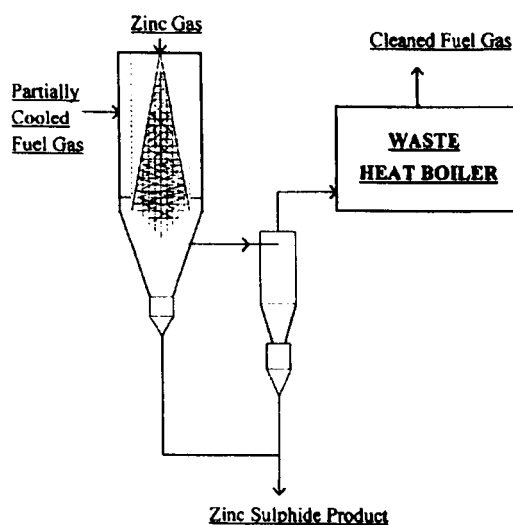
Figure 2.3 Zinc-based desulphurisation - Gaseous zinc jet process (Warner, 1997).

❑   *Zinc Liquid Metal Process (In-situ Zinc Gas Generation)*

In the alternative in-situ generation method (Figure 2.4), Zn gas is desorbed within the desulphurisation reactor from a molten Zn alloy stream, made up of Zn with a non-volatile liquid metal such as molten Pb or BiPb eutectic. Zn vapour is released deep within a moving

bed reactor, using energy from the sensible heat of the hot fuel gas to effect vaporisation. The system consists of a moving packed bed of 100 to 150 mm diameter balls irrigated by the molten Zn alloy stream, giving good direct gas-metal contact and hence efficient heat and mass transfer. The downward moving balls are entrained in the liquid metal circulation by an air-lift action which enables a closed-loop circulation of the balls between the moving packed bed and phase disengagement for particulate removal.

CRE Group Ltd assessed the commercial viability of the proposed zinc-based processes with reference to using zinc titanate regenerable sorbent for hot gas desulphurisation, all were applied to air-blown gasification cycle (ABGC) without limestone addition to the gasifier. It was found that all processes gave similar thermal efficiencies of about 50%. The estimated overall gas cleaning cost for the zinc liquid metal process was less than half of the regenerable sorbent reference process while the gaseous Zn jet process showed only a slightly lower overall cost than the reference process. Considering its substantial financial incentives, Warner (1997) proposed the zinc liquid metal process for commercial exploitation.
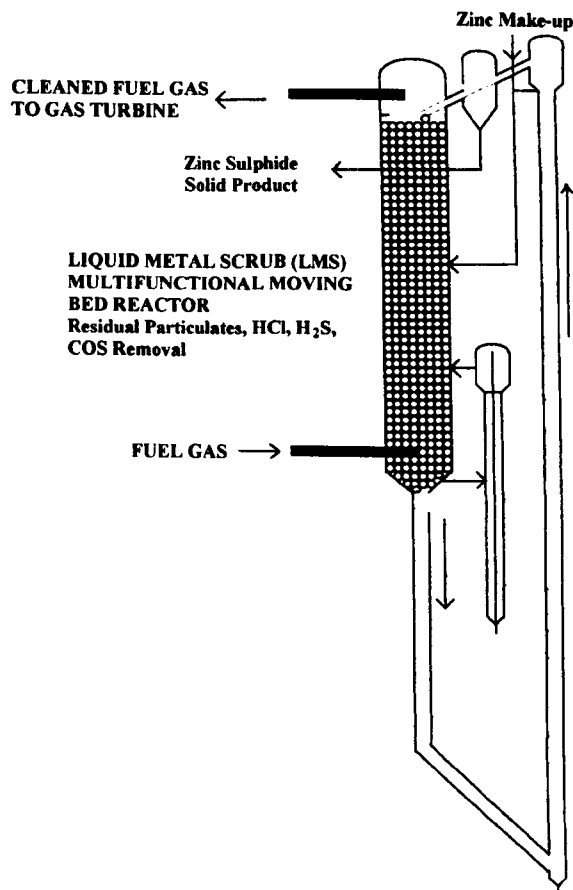
Figure 2.4 *Zinc-based desulphurisation – Zinc liquid metal process (Warner, 1997).*

2.4 Current Proposal: Gas Desulphurisation/Particulate Removal with Molten Tin in a Moving Packed Bed

From the initial proposal of a zinc-based desulphurisation process, Warner (2000, 2001) later put forward the concept of an integrated liquid tin based coal gasification and hot gas desulphurisation system. The gas desulphurisation process is discussed herein.

Concerns associated with aerosol formation, wall accretions, ZnS separation from ash and char, potential loss of liquid metal and heavy metal contamination of ash have forced a rethink

of the earlier proposed gaseous Zn-based hot gas desulphurisation processes (Warner, 2000). As a result, Warner modified the earlier scheme, putting forward a desulphurisation system involving direct absorption of H_2S and COS into a liquid metal with low vapour pressure instead. The process would take place in a non-wetting, liquid-metal irrigated moving packed bed similar to the one illustrated in Figure 2.4. Metal recovery would be effected externally by reacting the sulphided metal with molten Zn producing high quality ZnS solid product which in turn can be treated on-site or sold elsewhere to regenerate Zn metal for reuse.

□ *Selection of Liquid Metal System*

Three possible liquid metal systems were identified (Warner, 2000, 2001). They were lead (Pb), bismuth-lead mixture (Bi-Pb) and tin (Sn).

Lead is the most thermodynamically efficient among the three. It is relatively cheap and is inert to oxidation by fuel gas. Lead's melting point is 327°C. This can be lowered by adding Bi to form a 55.5% Bi - 44.5% Pb eutectic with a melting point of 127°C which would make system start-up and prolonged stand-by both easier and less energy-intensive. The Bi-Pb is also not susceptible to oxidation by fuel gas. In this mixture, Bi acts as just an inert diluent and by itself it is the least effective among the other options in sulphur removal. However, the use of either Pb or Bi-Pb is discouraged due to health hazards associated with in-plant exposure to lead as well as its emissions to the environment. Lead is a cumulative poison (ASM, 1984). Excessive lead intake either from air, food or water can build up in the body, which leads to lead poisoning.

Considering the health risks associated with lead, tin is the remaining choice of the liquid metal system. Tin and its inorganic compounds do not pose a health threat. Tin has a relatively low melting point of 232°C and negligible vapour pressure at high temperatures. This is a major advantage over lead, bismuth and zinc which have relatively higher vapour pressures, hence they are easier to evaporate or sublime at high temperatures causing massive metal loss. The vapour pressures of these metals are compared in Table 2.4, tin being the least volatile and zinc the most volatile.

In addition, molten tin has relatively low viscosity, hence giving easy flow and easy dispersion into small droplets on the packing surface. Molten tin's viscosity is 1.41 cP at 400°C as compared to that of water which is 1.13 cP at 15°C.

Table 2.4 *Vapour pressure comparison (Data taken from ASM, 1981).*

Vapour pressure (mm Hg)	Temperature (°C)			
	Tin	Lead	Bismuth	Zinc
10^{-4}	923	548	537	248
10^{-3}	1011	620	609	290
10^{-2}	1190	718	699	343
0.1	1271	821	721	405
760	2272	1745	1421	908

Increasing Volatility

⟶

❑ *Gas Desulphurisation*

Fuel gas is contacted countercurrently with molten tin in a moving packed bed of ceramic spheres (typically 100 to 150 mm in diameter). Gas desulphurisation is effected through direct absorption of H_2S and COS in the fuel gas into molten tin:

$$H_2S + Sn \rightarrow SnS + H_2 \tag{2.20}$$

$$COS + Sn \rightarrow SnS + CO \tag{2.21}$$

The reaction should proceed unimpeded as long as the dissolved sulphur in the molten tin is maintained below the saturation level with respect to SnS. This prevents surface drossing by solid SnS formation which can hinder further reaction between the liquid tin and the sulphurous gases as well as to avoid accretion problems which can block the packed bed.

This process differs from those employed by Schürmann's (1984) and Hedden *et al.* (1986) in which sulphur is removed as solid tin sulphide at unit activity. According to Warner (2000), it can be shown that the degree of sulphur removal when sulphur is removed as tin sulphide at unit activity is limited by thermodynamic constraints. Indications of this are the limited degree of sulphur removal at high temperature as noted by Schürmann, and at high partial pressure ratio of H_2 to H_2S as identified by both Schürmann and Hedden *et al.* These constraints are removed by maintaining a very low activity of dissolved sulphur in the molten tin, ensuring effective sulphur removal.

❑ *Particulate Removal*

In addition to gas desulphurisation, simultaneous solid particulate removal is possible in the packed bed which acts as a depth filter. Molten tin having high surface energy exhibits non-wetting droplet and rivulet flow on the ceramic packing surface. The liquid tin droplets and

rivulets act as capture sites for primary inertial deposition of solid particulates from the gas stream. A possible secondary entrapment method could be well provided by the naturally adhesive nature of ash and char particles at elevated temperatures, promoting deposition and retention on the packing surface. This latter secondary transfer of particulates to sticky packings may be further enhanced with minor flux additions of suitable fused salts.

The ability of the hot gas scrubber to function as a multicomponent clean-up device is advantageous as this reduces the number of required vessels and hence the capital cost of the overall gas cleaning system.

□ *Liquid Metal Circulation and Packing Transport Via Gas Lift*

Concern over solid deposition and extensive accretion formation in a fixed bed dictates a moving bed configuration with external cleaning of solid packings. A gas lift is used for liquid metal circulation with the packing spheres in entrainment round the closed-loop system. Injection of a compressed inert gas provides the means to lift the spheres entrained in the liquid metal to the top of the packed bed. Provided that there is sufficient submergence relative to the required lift, this is a simple but reliable method for liquid metal circulation and packing transport. Any solids (ash, unreacted char, solidified fused salts) adhering to the spheres are removed through vibratory or mechanical means at the top of the circulation loop, possibly aided by differential expansion from surface cooling of the deposited solids. The cleaned spheres are returned to the top of the packed bed while the separated solids are screened off and removed.

□ *Metal Recovery*

The dissolved sulphur in the molten tin has to be kept below the saturation level with respect to tin sulphide to enable the desulphurisation reaction to proceed unimpeded. Continuous regeneration of metallic tin is thereby essential to maintain a sufficiently low tin sulphide activity in the melt such as to preserve the effectiveness of the molten tin for desulphurisation. Metallic tin is regenerated externally by continuous treatment of the sulphided tin with liquid metallic zinc to produce a saleable premium grade ZnS solid product that is readily stored and transported (Warner, 2000):

$$Zn + SnS \leftrightarrow ZnS + Sn \qquad (2.22)$$

Regeneration takes place in a fluidised bed where coarse granular ZnS product is grown on seeds of fine ZnS in fluidised state. These coarse ZnS granules can be readily separated from the liquid metal. For zinc recovery, the currently available option is to send the ZnS product to an electrolytic zinc producer (an already well-established industry) for treatment while in the longer term, direct smelting (The Warner Zinc Process) (Warner, 1997) may be adopted.

❑ *Effect of Other Constituents in Gasification Fuel Gas*

The possibility of reaction between molten tin and typical fuel gas constituents apart from H_2S are considered as follows:

- **CO_2:**   Tin reacts with CO_2 at high temperatures according to the following reaction forming solid tin oxide (Hedges, 1960):

$$Sn + 2CO_2 \leftrightarrow SnO_2 + 2CO \qquad (2.23)$$

Using equal proportions of CO_2 and CO in the test gas, Nielsen and Sigurdardottir (1993) reported that the above equilibria was experimentally found to lie towards the right at a temperature range of 350°C to 500°C. However, markedly higher CO concentration compared to CO_2 typical of actual gasifier fuel gas would suppress the forward reaction and the formation of SnO_2.

- **Steam:**   Molten tin reacts with steam according to the following reaction forming solid tin oxide (Hedges, 1960; Nielsen and Sigurdardottir, 1993):

$$Sn + 2H_2O \leftrightarrow SnO_2 + 2H_2 \qquad (2.24)$$

The phase diagram depicting the above equilibria is shown in Figure 2.5. Either the H_2O/H_2 ratio in the fuel gas or the system operating temperature must be controlled in order to avoid the loss of tin as SnO_2. For wet gasifiers such as Texaco, the forward tin oxidation reaction is encouraged by the relatively high proportion of water vapour in the fuel gas relative to H_2. For these systems, the fuel gas temperatures must be kept above 500°C in the presence of molten tin to avoid SnO_2 dross formation. On the other hand, for dry gasifiers such as Shell, the forward tin oxidation reaction will be suppressed by the low proportion of H_2O to H_2 in the fuel gas.
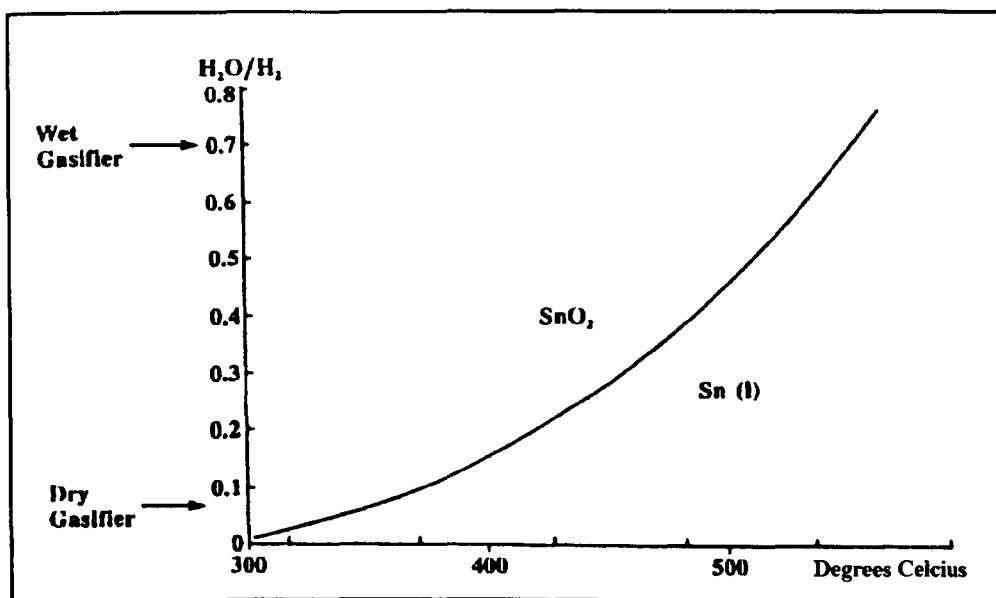
Figure 2.5 *Phase diagram H₂O/H₂ molar ratio versus temperature (Nielsen and Sigurdardottir, 1993).*

- **N₂:** Tin does not react directly with N_2 (Hedges, 1960).

- **H₂:** Tin does not react directly with H_2 (Hedges, 1960).

- **NH₃:** Tin does not react with NH_3 (Hedges, 1960).

- **HCl:** Tin readily reacts with Cl_2 forming volatile $SnCl_4$ (Hedges, 1960).

Although there is no information regarding the reaction between tin with HCl i.e. the main form of chlorine in gasifier fuel gas, it is possible that the reaction, if any, may take the following form:

$$Sn + 4HCl \leftrightarrow SnCl_4 + 2H_2 \qquad (2.25)$$
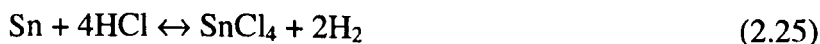
However the very high H_2 to HCl ratio in the fuel gas would suppress the forward reaction, and therefore the reaction of HCl with molten tin is highly unlikely.

- **Trace heavy metals:** Molten tin can potentially reduce arsenic, lead and mercury down to very low limits (Warner, 2001).

It is worth noting that contrary to Hedges (1960) and Nielsen and Sigurdardottir (1993), Hedden *et al.* (1986) reported that the presence of H_2, H_2O, CO and CO_2 did not affect the degree of H_2S conversion with tin in tests conducted in small-scale reactors at 400 to 700°C.

2.5   Summary

Current hot gas desulphurisation technologies are centred on the application of regenerable metal oxide sorbents for sulphur removal. The focus has shifted from the development of high operating temperature sorbents (above 600°C) to lower operating temperature sorbents (350 to 600°C), direct sulphur recovery processes and steam-resistant sorbents, all of which can potentially reduce the cost of the overall hot gas clean-up system. Zinc oxide-based materials are currently the leading sorbent for hot gas desulphurisation, capable of H_2S removal efficiency of 99% or greater. Bubbling and circulating fluidised bed reactors appear to be the most favourable for hot gas desulphurisation application in IGCC. However, the ideal regenerable sorbent is still a long way from commercialisation as issues relating to long-term sorbent performance such as mechanical strength, chemical attrition resistance, long-term durability and reactivity have yet to be fully addressed.

Various technologies have been proposed for hot gas particulate cleaning, however few have undergone sufficient development for commercial application in combined cycle power systems. Ceramic (rigid) barrier filters are currently the most advanced, commercially available particulate removal device, with the most promise for high temperature gas cleaning application. Field experience has demonstrated that ceramic barrier filters are capable of high collection efficiency with a relatively low pressure and temperature drop across the system. However, successful long-term commercial operation in IGCC systems has been limited to temperatures between 250 to 450°C. Further development will be required to enable operating temperatures above 500°C and up to 900°C necessary to fully realise the advantages of gas cleaning at high temperatures in advanced combined cycle designs. Cyclones are a cheap method to remove coarse particulates, however their efficiencies are unlikely to be significantly improved to sufficiently protect modern gas turbines in combined cycle systems. ESPs and fabric filters suffer from performance deterioration at high temperatures, hence are currently not viable for hot gas cleaning in advanced power generation. Metallic filters and granular beds offer some potential. Commercially available stainless steel filters look promising for application in gasification conditions at 400 to 500°C and at low sulphur concentrations. High-temperature, corrosion-resistant iron aluminide alloy filters are currently being tested. Granular bed filters are commercially available, showing promise as a multi-contaminant clean-up device for simultaneous removal of gaseous contaminants and solid particulates but unlikely to succeed as a stand-alone particulate filter.

Though the concept of gas cleaning using liquid metals is not entirely new, there has only been a handful of documented work to date. Meissner (1976) and then Meissner and Shora (1981) patented a system for liquid metal based gas cleaning with lead being one possible liquid reagent, but their idea was not explored any further. Schürmann (1984) showed that sulphur removal using liquid tin was thermodynamically possible and demonstrated it experimentally at bench scale. Dust separation with liquid tin spray was also performed at pilot scale. Schürmann went on to suggest combined sulphur and dust removal in a molten tin spray scrubber. Hedden *et al.* (1986) investigated gas desulphurisation with molten tin in small-scale reactors. Based on their experimental findings, they proposed a process in which the hot fuel gas is cleaned of sulphur and dust by a molten tin spray. The resulting SnS solid product is treated with O_2 and SO_2 giving SnO_2 and elementary sulphur. Liquid tin is regenerated by reduction of SnO_2 in a purified fuel gas stream. However the processes put forward by Schürmann and Hedden *et al.* involve the removal of sulphur as solid tin sulphide at unit activity, which according to Warner (2000) is limited by thermodynamic constraints. Warner (1997) proposed the removal of sulphur from fuel gases using gaseous metallic zinc producing saleable, premium grade solid ZnS. Two different processes were identified: the gaseous zinc jet process and the zinc liquid metal process. However, Warner (2000) later identified several concerns associated with the use of gaseous metallic zinc. Warner (2000, 2001) subsequently put forward the concept of an integrated liquid metal based coal gasification and hot gas desulphurisation system, this time being based on molten tin. In this most recent proposal, the hot gas scrubber is essentially a moving packed bed of ceramic spheres in which fuel gas is contacted countercurrently with molten tin. Gas desulphurisation takes place via direct absorption of sulphurous gases into molten tin. In addition, the scrubber offers the prospect of simultaneous particulate removal mainly through inertial deposition on discrete tin droplets and rivulets, possibly also via secondary entrapment on sticky packing surfaces. A simple gas lift provides the means for liquid circulation and packing transport to the top of the packed bed. Disengagement of solids adhering to the spheres is to be effected by vibratory or mechanical means at the top of the circulation loop, returning the cleaned spheres to the top of the bed and screening off the separated solids. Continuous tin regeneration is essential to maintain a sufficiently low tin sulphide activity in the melt for unimpeded gas desulphurisation. This is achieved by regenerating metallic tin externally by continuous treatment of the sulphided tin with liquid metallic zinc to produce a saleable premium grade ZnS solid product.

2.6   Defining The Research Scope:
Investigation of a Non-Wetting Packed Bed Gas Scrubber

A fresh and radical approach may provide the key to overcoming the inherent limitations of current regenerable metal oxide sorbents employed in hot gas desulphurisation. Warner's (2000, 2001) proposed liquid metal scrubber is one such innovative way forward in hot gas cleaning, possessing not only sulphur removal capability but the potential for particulate control as well. The novel liquid tin irrigated packed bed scrubber proposed by Warner (2000, 2001) as detailed in Section 2.4, and the molten tin-based desulphurisation and particulate removal processes are thereby of interest in this investigation. However, the regeneration of sulphided tin by metallic zinc is beyond this research scope and will not be pursued further.

The workings of the molten tin irrigated scrubber are replicated in this investigation using an analogous room temperature Perspex model. The model scrubber is essentially a small-scale packed column with a fixed bed of either polyethylene or paraffin waxed glass spheres. Water irrigation on the surface of these low surface energy packings simulate the non-wetting flow of molten tin in the liquid metal scrubber. Water introduced at the top of the packed bed disintegrates into discrete droplets and rivulets flowing downwards by gravity, countercurrently to an upward gas flow. Laboratory cold experiments would concentrate on the operational hydraulics, particulate removal and gas absorption performances of the packed column operating under non-wetting conditions. In addition, the performance of a small gas lift for liquid circulation through the packed column would be explored.

The room temperature analogue studies would provide insight and design data for subsequent development of the high temperature liquid metal scrubber.

It is pointed out herein that the system in the current study incorporates a fixed bed rather than a moving bed as in the proposed liquid metal scrubber. Accordingly, the gas lift studies are limited to liquid circulation and are not extended to packing transport. The relatively slow downward motion of the bed in the moving bed configuration compared to the velocities of the gas and liquid metal through the bed enables the preliminary quantitative treatment to be based on fixed bed behaviour. Nevertheless, the findings will undoubtedly be useful in advancing towards an actual moving packed bed scrubber.

Chapter Three

Packed Column and Gas Lift Operations: Theory and Review

This chapter reviews the fundamentals and theories governing the design and operation of packed columns and gas lifts. The major parts of a packed column are first considered along with important design criteria. The hydrodynamics of a counter-current packed column are then explored, encompassing the column pressure drop, loading and flooding phenomena as well as liquid holdup behaviour. Findings in the literature based on conventional wetting packed columns are examined followed by work reported for non-wetting systems. The final section focuses on gas lift operation for liquid transport.

3.1   Packed Column Operation

3.1.1   General Design of a Packed Column

The packed column is used for continuous gas-liquid contact in either counter-current or co-current flow. It consists of a vertical cylindrical column or tower with the following important features as illustrated in Figure 3.1 (for a typical counter-current operation):

- A gas inlet and distributing space at the bottom.

- A liquid inlet and distributor at the top.

- Gas and liquid outlets at the top and bottom respectively.

- A bed of inert solid devices with large surface area i.e. column packing.

Figure 3.1 A counter-current packed column.
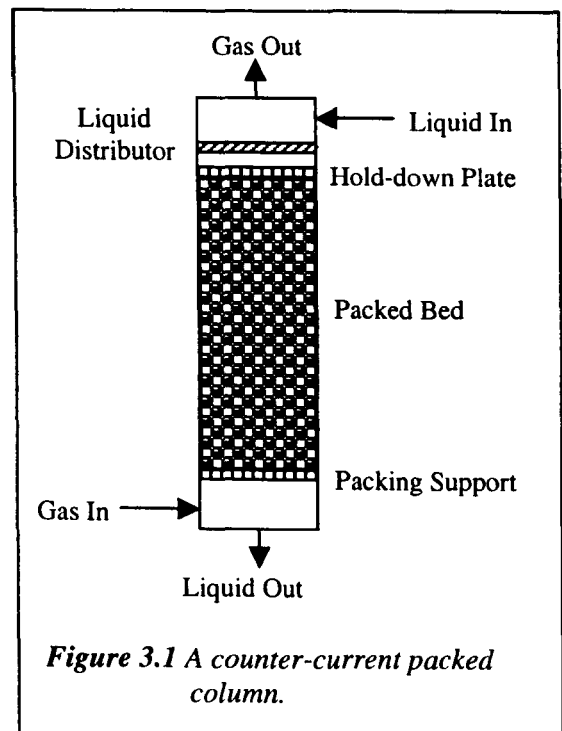
The liquid is distributed over the top of the packing and ideally wets the packing surfaces uniformly as it flows through the packed bed. The gas enters through the distributing space at the bottom of the packed bed, flows upwards through the interstices in the packing counter-currently to the liquid. The wetting of the packing by the liquid provides a large surface area to contact the gas, encouraging intimate gas-liquid interphase contact and hence effecting mass transfer.

44

There are numerous publications dedicated to the selection of packed column internals, among them are those by Fadel (1984), Chen (1984) Horner (1985) and Strigle (1994). The major features of a packed column are briefly described as follows:

❏ *Packing*

The column packing needs to provide a large interfacial surface between the liquid and gas. The packed bed must have a sufficiently large voidage such that it can accommodate large volumes of fluid flow through the column without flooding and with low gas pressure drop. Other favourable characteristics for the column packing are being chemically inert to the process fluids, having sufficient structural strength for ease of handling and installation, as well as low in cost. There are three principal types of column packing: random packings, stacked (or regular) packings and structured (or ordered) packings.

Random packings are packings that are simply dumped into the column during installation and allowed to fall randomly. They consist of individual units 6 to 75 mm in size and made from a wide range of materials such as ceramics, plastics, metals, glass, carbon and rubber. High packed bed voidage is attained by having irregular or hollow packing units so that they interlock into open structures with high porosity. The voidage obtainable with random packings ranges from approximately 0.45 to 0.95. Examples are Raschig rings, Pall rings, Berl saddles, Intalox saddles, Hy-Pak and Mini rings. In the main, bed porosity increases the bigger the size of the packing unit or the thinner the wall of the packing unit. The specific surface area of the bed and the gas pressure drop generally increase the smaller the size of the packing unit. Moreover, random packings cost more per unit volume in the smaller sizes.

Stacked or regular packings are those that are stacked by hand into the column. They have the advantages of low gas pressure drop and can allow higher fluid flow rates. Their flooding velocities are in general considerably greater than those of random packings. In addition, the flow channels are vertical and there is less tendency for the liquid to flow to the walls compared to random packings but they are more costly to install. They are significantly less used than random packings. The individual packing units are bigger than those of random packings being 50 to 200 mm in size. Examples are stacked Raschig rings and wood grids.

Structured or ordered packings have organised geometry made of perforated corrugated metal sheets. Adjacent sheets are arranged such that their surfaces are wetted by liquid flow while the corrugations provide channels for gas flow. Structured packings have low pressure drops, high

mass transfer efficiencies, high porosities above 90% and high specific surface areas. However the higher capacity and efficiency of structured packings are at the expense of higher cost compared to other packing types. Examples are Mellapak and Gempak.

❑ *Packing Support*

An open space has to be provided at the bottom of the column to ensure good distribution of gas into the packed bed. Therefore, the packing has to be supported above this open space. The support plate must be sufficiently strong to bear the weight of the packed bed and it must have sufficiently large free area for the gas and liquid passage such that the resistance to flow is minimal. The simplest packing support is a grid with relatively widely spaced bars. Another type is the gas injection plate.

❑ *Liquid Distribution*

Good initial distribution of liquid at the top of the packing is essential as dry sections of the packed bed are totally ineffective for mass transfer. The liquid distributor provides uniform irrigation to maximise the use of the packing. Examples are the simple orifice distributor, the notched chimney distributor, the notched trough distributor and the perforated ring distributor.

For a randomly packed column, the packing density (i.e. the number of packing units per unit volume of packed bed) is normally smaller adjacent to the column walls. This leads to channelling i.e. the segregation of liquid toward the walls and the tendency for gas flow in the centre of the column. The inclination for channelling or 'wall effect' is minimised when the column diameter is at least eight times larger than the size of the individual packing unit (Jesser and Elgin, 1943; McCabe *et al.*, 1993).

3.1.2   Pressure Drop, Loading and Flooding

Compared to an empty column shell, a column packed with packing pieces incurs a larger resistance to fluid flow. The resistance to the downward liquid flow usually is not that crucial as the liquid flows under gravitational influence, however the gas that flows upwards (counter-current operation) has to overcome the resistance due to the packing.

3.1.2.1   Pressure Drop in a Dry Packed Bed

For a packed column operating under dry conditions, the theory of gas flow through a bed of granular solids can be applied.

❑ *Specific Surface and Voidage*

The specific surface area of an individual solid particle, S (m²/m³) is defined as the surface area of the particle divided by its volume. For a given shape of particle, S increases as particle size decreases. For a sphere with diameter d, S is defined as follows:

$$S = \frac{\pi d^2}{\pi d^3/6} = \frac{6}{d} \qquad (3.1)$$

Generally, the structure of a bed of solid particles can be defined by the specific surface area of the bed, S_B and the voidage or porosity of the bed, ε. S_B (m²/m³) is the surface area of solids exposed to the fluid per unit volume of bed when the solid particles are packed in a bed. ε (dimensionless) is the fractional volume of the bed unoccupied by solid particles. Therefore the fractional volume filled with solid particles is (1-ε). For a randomly packed bed of particles, ε is approximately uniform throughout the bed and so the resistance to flow will be the same in all directions. This is with the exception of parts of the packed bed adjacent to the container walls where ε is larger. The voidage that results when solid particles are packed into a bed renders S unequal to S_B. Assuming only point contact between the solid particles such that an insignificant fraction of surface area is lost due to overlapping, S_B is related to S and ε as follows:

$$S_B = S(1-\varepsilon) \qquad (3.2)$$

❑ *Single-Phase Laminar Flow*

The Carman-Kozeny equation describes laminar flow through a randomly packed bed of solid particles (Kozeny, 1927, 1933 and Carman, 1937). The equation is as follows for a packed bed consisting of monosized spherical solid particles of diameter d (S = 6/d for spheres from equation 3.1) with porosity ε:

$$\frac{(\Delta P)}{l} = 180 \frac{\mu u}{d^2} \frac{(1-\varepsilon)^2}{\varepsilon^3} \qquad (3.3)$$

where   ΔP   = pressure drop across the bed (Pa)

      l   = bed thickness (m)

      u   = superficial fluid velocity through the bed i.e. volumetric flowrate divided by cross-sectional area of the bed (m/s)

      μ   = fluid viscosity (kg/ms)

For non-spherical particles, the surface-volume diameter (or Sauter diameter) d_{sv} is to be used in

place of d in equation 3.3. d_{sv} is the diameter of a sphere having the same ratio of volume to surface area as the particle in question.

The Carman-Kozeny equation applies only for laminar or streamline flow at low Reynolds number for packed bed flow (Re*) i.e. at Re* less than 1. Reynolds number for flow through the packed bed, Re* is defined as follows:

$$Re* = \frac{Re_p}{(1 - \varepsilon)} = \frac{\rho u d}{\mu(1 - \varepsilon)} \qquad (3.4)$$

where Re_p = single particle Reynolds number = $\rho u d/\mu$ (dimensionless)

ρ = fluid density (kg/m^3)

□ *Single-Phase Turbulent Flow*

An empirical correlation describing turbulent flow through a randomly packed bed of monosized spheres of diameter d at Re* greater than 2000 is provided by the Burke-Plummer equation (Burke and Plummer, 1928):

$$\frac{(\Delta P)}{l} = 1.75 \frac{\rho u^2}{d} \frac{(1 - \varepsilon)}{\varepsilon^3} \qquad (3.5)$$

□ *General Equation for Single-Phase Turbulent and Laminar Flow*

Based on experimental data obtained on various shapes of packings and over a wide range of flowrates, Ergun (1952) proposed the following general equation known as the Ergun equation covering a wide range of flow regimes (from Re* of 1 to over 2000) in a randomly packed bed of monosized spheres of diameter d:

$$\frac{(\Delta P)}{l} = 150 \frac{\mu u}{d^2} \frac{(1 - \varepsilon)^2}{\varepsilon^3} + 1.75 \frac{\rho u^2}{d} \frac{(1 - \varepsilon)}{\varepsilon^3} \qquad (3.6)$$

laminar component   turbulent component

The Ergun equation additively combines the viscous or drag energy losses (laminar component) and the kinetic energy losses (turbulent component). Viscous losses predominate at low velocities while kinetic energy losses predominate at high velocities. In fully laminar flow (Re* < 1), the second term on the right hand side of equation 3.6 becomes insignificant and the Ergun equation is reduced to the Carman-Kozeny equation, but with a constant of 150 rather than 180. The pressure gradient is directly proportional to the fluid superficial velocity and fluid viscosity

in laminar conditions. The second term dominates in fully turbulent flow (Re* > 2000) and the Ergun equation reduces to the Burke-Plummer equation, the pressure gradient increases with the fluid density and the square of the fluid superficial velocity. The complete Ergun equation is to be used in the transition regime when 1 < Re* < 2000. However in general practice, the Ergun equation is used to predict packed bed pressure gradient over the complete range of flow conditions. Like the Carman-Kozeny equation, if the Ergun equation is to be used for non-spherical solid particles, d has to be replaced by the surface-volume diameter (or Sauter diameter) d_{sv}. The Ergun equation has been applied with some success to packed beds with small pressure drop relative to the column operating pressure (Strigle, 1994).

❑ *Dry Packed Bed In Practice-Influence of Packing Shape*

In a bed of randomly dumped packings, the resulting flow channels do not possess a constant shape or diameter. The hydraulic radius (i.e. flow channel area divided by wetted perimeter) changes to a large extent with the flow channel shape. Furthermore, the flow channels are neither straight nor of the same length. The pressure drop across a given packed bed height is constant, hence the actual gas velocity in the flow channel varies with hydraulic radius and with the effective length of the channel. As a result, it is difficult to explicitly define from first principles the influence of packing shape on resistance to fluid flow through a packed bed even with single phase flow. Ultimately, the pressure drop across a randomly packed bed must still be empirically established (Strigle, 1994).

In general, the gas pressure drop is related to the gas flow rate in a dry packed bed (single phase gas flow) for turbulent flow as follows:

$$\frac{(\Delta P)}{l} = \alpha u_G{}^2 \rho_G = \alpha \frac{G^2}{\rho_G} \tag{3.7}$$

where $\Delta P/l$ = pressure gradient i.e. gas pressure drop per unit height of packing (Pa/m)

   G   = gas mass velocity (kg/m^{2}s)

   u_G = gas superficial velocity (m/s)

   ρ_G = gas density (kg/m^3)

   α = empirical constant (dependent on packing shape factor, bed voidage

           and packing diameter as indicated by the Burke-Plummer equation (3.5))

The value of the empirical constant α can be determined from the dry bed pressure drop plot for any packing type and size provided the gas flow is turbulent in the packed bed.

3.1.2.2 Pressure Drop, Loading and Flooding in an Irrigated Packed Column

For a packed column operating with gas and liquid flowing counter-currently to one another, the pressure drop across the irrigated bed is greater than that of a dry bed with gas flow alone. The gas pressure drop data for a randomly packed column is commonly described in a plot of log $\Delta P/l$ (pressure gradient) versus log G (gas mass velocity). An example is given in Figure 3.2. The gas flow in a packed column is usually turbulent in practice. In turbulent flow, the Reynolds number Re* is large and the slope of the pressure drop line for dry packing commonly ranges from about 1.8 to 2.0

log *G*, superficial gas mass velocity
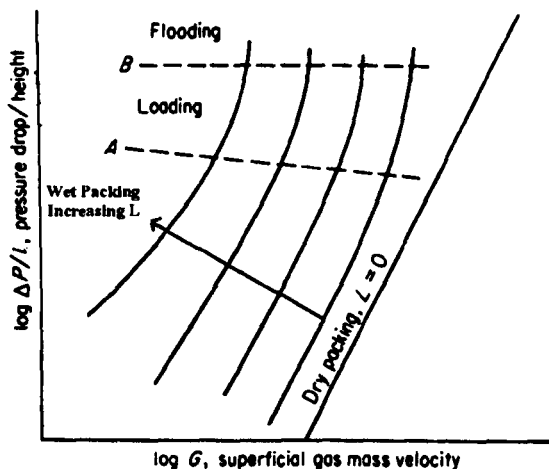
Figure 3.2 A typical gas pressure drop plot for countercurrent gas-liquid flow in a randomly packed column.

(Treybal, 1980) i.e. similar to the pressure gradient-gas velocity relationship in equation 3.7. If liquid flows down the column in addition to the upward gas flow, the effective space in the packed bed available for gas flow is reduced due to presence of the liquid. This results in a higher resistance to gas flow and hence a higher gas pressure drop for an irrigated packed bed. For a given gas velocity, increasing liquid rate gives rise to a greater pressure drop. At a constant liquid rate, the pressure drop line initially runs parallel to that for dry packing with a slope of approximately 2 (see region below line A). In this region, the amount of liquid held up in the bed i.e. the liquid holdup and hence the voidage are reasonably unaffected by the increasing gas velocity, though it increases with liquid rate. In the region A to B, the gas velocity is sufficiently high such that it impedes the downward flow of the liquid. Liquid holdup in the packed bed increases rapidly with gas rate reducing the effective voidage and the pressure drop line becomes steeper correspondingly. The point where the slope of log $\Delta P/l$ versus log G plot changes distinctly to greater than 2 is termed the loading point (White, 1935) (line A runs through the loading points) and the region between A and B is known as the loading region. With further increase in gas velocity, the pressure drop climbs even more rapidly and the line becomes almost vertical at a pressure drop of about 150 to 250 mm H_2O/m of packing (McCabe *et al.*, 1993). The point at which the pressure drop line becomes almost vertical is termed the flooding point (White, 1935) (line B runs through the flooding points) and it marks the maximum hydraulic capacity of the column. At and beyond this point, the column is said to be flooded. During flooding, phase inversion occurs i.e. liquid becomes the continuous phase while the gas becomes

the dispersed phase. Gas bubbles through the liquid which fills the column. Liquid droplets may be entrained with exiting gas.

The gas velocity must clearly be below the flooding velocity for a safe and stable operation. On the other hand, more packing is wetted the nearer it is to flooding, maximising the liquid-gas interfacial contact. The operating gas velocity has to be safely below the flooding limit but not too low such as to need a significantly larger column. Most columns tend to operate in the lower part of the loading region (Treybal, 1980).

3.1.2.3 Loading and Flooding Correlations

❑ *Loading*

There is no generalised correlation to readily predict the onset of loading, however several semi-empirical correlations are available (Coulson *et al.*, 1991). Morris and Jackson (1953) gave plots of $\varphi(u_G/u_L)$ at the loading rates for various wetting rates L_w (i.e. u_L/S_B, m^2/s) where φ is the gas density correction factor, $(\rho_G/\rho_{air,\,293K})^{0.5}$. Leva (1954) attempted to correlate the pressure drop at loading with fluid rates and packing properties but was unsuccessful. He stated that the explicit loading point as defined by White (1935) might not be so distinct and instead loading occurs over a range of flow and pressure drop rather than at a point. In Leva's (1954) proposed generalised pressure drop correlation, the loading points showed a much wider spread than the corresponding flooding points.

❑ *Flooding*

Flooding determines the maximum hydraulic capacity and marks the onset of instability in the operation of a packed column. Hence for design purposes, it is desirable to know the upper limits of gas and liquid flow rates in a packed column dictating the onset of flooding to ensure that the column operates within a safe operating range. The earliest generalised flooding correlation for randomly packed columns in counter-current operation was developed by Sherwood *et al.* (1938). The graphical correlation is depicted in Figure 3.3 which includes the flooding curve for stacked rings in addition to randomly dumped rings.

A column randomly packed with carbon Raschig rings which was mainly water-irrigated in air, hydrogen and carbon dioxide was used. Other liquid systems applied were aqueous glycerol, aqueous butyric acid and pure and aqueous methanol in air. Sherwood *et al.* found that the flooding velocities were influenced by gas and liquid densities as well as liquid viscosity, but

liquid surface tension was found to have a negligible effect within the range 26 to 73 dynes/cm. The abscissa of the graphical flooding correlation is termed the flow parameter and represents the square root of the ratio of liquid kinetic energy to gas kinetic energy. The ordinate incorporates the gas rate, the gas and liquid densities, the liquid viscosity and the S_B/ε^3 term which characterises the shape and size of the column packing. With the exception of the liquid viscosity term, the groups of variables on the ordinate and abscissa are dimensionless and hence are independent of the system of units employed as long as all the units are consistent. However, the liquid viscosity must be quoted in centipoise.

$$\frac{u_G^2 S_B \rho_G}{g\varepsilon^3 \rho_L}\mu_L^{0.2}$$

or

$$\frac{G^2 S_B \mu_L^{0.2}}{\rho_G \rho_L g \varepsilon^3}$$

G, L = gas and liquid superficial mass velocities (kg/m^{2}s)

u_G = superficial gas velocity (m/s)

S_B = specific surface area of packed bed (m^2/m^3)

g = gravitational acceleration (m/s^2)

ε = voidage or porosity of packed bed (-)

μ_L = liquid viscosity (cP)

ρ_G = gas density (kg/m^3)

ρ_L = liquid density (kg/m^3)

Investigators	Packing size	Tower dia.
o Uchida and Fujita	0.6"(15 mm.)	30.5 cm.
▲ Uchida and Fujita	1.0"(25 mm.)	30.5 cm.
□ Uchida and Fujita	1.4"(36 mm.)	30.5 cm.
x White	0.5"(12.7 mm.)	7.6 cm.
+ White	1.0"(25 mm.)	15.2 cm.
▲ Baker,Chilton,and Vernon	0.5"(12.7 mm.)	

All ratios dimensionless
μ = liquid viscosity centipoises

Stacked rings

Dumped rings

$$\frac{L}{G}\sqrt{\frac{\rho_G}{\rho_L}}$$

Figure 3.3 Sherwood et al.'s generalised flooding correlation for counter-current packed columns (Sherwood et al., 1938).

Since then, Sherwood *et al's* (1938) generalised flooding correlation has undergone several modifications based on work with mainly air and other liquids by Lobo *et al.* (1945), Leva (1954), Eckert (1961), Eckert *et al.* (1966), Eckert (1970) and Strigle (1994). Bain and Hougen (1944) fitted an equation using Sherwood *et al.*'s (1938) variable groups to their flooding data for Raschig rings, Berl saddles and wire helices. Lobo *et al.* (1945) demonstrated that the use of accurate values of specific surface area of packing and packing voidage is necessary for a good correlation of flooding velocity. They reported that the previously documented S_B/ε^3 ratio did not give an adequate prediction of the packing capacity. They proposed a capacity factor to describe

the packing characteristics based on observation of the actual flood point to substitute the S_B/ε^3 term on Sherwood's correlation. Improved graphical flooding correlations were presented, the first being based on the proposed capacity factors and the second being based on the ratio of experimentally ascertained S_B to ε^3. Leva (1954) extended Sherwood *et al.'s* correlation to include parameters of constant pressure drop, hence producing the first generalised pressure drop correlation (GPDC). An additional correction factor for liquid density, ψ^2 i.e. $(\rho_{water}/\rho_L)^2$ was added to the ordinate. Eckert (1961), Eckert *et al.* (1966), Eckert (1970) used a modification of Lobo *et al.'s* capacity factor and termed it the packing factor F to replace the S_B/ε^3 term. F decreases with increasing packing size or increasing porosity. Eckert's packing factors were obtained by averaging the experimentally observed bed capacities at operating pressure drops below flooding. Eckert also modified the ordinate of Leva's (1954) GPDC by changing the exponent of the liquid density correction factor ψ

(i.e. ρ_{water}/ρ_L) to 1 rather than 2 as the second power was found to be excessive in subsequent tower operation. Eckert's version of the GPDC is shown in Figure 3.4.

Several new pressure drop and flooding correlations have been introduced more recently in the past decade or so. Strigle (1994) modified Eckert's version of the GPDC, maintaining the flow parameter $L/G(\rho_G/\rho_L)^{0.5}$ in the abscissa but changing the ordinate term to $C_sF^{0.5}v_L^{0.05}$ (C_s the capacity factor = $u_G\{\rho_G/(\rho_L-\rho_G)\}^{0.5}$ (ft/s), F the packing factor (ft^{-1}) and v the kinematic liquid

Figure 3.4 Generalised pressure drop correlation for random packings (Eckert, 1966; 1970).

viscosity (cst). Also rather than the conventional log-log plot, a semi-log plot was employed with a linear scale for the ordinate. Kister and Gill (1991) correlated the pressure drop at flooding which then can be used with individual GPDCs (specific for a particular packing type and size) to predict flooding capacity. Mackowiak (1990) as well as Billet and Schultes (1995) presented a second type of flooding correlation distinct from the graphical GPDCs, based on theoretical treatment of two-phase flow through packed beds. However, their main drawback was that they relied on the use of empirically determined packing constants which were not readily available for every packing type.

Very recently, Piche *et al.* (2001a) presented a flooding correlation based on the combination of artificial neural network modelling and dimensional analysis. They compared the accuracy of the neural correlation and 14 existing flooding correlations against a wide collection of experimental data from the literature. Only 3 of the 14 existing flooding correlations reviewed "exhibited excellent precision", demonstrating similar if not better predictive accuracies than the neural correlation in evaluating flooding capacity in packed beds. These are the semi-empirical correlations of Billet and Schultes (1995) and Mackowiak (1990), plus Kister and Gill's GPDC (1991), each reportedly demonstrating about 10% average absolute relative error.

3.1.3 Liquid Holdup

In a packed column, the liquid holdup refers to the liquid retained in the bed of packings i.e. films or droplets on the surface of the packings or the liquid trapped in the interstitial space between the packings. The total liquid holdup, h_T (m^3/m^3) in a packed column is made up of 2 components:

$$h_T = h_S + h_D \text{ (volume of liquid/volume of packed bed)} \tag{3.8}$$

where h_S = static holdup (m^3/m^3)

h_D = dynamic (operating or moving) holdup (m^3/m^3)

Under operating conditions, the total liquid holdup h_T reduces the dry bed voidage ε to give the effective voidage ε_{eff}:

$$\varepsilon_{eff} = \varepsilon - h_T \tag{3.9}$$

3.1.3.1 Static Holdup

Static holdup is the volume of liquid per volume of packing that remains in the packed bed that has been fully wetted after the gas and liquid flows have stopped and the bed has drained. It is made up of very stagnant pools protected in the packing interstices, replaced very slowly by fresh liquid. Hence static holdup has been defined as a measure of the accumulated semi-stagnant liquid in the packed bed (Shulman *et al.*, 1955a).

Shulman *et al.* (1955a, 1955b) measured liquid holdups for ceramic Berl saddles, ceramic and carbon Raschig rings. Water irrigation was accompanied by air flow, whilst tests with aqueous and organic solutions were conducted at zero gas rate. They reported that static holdup is

independent of variations in gas and liquid flowrates (also Jesser and Elgin, 1943). Instead, it is a function of the nature of the packing i.e. its material of construction, shape and size and the liquid physical properties. Static holdup was found to increase with liquid surface tension and to a less extent by liquid viscosity, but decreased with liquid density. Shulman *et al.* (1955b) gave the following equation for static holdup:

$$h_S = \frac{C_1 \mu_L{}^{C_2} \sigma_L{}^{C_3}}{\rho_L^{0.37}}$$ (3.10)

where C_1, C_2 and C_3 = empirical packing constants $(C_2 < C_3)$

Unlike dynamic holdup, the effect of surface tension on static holdup is unaffected by liquid rate. Both the nature of the packing surface and the liquid surface tension influence the interfacial tension at the solid-gas-liquid contact points. This in turn determines the degree of wetting on the packing surface, the liquid retention at contact points between adjacent packings and capillary forces between the packings. A porous surface would also increase the static hold-up. The packing shape determines the contact points between packings, and therefore the availability of horizontal surface for liquid accumulation. The higher the liquid density, the stronger is the gravitational effect which tends to remove the liquid from the bed.

Static holdup for wettable packings has been correlated with the dimensionless Eötvös number (Charpentier *et al.*, 1968; Van Swaaij *et al.*, 1969; Saez and Carbonell, 1985). Charpentier *et al.* (1968) first empirically correlated static holdup, h_S in terms of Eötvös number, Eö which is the dimensionless ratio of gravitational force to surface tension force:

$$h_s = \frac{1}{20 + 0.9E\ddot{o}}$$ (3.11)

$$E\ddot{o} = \frac{\rho_L g d^2}{\sigma_L}$$ (3.12)

where ρ_L = liquid density (kg/m^3)

σ_L = liquid surface tension (N/m)

g   = gravitational acceleration (m/s^2)

d   = packing particle nominal diameter (m)

Van Swaiij *et al.* (1969) similarly correlated h_s against Eö for wettable packings.

Saez and Carbonell (1985) replaced d with a parameter $d_{equiv}\varepsilon/(1-\varepsilon)$ that is proportional to the packing particle equivalent diameter, d_{equiv} to give the corresponding modified Eötvös number, Eö* and an empirical correlation for static holdup, h_S:

$$d_{equiv} = 6\frac{V_p}{S_p}$$

(3.13)

where V_p = volume of a packing particle (m³)

   S_p = external area of a packing particle (m²)

$$E\ddot{o}* = \frac{\rho_L g d_{equiv}^{2}\varepsilon^{2}}{\sigma_L(1-\varepsilon)^{2}}$$

(3.14)

$$h_s = \frac{1}{20 + 0.9 E\ddot{o}*} \quad \text{for } 0.25 \le E\ddot{o} \le 30$$

(3.15)

The average absolute relative error reported for Saez and Carbonell's correlation for h_s was 25% whilst that of Charpentier *et al.* was 27% based on the same experimental data points. Saez and Carbonell attributed the inaccuracy to firstly, experimental errors and secondly, exclusion of solid-liquid contact angle i.e. solid wettability. The correlation assumes perfect wetting of solid by the liquid where the contact angle θ is zero. When this is not the case, the value of h_S would be less that that of perfect wetting and the correlation would tend to overestimate h_S. Dimensional analysis suggested that static holdup is a function of the Eötvös number, solid-liquid contact angle and packing geometry:

$$h_s = h_s(E\ddot{o}, \theta, \text{packing particle geometry})$$

(3.16)

Using 0.5 to 4.0 mm spherical glass beads and ensuring that contact angle is close to zero, Saez *et al.* (1991) measured the static holdup with water, methanol and kerosene. h_S was correlated against Eö without the influence of solid-liquid contact angle and particle geometry. The resulting correlation gave markedly less scatter than that of Saez and Carbonell (1985):

$$h_s = \frac{0.11}{1 + E\ddot{o}}$$

(3.17)

In absorption and desorption processes, solute transfer occurs between the bulk gas and bulk liquid. The liquid in the static hold-up rapidly becomes equilibrated with the adjacent gas while it is only displaced very slowly by fresh liquid. Hence, its interfacial surface becomes relatively ineffective to mass transfer (Shulman *et al.*, 1955a).

3.1.3.2 Dynamic (Operating or Moving) Holdup

Dynamic holdup is the volume of liquid per volume of packing that drains out of the bed after the gas and liquid flows have stopped. It is the liquid which continuously flows through the packing, rapidly and continuously substituted by fresh liquid flowing from upstream.

Elgin and Weiss (1939) measured dynamic holdup using clay packing of Berl saddles, Raschig rings and spheres, as well as porcelain saddles in an air-water system. They reported that dynamic holdup discernibly increased with liquid rate. However except at high liquid rates with packings having relatively small voidage of about 0.5, dynamic holdup was almost independent of the gas rate until just before the flooding point was reached, when it rose sharply. On a log-log plot of dynamic holdup versus gas velocity, an upper break point occurred coinciding with visually observed flooding. Dynamic holdup varied linearly with liquid rate except at low rates, with or without the presence of gas flow.

Jesser and Elgin (1943) measured dynamic liquid holdup without the presence of gas flow using glass spheres, Berl saddles and carbon rings. Liquid systems of water and aqueous solutions were employed. They found that previous conclusions that liquid holdup varied linearly with liquid rates were unsubstantiated. Instead they described the relationship between dynamic liquid holdup h_D with liquid rate as follows with the exponent b_2 ranging from 0.52 to 0.67:

$$h_D = b_1 L^{b_2} \qquad (3.18)$$

Dynamic holdup decreased slightly with decreasing surface tension at low liquid rates up to about 2.17 kg/m²s, however at higher liquid rates dynamic holdup was markedly increased with decreasing liquid surface tension. Dynamic holdup was found to increase with increasing liquid viscosity but decreasing liquid density. The effect of liquid physical properties on dynamic holdup were expressed as:

$$h_D = h_{D,w} \frac{\mu_s^{0.1}}{\rho_s^{0.78} \sigma_s^{b_3}} \qquad (3.19)$$

where   L   = liquid superficial mass velocity (kg/m²s)

       b_1 = empirical constant = obtained from y-intercept of log h_D versus log L; dependent on specific surface area of packed bed, S_B

       b_2 = empirical constant = slope of log h_D versus log L; constant for a packing type regardless of size

       $h_{D,w}$ = the corresponding dynamic liquid holdup of water at 20°C for a specific packing and at a specific L (m³/m³)

μ_s = ratio of viscosity of liquid to that of water at 20°C; independent of L

ρ_s = ratio of density of liquid to that of water at 20°C; independent of L

σ_s = ratio of surface tension of liquid to that of water at 20°C

b_3 = empirical exponent governing the effect of surface tension on h_D; varies with L

According to Shulman *et al.* (1955a, 1955b), dynamic holdup is mainly a function of liquid flow rate. Dynamic holdup was shown to be negligibly affected by gas rates up till the loading point especially at low liquid rates, however the effect of gas rate became more pronounced at high liquid rates. Unlike static holdup, the nature of the packing surface did not affect the dynamic holdup (also Shulman *et al.*, 1955a). Dynamic holdup increased with higher liquid viscosity but lower liquid density. Surface tension effect was found to vary with liquid flowrate. At low liquid flowrates, dynamic holdup increased with higher surface tension, whereas at high liquid flowrates, dynamic holdup increased with decreasing surface tension. The effects of liquid rate and liquid physical properties on dynamic holdup was summarised by Shulman *et al.* (1955b) as follows:

$$h_D = C_4 L^{0.57} \mu_L{}^{C_5} \left(\frac{1}{\rho_L}\right)^{0.84} \left(\frac{\sigma_L}{73}\right)^{c_6 - 0.262 \log L} \tag{3.20}$$

where σ_L is expressed in dynes/cm

C_4, C_5 and C_6 = empirical constants ($C_5 = 0.13$ for $\mu_L < 12$ cP)

Strigle (1994) reported that for relatively high surface tension liquids such as water (σ_L 72 dyne/cm), liquid surface tension does not affect the dynamic hold-up. However, for low surface tension liquids such as organic liquids (σ_L about 27 dyne/cm), the dynamic hold-up would be lower than that of water. The effect of surface tension on dynamic hold-up diminishes at liquid flowrates above 0.475 cm/s.

In absorption and desorption processes, the dynamic hold-up is effective to mass transfer rate as it is continuously replaced and regenerated, hence providing the residence time for gas-liquid interfacial contact.

3.1.3.3 Total Liquid Holdup

The total liquid hold-up is the total amount of liquid on the packing under dynamic conditions i.e. the sum of the static hold-up and dynamic hold-up. The main factor influencing total liquid

hold-up is the operating liquid flowrate or liquid superficial velocity. On top of that, Piche *et al.* (2001b) identified six other relevant physical parameters which also influence the total liquid hold-up. These are:

- Gas flowrate: or the gas superficial velocity
- Bed physical properties: Bed porosity and bed specific surface area.
- Gas physical property: Gas density.
- Liquid physical properties: Liquid density and surface tension.

The total liquid hold-up is almost unaffected by the gas rate in the pre-loading region, but then rises at an increasing rate with increasing gas velocity beyond the loading point till flooding is reached (also Shulman *et al*, 1955a; Gardner, 1956, Billet and Schultes, 1993). Therefore, the loading point in a packed bed is known as the first inflexion point in the total liquid hold-up versus gas flow plot. However, Shulman *et al.* (1955a) pointed out that although the total holdup is almost independent of the gas rate up till the loading point at low liquid rates, the effect of gas rate cannot be ignored for higher liquid rates and especially for smaller packings near the loading point.

Lower porosity beds give higher resistance to liquid drainage, therefore increasing liquid hold-ups and giving loading points at lower gas rates. Packings with large surface area provide more friction against liquid flow, hence increasing the liquid hold-up. Shulman *et al.* (1955a) reported that total holdup is approximately proportional to the packing density i.e. the number of packing units per cubic foot.

With higher gas density, the onset of loading occurs at lower gas velocity i.e. the pre-loading zone is narrower for pressurised gases. In the loading region, higher gas density gives higher total liquid hold-up at constant gas superficial velocity.

Higher liquid density means greater gravitational effects, hence improving bed drainage and reducing total liquid hold-up. For aqueous and organic solutions, liquids with higher surface tensions provide greater capillary forces, increasing the static hold-up and therefore the total hold-up. Changes in liquid viscosity do not appear to give a notable consistent effect on total liquid hold-up.

Very recently, Piche *et al.* (2001b) presented a total liquid holdup correlation applicable to both pre-loading and loading zones of packed beds based on the combination of artificial neural network modelling and dimensional analysis. They compared the accuracy of the neural

correlation and 11 other existing total liquid holdup h_T correlations against a wide collection of experimental data from the literature since the 1930s. Out of the 11 existing flooding correlations reviewed, only the semi-empirical correlation of Billet and Schultes (1993) "exhibited excellent precision" for predicting h_T in the pre-loading zone and it also gave the 'best' available correlation for the overall h_T prediction in both pre-loading and loading zones up till the flooding point, demonstrating slightly better predictive accuracies than the neural correlation. The remaining correlations compared were markedly inferior to Billet and Schultes' correlation and/or the neural correlation. For the same h_T data set, the correlation of Billet and Schultes reportedly gave an average absolute relative error of 11.3% whilst that of the neural correlation was 12.5% for the overall pre-loading and loading zones. Despite its accuracy, Billet and Schultes' correlation (1993) has one inherent drawback in that it requires the use of packing constants which are not readily available for all packing types.

3.1.4 Previous Work on Non-Wetting Systems

3.1.4.1 Definition of Wetting and Non-Wetting

The degree to which a liquid wets a solid is measured by the contact angle θ. A liquid is said to wet a solid if the contact angle θ between the liquid and the solid is zero or less than 90° such that the liquid spreads over the solid. This occurs when the attractive force of adhesion between the liquid and the solid is stronger than the attractive force of cohesion between the liquid molecules such that the liquid tends to cling to the solid surface. Non-wetting occurs when the contact angle is greater than 90° such that the liquid has a tendency to ball up forming droplets and roll off the solid surface easily. This is the result of a greater cohesive force than the adhesive force which encourages the liquid to cling more to itself rather than the solid surface. The following figure illustrates a typical liquid droplet on a solid surface under wetting and non-wetting conditions:
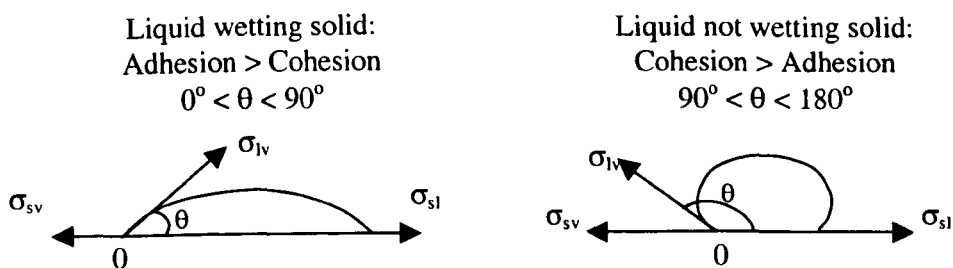
Figure 3.5 Wetting and non-wetting conditions.

Examples are water which wets glass, the contact angle being 14° (O'Brien, 1996), and mercury which does not wet glass having a contact angle of 128 to 148° (Adamson and Gast, 1997).

At equilibrium, a force balance of surface tensions exists at the line of common solid-liquid-air contact, intersecting at point 0. Surface tension is the required force acting parallel to the surface opposing the natural pull of the molecules in the surface to minimise the size of that surface. For both wetting and non-wetting cases, the force balance is given in the following equation which is known as the Young equation of wetting (Young, 1805):

$$\sigma_{sv} = \sigma_{sl} + \sigma_{lv} \cos\theta \qquad (3.21)$$

$$\therefore \cos\theta = \frac{\sigma_{sv} - \sigma_{sl}}{\sigma_{lv}} \qquad (3.22)$$

where σ_{sv} = solid-vapour surface tension (i.e. solid surface tension) (N/m)

σ_{sl} = solid-liquid surface tension (N/m)

σ_{lv} = liquid-vapour surface tension (i.e. liquid surface tension) (N/m)

Therefore the tendency of liquid to wet a solid surface depends on the surface tension of both substances. The ability of a liquid to wet and spread on a solid is measured by the spreading coefficient S_{sl} as in equation 3.23. A large positive value of S_{sl} indicates spontaneous wetting and spreading of the liquid on the solid. A negative value of S_{sl} implies lack of wetting and spreading by the liquid i.e. non-wetting tendency.

$$S_{sl} = \sigma_{sv} - \sigma_{sl} - \sigma_{lv} \qquad (3.23)$$

Another way to determine the wettability of a liquid on a solid surface is by knowing the critical surface tension of the solid σ_c. σ_c is an approximate measure of the surface free energy of the solid. Surface free energy is the work done to isothermally increase the surface by one unit area. Any liquid with a surface tension smaller than σ_c will wet or spread freely on the solid surface. Liquids with surface tension greater than σ_c will form discrete drops. In other words, wetting of the solid by the liquid is favoured when the surface free energy of the liquid is low and the surface free energy of the solid is high. Conversely, a high surface energy liquid will not wet a low surface energy solid.

3.1.4.2 Flooding in Non-Wetting Systems

The flooding correlations for packed columns reviewed in section 3.1.2.3 were largely based on aqueous and organic liquids with relatively low densities (800 to 1290 kg/m^3) and low surface

tensions (23 to 73 dyne/cm). This is a reflection of the conventional process fluids normally found in the chemical industry. In contrast, liquid metals have comparatively much higher densities and surface tensions. For example, molten tin, the liquid metal of interest herein has significantly high density and surface tension of 6980 kg/m^3 and 560 dyne/cm respectively at its melting point of 232°C. Due to their high surface tensions (or high surface free energies), liquid metals generally exhibit non-wetting type of flow on solid surfaces (Zisman, 1964) and this has been confirmed on various packing materials (Standish, 1968). As a result, liquid metal irrigation of a packed bed is characterised by discrete droplets and rivulets on the packing surface as opposed to the spreading (wetting) film flow in a packed bed irrigated by conventional fluids with relatively low surface tensions.

The significant difference in the physical properties and wetting characteristics of liquid metals compared to conventional process fluids raises the question of whether the former would fully conform to the flooding correlations based on the latter. This prompted a review on flooding correlations for packed columns operating under similarly non-wetting condition and/or better still with liquid metal irrigation. It was found that to date, there has only been a handful of documented work specifically focusing on the flooding criteria of non-wetting systems and this could be divided into two groups based on opposing conclusions obtained. The first group (Coughlin, 1969; Andrieu, 1975; Gaston-Bonhomme *et al.*, 1980) found that higher flooding capacities were obtained with wetting systems compared to non-wetting systems, whilst the converse was found to be true by the second group of investigators (Standish and Drinkwater, 1972; Szekely and Mendrykowski, 1972; Standish, 1973).

Coughlin (1969) investigated the effect of different liquid-packing surface interaction on pressure drop, loading, gas absorption and liquid holdup in a packed column. Nearly geometrically identical Raschig rings made of ceramic, Saran and polyethylene were irrigated by water and Na_2SO_3 solution. Both polymeric materials which were non-wettable gave identical loading points, with loading occurring at lower fluid rates compared to the fully wettable ceramic packing. Based on this observation, Coughlin surmised that there was increased tendency for flooding with decreased wettability of the packing material.

Andrieu (1975) investigated the influence of wettability on pressure drop, flooding and hold-up in a packed column in an air-demineralised water system using glass Raschig rings, both uncoated ($\theta = 0°$) and coated with silicone resin ($\theta = 93°$). Under dry condition, the pressure drop for both the coated and uncoated packing were in close agreement, whilst under irrigated

condition, the pressure drop was slightly higher for the coated packing at the same liquid rate. Flooding velocities were slightly lower for the coated packing than for the uncoated packing, this being attributed to the rapid increase in liquid holdup beyond the loading zone for the coated packing.

Gaston-Bonhomme *et al.* (1980) compared pressure drops, flooding velocities and holdups for non-wettable fluored polymer (PTFE, PVDF) and wettable glass Raschig ring packings in air-water and air-aqueous H_2SO_4 systems. Generally, the polymer packings gave higher pressure drops and lower flooding velocities than the glass packings. This was attributed to greater turbulence induced by the droplets and rivulets on the polymer surface.

Standish and Drinkwater (1972) determined the flooding points under wetting and non-wetting flow for packed columns in air-water system using coke particles, glass spheres and ceramic rings packings. The particles were waxed to render them non-wetting to simulate conditions in

blast furnaces where the bed of coke is non-wetting to the flow of slag and metal. It was found that non-wetting conditions exhibited higher flooding rates than wetting conditions. The flooding curve for non-wetting condition was displaced above that for wetting condition as shown in Figure 3.6. The sphericity term, ψ_s has been included in the ordinate to account for the different packing shapes and was found to reduce the scatter of the flooding points. The flooding curve under wetting conditions obey the original Sherwood *et al.*'s (1938) correlation for flooding in absorption columns.
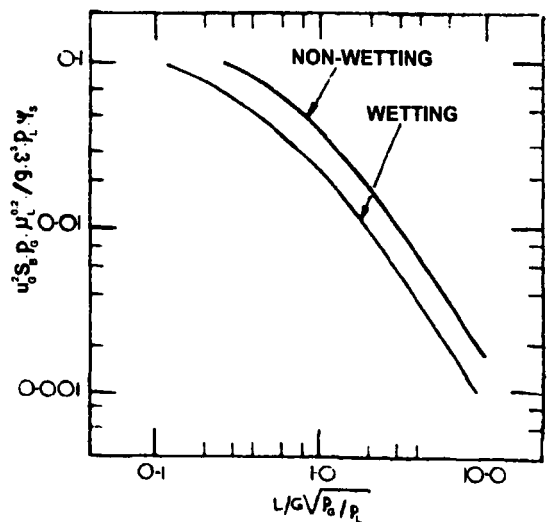
Figure 3.6 Comparison of flooding results for wetting and non-wetting packing (Standish and Drinkwater, 1972).

Szekely and Mendrykowski (1972) determined flooding conditions for nitrogen-mercury and helium-mercury systems using glass beads, ceramic cylinders and interlock saddles. Mercury has high density (1360 kg/m^3 at 20°C) and high surface tension (476 dyne/cm at 20°C). They reported the absence of loading points, which was thought to be due to sufficiently high fluid rates such that column operation was already within the loading range. The flooding points showed better agreement with the original Sherwood *et al.*'s (1938) flooding correlation (within a factor of 1.5 to 2) than with the *supposedly* 'Leva's modification' (Leva, 1954) of the flooding

correlation (within a factor of 10) (see Figure 3.7). Szekely and Mendrykowski attributed the discrepancy to the additional density correction factor, $\psi = \rho_{water}/\rho_{mercury} \approx 1/13.6$ on the ordinate in 'Leva's modification'. They went on to conclude that Sherwood *et al.'s* original correlation appeared to offer the best available flooding criteria at that time for dense liquids with high surface tensions. They added that the effect of surface tension on flooding while appearing to be generally small might depend on the nature of the packing, its wettability as well as on the liquid rate, ultimately the flooding criteria with liquids of high density and high surface tension would require more complex relationships than that of Sherwood *et al.*

(On an additional note, an error made by Szekely and Mendrykowski is pointed out herein. The *supposedly* 'Leva's modification' should by right be Eckert's (1961) modification of the generalised flooding correlation (see Section 3.1.2.3). Leva (1954) introduced the density correction factor ψ to the power of 2, and it was Eckert (1961) who actually modified the exponent to 1.)
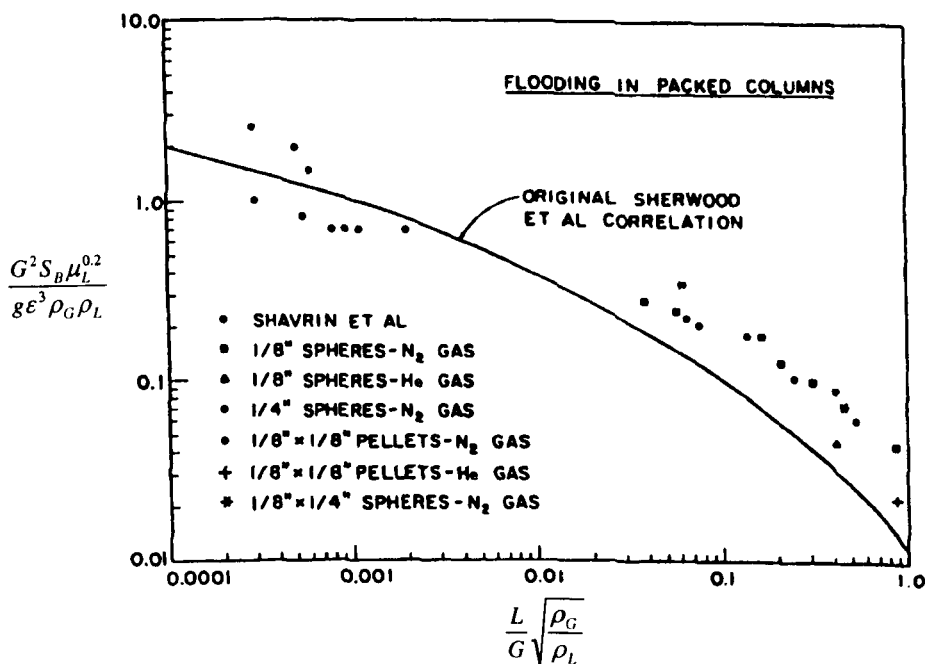
Figure 3.7 *Szekely and Mendrykowski's experimental data compared with Sherwood et al.'s flooding correlation. Also included are Shavrin et al.'s results obtained with molten slag (Szekely and Mendrykowski, 1972).*

Standish (1973) pointed out that Szekely and Mendrykowski's (1972) results for the mercury-irrigated system should be compared with the correlation for non-wetting conditions rather than for a wetting regime like that of Sherwood *et al.'s* (1938). Standish proceeded to compare Szekely and Mendrykowski's (1972) experimental results with Standish and Drinkwater's

(1972) correlation for non-wetting flow. A good agreement was obtained with the non-wetting line, better than with Sherwood *et al.*'s (1938) wetting correlation as illustrated by Figure 3.8. Kukarin and Kitaev's (1962) experimental results using molten Wood's metal (alloy of Bi, Pb, Sn and Cd) irrigated graphite packings was also compared, generally agreeing with the extrapolated Standish and Drinkwater's (1972) non-wetting correlation that was based on water irrigation of waxed packings. Standish thereby noted that the flooding points of molten metals appeared to be insensitive to surface tension, differing from the flooding points of aqueous and organic liquid systems which showed strong dependency on surface tension (Standish and Drinkwater, 1972).
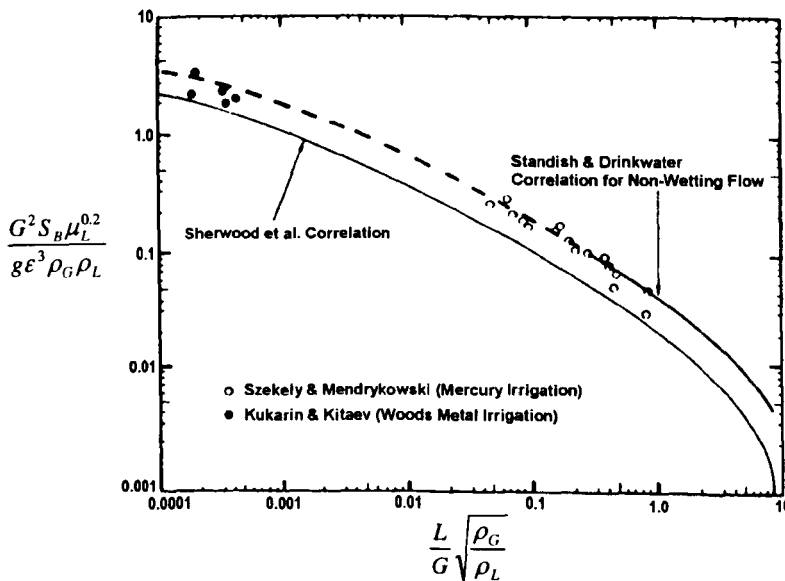
Figure 3.8 Comparison of liquid metal flooding results (Standish, 1973).

More recently, Szekely and Mendrykowski's (1972) flooding data for mercury-nitrogen and mercury-helium systems were among the wide collection of experimental data tested by Piche *et al.* (2001a) using their flooding correlation derived from artificial neural network modelling. The neural correlation reportedly gave average absolute relative errors of 14.3% and 41.1% for the two systems respectively.

3.1.4.3 Liquid Holdup in Non-Wetting Systems

Compared to conventional wettable systems, there have been significantly fewer documented studies and experimental data on the liquid holdup for columns incorporating non-wettable packings, not to mention systems irrigated by liquid metals.

Gardner (1956) studied the liquid holdup for water-irrigated beds of non-wettable coke having a contact angle of about 90°. The static holdup h_S was found to increase with decreasing packing size d:

$$h_S \alpha \frac{1}{d^{0.8}} \tag{3.24}$$

Warner (1959a) investigated liquid holdup and pressure drop for a packed bed of ¼ inch steel Raschig rings irrigated by mercury countercurrent to hydrogen and nitrogen gas flows. Unlike aqueous and organic liquid irrigations where static holdup was constant for a particular liquid and packing, static holdup for the mercury irrigation was found to decrease slightly with increasing liquid rates. An explanation given was that liquid metals have high densities, hence possessing greater kinetic energy than conventional liquids during irrigation and dispersing semi-stagnant pockets of static holdup more easily, this effect increasing with liquid rates. The increased mobility of the static holdup for liquid metals could render it almost as effective as the dynamic holdup in mass transfer. Liquid holdups and specific surfaces were found to be greater for the mercury-N_2 system compared to the mercury-H_2 system, this being attributed to the greater interfacial tension of mercury-N_2. Similar to conventional liquid systems, dynamic holdup was not solely affected by liquid rate, but by other factors as well. Higher gas rates generally gave greater dynamic holdup. Starting from the Ergun equation describing single phase pressure drop in granular beds (Ergun, 1952), and assuming fully turbulent gas flow, Warner correlated the total liquid holdup, gas pressure drop, true gas velocity and gas density data obtained with and without mercury irrigation as depicted in Figure 3.9.
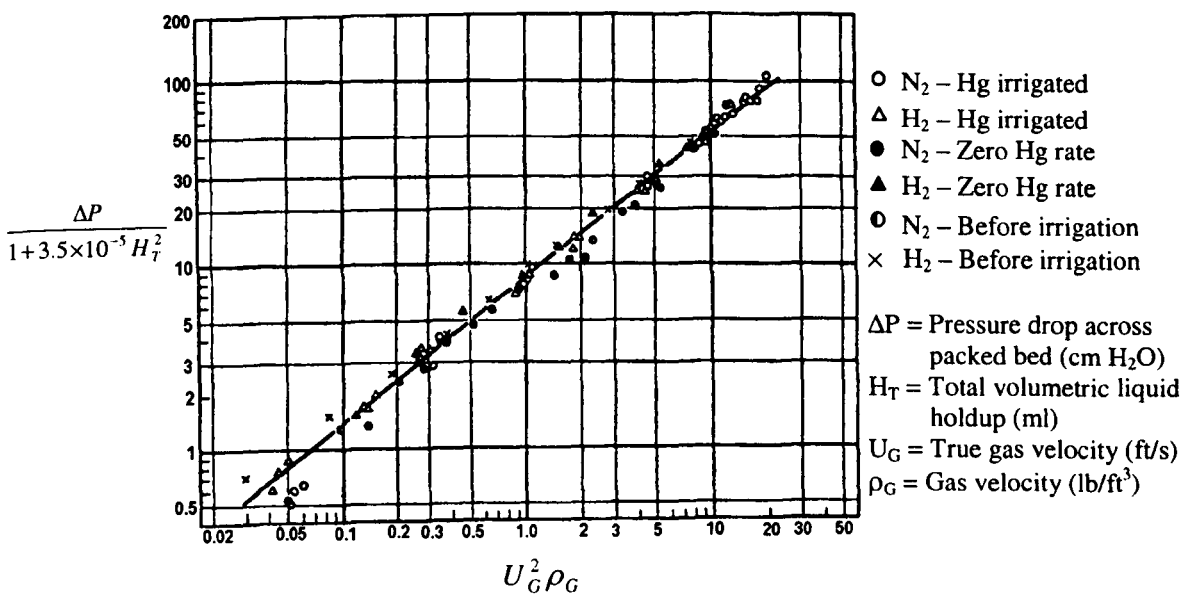
Figure 3.9 Warner's empirical correlation of total liquid holdup (Warner, 1959a).

The correlation was tested with water irrigation of the same packing, both unwaxed and waxed. It was found that the correlation 'applied reasonably well' to the water irrigated data. Warner thereby suggested that this method would be useful to estimate liquid holdups in systems where direct measurements are too complex and difficult, examples being high temperature liquid metal or molten slag systems, the correlation being derived from a simpler room temperature model with the same packing.

Standish (1968a) reported that existing dynamic holdup correlations for aqueous and organic liquids (including that of Shulman *et al.* (1955b)) cannot be applied to liquid metal systems. Using ¼ inch Raschig ring (steel, porcelain, carbon) and Berl saddle (porcelain) packings, Standish investigated the dynamic holdup (h_D) of cerrobend (an alloy of Pb-Bi-Cd-Sn) as well as the dynamic holdup of water in both wetting and non-wetting conditions, the latter with packings treated with silicone fluid. No gas flow was employed. Liquid rates ranged from 5.08 to 50.8 $cm^3/min.cm^2$. h_D seemed to be independent of packing shape and material. All test liquids exhibited higher h_D at greater liquid rates. h_D of cerrobend increased with lower temperatures while h_D of water was slightly higher in wetting than non-wetting conditions. Based on the liquid holdup data for cerrobend, wetting and non-wetting water from this study as well as that of mercury irrigation in a previous work (Standish, 1963), Standish presented the following generalised correlation for dynamic holdup with ¼ inch packings:

$$h_D = 6.0 \times 10^{-9} u_L^{0.95} \sigma_L^{0.27} v_L^{1/3} \tag{3.25}$$

where u_L = liquid superficial velocity (m/s)

σ_L = liquid surface tension (dynes/cm)

v_L = liquid kinematic viscosity (m^2/s) = μ_L/ρ_L

Non-wetting water gave good agreement with the above correlation. Water irrigation under wetting conditions was found to obey this correlation at low liquid rates. However at higher liquid rates, h_D for wetting water deviated from those of the non-wetting liquids with the exponent on u_L becoming less than 0.95. 'Very good agreement' was reportedly attainable when the correlation was applied to existing holdup data for aqueous and organic liquids in ¼ inch packings. Hence Standish suggested that experimental data obtained with non-wetting water could be used to predict dynamic holdup for liquid metals using similar size packings.

Standish (1968b) measured static holdup for irrigation of mercury, cerrobend and water under both wetting and non-wetting conditions on various ¼ inch packings at zero gas rate. Standish summarised that no unique relationship existed between the static holdup of metallic and non-metallic liquids investigated. The results obtained have been summarised in Table 3.1 for ease of comparison.

Table 3.1 *Static holdup h_s results reported by Standish (1968b) for various irrigating liquids.*

Influencing factors on h_s	Cerrobend	Mercury	Wetting water	Non-wetting water
Liquid rate, L	No significant effect	No significant effect for porcelain saddles. Slight but definite decrease in h_S of porcelain rings with increasing L, more pronounced with steel rings (agrees with Warner, 1959a)	No significant effect	No significant effect
Packing type (shape, material)	Strong effect	Strong effect	Strong effect	No significant effect
Application of Shulman *et al*'s. (1955b) h_S correlation (based on aqueous and organic liquids)	Large errors between calculated and measured h_s	Large errors between calculated and measured h_s	Calculated h_S is 1.7 to 2.2 times that of experimental h_s. Hence, correlation that was based on ½ - 1 ½ in. packings cannot be satisfactorily extrapolated to ¼ in. packings.	-
Other notes (T = temperature μ_L = liquid viscosity ρ_L = liquid density θ = contact angle)	As T increased, h_s decreased. Attributed to decrease in μ_L as T increased (ρ_L, θ did not vary much). μ_L affects adhesion of liquid to solid.	-	-	h_S of non-wetting water is notably lower than wetting water. h_S of non-wetting water comparable to h_S for coke packing (Gardner, 1956)

Coughlin (1969) measured liquid holdups for beds of approximately 3/8 inch Raschig rings made from wettable ceramic and non-wettable saran and polyethylene. Static holdup seemed to be greater for the ceramic packing compared to the polymer ones, however dynamic holdup did not seem to be affected by packing material. Gas rates did not affect h_D up till the loading point. h_D measured at zero gas flow gave the same values for all packing materials at the same liquid rates. All packings gave gradual, nearly linear increase in h_D with liquid rates.

Van Swaaij *et al.* (1969) reported that packing treated with silicone resin to render them non-wettable had lower static holdup and dynamic holdup than those of non-treated packing.

Andrieu (1975) investigated liquid hold-up in an air-demineralised water system using 10 mm glass Raschig rings, both uncoated ($\theta = 0°$) and coated with silicone resin ($\theta = 93°$). Static holdup was found to be lower for coated packings than for uncoated packings. At a liquid rate L of 3.15 kg/m^2s, dynamic holdup h_D for the coated packing was generally higher than the uncoated packing throughout the gas range employed except near zero gas rate. At L equals 4.725 kg/m^2s, h_D for the coated packing was lower before loading set in. At L equals 6.30 kg/m^2s liquid rate, h_D for the coated packing fell below the uncoated packing throughout the gas range employed. For both coated and uncoated packings, h_D at zero gas flow was found to be proportional to $L^{0.7}$.

Gaston-Bonhomme *et al.* (1980) compared liquid holdups for non-wettable PTFE, PVDF and wettable glass Raschig ring packings. They reported that static holdup of water taken at zero gas flow on the polymer packings was greater than on the glass packings. However dynamic holdup of water at zero gas flow was higher on the glass packing rather than on the polymer packings for the same liquid rates.

3.2   Air/Gas Lift Operation

Molten tin is to be circulated through the hot gas scrubber. The high temperature conditions, the highly corrosive nature of molten tin as well as the presence of solids in suspension render most conventional mechanical pumps unsuitable for this operation. A simple and yet reliable method is provided by the gas lift pump. The gas lift involves no moving parts that are susceptible to erosion or wear, and only requires a compressed gas supply as the transporting agent.

3.2.1   General Description

The gas lift is termed the air lift when compressed air is employed. The air lift pump is used particularly to raise corrosive or abrasive liquids, sludges or slurries from wells or vessels. It has an edge over submerged mechanical pumps as it has no moving parts in contact with the fluid, hence it is simple in design and construction and requires minimal maintenance. Besides finding wide application in underground petroleum and water recovery, the air lift pump has also been used to handle hazardous or radioactive process fluids such as in nuclear fuel reprocessing plants, archeological artifact recovery, coal recovery in mine shafts, deep sea mining as well as incorporated into the design of bioreactors (Clark and Dabolt, 1986; Zenz, 1993; Tramba *et al.*,

1995; Lawniczak *et al.*, 1999; Khalil *et al.*, 1999). Two simple configurations of the air lift pump are depicted as follows:
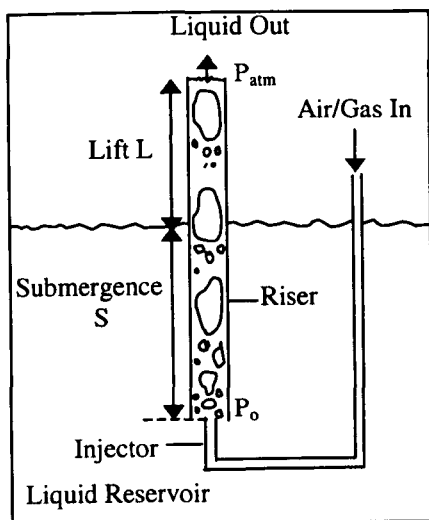
Figure 3.10 Air lift pump:
Riser immersed in reservoir.
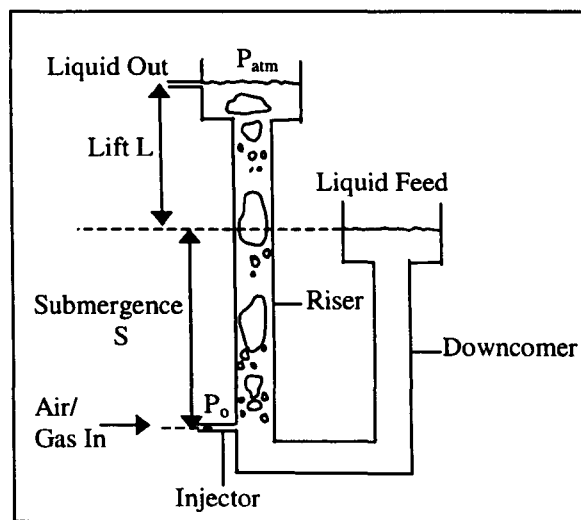
Figure 3.11 Air lift pump:
U-tube configuration.

In the first configuration of the air lift (Figure 3.10), a vertical tube (the riser) is partially submerged in a liquid reservoir. Compressed air or gas is injected near the bottom of the riser forming gas bubbles in the liquid. The gas bubbles reduce the density of the overall gas/liquid mixture in the riser compared to the liquid alone, providing a buoyancy force. Consequently, the gas-liquid mixture rises upwards where it is discharged at the top of the riser. The alternative setup for the air lift is that of the U-tube type (Figure 3.11) where submergence is provided by a downcomer tube connected to the liquid feed tank. Compared to the first configuration, frictional losses are more pronounced in the U-tube arrangement owing to the liquid flow in the downcomer leg.

The submergence S is measured from the air or gas injector exit level to the free surface level of the pumping fluid. The lift L is the distance from the free surface of the fluid to the point of discharge. The ratio of submergence S to the total height of submergence and lift (S + L) is termed the submergence ratio S_R.

Except for bioreactors, the practical design and operation for the air lift falls in the slug flow regime of the vertical, co-current upward flow of liquid-gas mixture (Todoroki *et al.*, 1973; Clark and Dabolt, 1986; Zenz, 1993). This is because among the four basic flow patterns in a vertical liquid-gas upflow in a tube: bubbly, slug (plug), churn and annular flows, the highest pumping efficiency is obtained in slug flow regime (Zenz, 1993; Tramba *et al.*, 1995) which

persists over a fairly wide range of gas and liquid velocities. In the slug flow regime, the gas flows as large pellet-shaped bubbles (known as Taylor bubbles) surrounded by an annular liquid film in contact with the riser wall. Adjacent large gas bubbles are separated by liquid slugs while some smaller gas bubbles are dispersed throughout the liquid.
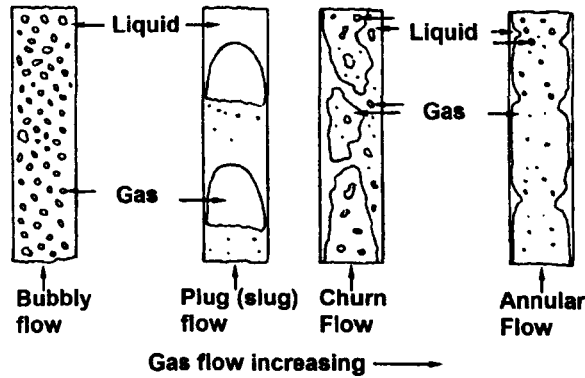
Figure 3.12 *Flow regimes for vertical upflow of liquid-gas mixture in a tube (Whalley, 1996).*

3.2.2 Prediction of Air/Gas Lift Performance

3.2.2.1 Theoretical Approach

□ *Energy Balance*

Despite the simplicity of its construction and operation, the theoretical treatment of air lift performance is not straightforward. The earliest theoretical approach was based on energy balance. If a volume of liquid V_L with density ρ_L is raised through a net height L by a volume of air $V_{G,atm}$ (at atmospheric pressure), the work done on the liquid is $V_L \rho_L g L$. Assume that air is introduced at the base of the air lift where the pressure is P_o, and then it expands isothermally to the pressure at the top of the riser, typically at atmospheric pressure P_{atm}. Isothermal expansion can be assumed on the basis of intimate liquid-air contact (Nicklin, 1963). The work done by the air in the isothermal expansion is $P_{atm} V_{G,atm} \ln(P_o/P_{atm})$. The efficiency of the pump η_p is then:

$$\eta_p = \frac{V_L \rho_L g L}{P_{atm} V_{G,atm} \ln(P_o / P_{atm})}$$

(3.26)

The volume of air $V_{G,atm}$ required to raise a volume of liquid V_L through a height L is therefore:

$$\frac{V_{G,atm}}{V_L} = \frac{\rho_L g L}{\eta_p P_{atm} \ln(P_o / P_{atm})}$$

(3.27)

If P_{atm} equals $h_{atm}\rho_L g$, then the pressure at the air inlet point P_o can be expressed as $(h_{atm}+S)\rho_L g$ where S is the submergence. The ratio $V_{G,atm}/V_L$ then becomes:

$$\frac{V_{G,atm}}{V_L} = \frac{\rho_L g L}{\eta_p P_{atm} \ln[(h_{atm} + S)/h_{atm}]}$$

(3.28)

A form of equation 3.28 is the Ingersoll-Rand equation dating back to 1929 (Genereaux *et al.*, 1973; Zenz, 1993) for air lifts of various heights to pump water. Tabulated empirical constants corresponding to fixed values of η_p are given along with the Ingersoll-Rand equation, with values ranging from approximately 35 to 50%, decreasing with the height of lift. However the energy balance approach has since been found to be insufficient for accurate design of air lifts (Clark and Dabolt, 1986; Zenz, 1993) as it assumes a fixed value of pump efficiency whereas the true efficiency can only be known during actual operation. Furthermore, the pump efficiency is not a fixed value, but changes with air rate. The Ingersoll-Rand equation has been shown to apply only at operating conditions of peak efficiency (Zenz, 1993).

More recent approaches utilised two-phase flow theory (Nicklin, 1963; Clark and Dabolt, 1986).

❑ *Nicklin's (1963) Theoretical Model*

Nicklin (1963) applied momentum balance to two-phase flow in the air lift using average point conditions. This was because the conditions in the riser change as the gas expands whilst its superficial velocity increases up the pipe. In Nicklin's model, the two-phase flow pressure gradient in the air lift riser consisted of hydrostatic head loss and wall frictional loss. Accelerative, entrance and exit losses were neglected. The average pressure gradient along the riser was equated to the submergence ratio of the air lift.

The bulk of the total energy dissipation is attributed to hydrostatic change across the riser which is due to the liquid weight in the riser and includes energy loss as a result of the gas phase slipping past the liquid phase. The hydrostatic component was determined using liquid holdup in the riser as calculated from a drift-flux model for slug flow (Nicklin *et al.*, 1962). Disregarding the contribution due to gas phase density, the hydrostatic pressure change across the riser having submergence S (m) and lift L (m) is:

$$\Delta P_H = (1-\alpha)\rho_L g(L+S)$$

(3.29)

where α = gas voidage fraction (dimensionless)

ρ_L = liquid density (kg/m^3)

g = gravitational acceleration (m/s^2)

The gas voidage fraction α from Nicklin *et al.*'s (1962) drift-flux model for steady-state two-phase vertical upward slug flow:

$$\frac{W_G}{\alpha} = 1.2(W_G + W_L) + 0.35(gD)^{1/2} \tag{3.30}$$

where W_G = gas superficial velocity in air lift tube (m/s)

W_L = liquid superficial velocity in air lift tube (m/s)

D = pipe inner diameter (m)

Nearly all the energy loss in an air lift pump is due to the gas-liquid slip. However where liquid velocities are high, the importance of wall friction cannot be neglected. According to Nicklin (1963), from continuity, the average velocity of the liquid slugs between the gas slugs is equivalent to the total superficial velocity ($W_G + W_L$). All the liquid is assumed to occupy the space between the gas slugs, hence taking up (1-α) fraction of the tube. Therefore the wall frictional pressure loss across the riser tube due to the liquid phase alone is derived using a modified pressure drop equation for single phase flow in a pipe:

$$\Delta P_W = (1 - \alpha)\frac{f_L(S + L)}{D} \cdot \frac{\rho_L(W_G + W_L)^2}{2} \tag{3.31}$$

where f_L = Moody friction factor from liquid phase physical properties (dimensionless)

The total pressure gradient in the riser is then the sum of the hydrostatic and wall friction components which is equivalent to the submergence ratio:

$$\frac{S}{(S + L)} = \frac{\Delta P_H}{\rho_L g(S + L)} + \frac{\Delta P_W}{\rho_L g(S + L)} \tag{3.32}$$

Hence
$$\boxed{\Delta P_H + \Delta P_W = S\rho_L g} \tag{3.33}$$

The equations describing the hydrostatic component and wall frictional losses were tested with air and water flowing in pipes ranging from 1.60 to 6.35 cm diameter. They were found to apply for slug flow and semi-annular flow regimes.

□ *Clark and Dabolt's (1986) Theoretical Model*

Clark and Dabolt (1986) criticised the theoretical treatment of Nicklin (1963) for being only accurate for short pumps as there was no provision for variation of gas volumetric flow rate over long risers. For longer pumps, Nicklin's method would require incremental application. Using two-phase flow momentum balance, Clark and Dabolt (1986) developed a general design equation for air lift pumps operating in slug or bubble flow regimes. The model was said to be valid for air lifts of any height. The design equation was obtained by integrating the total differential pressure gradient in the air lift tube over its whole length. The total differential pressure gradient consists of hydrostatic and wall frictional loss terms. Accelerative, entrance and exit losses were neglected.

Disregarding the contribution due to air phase density, the total differential pressure gradient across the air lift tube is:

$$-dP = [\rho_L g(1-\alpha) + F]dx \tag{3.34}$$

Similar to Nicklin's (1963) model, the air voidage fraction α is determined using the drift-flux model as described by Nicklin *et al.* (1962) i.e. from equation 3.30.

$$\frac{W_G}{\alpha} = 1.2(W_G + W_L) + 0.35(gD)^{1/2} \tag{3.30}$$

F is the wall frictional pressure gradient in the two-phase flow. It is estimated from an equation approximating the Lockhart and Martinelli's (1949) correlation for two-phase frictional pressure loss:

$$F = F_s(1+1.5\alpha) \tag{3.35}$$

F_s is the wall frictional pressure gradient in single liquid phase flow:

$$F_S = \frac{f_L}{D} \cdot \frac{\rho_L W_L^2}{2} \tag{3.36}$$

Combining equations 3.34 and 3.35 results in:

$$-dP = [\rho_L g(1-\alpha) + F_s(1+1.5\alpha)]dx \tag{3.37}$$

Equation 3.30 predicting the air voidage fraction is next substituted into equation 3.37. To account for the variation of the superficial gas velocity W_G with pressure over the pump height,

ideal gas behaviour is assumed and that the gas expands isothermally in the pump. Hence the superficial gas velocity at a level in the air lift where the pressure is P is:

$$W_G = \frac{G' P_{atm}}{A P \rho_G}$$ (3.38)

where G' = gas mass flowrate to base of pump (kg/s)

 P_{atm} = atmospheric pressure (Pa)

 A = tube cross-sectional area (m^2)

 ρ_G = gas density at atmospheric pressure and at pump temperature (kg/m^3)

Setting M = W_GP = G'P_{atm}/Aρ_G, and combining equations 3.30, 3.37 and 3.38:

$$-dP = \left[\rho_L g \left(1 - \frac{M}{1.2(M + W_L P) + 0.35(gD)^{1/2} P} \right) + F_s \left(1 + \frac{1.5M}{1.2(M + W_L P) + 0.35(gD)^{1/2} P} \right) \right] dx \quad (3.39)$$

The gas is assumed to expand from a pressure of P_0 at the gas injector level (x=0) to atmospheric pressure P_{atm} at the top of the riser (x=S+L). Hence, rearranging equation 3.39 and integrating between the entrance level [x=0, P=P_0] and the discharge level [x=(S+L), P=P_{atm}]:

$$\boxed{\frac{P_{atm} - P_0}{\rho_L g + F_s} - \left(\frac{1.5 F_s M - \rho_L g M}{(\rho_L g + F_s)^2 B'} \right) \log \left(\frac{A' + (\rho_L g + F_s) B' P_{atm}}{A' + (\rho_L g + F_s) B' P_0} \right) + (S + L) = 0}$$ (3.40)

where A' = 0.2ρ_LgM + 2.7F$_s$M (kg^2/s^{5}m^2)

 B' = 1.2W$_L$ + 0.35(gD)$^{1/2}$ (m/s)

 P_0 = P_{atm} + Sρ_Lg (Pa)

Clark and Dabolt's design equation is essentially equation 3.40. It cannot be arranged in a closed form to express the liquid flowrate in terms of the gas flow rate given the lift and submergence. Clark and Dabolt recommended a trial-and-error method to obtain the pump operating curve, adjusting the liquid flow rate at a given gas flow rate until the predicted lift matches the actual pump lift.

The design equation was tested using experimental data obtained with various liquids in an air lift with a total height of about 15 m, a riser diameter of 3.8 cm and with submergence ratios of 0.6, 0.7 and 0.8. 'Favourable' agreement was found between the model and the experimental data as well as data in the literature for very tall air lifts.

3.2.2.2 Empirical Correlations

Lawniczak *et al.* (1999) gave an empirical correlation to predict the water pumping rate given an air flowrate. But it is limited to the air-water system and only for their experimental range used.

Figure 3.13 shows a generalised graphical correlation for the design of air lift pumps introduced by Zenz (1993). This correlation was based on published air-water lift data with lift heights ranging from 12.7 cm to 19.8 m and pipe diameters ranging from 1.27 to 38.10 cm. Both the gas volume and the gas density are based on discharge conditions. To enable the application of the correlation on other fluids to be pumped apart from water, correction factors for fluid density, viscosity and surface tension were added to the ordinate. All the different regimes of co-current multiphase upward flow are also marked on the graphical correlation. o/A is the ratio of annular liquid film cross-sectional area to pipe cross-sectional area which is used as a parameter on the graphical correlation. The fluid lifting rate V_L drops sharply when the gas rate V_G is either less (i.e. in the bubbly flow regime) or greater (i.e. in the annular flow regime) than the optimum slug flow operating range.
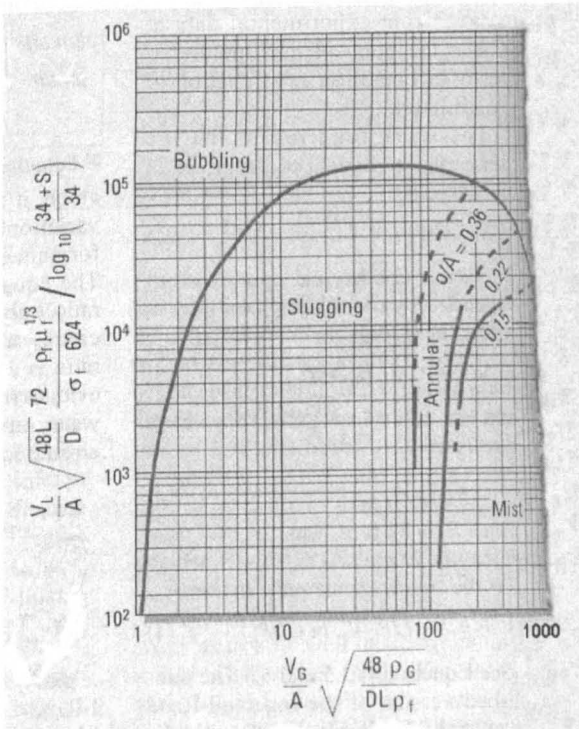
Nomenclature:

o	= cross-sectional area of annular flow (ft^2)
A	= pipe cross-sectional area (ft^2)
D	= pipe inside diameter (in)
L	= lift (ft)
S	= submergence (ft)
V_G	= gas flow at discharge conditions (ft^3/min)
V_L	= dense phase flow (gal/min)
μ_f	= viscosity of lifted fluid (cP)
σ_f	= surface tension of lifted fluid (dynes/cm)
ρ_f	= density of lifted fluid (lb/ft^3)
ρ_G	= gas density (lb/ft^3) (based on discharge condition)

Figure 3.13 *Capacity correlation for gas lift pump design showing multiphase co-current vertical upflow regimes (Zenz, 1993).*

3.2.3 Factors Affecting Air/Gas Lift Performance

As indicated by Zenz' graphical correlation in Figure 3.13, the parameters that influence the

performance of an air lift pump are: air or gas flow rate; liquid flow rate; air or gas density; liquid physical properties (density, surface tension, viscosity); physical geometry of the air lift pump (riser diameter, total height, submergence and lift, hence submergence ratio).

Todoroki *et al.* (1973) tested an air lift with a total riser length of 7.5 m, a pipe diameter of 2.83 cm and submergence ratio varying from 0.4 to 0.8, whilst Kouremenos and Staicos (1985) investigated a short air lift pump having a total length of 93 cm, diameters from 1.2 to 1.9 cm and submergence ratio varying from 0.55 to 0.70. Both investigations showed that the water pumping rate improved as the submergence ratio increased for a specific air flowrate.

Besides the above-mentioned factors, the air lift performance has also been found to be affected by the entrance geometry of the riser tube as well as the injector design (Morrison *et al.*, 1987; Lawniczak *et al.*, 1999; and Khalil *et al.*, 1999).

Morrison *et al.* (1987) tested an air lift pump with an inner diameter of 3.81 cm, a total length of 3.24 m and a submergence ratio of 0.69 on water transport. A four-port and an eight-port radial injectors were tested, the total cross-sectional area of the ports for each injector being 25.8 mm^2. It was shown that the air lift pumping efficiency is dependent on the air flowrate and the injector design. The efficiency increased with rising air flowrate to a peak efficiency value, after which it decreased. The eight-port injector was found to give more efficient pumping, especially in the bubbly and slug flow regimes. The eight-port and four-port injectors demonstrated maximum efficiencies of 38% and 33% respectively, both at about the same air flowrate. Compared to the four-port injector, the time-averaged local liquid velocities along the lift section were higher for the eight-port injector resulting in lower air-water slip velocities in the lift section for the latter. This slippage of gas bubbles past the liquid is the main contributor to energy loss in the air lift pump, increasing as bubble size increases, hence reducing efficiency. Bubble size is affected by the design of the injector. As the number of air ports on the injector increase and the air ports cross sectional area decreases, smaller bubble sizes are obtained. Consequently, the number of bubbles and pump efficiency increase for the same gas volumetric flowrate.

Lawniczak *et al.* (1999) investigated a short air lift pump of a total length of 1 m, internal diameter of 3 and 5 cm and operating at low submergence ratios between 0.2 to 0.6 with water as the pumping liquid. Longitudinal air injectors were used with variable ratios of riser flow area to injector flow area. At low air rates, the water pumping rate increased linearly with air rate, rising exponentially at higher air rates. The corresponding pumping efficiency η_p increased sharply with air rate reaching a peak value and then decreased exponentially at higher air rates. The

pumping rate improved with higher submergence ratio. As the submergence ratio increased, the maximum value of pumping efficiency η_p improved with maximum η_p occurring at lower air rates but higher water rates. For small values of riser to injector flow area ratio where entrance frictional losses were pronounced, pumping efficiency η_p increased with increasing ratio. On the other hand at higher flow area ratio, there was negligible effect on η_p.

Khalil *et al.* (1999) investigated the performance of an air lift having a total length of 2 m and a diameter of 2.54 cm. Four submergence ratios (0.5 to 0.75) were used together with nine different air injectors having varying number of air ports from 1 to 48, each air injector having a total port cross-sectional area of 10 mm^2. For each combination of air injector and submergence ratio, the pump efficiency increased with air rate up to a maximum, after which it decreased. It was found that for any injector type, the largest submergence ratio of 0.75 gave the highest water discharge rate, hence the best efficiency. Among the various injectors, the 3-port air injector gave the highest value of maximum efficiency at all submergence ratios. However, no single injector consistently gave the best pump efficiency for all operating conditions, not even the 3-port injector. In general, there was no consistent pattern between the number of air ports on the injector and the pumping efficiency.

3.3   Summary

Important hydrodynamic properties of an irrigated counter-current packed column includes bed pressure drop, loading and flooding phenomena as well as liquid holdup behaviour.

❑ *Loading and Flooding*

No generalised correlation is available to readily predict the onset of loading. The earliest generalised flooding correlation for randomly packed columns in counter-current operation was introduced graphically by Sherwood *et al.* back in the 1930s. Since then, the classical Sherwood *et al.*'s graphical flooding correlation has undergone a number of modifications by other investigators. The correlation which initially consisted of only a flooding line has evolved into several versions of graphical generalised pressure drop correlations (GPDCs) which include isobars below the flooding line. Recently, other types of flooding correlations distinct from the graphical types have been presented.

The available flooding correlations for packed columns were mainly based on aqueous and organic liquids with relatively low densities and low surface tensions. These columns are largely

wettable by the test fluids due to their low surface tensions. In comparison, there have only been a few documented studies specifically concentrating on non-wettable packing. Using packing elements of similar geometry, these investigations have demonstrated that the flooding capacities of non-wettable packed beds differ from those that are wettable. Some studies have found that there is increased tendency for flooding with decreased wettability of the packing material, whilst some have found that the converse is true. Very little flooding data is available for liquid metal irrigation. The handful of data obtainable seems to suggest that the flooding capacity of liquid metal systems are dictated by their non-wetting characteristic. Their flooding capacity was found to obey the non-wetting flooding line of Standish and Drinkwater (1972) although this line was originally based on a non-wetting air-water system. Among the more recent work on flooding prediction in packed columns reviewed, only the neural correlation of Piche *et al* (2001a) was tested on a non-wetting liquid metal system.

❑ *Liquid Holdup*

Total liquid holdup in a packed bed consists of static and dynamic holdup. For conventional wettable systems, static holdup has been found to be independent of gas and liquid flowrates, instead it is influenced by the nature of the packing and liquid physical properties. Several investigators have correlated static holdup for wettable packings with the dimensionless Eötvös number. It has been suggested that in addition to the Eötvös number, an empirical static holdup correlation should include the influence of contact angle and local geometry as well. Due to the very slow renewal of static liquid holdup by fresh liquid, it is deemed ineffective to mass transfer. Dynamic holdup for wettable systems has been found to be mainly a function of liquid rate. Generally, gas rates negligibly affect dynamic holdup up till the loading point. However beyond the loading point, dynamic holdup rises rapidly with gas rate. Dynamic holdup is also influenced by liquid physical properties, but independent of the nature of the packing. Due to its constant regeneration, dynamic holdup contributes effectively to mass transfer. Total liquid holdup, being a combination of both static and dynamic holdups is mainly influenced by liquid rate. Other factors affecting total liquid holdup are gas rate, bed physical properties, gas and liquid physical properties.

Compared to conventional wettable systems, there have been significantly fewer documented studies and experimental data on the liquid holdup for columns incorporating non-wettable packings, not to mention systems irrigated by liquid metals. In studies comparing holdups in water-irrigated wettable and non-wettable systems using packing of similar geometry, static

holdup and dynamic holdup were mostly found to be higher for the wettable packing. There were several exceptions though, whereby static holdup was found to be higher for the non-wettable packing whilst dynamic holdup has also been reported to be higher for the non-wettable packing at low liquid rates or even unaffected by the packing wettability. Dynamic holdup for non-wetting systems irrigated by water is reported to increase with liquid rates but be unaffected by gas rate up till the loading point and independent of packing shape and material. Static holdup for non-wetting systems irrigated by water and cerrobend metal have been reported to be unaffected by liquid rate. However the static holdup for mercury irrigation has shown a slight but definite decrease with increasing liquid rates, suggesting that it could be an effective component in mass transfer. Static holdup for liquid metal irrigation is greatly affected by packing shape and material. Dynamic holdup for liquid metals has been found to increase with both gas and liquid rates and be affected by liquid physical properties but independent of packing shape and material. Existing static and dynamic holdup correlations based on conventional wetting systems have been found to be inapplicable where liquid metal systems are concerned. However, it has been suggested that total and dynamic liquid holdup correlations developed based on non-wetting systems irrigated by water could be used to predict liquid holdup for liquid metal systems using packings of identical geometry or similar size respectively.

❑ *Air/Gas Lift*

The gas lift is selected for liquid tin transport in the hot gas scrubber due to its ease of design, construction and operation. The practical design and operation for the gas or air lift falls in the slug flow regime which gives the highest pumping efficiency in two-phase vertical upflow. Theoretical models and empirical correlations have been developed to predict the pumping performance of air lifts. The earliest hypothetical approach was based on energy balance whereby the volume of water lifted to a certain height was determined from the isothermal work done by the gas during expansion and assuming a value for pump efficiency. This method has since been found to be inaccurate as the pump efficiency is not a fixed value but changes with gas rates. More recent theoretical models integrate momentum balance with two-phase flow theory in the slug flow regime. A generalised graphical design correlation has also been put forward. Investigators have found that the air lift pumping performance is a function of gas and liquid flow rates, gas and liquid physical properties, as well as the physical geometry of the air lift pump.

Chapter Four

Gas Scrubbing: Theory and Review

In the present chapter, the theoretical fundamentals governing gas-solid separation and gas absorption are considered. The former includes the basics of particle collection, gas-solid separation efficiencies as well as the principles of wet collectors or scrubbers in particulate removal. The latter covers gas-liquid equilibrium considerations, interphase mass transfer, as well as concepts of mass transfer coefficients and transfer units in gas absorbers. Previous findings and correlations in the literature on relevant work in the field, particularly those pertaining to irrigated packed bed gas scrubbers are also reviewed.

4.1   Gas-Solid Separation

The term gas-solid separation used herein refers to the removal of solid particles from a gas stream or the dedusting of the gas. Three main processes are involved in the separation of solid particles from a gas:

1. Particle transport from the gas onto a collector surface and its retention on the collector.
2. Removal of the retained particles from the collector surface.
3. Solids disposal from the gas cleaning equipment.

The theory of gas-solid separation is well-documented by Svarovsky (1981; 1990).

4.1.1   Particle Collection

The first phase of gas-solid separation during which solid particles carried by the gas stream are brought into contact with the collector surface is termed the 'collection', 'capture' or 'collision' process. There are four mechanical collection processes: Brownian diffusional capture; inertial deposition; gravitational settling and direct interception (Coury *et al.*, 1987; Thambimuthu, 1993). In diffusional, inertial and gravitational capture, internal or external forces cause the trajectory of the dust particle to deviate from the gas streamlines flowing around the collector surface.

- Brownian diffusional capture – Random Brownian motion due to collision with gas molecules and other dust particles transports the dust particles to the collector surface.

Dominant for dust particles smaller than 0.1 µm (Calvert, 1977a; 1977b), i.e. when particles are sufficiently small such that they are buffeted by gas molecules and zigzag randomly through the gas. Closely analogous to mass transfer in packed beds.

- Inertial deposition – When a gas stream flows around a collector, the dust particle's own mass tends to make it travel in a straight line, causing its trajectory to deviate from the gas streamlines and impact on the collector. Dominant for dust particles bigger than about 0.5 µm (Jackson and Calvert, 1966).

- Gravitational settling – Dust particle settles across the gas streamlines due to gravity. Most effective when gas is in downflow.

- Direct interception – Dust particle contacts the collector surface simply due to its finite size. A dust particle carried by the gas streamlines around the collector is captured when the centre of the particle approaches the collector surface within a distance of half the particle diameter.

Besides the four purely mechanical processes, particle capture can also arise from diffusiophoretic, thermophoretic and electrophoretic effects. However they are usually insignificant in the absence of very strong diffusion, thermal gradients or electric fields (Thambimuthu, 1993).

4.1.2 Particle Rebound or Retention

The 'capture' by the aforementioned mechanisms of a dust particle on the collector surface is not the only deciding factor in ensuring its removal from the gas stream. A dust particle that collides with the collector surface may either rebound and be re-entrained back into the gas stream or alternatively it will be retained and thereby removed from the gas. As a result, dust retention is always less than dust collection.

Whether particle 'rebound' or 'retention' takes place depends on the relative strengths of the energy of the impacting particle and the detachment energy required to separate the particle from the collector surface (Coury *et al.*, 1987; Seville and Clift, 1997). The total energy of the impacting particle is a summation of its kinetic energy (includes effects due to long-range electrostatic force and fluid drag force) and energy due to short-range Van der Waals forces. The detachment energy arises from adhesion forces due to Van der Waals interaction, electrostatic and surface tension capillary effects that tend to hold the dust particle against the collector surface, all of which are dependent on the properties of the collector surface and the dust particle

itself. Therefore any effects that tend to raise the detachment energy or lower the particle's approaching energy will favour adhesion upon impact. An example of the latter is plastic deformation on collision due to the presence of liquid or adsorbed/condensed films or soft layers on either the dust or collector surface that dissipates the particle's energy. In addition, although capture due to inertial impaction increases as particle inertia increases, the tendency for rebound increases as well and this may eventually dominate.

4.1.3 Separation Efficiency

Consider the following gas-solid separator:

M_{in} = mass flowrate of feed (challenging) dust (kg/s)

M_c = mass flowrate of coarse (separated) dust in underflow (kg/s)

M_f = mass flowrate of fine (unseparated or penetrating) dust in overflow (kg/s)

$\omega_{in, x}$ = mass fraction of feed dust at particle size x (kg/kg)

$\omega_{c, x}$ = mass fraction of coarse (separated) dust at particle size x (kg/kg)

$\omega_{f, x}$ = mass fraction of fine (unseparated or penetrating) dust at particle size x (kg/kg)

x = dust particle size (μm)

Figure 4.1 Schematic diagram of a gas-solid separator.

Provided no dust particle accumulation occurs within the separator, the total mass balance is:

$$M_{in} = M_c + M_f \tag{4.1}$$

The mass balance is equally applicable for each particle size x present in the feed, as long as there is no change in solid particle size within the separator i.e. no agglomeration or comminution:

$$M_{in, x} = M_{c, x} + M_{f, x} \tag{4.2}$$

The total mass flowrate of a sample (M) multiplied by the particle size distribution frequency i.e. the mass fraction of particles of size x in the sample (ω_x) gives the total mass flowrate of particles of size x for that sample (M_x). Therefore equation 4.2 becomes:

$$(M_{in})(\omega_{in, x}) = (M_c)(\omega_{c, x}) + (M_f)(\omega_{f, x}) \tag{4.3}$$

4.1.3.1 Total Efficiency, E_T and Number of Transfer Units, N_t

The total or overall efficiency E_T is defined as the ratio of mass of all particles separated to the total mass of solids fed into the separator. Hence:

$$E_T = \frac{M_c}{M_{in}} \qquad \text{or} \qquad E_T = 1 - \frac{M_f}{M_{in}} \tag{4.4}$$

Therefore equation 4.3 can be re-expressed as:

$$\omega_{in,x} = E_T(\omega_{c,x}) + (1-E_T)(\omega_{f,x}) \tag{4.5}$$

The total efficiency E_T is largely dependent on the size distribution of the feed material and hence is unsuitable as a general criterion of efficiency for a gas-solid separation equipment.

Efficiency is generally an exponential function of the process variables for most types of collecting devices and therefore is an insensitive function for correlation purposes in the high efficiency range. In this case, the penetration $(1-E_T)$ is generally preferable. Even better is the number of transfer units N_t:

$$N_t = \ln\left(\frac{1}{1-E_T}\right) \tag{4.6}$$

or

$$E_T = 1 - exp(-N_t) \tag{4.7}$$

4.1.3.2 Grade Efficiency, G(x)

Generally for most gas-solid separators, the separation efficiency is dependent on particle size, which brings about the application of grade efficiency $G(x)$. The gravimetric grade efficiency $G(x)$ is defined as the mass separation efficiency for a specific particle size x:

$$G(x) = \frac{M_{c,x}}{M_{in,x}} \tag{4.8}$$

Using the same argument as that in obtaining equation 4.3:

$$G(x) = \frac{(M_c)(\omega_{c,x})}{(M_{in})(\omega_{in,x})} \tag{4.9}$$

From the definition of total efficiency E_T from equation 4.4:

$$G(x) = E_T \frac{(\omega_{c,x})}{(\omega_{in,x})} \tag{4.10}$$

Combining equation 4.5 with equation 4.10:

$$G(x) = 1 - (1 - E_T)\frac{(\omega_{f,x})}{(\omega_{in,x})}$$

(4.11)

❏ *Grade Efficiency Curve*

A typical grade efficiency curve with the grade efficiency function G(x) plotted against particle size x is shown in Figure 4.2. The grade efficiency curve is usually independent of solids size distribution and density and is constant for a specific set of operating conditions. It gives the probability at which particles of any given size in the challenging gas stream will separate from or be retained within the gas stream. The grade efficiency G(x) generally increases from

Figure 4.2 A typical grade efficiency curve (Svarovsky, 1981).

zero for ultrafine particles to 100% for coarse particles. The grade efficiency concept is generally applicable to solid-gas separation equipment whose performance does not vary with time if all operational variables are kept constant. Examples of such equipment are cyclones and scrubbers. The grade efficiency when integrated over the particle size distribution gives the total collection efficiency E_T.

❏ *Cut Size, x_{50}*

The particle size corresponding to 50% probability of separation on the grade efficiency curve is termed the 'equiprobable size', x_{50} and is usually taken as the 'cut size' of the gas-solid separator. The cut size can be viewed as the equivalent aperture size of an ideal screen that would result in the same separation performance as the gas-solid separator in question. It is taken as the most significant single parameter to describe both the difficulty of dust separation and the performance of the scrubber.

❏ *Limit of Separation, x_{max}*

The 'limit of separation', x_{max} is defined as the particle size above which the grade efficiency is 100% for all x. This is the size of the largest particle that can escape with the overflow gas

stream. However in practice, the limit of separation is often difficult to be ascertained accurately. In this case, an easier defined point termed the 'approximate limit of separation', x_{98} which is the size corresponding to 98% efficiency, is then measured and used.

◻ ***Sharpness of Cut***

The general slope of the grade efficiency curve can be expressed in terms of a 'sharpness index'. It sometimes is defined simply as the gradient of the tangent to the curve at x_{50}. More often it is defined as the ratio of two sizes corresponding to two different percentages on the grade efficiency curve on either side of 50%. For instance:

$$H_{25/75} = x_{25}/x_{75} \quad \text{or} \quad H_{35/65} = x_{35}/x_{65} \tag{4.12}$$

or alternatively, defined as the reciprocal values of these.

4.1.3.3 Factors Affecting Separation Efficiency

The grade efficiency curve is a function of the following factors:

- Gas flowrate
- Gas viscosity
- Solids density
- Solid particle shape
- Gas moisture content (affects dispersion of particles in the gas)
- Solids feed concentration (negligible effect within a few g/m^3 but often large influence at higher concentrations)
- Specific water consumption (for wet scrubbers)

4.1.4 Scrubbers (Wet Collectors or Wet Separators)

The theory of scrubbers has been well documented by notably Calvert (1977a; 1977b) as well as Svarovsky (1981; 1990).

4.1.4.1 General

In scrubbers, particle separation from the gas stream is aided by the addition of a liquid, this usually being water. The liquid plays a key role in the three processes of gas-solid separation:

1. Particle entrapment onto the collector surfaces, these being either the liquid droplets or the wet surfaces of the scrubber internals, preventing particle re-entrainment.

2. Washing off of particles from the collector surfaces by the liquid.

3. Disposal of solids from the scrubber in a slurry form.

The primary collection mechanisms involved in a scrubber are inertial deposition (most important (Calvert, 1977a; 1977b; Dunson, 1997)), diffusional capture and direct interception. Secondary mechanisms include diffusiophoresis, thermophoresis and particle growth due to liquid condensation on the particles.

Scrubbers are generally more efficient than dry separators, capable of separating particles down to less then 1 μm in size. This is mainly attributed to the presence of the liquid which prevents re-entrainment of solid particles back into the gas stream. They can be used to remove cohesive powders and can be employed for simultaneous absorption of gaseous pollutants using suitable scrubbing liquids. An accompanying slurry handling and disposal system is required. Hazards associated with explosion of dry dust are unlikely. The pressure drop of scrubbers is usually small. The separation efficiency generally increases with pressure drop.

An important operating parameter for scrubbers is the specific liquid consumption. It is the ratio of the amount of liquid needed to the amount of gas treated, either expressed as a volume ratio or a mass ratio. Separation efficiency usually increases with liquid consumption up to a certain level, dictated by other factors, for instance flooding.

There are various types of scrubbers. The *Scrubber Handbook* (Calvert *et al.*, 1972) gives the following list of scrubber designs according to their basic separation mechanism: plate scrubbers; massive packing scrubbers; fibrous packing scrubbers; pre-formed spray scrubbers; gas-atomised spray scrubbers; centrifugal scrubbers; baffle-type scrubbers; impingement-and-entrainment scrubbers; mechanically aided scrubbers; moving bed scrubbers; and other combination scrubber designs.

4.1.4.2 Separation Efficiency

Generally, inertial deposition is the most important collection mechanism for particulate scrubbers (Calvert, 1977a; 1977b). For inertial deposition, the particle characteristic size is its aerodyamic diameter, x_{ae}. As the particle inertia (as measured by its mass) is central to this

mechanism, the aerodynamic diameter describes the particle properties of importance i.e. its size and density (Calvert, 1977a; 1977b):

$$x_{ae} = x \, (\rho_p C')^{1/2} \qquad (4.13)$$

where x_{ae} = particle aerodynamic diameter (μm(g/cm^3)$^{1/2}$ = μmA)

   x   = particle physical diameter (μm)

   C'   = Cunningham slip correction factor (dimensionless)

   ρ_p = particle density (g/cm^3)

Other particle properties may be more significant when other separation mechanisms are important, but in general this will happen only for submicron particles (x < 1 μm).

The Cunningham correction factor C' allows for slip effects arising when the particle diameter is comparable to the mean free path of the gas molecules λ. It is approximated from this equation for spherical particles (Davies, 1945):

$$C' = 1 + Kn \left[2.514 + 0.8 \exp\left(\frac{-0.55}{Kn}\right) \right] \qquad (4.14)$$

where the dimensionless Knudsen number: $Kn = \dfrac{\lambda}{x}$ (4.15)

The mean free path of gas molecules, λ (μm) with gas viscosity μ_G (kg/ms), gas density ρ_G (kg/m^3) and at pressure P (bar) can be estimated as follows (Beard, 1976):

$$\lambda = 3200 \mu_G \sqrt{\frac{\pi}{2\rho_G P}} \qquad (4.16)$$

A typical grade efficiency curve for a particulate scrubber generally has a characteristic 'most penetrating particle size' (about 0.3 μmA) at which the efficiency is a minimum (Figure 4.3). This is a consequence of the two principal collection mechanisms in particulate scrubbers i.e. inertial deposition and Brownian diffusion. Above the most penetrating particle size, inertial deposition prevails and the efficiency rises with particle size. Below this size, Brownian diffusion dominates and efficiency increases as particle size decreases.
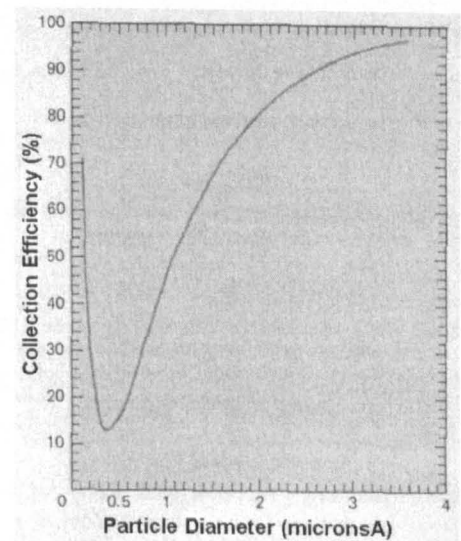
Figure 4.3 A typical grade efficiency curve for scrubbers. (Calvert, 1977a).

The grade efficiency function of scrubbers where the inertial mechanism is the main separation method conforms to a general form i.e. as a function of the particle aerodynamic diameter x_{ae} (Calvert, 1977a; 1977b):

$$G(x) = 1 - exp(-Ax_{ae}^B) \qquad (4.17)$$

Or alternatively as a function of the particle physical diameter x (Svarovsky, 1981):

$$G(x) = 1 - exp(-A'x^B) \qquad (4.18)$$

A, A' and B are dimensionless empirical constants. The constant A' is dependent on the type of scrubber, specific liquid consumption, other operational variables and the nature of the dust especially its affinity to the liquid. B is 2 for packed columns, sieve-plate columns and Venturi scrubbers (i.e. gas-atomised spray scrubber) whilst for centrifugal scrubbers, B is about 0.67.

In general, the greater the power consumption of the scrubber, the higher the collection efficiency (Semrau, 1960). The power consumption for a specific efficiency increases as the dust particle size decreases. The required power consumption to give a specific efficiency for a specific dust does not vary widely using markedly different equipment (Dunson, 1997).

4.1.4.3 Packed Bed Scrubber

The scrubber of interest herein is the massive packing scrubber (or simply called the packed bed scrubber in this study) i.e. columns packed with various packing elements usually used for mass transfer. The packing breaks down the liquid flow into a film with high surface area. Packing elements are generally too large to serve as effective collectors except for very large dust particles. In the collection of fine particles, the packings serve mainly to promote fluid turbulence, enhancing particle deposition on liquid films or droplets. The main collection mechanism is inertial deposition, with some contribution from diffusion for sufficiently small dust particles.

Packed bed scrubbers are efficient for separating particles of 10 µm or larger (Strigle, 1994). Smaller packings give better scrubber efficiencies. Unlike in mass transfer, packing shape is relatively unimportant for gas-solid separation; hence minimal pressure drop is the main selection criterion. Packing elements are subject to plugging, but are removable for cleaning. At high solid loadings, larger packing elements should be used to prevent blockage by the solids; higher liquid rates should also be employed to flush off the deposited solids. In a countercurrent packed bed scrubber, the power supply to the system (as reflected in the bed pressure drop) is limited by flooding of the column, hence restricting the achievable separation efficiency.

4.2   Gas Absorption

Gas absorption is a mass transfer operation involving the transfer of a solute from the bulk gas phase to the bulk liquid phase, the driving force provided by the solute concentration gradient. In a gas absorption process, a mixture of a soluble gas with an inert gas is brought into intimate contact with a liquid. The soluble component is preferentially dissolved into the liquid, separating it from the inert gas.

4.2.1   Gas-Liquid Equilibrium Considerations

Under a specific condition of temperature and pressure in a gas absorption operation, the solute molecules are transferred from the gas phase to the liquid phase across the gas-liquid interfacial surface. Some solute molecules escape back into the gas phase, the rate being proportional to their concentration in the liquid. As the concentration of the solute in the liquid increases, its rate of return to the gas phase increases as well. In due course, the rate at which the solute enters the liquid equals its rate of return to the gas phase. Simultaneously, each phase achieves uniform concentration through diffusion. A dynamic equilibrium is achieved whereby the net transfer of solute between the phases is zero and the concentration in each phase becomes constant.

Hence for a gas-liquid system not in equilibrium, interphase diffusion of the components will take place to eventually bring the system to an equilibrium state. At equilibrium, no net diffusion of components exists between the phases.

For ideal solutions, the gas-liquid equilibrium is described by Raoult's Law:

$$p_A{}^* = p^o{}_A x_A \qquad (4.19)$$

where $p_A{}^*$ = equilibrium partial pressure of component A in gas phase (Pa)

   $p^o{}_A$ = vapour pressure of pure A at the same temperature and pressure (Pa)

   x_A = mole fraction of component A in liquid phase (mol/mol)

Raoult's Law is generally true only for large values of x_A.

For slightly soluble gases forming low concentrations of solute in the liquid phase (low x_A) i.e. resulting in only simple solutions with negligible gas-liquid molecules interaction, Henry's Law applies:

$$p_A{}^* = H x_A \qquad (4.20)$$

where H = Henry's Law constant (Pa)

The value of H increases with liquid phase temperature but is relatively independent of pressure. Henry's Law generally describes the equilibrium relationship for dilute concentrations of most gases.

The partial pressure of component A in the gas phase is proportional to its concentration:

$$p_A = y_A P \qquad (4.21)$$

where y_A = mole fraction of component A in gas phase (mol/mol)

P = total pressure (Pa)

Combining equations 4.20 and 4.21, the gas phase mole fraction at equilibrium with the liquid phase y* is:

$$y^* = \frac{p_A{}^*}{P} = \frac{H\,x_A}{P} \qquad (4.22)$$

Absorption will take place as long as the solute partial pressure in the gas phase p_A is higher than the solute vapour pressure above the liquid phase $p_A{}^*$.

Another way to describe vapour-liquid equilibrium is by the use of the vapour-liquid equilibrium constant, K or alternatively m:

$$y_A{}^* = K\,x_A \quad \text{or} \quad y_A{}^* = m\,x_A \qquad (4.23)$$

4.2.2 Mass Transfer Across A Phase Boundary

Several theories have been put forward to describe the conditions at the phase boundary during mass transfer of a solute from the gas phase to the liquid phase. Whitman (1923) put forward the Two-Film Theory treating the mass transfer resistance in each phase as a thin film next to the interface. Steady-state molecular diffusion mass transfer occurs across these films whilst bulk fluid turbulence dies out at the interface. Higbie (1935) propounded the Penetration Theory which assumes that fluid eddies bring fresh material to the interface and unsteady-state molecular mass transfer into the eddies takes place for a fixed period of time at the freshly exposed surface before the next mixing starts again. Danckwerts (1951) extended the Penetration Theory, resulting in the Surface-Renewal Theory. Whereas the former assumes the same exposure time for each fluid contact with the interface, the latter employs a wide spectrum of exposure times and averages the varying degrees of penetration. Toor and Marchello (1958) described the Film-Penetration Theory in which the Film and Penetration Theories were shown to be limiting cases of this more general model.

❑ *The Two-Film Theory*

The Two-Film Theory by Whitman (1923) is extensively used as it gives expressions that are easily applicable to generally available experimental data. In a gas absorption process, the Two-Film Theory assumes that the bulk gas phase is separated from the bulk liquid phase by a thin gas film adjacent to a thin liquid film. Completely mixed turbulent flow exists in both the bulk gas and the bulk liquid phases. Mass transport is by convection currents such that no concentration gradient is present in the bulk phases. The convection currents die out at the vicinity of the thin fluid films. Laminar flow exists in both the gas and liquid films and a solute concentration gradient exists across both films. Resistance to mass transfer is considered to entirely lie in these two films in which mass transport is totally by molecular diffusion. The solute concentration in the gas film at the interface is at equilibrium with the solute concentration in the liquid film at the interface. No resistance to mass transfer exists across the interface.

Figure 4.4 illustrates the Two-Film Theory. Solute A diffuses from the gas phase to the liquid phase. The partial pressure of solute A in the main body of the gas is p_A and this falls to p_{Ai} at the gas-liquid interface. Similarly, the solute concentration in the liquid phase falls from c_{Ai} at the interface to c_A in the main bulk liquid. The broken lines in the figure represent the hypothetical concentration gradients and the effective film thicknesses are given by z_G and z_L respectively. p_{Ai} and c_{Ai} are equilibrium values, given by the system's gas-liquid equilibrium relationship.
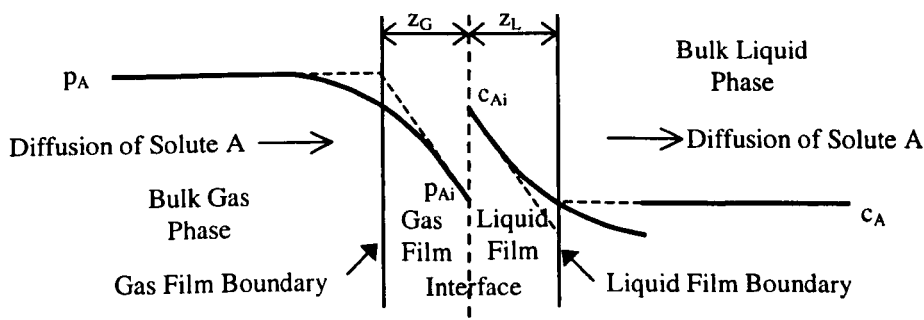
Figure 4.4 The Two-Film Theory as applied to gas absorption process.

The rate of mass transfer of solute A from the bulk gas phase through the gas film to the interface is expressed as:

$$N_A = k_G (p_A - p_{Ai}) \qquad (4.24)$$

where N_A = total molar flux of substance A (kmol/m²s)

k_G = gas film mass transfer coefficient (kmol/m^{2}sPa)

p_A = partial pressure of substance A in bulk gas phase (Pa)

p_{Ai} = partial pressure of substance A at interface (Pa)

Similarly, solute A is transported from the interface through the liquid film to the bulk liquid phase as follows:

$$N_A = k_L \, (c_{Ai} - c_A) \qquad (4.25)$$

where N_A = total molar flux of substance A (kmol/m^{2}s)

k_L = liquid film mass transfer coefficient (m/s)

c_A = concentration of substance A in bulk liquid phase (kmol/m^3)

c_{Ai} = concentration of substance A at interface (kmol/m^3)

For a steady-state mass transfer process, there is neither accumulation nor depletion of A at the interface. This means that the rate at which solute A diffuses from the bulk gas phase to the interface equals the rate at which it diffuses from the interface to the main body of the liquid phase. Hence,

$$N_A = k_G \, (p_A - p_{Ai}) = k_L \, (c_{Ai} - c_A) \qquad (4.26)$$

$$\frac{k_L}{k_G} = \frac{(p_A - p_{Ai})}{(c_{Ai} - c_A)} \qquad (4.27)$$

For dilute liquid concentrations, $k_L = \dfrac{D_L}{z_L}$ $\qquad (4.28)$

where D_L = liquid phase diffusivity (m^2/s)

z_L = liquid film thickness (m)

4.2.3   Overall and Film Mass Transfer Coefficients

In most experimental determinations of mass transfer rate, it is not ordinarily possible to obtain direct measurements of the interface concentrations and hence the film mass transfer coefficients (k_G, k_L). Instead the resulting rates of mass transfer can be expressed in terms of overall mass transfer coefficients which can be derived from solute concentrations in the bulk fluids:

$$N_A = K_G \, (p_A - p_A^*) = K_L \, (c_A^* - c_A) \qquad (4.29)$$

where K_G = overall gas phase mass transfer coefficient (kmol/m²sPa)

  K_L = overall liquid phase mass transfer coefficient (m/s)

  p_A^* = partial pressure of A in equilibrium with concentration c_A in liquid phase (Pa)

  c_A^* = concentration of A in liquid phase in equilibrium with partial pressure p_A in gas phase (kmol/m³)

For dilute solutions, Henry's Law applies (H in Pa.m³/kmol):

$$p_A^* = H\, c_A \tag{4.30}$$

It can be shown that when the solution obeys Henry's Law, the relationships between the overall mass transfer coefficients with the film coefficients are in the form of addition of resistances as follows:

$$\frac{1}{K_G} = \frac{1}{k_G} + \frac{H}{k_L} \tag{4.31}$$

$$\frac{1}{K_L} = \frac{1}{k_L} + \frac{1}{H k_G} \tag{4.32}$$

and

$$\frac{1}{K_G} = \frac{H}{K_L} \tag{4.33}$$

For equations 4.31 to 4.33 to be valid, there must be no variation in H over the equipment, there has to be negligible interfacial resistance and the two film coefficients must be independent of one another.

The mass transfer equations can be expressed in terms of mol fractions as follows assuming the total concentration in the liquid phase remains constant:

$$N_A = k'_G(y_A - y_{Ai}) = K'_G\,(y_A - y_A^*) \tag{4.34}$$

$$N_A = k'_L(x_{Ai} - x_A) = K'_L\,(x_A^* - x_A) \tag{4.35}$$

where x_A, y_A = mol fraction of soluble component A in liquid and gas phases respectively (mol/mol)

  x_A^*, y_A^* = equilibrium mol fractions (mol/mol)

  k'_G, k'_L, K'_G, K'_L = mass transfer coefficients in terms of mol fractions (kmol/m²s)

If the equilibrium curve relating the solute concentration in the gas phase to the solute concentration in the liquid phase at equilibrium has a slope m (mol/mol), then:

$$\frac{1}{K'_G} = \frac{1}{k'_G} + \frac{m}{k'_L} \qquad (4.36)$$

$$\frac{1}{K'_L} = \frac{1}{k'_L} + \frac{1}{mk'_G} \qquad (4.37)$$

and

$$\frac{1}{K'_G} = \frac{m}{K'_L} \qquad (4.38)$$

The relationships between the mass transfer resistances are as follows:

$$\frac{Resistance\ in\ gas\ film}{Total\ resistance, both\ films} = \frac{1/k_G}{1/K_G} = \frac{1/k'_G}{1/K'_G} \qquad (4.39)$$

$$\frac{Resistance\ in\ liquid\ film}{Total\ resistance, both\ films} = \frac{1/k_L}{1/K_L} = \frac{1/k'_L}{1/K'_L} \qquad (4.40)$$

4.2.4 Gas Film or Liquid Film Controlled Processes

If m is small such that at equilibrium only a small solute concentration in the gas will provide a very large solute concentration in the liquid (i.e. very soluble solute in liquid), the liquid film resistance m/k'_L in equation 4.36 becomes minor compared to that of the gas film $1/k'_G$. The rate of mass transfer is said to be gas film controlled. In the extreme,

$$1/K'_G \approx 1/k'_G \qquad (4.41)$$

or

$$(y_A - y_A^*) \approx (y_A - y_{Ai}) \qquad (4.42)$$

In this case, the mass transfer rate is best improved by reducing the gas film resistance as fairly large changes in k'_L will not affect K'_L significantly.

Conversely, where values of m are large (i.e. solute relatively insoluble in the liquid), the gas film resistance $1/mk'_G$ in equation 4.37 becomes negligible relative to that of the liquid film $1/k'_L$. The rate of mass transfer is then considered to be liquid film controlled. Ultimately,

$$1/K'_L \approx 1/k'_L \qquad (4.43)$$

or

$$(x_A^* - x_A) \approx (x_{Ai} - x_A) \qquad (4.44)$$

Under such conditions, the rate of mass transfer is best improved by reducing the liquid film resistance, i.e. increasing k'_L.

4.2.5 The Transfer Unit in Gas Absorption

It is necessary to account for changes in the gas-liquid interfacial area which is not normally directly measured in mass transfer experiments. The interfacial area is allowed for by the use of the volumetric coefficients $K'_G a$, $K'_L a$, $k'_G a$ and $k'_L a$ (kmol/m^{3}s) where 'a' is the interfacial area per unit volume of column (m^2/m^3).

Figure 4.5 illustrates a gas absorption column through which the gas flows through the column at a flowrate of G' (kmol/m^{2}s) countercurrently to the downflowing liquid at a flowrate of L' (kmol/m^{2}s).
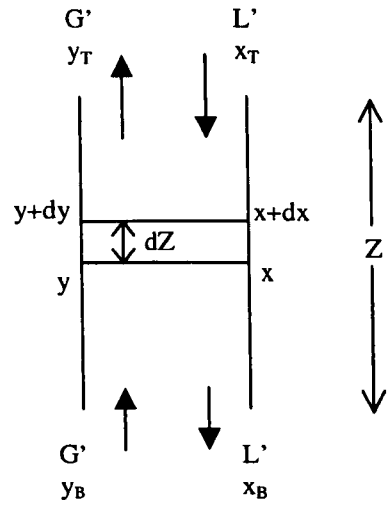
Figure 4.5 Countercurrent gas absorption column.

It is assumed herein that the amount of solute transferred is small, hence only dilute solutions are formed and concentration changes in the column are small. This is such that $K'_G a$, as well as the gas and liquid molar flowrates G' and L' are constant throughout the column. With these assumptions, the height of the packed bed Z (m) required to provide a change in gas concentration from y_B (mol/mol) at the bottom to y_T (mol/mol) at the top is given by:

$$\int_0^Z dZ = Z = H_{OG} \times N_{OG} = \frac{G'}{K'_G a} \int_{y_B}^{y_T} \frac{dy}{y^* - y} \tag{4.45}$$

where   Height of an overall gas phase transfer unit, $H_{OG} = \dfrac{G'}{K'_G a}$ (m) $\tag{4.46}$

Number of overall gas phase transfer units, $N_{OG} = \displaystyle\int_{y_B}^{y_T} \frac{dy}{y^* - y}$ $\tag{4.47}$

The concept of the transfer unit was first put forward by Chilton and Colburn (1935). Similar equations can be written involving the overall liquid transfer coefficient as well as for the individual film coefficients, assuming that dilute solutions are formed and that concentration changes are small:

$$Z = H_{OL} \times N_{OL} = \frac{L'}{K'_L a} \int_{x_B}^{x_T} \frac{dx}{x - x^*} \tag{4.48}$$

$$Z = H_G \times N_G = \frac{G'}{k'_G a} \int_{y_B}^{y_T} \frac{dy}{y_i - y} \tag{4.49}$$

96

$$Z = H_L \times N_L = \frac{L'}{k'_L a} \int_{x_B}^{x_T} \frac{dx}{x - x_i} \qquad (4.50)$$

where H_{OL} = height of an overall liquid phase transfer unit (m)

H_G, H_L = height of a gas and liquid film transfer unit respectively (m)

N_{OL} = number of overall liquid phase transfer units

N_G, N_L = number of gas film and liquid film transfer units respectively (m)

For dilute solutions, the operating line and equilibrium line are straight. Conducting a material balance over the lower section of the column in Figure 4.5, the operating line:

$$L'(x_B - x) = G'(y_B - y) \quad \text{or} \quad y_B - y = \frac{L'}{G'}(x_B - x) \qquad (4.51)$$

The equilibrium line: $y^* = mx + c$ (4.52)

where m is the slope of the equilibrium line and c the y-axis intercept.

For dilute solutions (straight operating and equilibrium lines), it can be shown from equations 4.47, 4.51 and 4.52 that the number of overall gas transfer units is:

$$N_{OG} = \frac{y_B - y_T}{\dfrac{(y - y^*)_B - (y - y^*)_T}{\ln \dfrac{(y - y^*)_B}{(y - y^*)_T}}} = \frac{y_B - y_T}{(y - y^*)_{lm}} \qquad (4.53)$$

$(y-y^*)_{lm}$ is the logarithmic mean of the driving forces at the ends of the column, $(y-y^*)_B$ and $(y-y^*)_T$. The height of an overall transfer unit is the height of a packed section necessary to achieve a change in concentration equal to the average driving force in that section, this average driving force being $(y-y^*)_{lm}$.

Therefore the rate of mass transfer taking place in the column is as follows:

$$NA = G'(y_B - y_T)A = K'_G aAZ(y - y^*)_{lm} \qquad \text{(kmol/s)} \qquad (4.54)$$

where   A = column cross-sectional area (m^2)

N = molar rate of absorption per unit area (kmol/m^{2}s)

Similar to the mass transfer coefficients, the addition of resistances following the Two-Film Theory can also be applied to the heights of the transfer units, this being first noted by Colburn

(1939). The relationships between the film and overall heights of transfer units are as follows, where m is the slope of the equilibrium line and L'/G' is the slope of the operating line. Where mass transfer resistance is essentially all in the gas phase and for dilute solutions:

$$H_{OG} = H_G + \frac{mG'}{L'} H_L \qquad (4.55)$$

Where mass transfer resistance is essentially all in the liquid phase and for dilute solutions:

$$H_{OL} = H_L + \frac{L'}{mG'} H_G \qquad (4.56)$$

4.2.6 Mass Transfer Correlations

There has been a considerable number of studies to determine the mass transfer efficiencies in packed gas-liquid contactors both empirically and theoretically. The available published correlations for the mass transfer coefficients or the height of transfer units are extensive and have been tabulated (Table 5-28 in Knudsen *et al.*, 1997). Key parameters in the correlations include gas and liquid rates, gas and liquid physical properties (density, viscosity, surface tension, diffusivity), packing type and dimension, and overall bed dimension.

4.2.6.1 Overall Gas Phase Mass Transfer Coefficient

In gas absorption operations, the overall volumetric gas phase mass transfer coefficient values $K'_G a$ (kmol/m^{3}s) are normally used as the composition of the gas phase are usually of interest. $K'_G a$ in absorption is a function of both the liquid L (kg/m^{2}s) and gas phase G (kg/m^{2}s) flowrates (Strigle, 1994):

$$K'_G a \propto L^a G^b \qquad (4.57)$$

In gas film controlled processes, the exponent 'a' varies between 0.22 and 0.34 for most randomly dumped packings, the exact value depending on the type of packing used whilst the exponent 'b' varies from 0.67 to 0.80. In any case, the sum of the exponents 'a' and 'b' is greater than 1.0.

In liquid film controlled processes, $K'_G a$ is mainly a function of the liquid flowrate. The exponent 'a' has the same value as that for the gas film controlled processes whilst 'b' is only 0.06 to 0.08, a reflection of the small effect of gas rate.

4.2.6.2 Gas Film Mass Transfer Coefficient

The volumetric gas film mass transfer coefficient k'$_G$a has been found to be related to the dimensionless gas phase Schmidt number:

$$k'_Ga \; \alpha \; (Sc_G)^{-0.5} \quad or \quad H_G \; \alpha \; (Sc_G)^{0.5} \quad where \quad Sc_G = \frac{\mu_G}{\rho_G D_G} \quad (4.58)$$

μ_G is the gas viscosity (kg/ms), ρ_G is the gas density (kg/m^3) and D_G is the gas molecular diffusivity (m/s). The exponent was initially thought to have a value of 0.67 (Chilton and Colburn, 1934) but was later modified to 0.5 (Cornell et al., 1960). This latter value has since been retained for application in ensuing texts (Sherwood et al., 1975; Knudsen et al., 1997). For all practical purposes, the gas film mass transfer coefficient k'$_G$ is unaffected by temperature and pressure in the normal ranges of these variables, the gas phase Schmidt number itself being independent of temperature (Knudsen et al., 1997).

4.2.6.3 Liquid Film Mass Transfer Coefficient

There has been some debate whether the volumetric liquid film mass transfer coefficient should vary with the square root of the liquid phase diffusivity $D_L^{0.5}$ (Sherwood and Holloway, 1940b) or as the liquid phase Schmidt number to the –0.5 power i.e. $Sc_L^{-0.5}$ (Cornell et al., 1960). Recent reviews have accepted that the volumetric liquid film mass transfer coefficient is related to the liquid phase diffusivity as follows (Sherwood et al., 1975; Knudsen et al., 1997):

$$k'_La \; \alpha \; D_L^{0.5} \quad or \quad H_L \; \alpha \; D_L^{-0.5} \quad (4.59)$$

Since the interfacial area 'a' is independent of D_L:

$$k'_L \; \alpha \; D_L^{0.5} \quad (4.60)$$

However, when the liquid phase Reynolds number (Re$_L$= $\rho_L u_L d/\mu_L$) is held constant:

$$k'_L \; \alpha \; (Sc_L)^{-0.5} \quad where \quad Sc_L = \frac{\mu_L}{\rho_L D_L} \quad (4.61)$$

Temperature has a significant effect on the liquid film mass transfer coefficient. It increases with temperature due to reduced liquid viscosity and increased diffusivity. The effects of system pressure and hence the solute partial pressure on the liquid film mass transfer coefficient k'$_L$ can be ignored for all practical applications (Strigle, 1994; Knudsen et al., 1997).

4.2.7 Previous Work on Non-Wetting Systems

While there are numerous published mass transfer studies using conventional wetting systems irrigated by water, aqueous and organic liquids (extensive reviews available from Sherwood *et al.*, 1975; Treybal, 1980; Coulson, *et al.*, 1991; Knudsen *et al.*, 1997), in contrast there is only a handful of reported work on mass transfer in non-wettable systems as revealed by the literature search herein.

Sherwood and Holloway (1940a) first noted that in the mass transfer studies by Rennolds (1939) using carbon Raschig rings, the overall volumetric mass transfer coefficients were considerably reduced when paraffin waxed packing was used in replacement of non-treated ones. This was attributed to the reduction in interfacial area as the liquid tends to flow in thick rivulets on the waxed packing surface as opposed to thin layers on untreated packing. In tests involving vaporisation of water into dry air, $K_G a$ (kmol/m^{3}s Pa) for coated packing was found to be about 50% lower than that of the untreated packing. In tests involving CO_2 desorption from water, $K_L a$ (s^{-1}) for the coated packing was about 30% lower that for the untreated packing. That there was a smaller extent of reduction in $K_L a$ for CO_2 desorption (liquid film controlling) compared to $K_G a$ for water vaporisation (gas film controlling) by wax coating suggested that the liquid rivulets on coated packing were more agitated than the liquid layer on untreated packing, aiding mass transfer. Hence in liquid film controlling process, the reduction in interfacial area 'a' by wax coating was partially offset by the increase in K_L due to enhanced convective transport within the liquid in rivulet flow.

Warner (1959b) conducted studies in which zinc vapour in nitrogen was absorbed into a countercurrent flow of molten lead in a column packed with ¼ inch steel Raschig rings. This process was shown to be gas film diffusion controlled under the experimental conditions employed, H_{OG} obtained from the experiments being equal to H_G. Therefore it could be and was compared against other gas film controlled process, this being the absorption of ammonia from a dilute ammonia-air mixture into water. The ammonia absorption data was obtained from a room temperature non-wetting system model using the same Raschig ring packing, but with both the column walls and packing coated with paraffin wax. Warner empirically correlated both gas film controlled zinc and ammonia absorption data using the effective liquid holdup, defined as the liquid holdup which gives effective contribution to the absorption process. In the zinc vapour absorption process, the total liquid holdup was effective to absorption due to mobility of the lead static holdup whereas only the dynamic holdup was considered to be effective in the ammonia

absorption process. Two empirical correlations satisfying both the zinc and ammonia absorption data were obtained. The first correlation involved the gas inertia term $U_G^2\rho_G$:

$$H_G = \beta (U_G^2 \rho_G)^a (h_E)^b (Sc_G)^{2/3} \qquad (4.62)$$

where β, a, b = empirical constants; b in this case = -0.42

U_G = true gas velocity based on irrigated bed porosity (m/s)

Sc_G = gas phase Schmidt number = $\dfrac{\mu_G}{\rho_G D_G}$ (dimensionless)

h_E = effective liquid holdup (m^3/m^3)

The other correlation used the relative velocity of gas and liquid streams U_R (m/s) and the relative Reynolds number $Re_R = dU_R\rho_G/\mu_G$:

$$H_G = \beta' \left(\frac{U_G}{U_R} \right) (Re_R)^a (h_E)^b (Sc_G)^{2/3} \qquad (4.63)$$

where β', a, b = empirical constants; b in this case = -0.42

d   = characteristic length of packing particle (m)

The ability to simultaneously correlate the zinc and ammonia absorption data suggested that simpler room temperature analogues could be used to estimate experimentally complex high temperature mass transfer performance. Comparison was also made on the mass transfer efficiency in the ammonia absorption process for wettable and non-wettable packings. The non-wettable packing gave a higher height of a transfer unit than its wettable counterpart.

Coughlin (1969) reported that mass transfer efficiency diminished with decreased wetting of packing. The volumetric overall liquid phase mass transfer coefficient K'_La for the absorption of oxygen into sodium sulfite solution with cupric ion as catalyst was found to be about 25% higher for ceramic packing compared to polymeric packings of saran and polyethylene. A possible reason put forward for this was that the wettable ceramic packing provided the greatest interfacial area 'a' for mass transfer, hence resulting in highest K'_La values.

Mackey and Warner (1973) studied the vaporisation of mercury flowing countercurrent to air in irrigated packed beds of 10 mm glass spheres, ¼ inch steel Raschig rings and ½ inch carbon Raschig rings. Mercury vaporisation is a solely gas film controlled process, with no diffusional resistance in the liquid. Therefore, the overall gas phase mass transfer coefficient equalled the

gas film mass transfer coefficient. The height of transfer unit for mass transfer was correlated in terms of the gas phase Reynolds number Re_G and liquid superficial velocity u_L in the following form:

$$H_G = \beta \ (Re_G)^a \ (u_L)^b \tag{4.64}$$

Re_G (equals $dU_G\rho_G/\mu_G$) was calculated using the true gas velocity, U_G which takes into account the irrigated bed porosity i.e. $U_G = u_G/\varepsilon_{eff}$. Spheres were found to be more efficient than Raschig rings thought to be due to higher tendency for drop flow on spheres resulting in greater interfacial area. At the same liquid and gas mass velocities, the mass transfer rate for mercury vaporisation was found to be lower than that reported in the literature for water vaporisation into air on Raschig rings. This was attributed to the non-wetting nature of the liquid metal on the packing resulting in lower interfacial area as well as the possible lowering of gas film coefficient k_G by droplet and rivulet liquid flow pattern. Otherwise, increasing gas and liquid flow rates improve the mass transfer in both mercury vaporisation (non-wetting) and aqueous systems (wetting). The data from mercury vaporisation together with the zinc absorption data into molten lead by Warner (1959b) were well correlated in terms of relative velocity and the total liquid holdup as in equation 4.63 (by Warner, 1959b), suggesting that the total liquid holdup is effective in gas phase transfer processes in liquid metal irrigated systems. The mercury vaporisation data was also similarly correlated along with ammonia absorption data based on non-wettable waxed Raschig ring packings.

Andrieu (1975) reported that the reduction in interfacial area 'a' for silicone resin coated glass Raschig ring packing was about 50% compared to that for the untreated glass packing.

Tait (1998) determined H_G based on water vaporisation into air and H_L based on oxygen desorption from water into air for both waxed and unwaxed spherical polypropylene packings, 20 and 45 mm in size. At the same gas and liquid rates, H_G was found to be lower for the wax treated spheres, however H_L was higher for the waxed spheres compared to the untreated packing. Both H_G and H_L were correlated in the same form as equation 4.64 (by Mackey and Warner, 1973) but with addition of the Schmidt number to allow for application to different diffusing species:

$$H_G = \beta \ (Re_G)^a \ (u_L)^b \ Sc_G^{2/3} \quad ; \quad H_L = \beta' \ (Re_L)^c \ (U_G)^d \ Sc_L^{0.5} \tag{4.65}$$

H_G was also correlated against the effective liquid holdup h_E in the same form as equation 4.63 (by Warner, 1959b).

4.3   Summary

❏ *Gas-Solid Separation*

In a gas-solid separator, solid particulates are transported by the gas stream and brought into contact with the collector surface. Collection is mainly mechanical via Brownian diffusional capture, inertial deposition, gravitational settling and direct interception. For dust particles smaller than 0.1 μm, Brownian diffusional capture is dominant whilst inertial deposition becomes the prevailing collection mechanism for dust particles larger than 0.5 μm. The collected dust particle may either rebound and be re-entrained back into the gas stream or else be retained and removed from the gas depending on the relative magnitudes of the impacting particle energy and the detachment energy required to separate the particle from the collector surface.

The overall efficiency E_T of a gas-solid separator quantifies the mass ratio of the separated particles to the total solids fed into the separator and is largely dependent on the size distribution of the feed. A better alternative to describe the efficiency of a gas-solid separator is the grade efficiency $G(x)$ curve which gives the mass separation efficiency for a specific particle size x.

In scrubbers (wet collectors or wet separators), gas-solid separation is aided by the addition of a liquid. The principal collection mechanisms are inertial deposition (most important), diffusional capture and direct interception. Secondary mechanisms include diffusiophoresis, thermophoresis and particle growth due to liquid condensation. Scrubbers in general have higher efficiency than dry separators, capable of separating particles down to less then 1 μm. The separation efficiency generally increases with pressure drop or liquid consumption, and hence the power consumption. As dust particle size decreases, the power consumption for a specific efficiency increases.

The type of scrubber employed in this study is the packed bed scrubber. The packing elements are usually too large to serve as effective collectors except for very large dust particles. In the collection of fine particles, the packings promote fluid turbulence, enhancing particle deposition on liquid films or droplets. Inertial deposition is the main collection mechanism, with some contribution from diffusion for sufficiently small dust particles.

❏ *Gas Absorption*

Gas absorption is a mass transfer operation involving the transfer of a solute from the bulk gas phase to the bulk liquid phase, the driving force provided by the solute concentration gradient. Whitman's (1923) Two-Film Theory is extensively used to describe the conditions at the phase boundary during mass transfer. The theory treats the mass transfer resistance in each phase as a

thin film next to the gas-liquid interface. Steady-state molecular diffusion mass transfer occurs across these films whilst bulk fluid turbulence dies out at the interface. The solute concentrations in both the gas and liquid films at the interface are at equilibrium. No resistance to mass transfer exists across the interface. For ideal solutions, the gas-liquid equilibrium is described by Raoult's Law. For slightly soluble gases forming dilute solutions, Henry's Law applies.

The efficiency in mass transfer is described by the mass transfer coefficient, defined as the ratio of the mass transfer rate to the concentration difference. In line with the Two-Film Theory, the overall mass transfer coefficients are related to the film coefficients in the form of addition of resistances. Where the resistance lies predominantly in the gas (or liquid) film, the process is gas (or liquid) film controlled and in the extreme cases, the overall gas (or liquid) phase coefficient equals the gas (or liquid) film coefficient.

The efficiency of a gas absorber can be expressed in terms of height of a transfer unit which is inversely proportional to the mass transfer coefficient. The specified composition change determines the number of transfer units required. The height of a transfer unit multiplied by the number of transfer units required gives the absorber height to produce a certain separation. Similar to mass transfer coefficients, transfer units can be defined for the overall bulk phases as well as the liquid and gas films. The additive resistances concept of the Two-Film Theory can also be extended to the heights of the transfer units.

There are extensive published correlations on mass transfer efficiencies in packed gas-liquid contactors for conventional wetting systems. In stark contrast, there is only a handful of reported work that concentrated on mass transfer in non-wettable systems. The mass transfer efficiency for non-wettable packing has been generally found to be lower than that of their wettable equivalent. This has been attributed to the lowering of the gas-liquid interfacial area for mass transfer as a result of poorer wetting. The effect of differing liquid flow pattern i.e. film flow in wettable systems as opposed to droplet or rivulet flow in non-wettable systems on the mass transfer coefficient has also been discussed. The mass transfer efficiency for non-wettable systems including those of liquid metals has been empirically correlated against the fluids Reynolds number and the fluids superficial velocity. The effective liquid holdup, defined as the liquid holdup which is active in an absorption process has also been used as a correlating parameter. The ability to simultaneously correlate absorption data based on liquid metal and non-wettable aqueous systems have been demonstrated. This suggests that the use of simpler room temperature analogues to estimate experimentally complex high temperature mass transfer performance involving liquid metals is feasible.

Chapter Five

Experimental Programme

This chapter sets out the experimental programme undertaken during the course of this research project. Details on the experimental setup and procedure for each type of investigation are documented. The design of the cold gas scrubber is also discussed. The experimental studies performed and their aims are summarised as follows:

Table 5.1 *Summary of experimental studies undertaken.*

Preliminary Gasification Studies	
Experiments	**Objectives**
Gasification without tin	To determine the amount of H_2S produced from the gasification of a known mass of fuel sample.
Gasification in the presence of tin	To investigate the effect of molten tin on the H_2S produced from the gasification of a known mass of fuel sample.
Cold Gas Scrubber Studies	
Experiments	**Objectives**
Flow visualisation	To provide insight and understanding to the nature of non-wetting flow on spherical packings.
Flooding	To determine the flooding points of a packed column operating under non-wetting flow conditions.
Liquid holdup	To study the variation of static and dynamic liquid holdups with gas and liquid flowrates for a packed column operating under non-wetting flow conditions.
Gas lift	To investigate the performance of a small air lift for liquid transport with differing air injectors and submergence ratios.
Particulate removal	To determine the total efficiency and grade efficiency of particulate separation by a packed bed gas scrubber operating under non-wetting flow conditions.
Gas absorption	To establish the mass transfer efficiency of a packed bed gas scrubber operating under non-wetting flow conditions.

5.1 Preliminary Gasification Studies

Preliminary small-scale gasification tests were carried out in an electrically heated horizontal furnace using petroleum coke fuel samples. A steam/nitrogen mixture was used as the gasifying medium. Gasification of a known mass of fuel sample was carried out with and without the presence of tin. The amounts of H_2S sampled from the product gas exiting the gasification furnace under both conditions were then compared. The effect of molten tin on H_2S in the product fuel gas was investigated.

5.1.1 Experimental Setup

Plate 5.1 and Figure 5.1 illustrate the overall experimental rig used for the gasification studies. Pumped feedwater and high-purity N_2 gas (99.95%) supplied from a compressed gas cylinder were mixed prior to entering the steam generator/N_2 preheater. The water and N_2 gas mixture was heated up to generate a gasifying medium of superheated steam/hot N_2 gas mixture at atmospheric pressure. The gas mixture then entered the gasification furnace in which a crucible containing the fuel sample was placed at the central hot zone. The hot product gas exiting from the gasification furnace was first cooled by a water-cooled heat exchanger (cold finger) in which water vapour was condensed and removed from the gas. The product gas was then filtered before being bubbled through Dreschel gas washing bottles for H_2S capture. Downstream of the washing bottles, the product gas was dried and then filtered before passing through a gas pump and then finally a low-range CO analyser. Finally, from the gas analyser, the product gas was removed via a gas extractor.
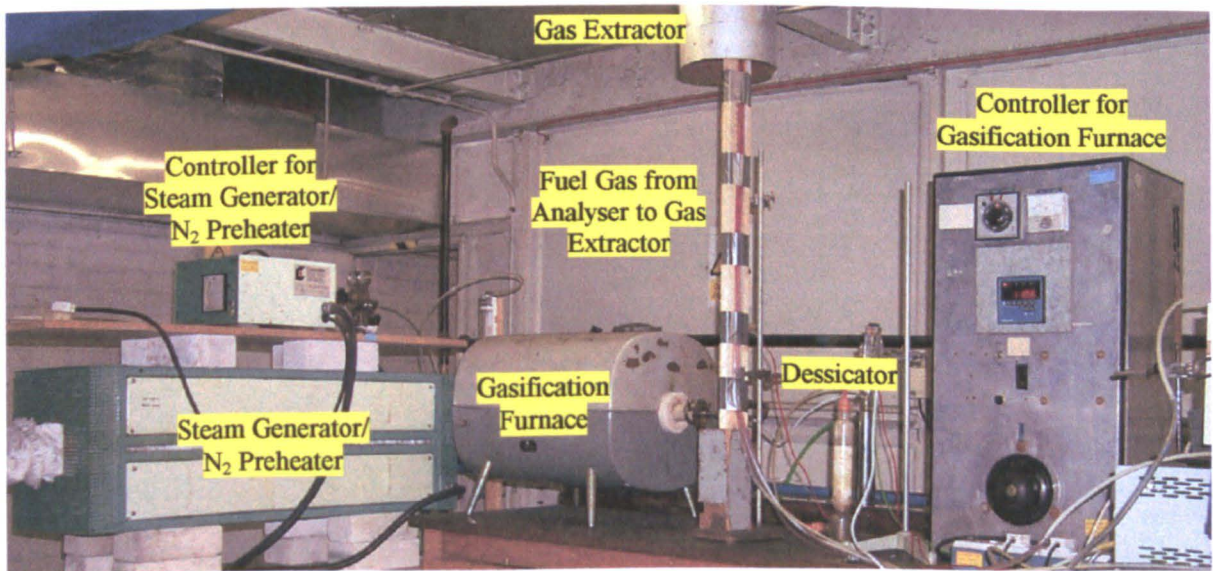
Plate 5.1 Experimental setup for preliminary gasification studies.

Figure 5.1 *Experimental setup for preliminary gasification studies.*

Legend:
- Water Stream
- Gas Stream
- Water/N_2 Stream
- Electrical Signal
- Thermocouple

Labels in figure:
- N_2 Gas
- Rotameter
- Nitrogen Gas Tank
- Water
- Water Pump
- Steam Generator/ N_2 Preheater
- N_2 / Steam Mixture
- K-Type Digital Thermometer
- Thermocouple Signals
- Gasification Furnace
- Fuel Sample
- Voltmeter
- Fuel Gas
- Water To Drain
- Gas Cooler
- Cooling Water
- Condensed Water
- Filter
- Dreschel Gas Washing Bottles
- Dessicator
- Filter
- Gas Pump
- Low-range CO Analyser
- Fuel Gas To Extractor
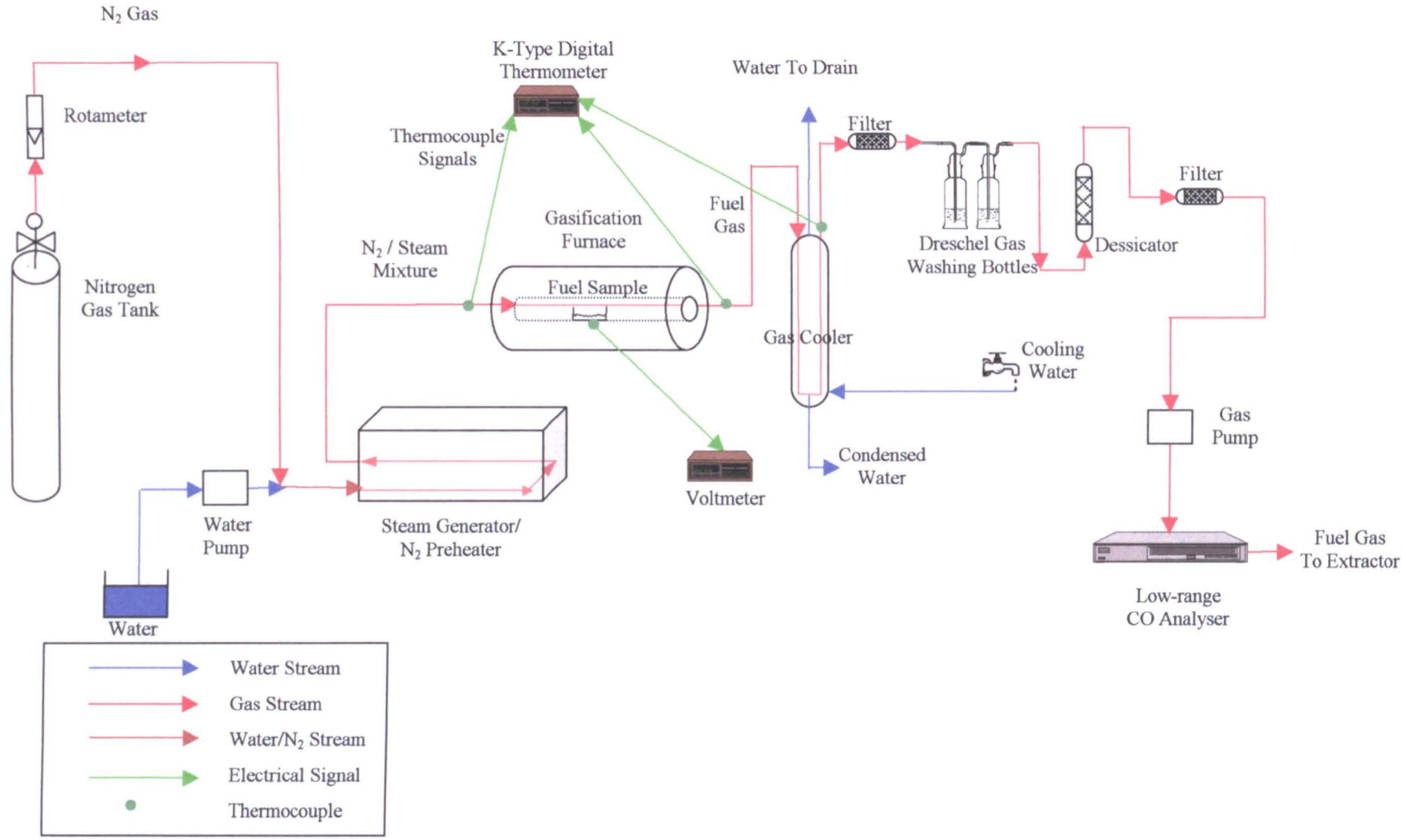
Table 5.2 *Instrument specifications for preliminary gasification studies.*

Instrument	Specifications
Water pump	DCL reciprocating-type pump. Range 1-14 cm^3/min at 100 strokes/min.
Steam generator/N_2 preheater	240V electrically heated furnace by Carbolite. Portable controller. Maximum operating temperature 1000°C.
Gasification furnace	150V horizontal, electrically heated furnace, model K.44.A by GMC. Separate controller by Honeywell. Maximum operating temperature 1350°C.
Gas cooler	Stainless steel mini shell-and-tube heat exchanger. 1 shell pass and 2 tube passes. Cooling water in shell, fuel gas in tube.
Dessicator	Contains fused granular $CaCl_2$.
Filter	Disposable in-line Whatman Minifilter. 0.9 µm pore size nylon housing with resin-bonded glass microfibre filter tube.
CO analyser	Model Xentra 4900 by Servomex. Range 0-3000 ppm CO. Low calibration with ambient air, high calibration with BOC calibration gas containing 2400 ppm CO in nitrogen.
Microbalance	Model Precisa 125A by Swiss Quality. Sensitivity 0.0001 g.

The gasification furnace has double concentric combustion tubes fitted through its centre longitudinally. The inner tube is 70.0 cm in length and has a 3.2 cm inner bore whilst the outer tube is 76.0 cm in length and has a 3.8 cm inner bore. Both ends of the outer combustion tube were sealed by removable stainless steel covers coated with foliac graphite pipe joint compound for improved seal. An approximately 5 mm hole was drilled into each cover to serve as the inlet and outlet for the gas stream. The stainless steel piping connecting the steam generator/N_2 preheater with the gasification furnace was insulated with insulating wool to minimise heat loss. The fuel sample contained in a silica-based crucible sized 60 mm × 29 mm × 12 mm was placed in the centre of the inner combustion tube i.e. at the hottest zone. Figure 5.2 illustrates the gasification furnace containing the fuel sample for tests without tin.
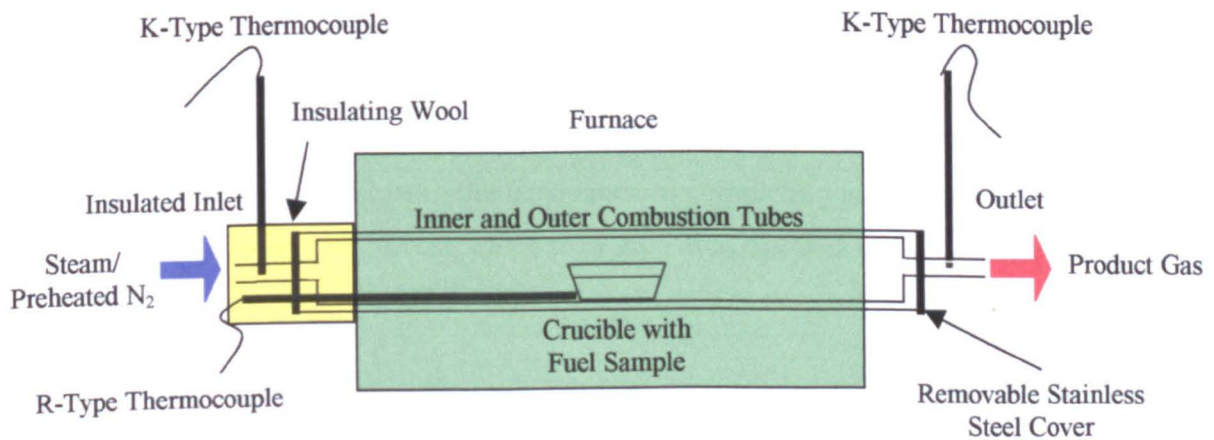
Figure 5.2 *Gasification furnace (without tin).*

K-type Nickel-Chromium/Nickel-Aluminium thermocouples (temperature range: -270°C to 1370°C) were used to measure the steam/N_2 mixture temperature at the combustion tube inlet, the product gas temperature at the combustion tube outlet, and the cooled product gas temperature at the gas cooler outlet. These thermocouples were connected to a K-type digital thermometer from E.T.I. Ltd. on which the temperatures were indicated. An R-type Platinum-13% Rhodium/Platinum thermocouple (temperature range: -50°C to 1760°C) was used to measure the temperature at the central hot zone of the combustion tube in the gasification furnace. R-type digital thermometers were unavailable. Instead, this thermocouple was connected to a voltmeter, Black Star-4503 Intelligent Multimeter from RS Components Ltd. The voltage displayed was converted to the equivalent temperature using R-type thermocouple temperature-voltage tables.

5.1.2 Operating Parameters

Temperatures: Gasification was carried out at 1200°C (set point of the furnace) i.e. the temperature of the central hot zone in the combustion tube. The incoming steam/N_2 mixture temperature to the gasification furnace was approximately 200°C, limited by the slow heat up rate of the N_2 preheater/steam generator.

Nitrogen Gas: A continuous flow of nitrogen gas at approximately 2 litre/min was supplied through the gasification furnace while the furnace was being heated up to 1200°C. This flushed out the air in the combustion tube and helped maintain an inert atmosphere, preventing oxidation of the fuel sample. The nitrogen gas was maintained at 2 litre/min throughout the gasification process. The nitrogen diluted the steam in the gasifying mixture, preventing over-vigorous reaction with the small amount of fuel sample in the crucible. It also acted as a carrier gas, aiding the flow of product gas through the complete gas circuit.

Steam: The feed water pump used was of a variable flow type. The higher the feed water (hence steam) flow, the faster would be the gasification reaction and the shorter the time required to completely gasify the fuel sample. Considering the amount of fuel sample in the crucible (about 2 g) and the particle size (212 μm), the time taken to completely gasify the fuel sample would be relatively short. Hence, the lowest water flow rate was applied (approximately 1 cm³/min) to lengthen the reaction time.

Fuel Sample: Petroleum coke with sulphur content of 4.4% by weight (as-received) was used as fuel sample. The sulphur content was determined following the High Temperature Method outlined in BS 1016: Part 6: 1977 (see Appendix 1). Approximately 2 g of fuel sample ground to pass a 212 μm sieve was used in each test. The amount of fuel sample was limited by the size of

the crucible that could fit inside the inner combustion tube. The full mass composition of the petroleum coke is as follows (as-received basis): carbon 89.7%, hydrogen 3.2%, sulphur 4.4%, oxygen and nitrogen 0.1%, moisture 1.0% and ash 1.6%.

5.1.3   Experimental Procedure

5.1.3.1 Gasification Without Tin

❑ *Fuel Sample Gasification*

Approximately 2 g of petroleum coke sample contained in a crucible was heated in the central hot zone of the gasification furnace (Figure 5.2) from room temperature to approximately 1200°C in an inert N_2 atmosphere, preventing fuel oxidation. Once the central hot zone temperature in the furnace reached about 1200°C i.e. when the voltmeter read 0.01312V, superheated steam was introduced into the system initiating fuel gasification. The product gas was cooled and filtered before passed into two Dreschel gas washing bottles in series containing 60 ml ammoniacal zinc sulphate solution each for sulphur analysis. The gasification of the fuel sample proceeded for typically 1 hour, its completion was indicated by zero CO concentration in the outlet gas stream, read from the CO analyser.

❑ *H₂S Analysis*

The H_2S determination was based on BS 3156: Part 2: 1968, under Special Determinations - H_2S In Crude Gas. In this method, the sampled gas is passed through ammoniacal zinc sulphate solution in which H_2S in the gas is precipitated as zinc sulphide. The sulphide is quantitatively determined using the iodimetric method which utilises the following reversible reaction:

$$H_2S + I_2 \leftrightarrow 2H^+ + 2I^- + S \tag{5.1}$$

The white precipitate of zinc sulphide is dissolved in excess of acidified iodine. The sulphide reacts with HCl acid in the solution forming H_2S,

$$S^{2-} + 2H^+ \rightarrow H_2S\uparrow \tag{5.2}$$

which in turn reacts with I_2 in reaction 5.1, precipitating sulphur. The excess of iodine is titrated with standard sodium thiosulphate solution, using sodium starch glycollate solution as indicator:

$$I_2 + 2S_2O_3^{2-} \leftrightarrow 2I^- + S_4O_6^{2-} \tag{5.3}$$
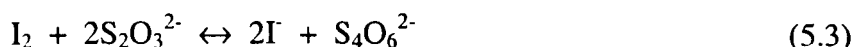
• The ammoniacal zinc sulphate solution was prepared from 14.5 g of crystalline zinc sulphate dissolved in 500 ml of water. Sufficient ammonia solution (s.g 0.88) was then added to the

solution to re-dissolve the zinc hydroxide precipitate first formed.

- After the gasification experiment, the white zinc sulphide solid precipitate collected in the first Dreschel bottle (none collected in the second) was filtered off and washed with distilled water. The filtered paper containing the precipitate was placed in a hollow glass stopper of a wide-necked bottle.

A measured volume of 0.1N iodine solution (in excess of that required) was added together with 6 ml of hydrochloric acid (s.g. 1.18) into a wide-necked bottle. The greased glass stopper containing the filter paper was inserted into the bottle mouth, taking care not to release the filter paper and its contents until the bottle was sealed. The top of the bottle was sharply tapped, allowing the filter paper and its contents to fall into the iodine solution. The bottle was then shaken well and the aqueous mixture was diluted to 200 ml. The excess of iodine was titrated against 0.1N sodium thiosulphate solution, using 2 ml of 1% sodium starch glycollate solution as indicator. The amount of sodium thiosulphate solution used was noted.

A blank determination was then carried out. A volume of 0.1N iodine solution, equal to that used in the test was measured into a 500 ml flask. 6 ml of hydrochoric acid (s.g. 1.18) was added to the iodine solution. The mixture was diluted to 200 ml and titrated with 0.1N sodium thiosulphate solution, using 2 ml of 1% sodium starch glycollate solution as indicator. The amount of sodium thiosulphate solution used was noted.

5.1.3.2 Gasification In The Presence of Tin
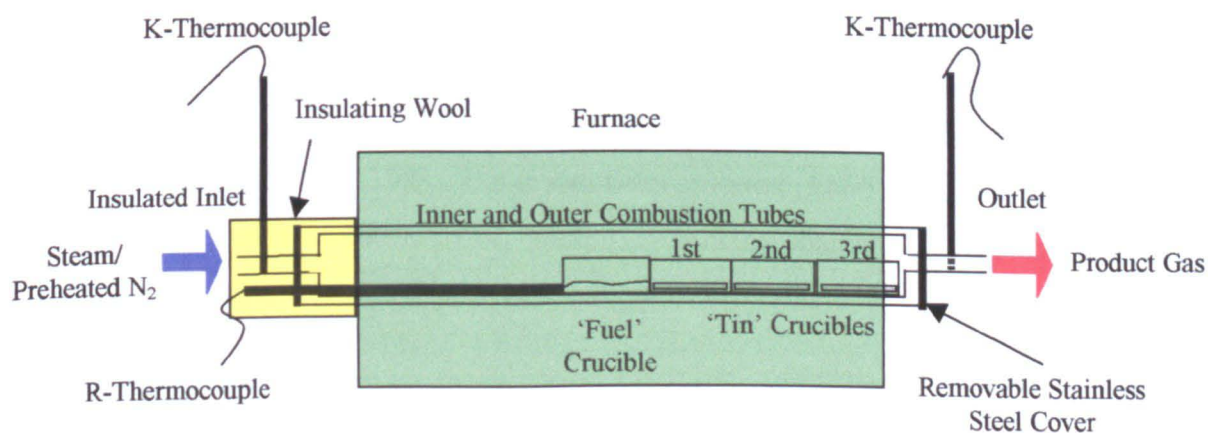
Figure 5.3 Arrangement of crucibles for gasification in the presence of tin.

Essentially the same experimental procedure as that outlined in Section 5.1.3.1 was adopted herein. The only difference was the addition of crucibles into the gasification furnace containing tin strips, illustrated in Figure 5.3. Three additional ceramic crucibles (86 mm × 13 mm × 8 mm)

containing high-purity (99.95%) tin strips were placed downstream of the fuel sample. Each 'tin' crucible held four tin strips of about 8 mm length each. All the crucibles plus their contents were weighed before and after each test run. For the latter, the crucibles were left to cool to room temperature in a nitrogen atmosphere before weighed.

5.2   Cold Gas Scrubber Studies

A room-temperature non-wetting packed bed system was used to simulate the workings of the liquid metal irrigated hot gas scrubber. The concept of using a similar low-temperature system as an analogue of a high-temperature model is not unprecedented, having been employed by Gardner (1956) and Warner (1959b). The former used a system of water flowing over silicon-treated coke packing to model a high-temperature slag-coke system whilst the latter used water irrigation of paraffin waxed Raschig rings to simulate molten lead flow on the same packing.

5.2.1   Design of Main Scrubber Unit

❑ *Column*

The cold gas scrubber consists of a column shell that is made of Perspex and is transparent, allowing visual observation of flow on the packed bed. The column has an internal diameter of 7.8 cm with a packed bed depth of approximately 19 cm. The model cold gas scrubber is to function as a room-temperature analogy for the molten tin irrigated hot gas scrubber and both are to have the same column size. An initial plan to fit the hot scrubber within a furnace of 38.0 cm depth, 17.8 cm length, and 15.2 cm width has limited its size, and consequently the size of the Perspex column of the cold scrubber as well.

It was ensured that the column diameter was at least about 8 times the size of the packing used. Channelling is minimised when the column diameter conforms to the above criteria (Jesser and Elgin, 1943; McCabe *et al.,* 1993). It has also been reported (Lobo *et al.,* 1945) that the packing factor S_B/ε^3 decreases as the ratio of column to packing diameter falls below 6. Hence the packing factor can be considered to be constant above this ratio.

❑ *Packing*

Due to their high surface free energies, liquid metals generally exhibit non-wetting type of flow on solid surfaces (Zisman, 1964). This non-wetting flow behaviour is to be simulated at room conditions during the cold tests. The room temperature system would be irrigated by water for convenience. The selected solid packing material has to be hydrophobic i.e. water-repelling to set up an analogous non-wetting room temperature system. This means that the contact angle of

water on the selected solid material has to be greater than 90°. The surface tension of water at room conditions is 73 dynes/cm. Hence low surface energy solid packings have to be selected such that the critical surface tension σ_c of the solid packings is smaller than 73 dynes/cm such that water will not wet the solid surface. Two types of packing were eventually chosen for the room temperature model scrubber. These are spherical polyethylene beads as well as glass beads coated with paraffin wax. The critical surface tension of solid polyethylene is 31 dynes/cm (Osipow, 1962; Zisman, 1964; Clayfield *et al.*, 1985), well below the surface tension of water. Glass on the other hand is a high surface energy solid, the critical surface tension has been documented to be 170 dynes/cm (Lyman *et al.*, 1965). The contact angle of water on glass is small (Adamson and Gast, 1997), having been reported to be 14° (O'Brien, 1996). Therefore the surface energy of the glass spheres is reduced by treating them with a coat of paraffin wax. Paraffin has a critical surface tension of 22 to 26 dynes/cm (Lyman *et al.*, 1965), well below the surface tension of water. The contact angle of water on paraffin wax surface is 109° (Craig *et al.*, 1960) while the average contact angle of water on polyethylene surface is 95° (Adamson and Gast, 1997). Since the contact angle for both systems are greater than 90°, water is confirmed not to wet these two types of solid packings. The internal wall of the Perspex column is also waxed to prevent preferential wetting of the column walls.

9.53 mm (3/8") solid high density polyethylene beads and 10 mm (+/-0.5 mm) soda lime glass beads treated with paraffin wax were used as packing materials. The polyethylene beads were supplied by The Precision Plastic Ball Co. Ltd. while the soda lime glass beads were supplied by Sigmund-Lindner.

Table 5.3   Characteristics of packings used.

Packing	Polyethylene beads	Glass beads coated with paraffin wax
Diameter d (mm)	9.53	10.0*
Column to packing diameter ratio (m/m)	8.2	7.8
Packing element specific surface area $S = 6/d$ (m^2/m^3)	630	600
Packed bed porosity ε (m^3/m^3)	0.45	0.45
Packed bed specific surface area $S_B = S(1-\varepsilon)$ (m^2/m^3)	346	330
Packing specific gravity (dimensionless)	0.96	2.5
Packing material critical surface tension** σ_c (dyne/cm)	31	22-26
Water-packing material contact angle** θ (degrees)	95	109

* Diameter of uncoated glass beads.
** Extracted from sources outlined in the preceding paragraph.

The porosity of the waxed glass beads was determined by measuring the weight of water that fully filled the void in the bed, ensuring that the bottom of the bed was fully sealed. The volume of water occupying the void between the spheres was calculated from the density of water at room conditions. The total volume of the packed bed was calculated from the height of the

packed bed and the column diameter. The height of the packed bed was measured from the base of the bed up to the height of a flat plate placed level at the top of the bed. The ratio of volume of water used to the total volume of the packed bed gave the porosity of the bed.

Since the polyethylene beads were less dense than water, it was not possible to use the above method to determine the porosity of the packed bed. Instead, the total number of polyethylene beads used was calculated to determine the total volume taken up by the solid packings. The fraction of space occupied by the beads was calculated and the remaining was the porosity of the bed. This method was not used for the waxed glass beads because the size of each bead would have been slightly different due to the wax coating.

□ *Packing Support Plate*

The packed bed is supported on a sieve-type of packing support plate. The support plate is made simply from a 9.0 cm diameter circular stainless steel flat plate with evenly-spaced 5 mm perforations, sufficiently small such that the packing elements would not fall through. The plate is held in place between the flanges of the column and the bottom reservoir. The total fractional free area of the packing support plate is about 0.50, larger than the porosity of the packed bed which is 0.45. This satisfies the condition that the packing support plate must have a free area that is as large as, or larger than that of the packing to avoid premature flooding (Fadel, 1984; Fair *et al.*, 1997). Also, the support plate is sufficiently strong to withstand the weight of the glass packing (about 2.5 times heavier than the polyethylene packing) without sagging.

□ *Liquid Distributor*

A simple orifice type of liquid distributor is used, as preferred for small-diameter columns (Chen, 1984). The liquid distributor is constructed from Perspex and is held in place between the flanges of the top lid and the column. The orifice type liquid distributor provides separate paths for gas and liquid flows. The gas flows up through risers whilst the liquid flows down through orifices on the distributor floor.

The design of the orifice type liquid distributor is governed by 2 important criteria (Fadel, 1984):

1. The riser height must be higher than the liquid head h_L corresponding to maximum liquid rate. The risers must be high enough to prevent overflowing of liquid into the risers at high liquid rates to prevent liquid maldistribution at the top of the bed.

2. Also, the liquid head h_L at minimum liquid rate must be higher than the gas pressure drop through the riser ΔP, ensuring against local flooding at the distributor which will eventually

lead to flooding of the whole packed bed. This means that the orifices are sufficiently covered by a liquid layer even at low liquid rates to prevent gas flow through them.

Fadel (1984) gave the following equations to calculate the liquid head above the orifice h_L and gas pressure drop through the riser ΔP:

$$h_L = \left(\frac{Q_L}{19.65 N_o C_o d_o^2}\right)^2 \tag{5.4}$$

where h_L = liquid head (ft)

$\quad\quad\quad Q_L$ = liquid rate (gal/min)

$\quad\quad\quad N_o$ = number of orifices

$\quad\quad\quad d_o$ = orifice diameter (inch)

$\quad\quad\quad C_o$ = orifice coefficient, typically 0.61

The gas pressure drop through the riser is the summation of entrance (sudden contraction) losses, wall frictional losses in the straight section of the riser (considered negligible), and exit (sudden expansion) losses. The gas pressure drop is calculated as:

$$\Delta P = 0.000108 \rho_G u_G^2 (K_c + K_e) \tag{5.5}$$

where ΔP = gas pressure drop (psi)

$\quad\quad\quad \rho_G$ = gas density (lb/ft^3)

$\quad\quad\quad u_G$ = gas velocity through riser (ft/s)

$\quad\quad\quad K_c$ = sudden contraction loss coefficient = 0.5

$\quad\quad\quad K_e$ = sudden expansion loss coefficient = 1.0

According to Chen (1984), the riser area should range from 15 to 45% of column cross-sectional area. Chen (1984) gave the following equations to determine the liquid head above the orifice h_L (ft. of liquid) and the gas pressure drop through the riser ΔP (in. of liquid):

$$h_L = \left(\frac{Q_L}{18.90 N_o C_D d_o^2}\right)^2 \tag{5.6}$$

$$\Delta P = 0.46 \frac{\rho_G}{\rho_L} u_G^2 \tag{5.7}$$

where Q_L = liquid rate (gal/min)

$\quad\quad\quad N_o$ = number of orifices

$\quad\quad\quad C_D$ = discharge coefficient, for punched holes is 0.707

$\quad\quad\quad d_o$ = orifice diameter (inch)

$\quad\quad\quad \rho_G, \rho_G$ = gas and liquid densities respectively (lb/ft^3)

$\quad\quad\quad u_G$ = gas velocity through riser (ft/s)

Details of the liquid distributor of suitable geometry are as follows. Using equations 5.4 to 5.7, the liquid distributor was checked to conform to the aforementioned design conditions as demonstrated in Table 5.4.

- Riser : Total = 6; Height = 2.0 cm; Internal diameter = 1.5 cm;
  Total flow area = 22% of column cross-sectional area
- Orifice : Total = 6; Diameter = 0.6 cm

Table 5.4 Checking liquid distributor geometry against design criteria.

1. Riser height (2.0 cm) must be higher than liquid head h_L:
Worst case scenario: Maximum h_L i.e. highest operating liquid rate:
Highest operating water rate = 3.0 litre/min = 10.48 kg/m^{2}s
Corresponding h_L from equation 5.4 (Fadel, 1984) = 11.89 mm of water Corresponding h_L from equation 5.6 (Chen, 1984) = 9.56 mm of water
∴ In both equations by Fadel and Chen respectively, h_L < riser height (20 mm).
2. Liquid head h_L must be higher than gas pressure drop through riser ΔP:
Worst case scenario: Smallest h_L i.e. smallest operating liquid rate and highest ΔP i.e. highest operating gas rate:
Smallest operating water rate = 1.0 litre/min = 3.49 kg/m^{2}s Highest operating air rate   = 165 litre/min = 0.71 kg/m^{2}s
Corresponding h_L from equation 5.4 (Fadel, 1984) = 1.32 mm of water
Corresponding ΔP from equation 5.5 (Fadel, 1984) = 0.63 mm of water
Corresponding h_L from equation 5.6 (Chen, 1984) = 1.06 mm of water
Corresponding ΔP from equation 5.7 (Chen, 1984) = 1.04 mm of water
∴ In both sets of equations by Fadel and Chen respectively, h_L > ΔP.

Note: All fluid physical properties taken at 15°C.

☐ *Loading of packing into column*

The same method was employed each time to load the packing into the column. The packing spheres were first placed into a container and with the column top lid removed, the packing was poured into the empty column. This is to minimise changes to the packed bed voidage as it has been found that different methods of loading the packing pieces into a packed bed affect the resulting bed density and voidage, hence the packing factor S_B/ε^3 (Lobo *et al.*, 1945).

□ *__Air Injector__*

Air enters the column via an air injector which is made from a 1.25 mm brass pipe with 4 ports distributed at its side at one end, and the end sealed to prevent liquid from falling through the pipe. The air was supplied by a compressor and was controlled by a pressure regulator.
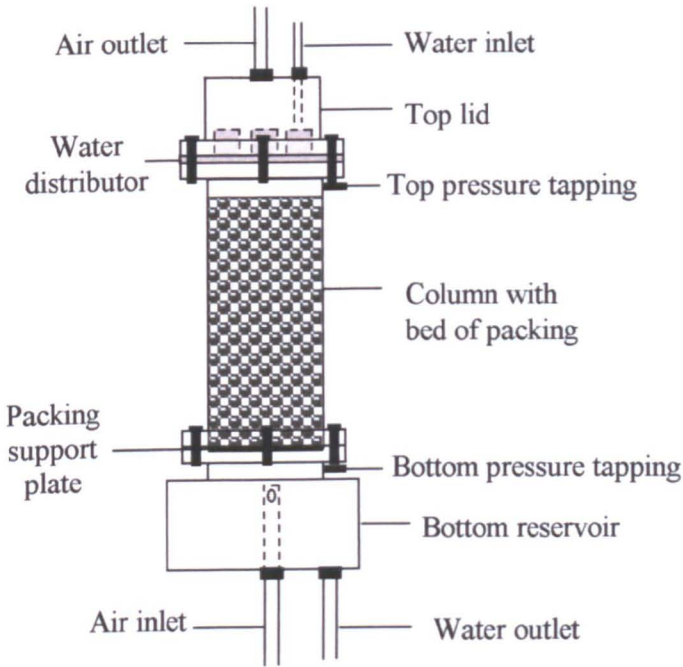
Figure 5.4 Main scrubber unit.
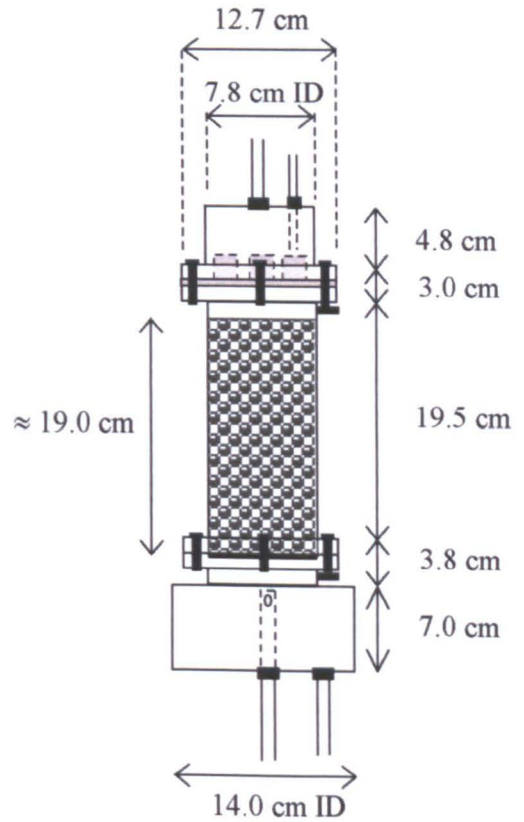
Figure 5.5 Dimensions of main scrubber unit.

Plate 5.2 Sieve-type packing
support plate positioned
at column base.
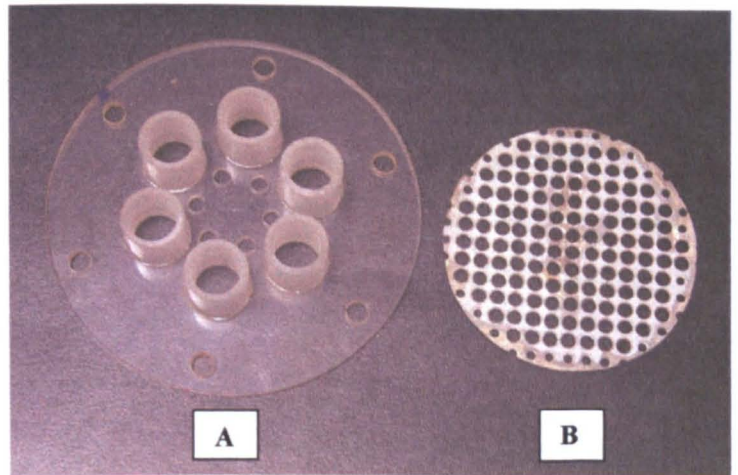
Plate 5.3 A: Orifice-type liquid distributor.
B: Sieve-type packing support plate.
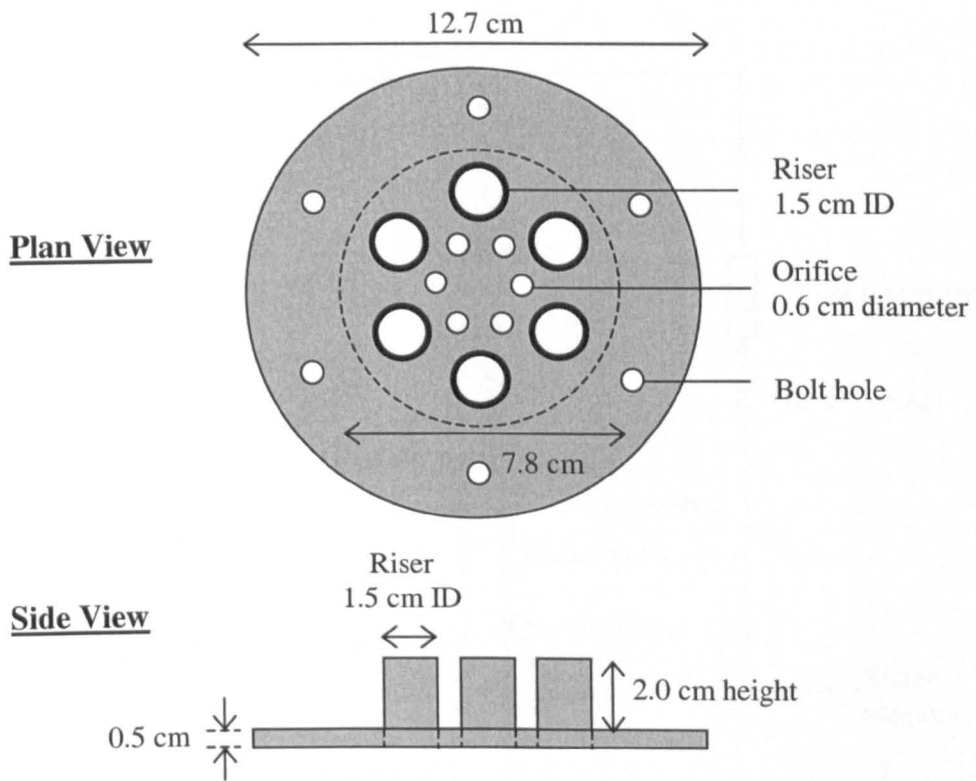
Figure 5.6 Orifice type liquid distributor and its dimensions.

5.2.2 Flow Visualisation

The observation of water flow over polyethylene beads and paraffin-waxed glass beads was carried out, complemented by high speed digital imaging using a Redlake MotionScope PCI Series monochrome camera (Model PCI 8000 S) manufactured by Redlake MASD, Inc. The camera was used to capture high-speed digital images directly to a computer for the motion analysis of droplets and rivulets on the packing surfaces.

The MotionScope camera requires a high illumination for high-speed operation. Hence, a halogen lamp was used to provide sufficient lighting for the camera. A satisfactory image was obtained by adjusting the lens aperture that controlled the degree of illumination through the camera as well as adjusting the horizontal distance of the camera (set on a tripod) from the packed column. All video images were captured using a 75 mm focus lens at a record rate of 50 frames/second and a shutter speed of 1×(1/50 seconds). Due to the memory limitation of the camera, the maximum number of frames recordable per video file was 512 frames in a total recording time of 10.24 seconds. The images obtained have a resolution of 480×420 pixels.

5.2.3 Flooding

❑ *Experimental Setup*
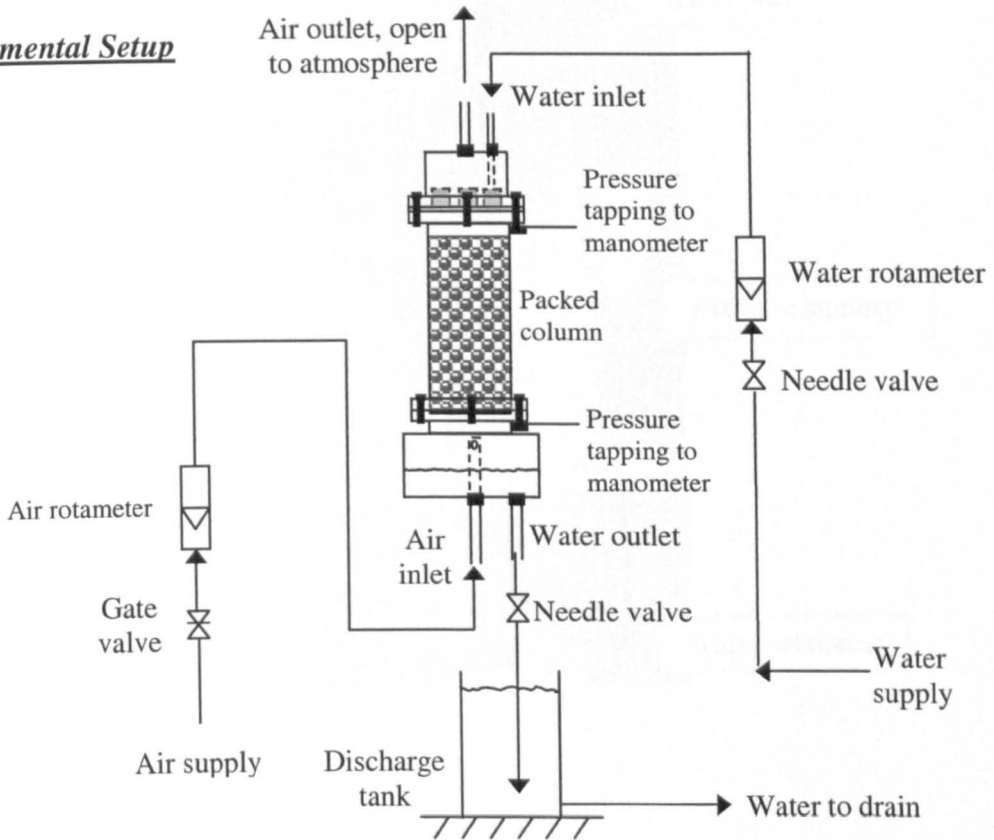
Figure 5.7 Experimental setup for flooding tests.

Compressed air was fed to the bottom of the column, its flowrate controlled by a gate valve. Water from the mains was supplied to the top of the column, its flowrate controlled by a needle valve. Both the air and water flowrates were determined using rotameters. The outlet air was vented to the atmosphere at the top of the column. At the bottom of the column, the water was discharged into a tank. The water outlet tubing was submerged sufficiently low below the tank's water surface. This was to maintain a sufficient hydrostatic head to prevent air bubbles escaping with the water through the outlet tubing. In addition, a needle valve at the water exit provides the means to maintain a water level in the column reservoir to prevent the escape of air through the water outlet. The pressure drop across the column was measured using an inclined manometer.

Table 5.5 Instrument specifications for flooding tests.

Instrument	Specifications
Air rotameter	By KDG Mobrey Ltd. Range 20-200 litre/min @ 15°C, 1.013 bar abs. Smallest graduation 5 litre/min.
Water rotameter	By MFG Co. Ltd. Range 0.5-5 litre/min @ 20°C. Smallest graduation 0.1 cm. Flowrate obtained from calibration chart with average gradient 5.8 cm/1.0 litre/min.
Manometer	By Airflow Development Ltd. Smallest graduation 0.1 cm H_2O. Tube position: Vertical Range: 0-50 cm H_2O Tube position: Top inclined Range: 0-10 cm H_2O Tube position: Bottom inclined Range: 0-5 cm H_2O
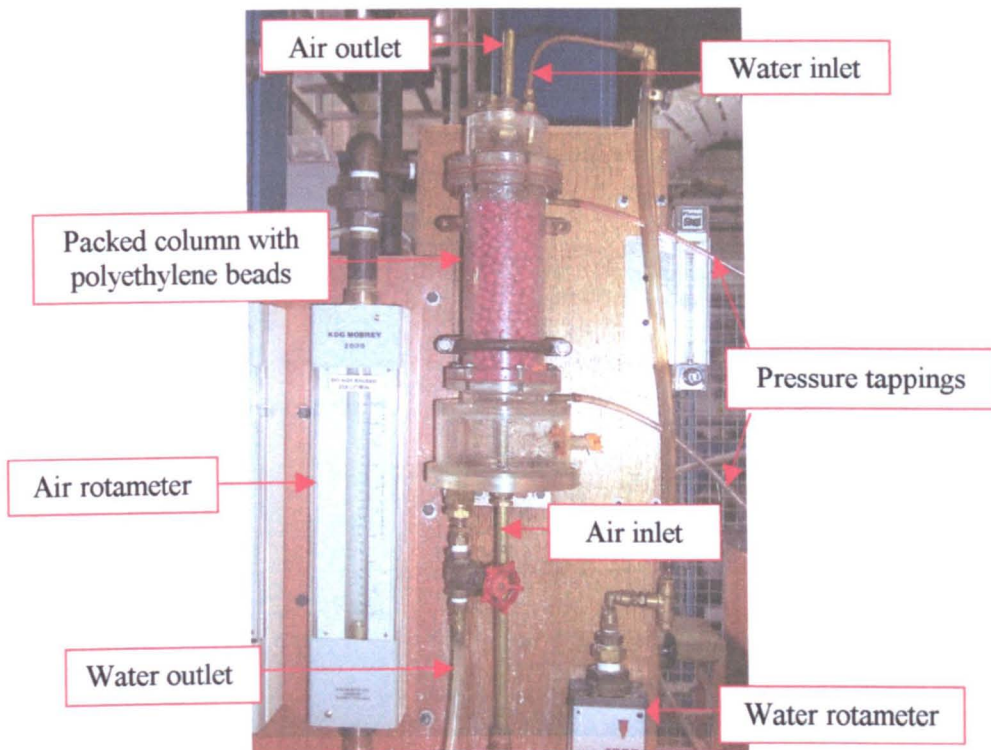
Plate 5.4 *Experimental setup for flooding tests.*

□ *Experimental Procedure*

- Air was passed through the packed bed starting at a low flowrate of 20 or 25 litre/min, the flowrate being controlled using the gate valve. The water flowrate was set to the desired value by adjusting the needle valve that controlled the water supply to the top of the column. The needle valve at the water exit was adjusted such that a water level of about 2 cm was maintained in the bottom reservoir to prevent air escaping through the water outlet.

- 4 to 6 minutes were allowed for the fluid flows through the column to stabilise. A steady state was assured by a constant pressure drop reading across the column. Once this was achieved, the pressure drop across the column was read off the inclined manometer.

- While maintaining a constant water flowrate, the air flowrate was increased in a stepwise manner until flooding was achieved, the pressure drops being noted for each air flowrate after the flow has stabilised and steady state has been achieved as indicated by a constant pressure drop reading. Flooding was determined visually from the following two indicators: Accumulation of water throughout the whole packed bed including the top section of the bed; and wild fluctuations in pressure drop reading as flooding sets in.

- The above procedure was repeated for other water flowrate settings.

5.2.4 Liquid Holdup

❑ *Experimental Setup*
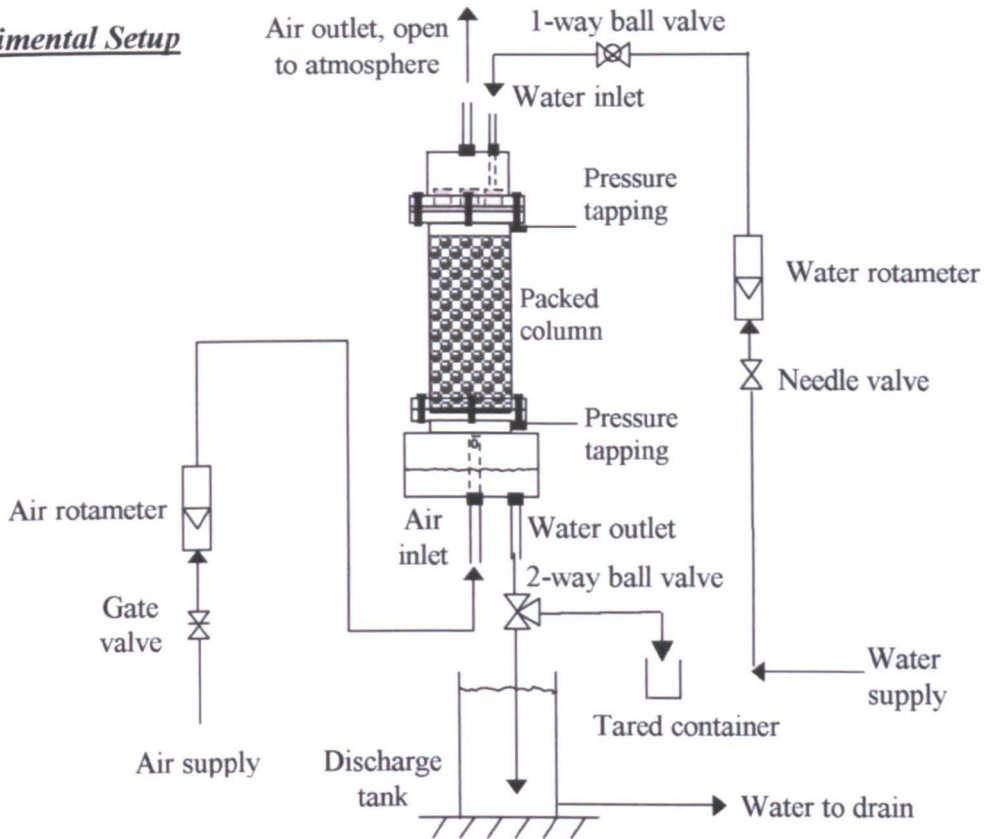
Figure 5.8 Experimental setup for liquid holdup tests.

Plate 5.5 Experimental setup for liquid holdup tests.
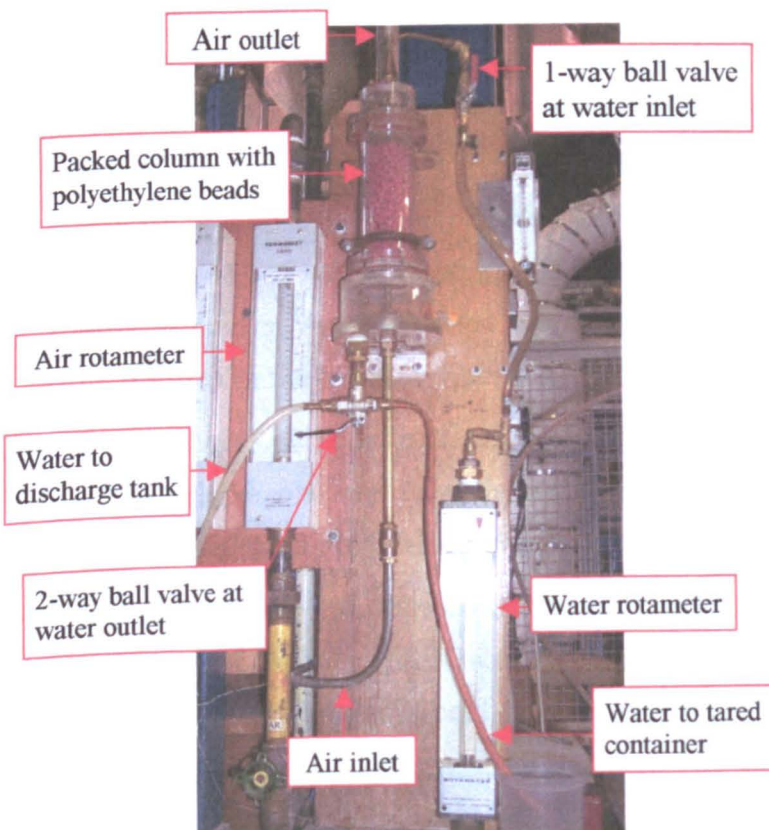
The experimental setup for the liquid holdup tests was essentially the same as that for the flooding tests with the exception of fast-acting ball valves at the water inlet and water outlet. The additional water outlet line from the 2-way ball valve led to a tared container for water collection.

Table 5.6 Instrument specifications for liquid holdup tests.

Instrument	Specifications
Air rotameter	Same as in flooding tests.
Water rotameter	Same as in flooding tests.
Manometer	Same as in flooding tests.
Weighing balance	Model Precisa 2200c by Swiss Quality. Sensitivity 0.01g
Digital stop clock	Model TMZO by A.T.P. Sensitivity 0.01 s.

□ ***Experimental Procedure***

Dynamic Holdup Measurement

- With the packing in place, the 1-way ball valve at the water inlet to the column was opened fully. The 2-way ball valve was opened such that full flow was directed into the discharge tank.

- The water supply was turned on at the desired rate. Air was passed through the packed bed at a low flowrate of 40 litre/min.

- 4 to 6 minutes were allowed for the flow to stabilise as indicated by a constant column pressure drop (from the inclined manometer reading). Once a steady-state was achieved, the 1-way ball valve was closed fully and swiftly and the 2-way ball valve turned towards full flow

Plate 5.6 Experimental setup to determine 'end effects' of dynamic holdup measurements.

into the tared container simultaneously. Both the water and air supplies were switched off.

- The packed bed was allowed to drain for about 5 minutes with the water collected into the tared container. An earlier trial run showed that beyond this amount of time, further water drainage from the bed was negligible.

- The collected water in the tared container was weighed. This is the 'gross' dynamic holdup of the column which included the water held-up in the water distributor above the packed bed as well as in the bottom reservoir below the packed bed.

- The above steps were repeated at the same water flowrate, but at higher air flowrates till just before the flooding point. Once this was completed, the procedure was again repeated to obtain the 'gross' dynamic hold-ups for other water flowrate settings.

- The whole procedure was then repeated but this time without the packing and with only the top water distributor and bottom reservoir sections put together omitting the middle column section and the packing support plate as shown in Plate 5.6. This was to determine the

portion of 'gross' dynamic holdup contributed by the water held up in the water distributor and the bottom reservoir. This figure was deducted from the earlier determined 'gross' dynamic holdup to give the actual dynamic holdup in the packed bed.

Static Holdup Measurement

- The dry spherical beads were weighed prior to being loaded into the Perspex column. The top lid and water distributor were put into place and the connecting flanges of the column and top lid sealed. The 1-way ball valve at the water inlet to the column was opened fully. The 2-way ball valve was opened such that full flow was directed into the discharge tank.

- The water supply was turned on at the desired rate. Air was passed through the packed bed at a low flowrate of 40 litre/min.

- 4 to 6 minutes were allowed for fluid flows through the column to stabilise as indicated by a constant pressure drop across the column (from inclined manometer reading). Once a steady-state was achieved, the 1-way ball valve was closed fully and swiftly, cutting off the water supply to the column. Both the water and air supplies were switched off.

- The packed bed was allowed to drain for about 5 minutes. An earlier trial run showed that beyond this amount of time, further water drainage from the bed was negligible.

- A dry container holding several precision wipes were placed on the weighing balance and the reading tared. The wipes were then removed from the container.

- The top lid of the column and the water distributor were removed.

- The wet spherical beads were poured into the empty container. The wet walls of the column were wiped dry with the precision wipes which were then added into the container holding the wet beads. The container with its contents was weighed. This reading minus the initial mass of the dry beads gave the static hold-up.

- The above procedure was repeated whilst maintaining the same water flowrate, but each time at higher air flowrates till just before the flooding point. Once this was completed, the procedure was again repeated to obtain the static hold-ups for other water flowrate settings.

5.2.5   Gas Lift

❑ *Experimental Setup*

The air lift was constructed from semi-rigid low density polyethylene (LDPE) tubing. Where bends were required, brass pipe fittings were used. The air lift tubing was taped to a metal back support, ensuring that it was vertically straight. The water overflow from the bottom reservoir and the continuous supply of water provided an approximately constant water level in the

reservoir (i.e. the level of the overflow). This was important to maintain constant submergence and lift heights in the air lift throughout each test run.
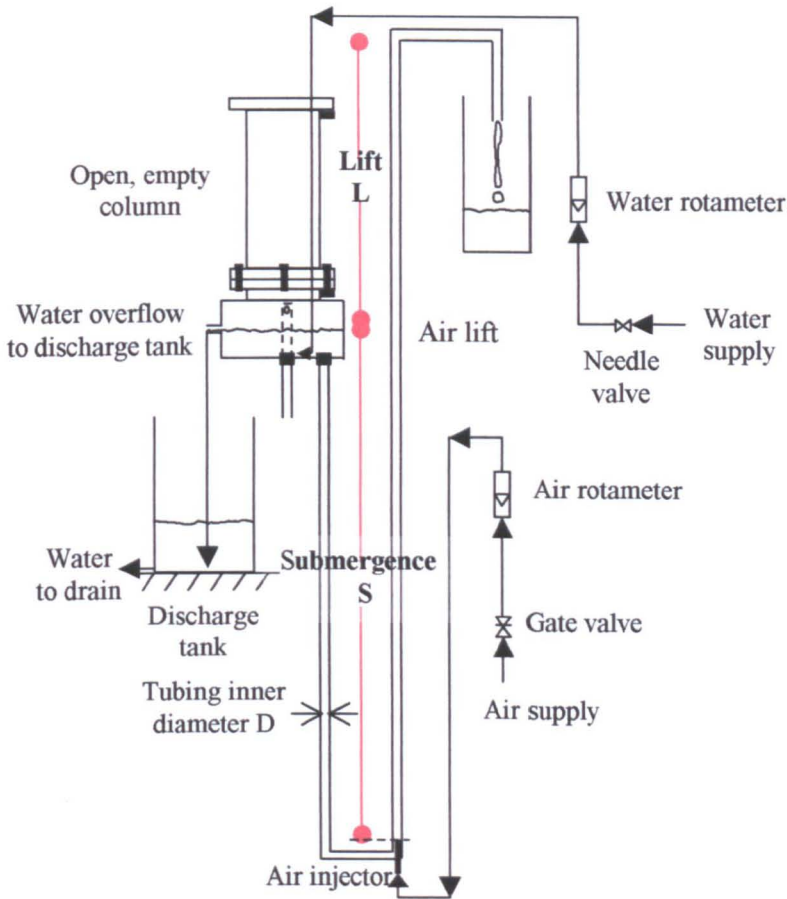
Figure 5.9 *Experimental setup for air lift tests.*

Table 5.7 *Air lift geometry.*

Test	Riser inner diameter D (cm)	Submergence S (cm)	Lift L (cm)	Submergence ratio $S_R = S/(S+L)$
Test 1	1.59	80	33	0.71
Test 2	1.59	65	45	0.59

Table 5.8 *Air injectors used.*

Injector	No. of air ports	Size of each port (mm)	Cross-sectional area of each port (mm²)	Total cross-sectional area for air flow on injector (mm²)
Longitudinal	1	5.00	19.63	19.63
4-Port Radial	4	2.54	5.07	20.27
12-Port Radial	12	2.54	5.07	60.80

Each injector was constructed from a 5 mm inner diameter brass pipe.

Table 5.9 *Instrument specifications for air lift tests.*

Instrument	Specifications
Air rotameter	By Platon. Range 1-10 litre/min. Smallest graduation 0.5 litre/min @ 20°C, 1.013 bar abs.
Water rotameter	Same as in flooding tests.
Weighing balance	Model Precisa 2200c by Swiss Quality. Sensitivity 0.01 g.
Digital stop clock	Model TMZO by A.T.P. Sensitivity 0.01 s.
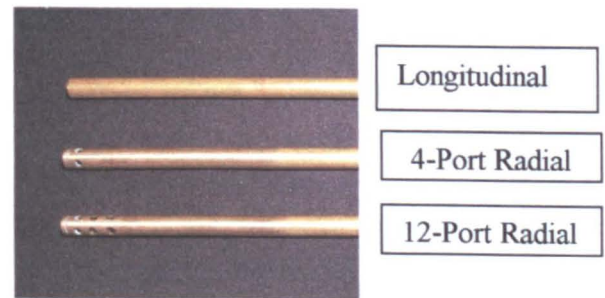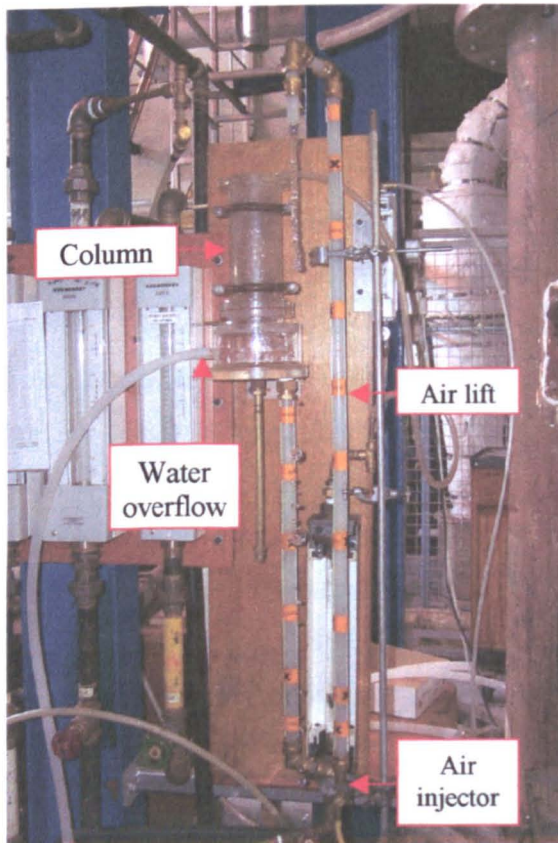
Plate 5.7 Air injectors.

Plate 5.8 Experimental setup for air lift tests.

□ **Experimental Procedure**

• The water supply was turned on, allowing water to flow into the air lift legs via the column reservoir. The air lift was filled until the water in the reservoir reached the overflow level and exited to the discharge tank. The water rate was then adjusted to maintain a constant level in the reservoir i.e. at the overflow level. This ensured constant submergence and lift heights.

• The air supply to the air injector was turned on to the lowest flow rate at 0.5 litre/min. With the air lift in operation, the water rate was adjusted via the needle valve such that the water level in the reservoir was approximately constant at the overflow level.

• Once a steady-state was achieved, a tared 2 litre container was put in place to collect the water discharging at the top of the air lift riser. Timing was started simultaneously.

• The container was removed and the time noted once sufficient water was collected. The air

supply was turned off and the amount of water collected was weighed.

- One or two additional readings were obtained at the same air flowrate.

- The whole procedure was then repeated with increasing air flowrate, each time with an increment of 0.5 litre/min.

5.2.6 Particulate Removal

5.2.6.1 Particle Size Analysis

Laboratory-prepared fine glass powder supplied by Aldrich Chemical Co. was selected to be the test dust as it is dry and free flowing, hence could be well dispersed in the air stream. In addition, the glass powder does not dissolve in nor react with water. The powder consists of hollow, spherical particles with a uniform density of 1100 kg/m^3. To ensure that the glass powder remains dry and to prevent it from clumping together, samples were dried in the dessicator before being used. Plate 5.9 shows the image of the glass beads dispersed in water, taken using a Carl Zeiss' Axiotech reflected and transmitted light microscope at 20× magnification.
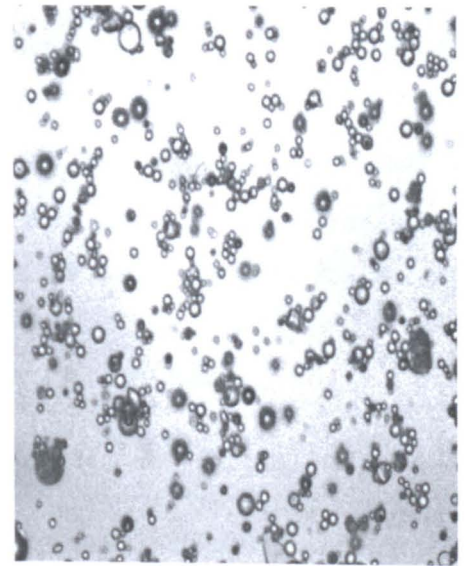
Plate 5.9 Hollow, spherical glass beads dispersed in water (20 ×magnification).

The particle size distribution of the glass powder was determined on Particle Sizing Systems' AccuSizer 780A Single Particle Optical Sizer. The instrument uses the single particle optical sensing (SPOS) technique to size individual particles. Autodilution of the sample controls the rate of particle flow that passes the single optical particle sensor to a countable rate, preventing coincidence. The optical particle sensor uses the light scattering principle for sizing of particles smaller than several microns and the light obscuration method for larger particles. Individual particles are passed through a laser beam and either the scattering intensity or the amount of light blocked by each particle is measured and transmitted into an electrical pulse. For the former, the scattered intensity pulse height corresponds to the particle diameter. For the latter, the amount of light blocked and thus the height of the pulse corresponds to the particle's cross sectional area i.e. the square of the particle diameter. Size distributions are generated from the measurement of thousands of particles. High-resolution particle size analysis is achieved from individual particle sizing. The AccuSizer uses the laser sensor model LE400-0.5SUM having a detectable particle size range from 0.5 to 490 µm. The AccuSizer is controlled via the windows-based CW770 software program.

❑ *Procedure*

- To ensure a representative sampling of the glass powder from its containing bottle, the bottle was gently rolled changing its orientation continuously such that large and fine particles were mixed thoroughly. A small amount was then taken from the bottle.

- The sample of glass powder was mixed with and dispersed in distilled water in a small container. Using a pipettor (10-100 µl), 100 µl of this sample was transferred into the AccuSizer dilution chamber containing 60 ml of ultra-filtered, distilled water as the diluent. Sampling was then initiated for 50 ml of the sample suspension at a rate of 1 ml/s. Mixing of the sample particles with the diluent was effected by means of a mechanical agitator.

- A total of 3 samplings were carried out and the average particle size distribution obtained.

- For each sampling, the total number of particles sized was checked such that the maximum limit of 9000 particles/ml (i.e. 450 000 particles for 50 ml) was not exceeded for optimum AccuSizer sampling performance. If this limit was exceeded, the sample in the small container was diluted with distilled water, and the sampling was repeated.

- Background check: To check whether the distilled water contains particles that can contribute significantly to the overall particle size distribution, the above procedure was repeated but this time without the glass powder i.e. only the distilled water was sampled.

5.2.6.2 Determination of Total Efficiency

❑ *Experimental Setup*
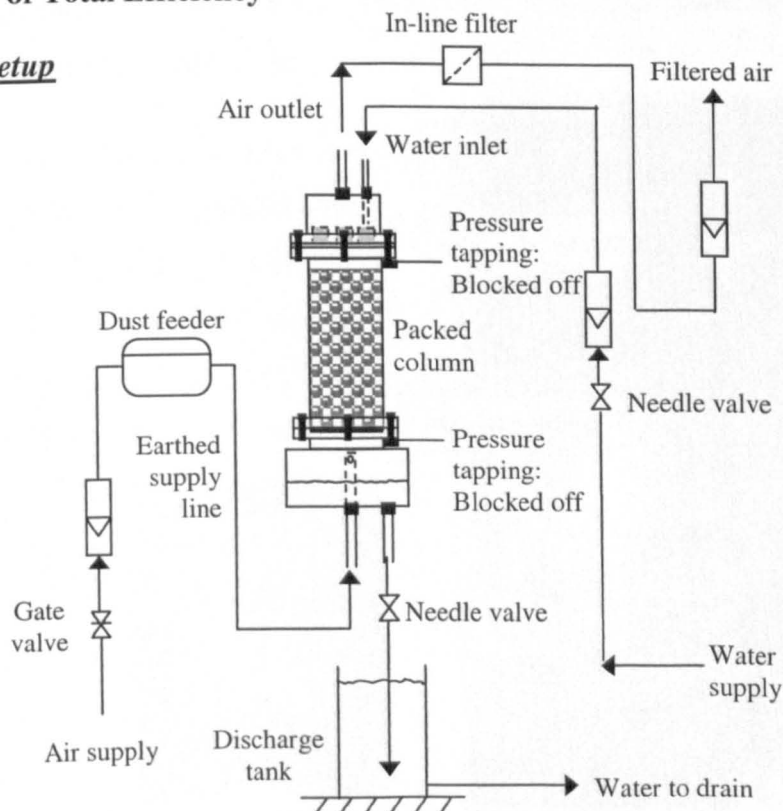
Figure 5.10 Experimental setup to determine total efficiency of particulate removal.

The glass powder was fed into the air supply line using Malvern's Qspec Dry Powder Feeder. The sample hopper vibrates, causing the dry powder sample to travel down the hopper until it eventually falls into a wire sieve filled with ball bearings and then into the main feed mechanism. The vibrating bearings smooth the sample flow as well as break up agglomerates in the sample. As the sample falls through the sieve, it is accelerated by a compressed, shearing air flow produced by a venturi which is the main dispersive mechanism. The sample feed rate is dictated by the gap between the feed gates on the sample hopper and the vibration amplitude of the sample hopper. The latter is controlled by a feed rate dial on the front panel. A jet pressure dial controls the air feed pressure that enables precise control of the dispersion.

Isokinetic sampling of the outlet air stream using a sampling probe directed into the air stream was not feasible on this small-scale scrubber due to the small flow area of the exit air line employed (about 1.5 cm internal diameter tubing). Instead the penetrating glass powder in the outlet air stream was captured using Whatman's Gamma-12 in-line filter. This filter was selected for use due to several compelling reasons: it uses disposable, resin-bound glass microfibre filter tubes that give exceptionally high particle retention and high loading capacity; also the disposable filter tubes are easily changed in seconds without the need for additional tools. The housing is made from clear polycarbonate resin, closed by a blue polycarbonate cap incorporating a fluoroelastomer O-ring seal. Filter tube grade 10 with 1.0 μm particle retention capability was selected for use.
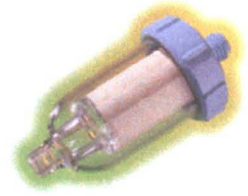
Figure 5.11 Gamma-12 in-line filter.

The outlet air stream was filtered to determine gravimetrically the mass of test dust unseparated by the packed bed scrubber. The mass of separated dust when divided by the total mass of test dust fed into the column over the period of the experiment gave the total efficiency of particulate removal.

Figure 5.12 Qspec Dry Powder Feeder.

Plate 5.10 Paper boat containing feed powder on dust feeder hopper.
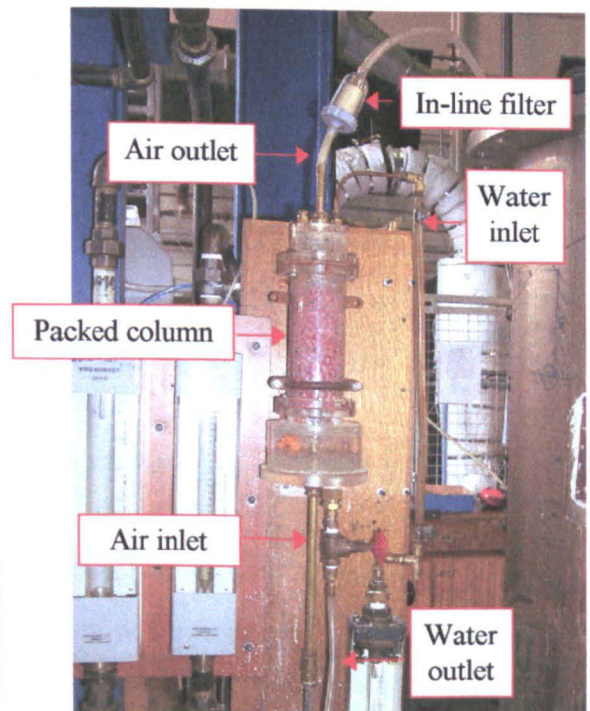
Plate 5.11 Experimental setup to determine total efficiency of particulate removal.

Table 5.10 Instrument specifications for particulate removal tests.

Instrument	Specifications
Air inlet rotameter	Same as in flooding tests.
Air outlet rotameter	By Croydon. Range 20-160 litre/min @ 15°C, 760 mm Hg abs. Smallest graduation 2 litre/min.
Water rotameter	Same as in flooding tests.
Manometer	Same as in flooding tests.
Microbalance	Model Precisa 125A by Swiss Quality. Sensitivity 0.0001 g.
Digital stop clock	Model TMZO by A.T.P. Sensitivity 0.01 s.

□ *Experimental Procedure*

- A plastic weighing container holding an unused filter tube and a cotton bud was wiped with an anti-static cloth to remove any superficial material and then weighed on a microbalance. The microbalance was positioned close to the experimental rig to minimise exposure of the materials to air-borne dust. About 10 minutes were allowed for a constant, equilibrium reading to be reached. Prior to this, the container with its contents has been dried in an oven and left to cool in a dessicator.

- The filter tube was fitted inside its housing and the whole filter unit was then connected to the column air outlet. The plastic container with the cotton bud were left in the dessicator.

- Approximately 15 g of glass powder in a paper boat was weighed on the microbalance. The reading was taken after about 2 minutes, i.e. after the reading has stabilised. Prior to its use, the glass powder was dried and kept in a dessicator. This was to ensure that it remained non-cohesive and free-flowing in order to disperse well in the powder feeder.

- The paper boat containing the glass powder was then placed into the hopper of the powder feeder. The paper boat has been sized such that it fitted snugly within the hopper.

- The air supply to the column was turned on to the desired rate (as indicated by the outlet air rotameter) followed by the water supply. The needle valve at the water exit was adjusted such that a water level about 2 cm was maintained in the bottom reservoir to prevent air escaping through the water outlet. Sufficient time was allowed for the fluid flows to stabilise. Previous pressure drop measurements have shown that a steady-state was achieved within 4 to 6 minutes.

- The dust feeder was switched on at the required feed rate. Timing was started simultaneously. After approximately 15 to 20 minutes, the dust feeder was switched off and timing was stopped simultaneously. The water and air supplies were turned off.

- The paper boat containing the remaining glass powder was removed from the hopper and weighed. The reading was taken after about 2 minutes, i.e. after the reading has stabilised.

- The filter tube was removed from its housing. The short tubing connecting the column air

outlet and the filter was knocked to displace any sticking powder into the weighing plastic container. The cotton bud was slightly wetted and was used to wipe off any visible powder on the interior of the filter housing which was in contact with the filter tube.

- The used filter tube and cotton bud were placed into the plastic weighing container. They were transported in an enclosed dessicator to an oven where they were dried at approximately 80°C for about 40 minutes. Previous control tests have confirmed that there was negligible individual weight change to the filter tube, cotton bud and the plastic container at this temperature and at this same period of time. This ensured that any change in weight was not contributed by thermal degradation of these materials, but due to the powder retained on the filter tube.

- After about 40 minutes, the plastic container with its contents was removed from the oven and cooled in the dessicator to room temperature. The container was then wiped with an anti-static cloth to remove any superficial material and then weighed on the microbalance. Again, about 10 minutes was allowed for a constant, equilibrium reading to be reached.

- After each run, the polyethylene spheres were removed from the column. The empty column and the packings were rinsed clean of solid deposits before being used for the next run.

5.2.6.3 Determination of Grade Efficiency

The test dust exiting the packed bed scrubber was collected into an impinger (Figure 5.13 and Plate 5.12) with water as the collecting medium. The particle size distribution of the resulting dust suspension was then determined. This data when used together with the total efficiency determined earlier at the same fluid flowrates and dust loading, and the inlet dust particle size distribution gave the grade efficiency.
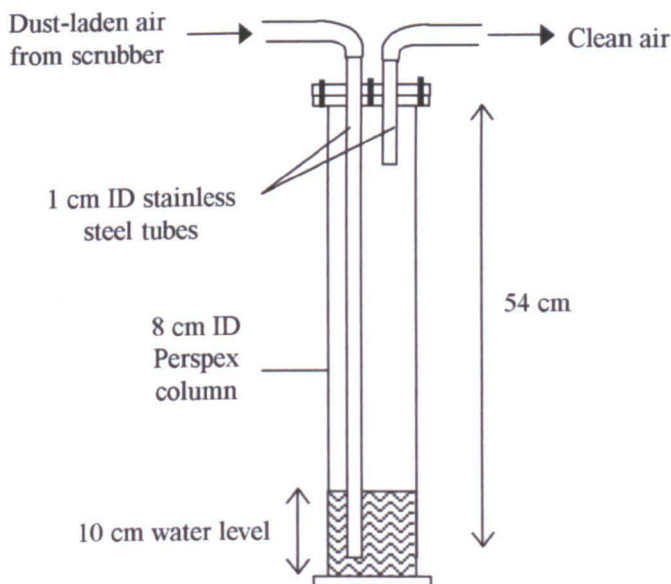
Figure 5.13 Dust impinger.

Plate 5.12 Dust impinger.

□ *Experimental Setup*
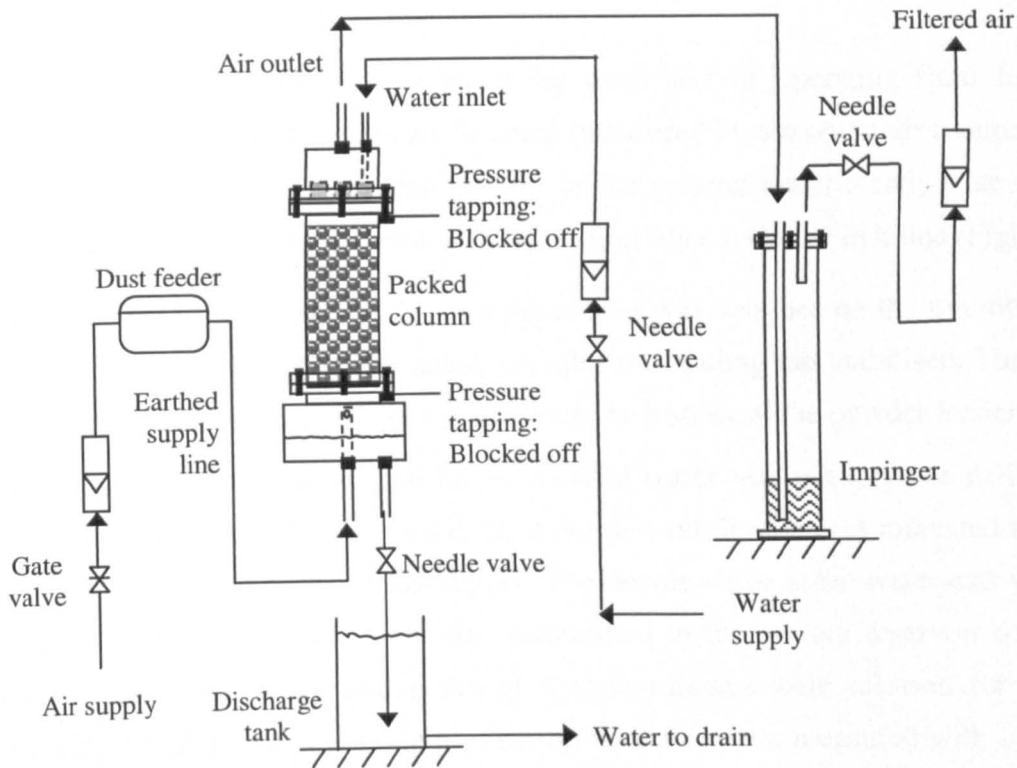
Figure 5.14 Experimental setup to collect unseparated dust particles for particle size analysis.

The experimental setup was essentially the same as that used to determine the total efficiency with the exception of the dust impinger and a needle valve in place of the in-line filter. The dust-laden air that exited the scrubber entered the impinger via an inlet pipe submerged in about 500 ml of distilled water at a level of about 10 cm. Solid particles entrained in the air stream were removed by direct impingement into water. The clean air then exited the impinger via an outlet pipe that was connected to a rotameter that measured the outlet air flowrate.

The column pressure drop affects the particulate removal efficiency. Generally as column pressure drop increases, the efficiency of dust separation increases. It was therefore essential that the column pressure drop whilst using the impinger was the same as that when the in-line filter was in use at the same operating fluid flowrates. By controlling the needle valve downstream of the impinger, it was possible to operate at the same column pressure drop with the same operating fluid flowrates as when the in-line filter was in place. This ensured that the dust collected in the impinger would be representative of the dust collected on the filter at the same operating fluid flowrates.

One impinger was found to be sufficient for full collection of the dust in the exit air stream. Tests with two impingers in series showed that there were negligible solid particles collected in the second impinger.

□ *Experimental Procedure*

Dust collection into the impinger:

The dust exiting the scrubber was collected for three sets of operating fluid flowrates: 53 litre/min, 61 litre/min and 85 litre/min air flowrate (measured by the outlet air rotameter); and all at 2 litre/min water flowrate. The pressure drop of the column under steady-state operation at these fluid flowrates were first measured with the in-line filter at the air exit line (Figure 5.10).

- Approximately 15 g of glass powder in a paper boat was weighed on the microbalance. The reading was taken after about 2 minutes, i.e. after the reading has stabilised. The paper boat containing the glass powder was then placed into the hopper of the powder feeder.

- The impinger containing about 500 ml of distilled water was put in place as illustrated in Figure 5.14. The air supply was turned on at the desired flowrate (as indicated by the outlet air rotameter) followed by the water supply. The needle valve at the water exit was adjusted such that a water level about 2 cm was maintained in the bottom reservoir to prevent air escaping through the water outlet. About 4 to 6 minutes were allowed for steady-state condition to be achieved. The column pressure drop was then measured with a manometer. The needle valve downstream of the impinger was adjusted until the same column pressure drop was obtained as when the in-line filter was used at the same fluid flowrates. Once this was achieved, the pressure tappings were blocked off.

- The dust feeder was switched on at the required feed rate. Timing was started simultaneously.

- After approximately 15 to 20 minutes, the dust feeder was switched off and timing was stopped simultaneously. The water and air supplies were turned off.

- The paper boat containing the remaining glass powder was removed from the hopper and weighed. The reading was taken after about 2 minutes, i.e. after the reading has stabilised.

- The impinger containing the dust suspension was removed for particle size distribution analysis of the suspension.

- The impinger, column and packing spheres were cleaned off solid deposits before being used for the next run.

Particle size analysis of collected dust suspension:

- The dust suspension in the impinger was transferred into a 500 ml beaker. The content of the beaker was magnetically stirred (Magnetic Stirrer SM5 by Stuart Scientific) to ensure uniform mixing of the solid particles in the water. While being stirred, a small amount of

sample was drawn off using a pipette into a small container. Then, using a pipettor (10-100 μl), 100 μl of the sample was transferred into the AccuSizer dilution chamber containing 60 ml of ultra-filtered, distilled water as the diluent. Sampling was then initiated for 50 ml of the sample suspension at a rate of 1 ml/s. Mixing of the sample particles with the diluent was effected by means of a mechanical agitator.

- For each sampling, the total number of particles sized was checked such that the maximum limit of 9000 particles/ml (i.e. 450 000 particles for 50 ml) was not exceeded for optimum AccuSizer sampling performance. If this limit was exceeded, the sample in the small container was diluted with distilled water, and the sampling was repeated.
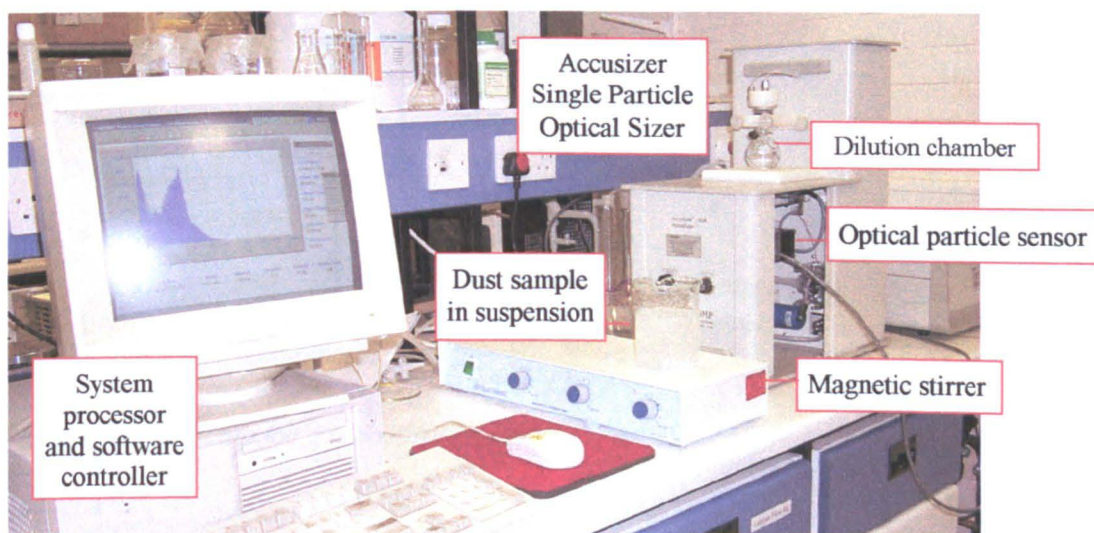
Plate 5.13 *Particle sizing system.*

5.2.7 Gas Absorption

❏ *Experimental Setup*

Ammonia from a gas cylinder was mixed with air to provide an inlet gas concentration of 950 ppm NH_3 into the column. As the gas mixture rose through the column, ammonia was absorbed into the counter-current flow of water. The gas concentration at the top of the packed bed was measured by an ammonia gas analyser via a stainless steel sampling tube positioned with its open end slightly above the packed bed. The gas that exited the top of the column was directed into a gas extractor. The provision of a 2-way valve at the water outlet enabled the collection of water samples to be analysed for dissolved ammonia content. The gas absorption test was conducted on two different packed bed heights to determine end effects. At all occasions, the open end of the gas sampling tube was positioned slightly above the top surface of the packed bed.
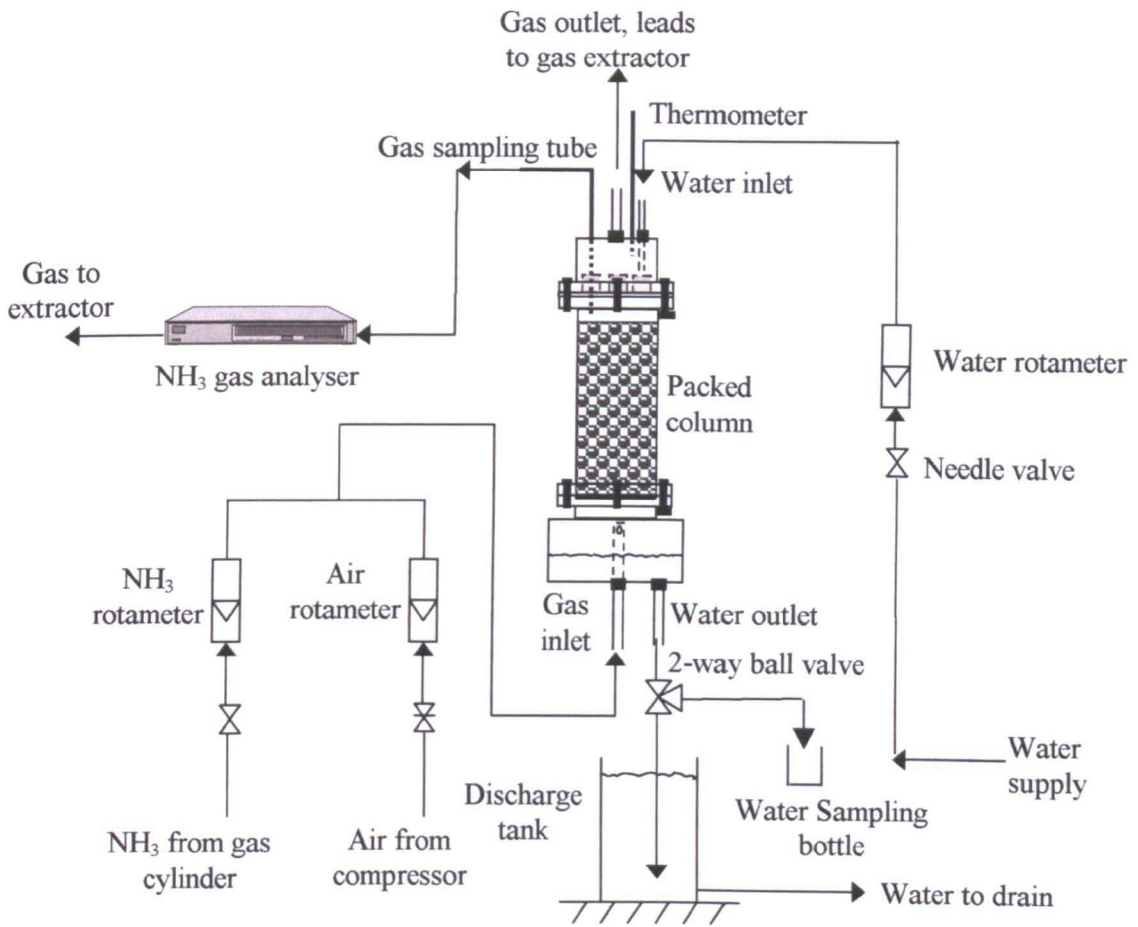
Figure 5.15 Experimental setup for gas absorption tests.
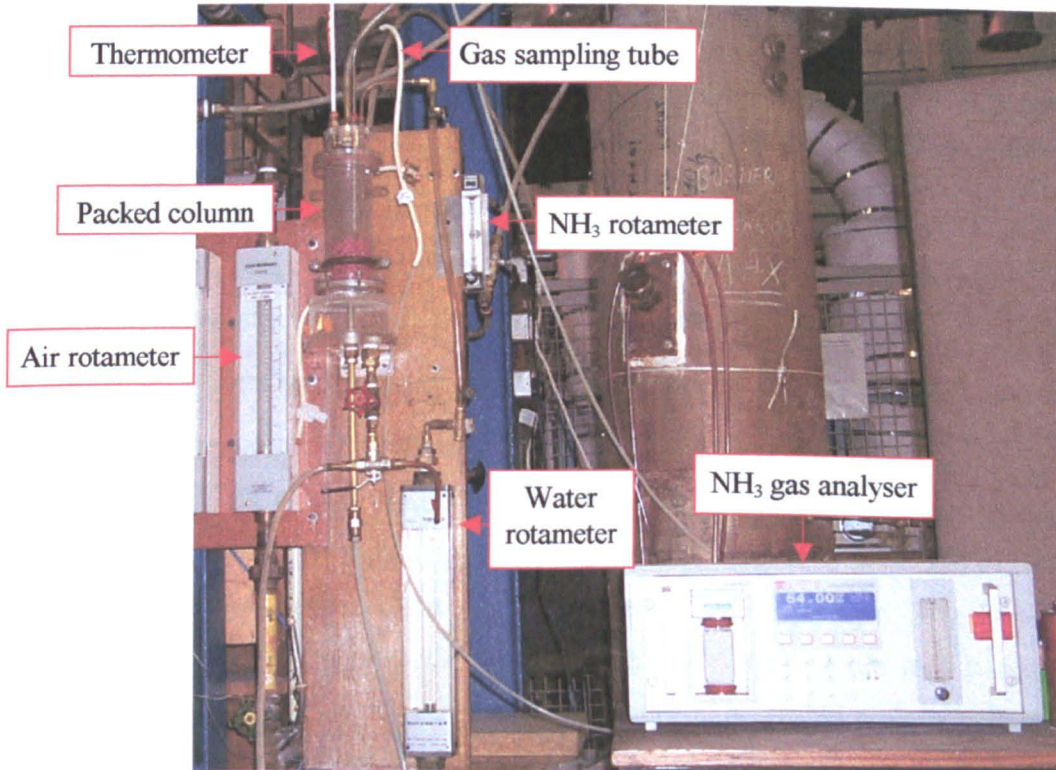
Plate 5.14 Experimental setup for gas absorption tests.

134

Table 5.11 *Instrument specifications for gas absorption tests.*

Instrument	Specifications
Air rotameter	Same as in flooding tests.
Water rotameter	Same as in flooding tests.
NH_3 rotameter	Air rotameter by Platon. Range 5-100 cm^3/min @ 20°C, 1.013 bar abs. Smallest graduation 5 cm^3/min. Calibrated for NH_3 flow.
NH_3 gas analyser	Model ADC 7000 by The Analytical Development Co. Ltd. Range 0-1000 ppm NH_3. With in-built dessicator. Low calibration with ambient air, high calibration with BOC calibration gas: 800 ppm NH_3 in N_2.
Thermometer	Range 0-30°C. Smallest graduation 0.1°C.
Photometer	Model LASA 20 Sensor Array Photometer by Dr Lange. Used with Dr Lange ammonium cuvette test LCK 303. Range 2.5-60.0 mg/litre of ammonium (NH_4) ions.

□ **_Experimental Procedure_**

- The gas extractor was turned on. Air was passed through the packed bed starting at a low flowrate of 30 or 40 litre/min, the flowrate being controlled using the gate valve.

- The water flowrate was set to the desired value by adjusting the needle valve that controlled the water supply to the top of the column. The needle valve at the water exit was adjusted such that a water level about 0.5 cm was maintained in the bottom reservoir to prevent air escaping through the water outlet.

- NH_3 gas was supplied at a predetermined rate corresponding to the inlet air rate such that the NH_3 concentration was approximately 950 ppm in the inlet air.

- 30 to 50 minutes were allowed for the system to stabilise as indicated by a reasonably constant NH_3 concentration reading on the gas analyser. Once this was achieved, the fluid temperatures were taken and a sample of the water exiting the column was collected.

- The NH_3 gas was turned off. The column was left to be flushed through by water.

- The above steps were repeated at higher air flowrates whilst maintaining the same water flowrate till just before the flooding air velocity was reached (from previous flooding tests).

- The overall procedure was repeated at a different water flowrate.

- The water samples collected in sealed glass jars were removed to the analytical laboratory for photometry sampling of the dissolved NH_4 ions. The foil on the screwed-on DosiCapZip on the cuvette was carefully removed. The DosiCapZip was then unscrewed. 200 μl of the sample was pipetted from the glass jar into the LCK 303 cuvette. The DosiCapZip was immediately screwed back onto the cuvette with the fluting at the top, hence mixing the reagents contained in the DosiCapZip into the sample. The sealed cuvette was shaken firmly back and forth 2 or 3 times and then left to stand. After 15 minutes, the cuvette was thoroughly wiped on the outside and then inserted into the photometer and evaluated.

135

Chapter Six

Experimental Results and Discussion

This chapter presents results obtained from experimental studies performed during the course of this research project. The findings are comprehensively discussed and correlations are made between the quantities of interest and the experimental parameters. Comparisons are also made with published findings of other investigators in the field. The results obtained from the preliminary gasification studies are first considered, followed by those acquired from the series of tests carried out on the non-wetting flow cold gas scrubber. This encompasses the studies on flow visualisation, flooding, liquid holdup, gas lift, particulate removal and gas absorption under non-wetting condition in the packed bed gas scrubber.

6.1 Preliminary Gasification Studies

6.1.1 Gasification without Tin

❑ *Experimental Observation*

Three separate test runs were carried out to determine the total sulphur collected from the gasification of the petroleum coke sample. In each run, it was observed that precipitation occurred only in the first Dreschel bottle as shown by Plate 6.1. Therefore, it was only necessary to chemically analyse the contents in the first bottle from each run.
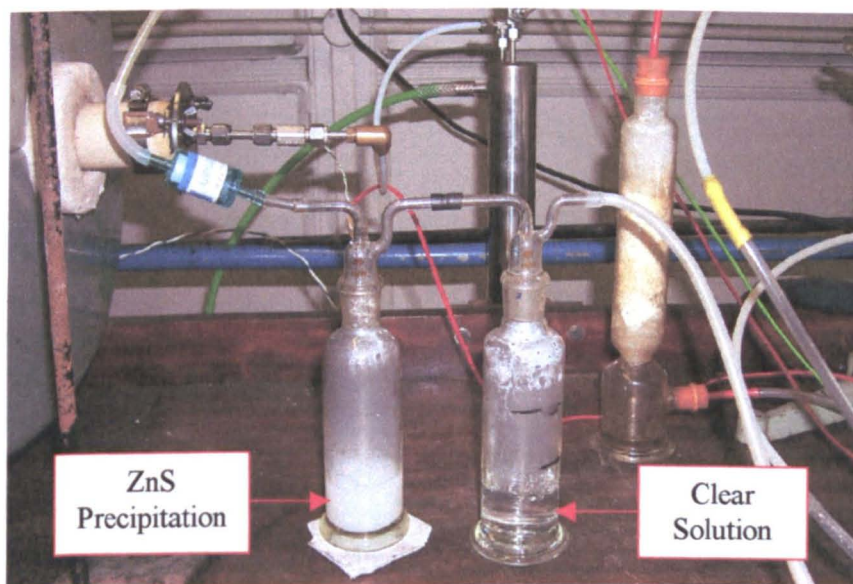
Plate 6.1 Dreschel gas washing bottles used in H_2S determination.

It was noted that slight precipitation occurred before steam was introduced into the system. This initial formation of H_2S could be attributed to the reaction of sulphur with hydrogen in the fuel sample itself released during pyrolysis of the fuel sample. Once steam entered the gasification furnace, the bubbling of the gas through the $ZnSO_4$ solution became very vigorous. The precipitation increased significantly as the steam reacted with the sulphur in the fuel sample forming H_2S.

□ *Amount of Sulphur Collected*

The difference in the volume of sodium thiosulphate solution required to fully remove the excess iodine in the blank solution and that in the test solution was equivalent to the iodine consumed by the sulphide.

The H_2S content in the product gas was derived from the following equation given in BS 3156 (British Standard, 1968):

$$\text{Hydrogen sulphide (g/m}^3\text{) at reference conditions} = \frac{(v_2 - v_1) \times 0.0017}{V} \tag{6.1}$$

where V   = Volume of gas passed at reference conditions (m^3)

  v_1 = Volume of 0.1N sodium thiosulphate solution used for test solution (ml)

  v_2 = Volume of 0.1N sodium thiosulphate solution used in blank determination (ml)

However, the value of interest is the total H_2S collected from the gasification of the petroleum coke sample. Rewriting equation 6.1:

$$\text{Total } H_2S \text{ collected (g)} = (v_2 - v_1) \times 0.0017 \tag{6.2}$$

The total sulphur collected can then be calculated as follows:

$$\text{Total sulphur collected (g)} = (v_2 - v_1) \times \frac{0.0017 \times Atomic\ mass\ of\ Sulphur}{Molecular\ mass\ of\ H_2S}$$

$$= (v_2 - v_1) \times \frac{0.0017 \times 32.066}{34.082}$$

$$\therefore \boxed{\text{Total sulphur collected (g)} = (v_2 - v_1) \times 0.0016} \tag{6.3}$$

The amount of sulphur collected from each test run in the absence of tin is shown in Table 6.1.

Table 6.1 *Results of sulphur determination for gasification in the absence of tin.*

	Run 1	Run 2	Run 3	Mean
Petroleum coke used (g)	1.9343	1.9987	1.9975	
Residue left after test (g)	0.0177	0.0158	0.0124	
Residue as weight % of petroleum coke sample	0.92	0.79	0.62	
I_2 used (ml)	50.00	55.00	60.00	
$Na_2S_2O_3$ used for test solution v_1 (ml)	6.80	4.60	17.80	
$Na_2S_2O_3$ used in blank determination v_2 (ml)	49.40	52.75	58.95	
Total H_2S (g)	0.0724	0.0819	0.0670	0.0738
Total Sulphur (g)	0.0682	0.0770	0.0658	0.0703
Sulphur captured as weight % of petroleum coke sample	3.53	3.85	3.29	3.56

The sulphur content initially determined for the petroleum coke was 4.4 wt.% (as-received). Comparing this figure to the figures in Table 6.1, the total sulphur captured in the Dreschel bottle averaged at about 80% of the total sulphur expected in the fuel sample. The discrepancy could be attributed to several possible reasons:

- The ZnS precipitate could not be completely removed from the Dreschel bottle onto the filter paper. Visible traces were left on the walls of the gas inlet tube and the bottle itself.

- Traces of ZnS could have been lost when transferring the filter paper containing the ZnS precipitate from the funnel to the wide-necked bottle stopper and then into the bottle itself.

- The filter paper with its contents were not supposed to be released into the acidified I_2 solution in the wide-necked bottle until the stopper was inserted and the bottle properly sealed. This was to prevent the escape of H_2S which was formed upon contact of ZnS with HCl acid in the solution. Unfortunately it was not possible to adhere to this rule, as the filter paper tended to stick to the stopper, necessitating some prodding with a spatula before the stopper completely sealed the mouth of the bottle. Traces of H_2S may have escaped before the bottle was completely sealed.

- The determination of sulphur content using the High-Temperature Method as outlined in BS 1016: Part 6: 1977 (see Appendix 1) involved the addition of aluminium oxide to the petroleum coke sample to facilitate decomposition of the sulphate, hence preventing retention of sulphur in the ash. During the gasification tests, aluminium oxide was not used which meant that some sulphur could have been retained in the residual ash.

- Black particles were collected in the in-line gas filter indicating that traces of petroleum coke particles had been entrained into the nitrogen gas stream before having the chance to react with steam, adding to the loss of sulphur.

- There is also the possibility of a very small fraction of the sulphur in the fuel gas existing in the form of COS. COS hydrolyses in water forming CO_2 and H_2S (US EPA, *no date*). Hence any dissolved COS will liberate H_2S and the sulphur content should be accounted for in the method employed for H_2S analysis. However, the solubility of COS in water is about 4 to 5 times lower than that of H_2S at 15°C to 20°C (Liley *et al.*, 1997). Any undissolved COS will constitute a loss in sulphur content of the fuel sample.

These would collectively explain the missing 20% of sulphur from the petroleum coke sample.

6.1.2 Gasification with Tin

□ *Amount of Sulphur Collected*

Precipitation occurred only in the first Dreschel bottle. Therefore, only the contents in the first washing bottle from the test was chemically analysed for sulphur content. The results are tabulated in Table 6.2.

Table 6.2 Results of sulphur determination for gasification in the presence of tin.

Petroleum coke used (g)	1.9846
Residue left after test (g)	0.0146
Residue as weight % of petroleum coke sample	0.70
I_2 used (ml)	60.00
$Na_2S_2O_3$ used for test solution v_1 (ml)	18.40
$Na_2S_2O_3$ used in blank determination v_2 (ml)	58.35
Total H_2S (g)	0.0679
Total Sulphur (g)	0.0639
Sulphur captured as weight % of petroleum coke sample	3.22

The average amount of sulphur captured during gasification tests in the absence of tin was 3.56 wt.% of the fuel sample. When compared to the result obtained in the presence of tin which is 3.22 wt.%, the amount of H_2S reduction was small, at only about 10%. This however, was hardly surprising as the available surface area of the tin for reaction was insufficient for significant desulphurisation to take place.

❑ ***Reaction With Tin***

The product gas reacted with tin forming a soft pale yellow substance in the second 'tin' crucible and the deposition of the same substance in the interiors of the combustion tube surrounding the second crucible. Plate 6.2 shows the original tin strips prior to the experiment. Both Plates 6.3 and 6.4 show the cooled 'tin' crucibles containing the residues after the test. Plate 6.5 shows the solid deposition inside the combustion tube.
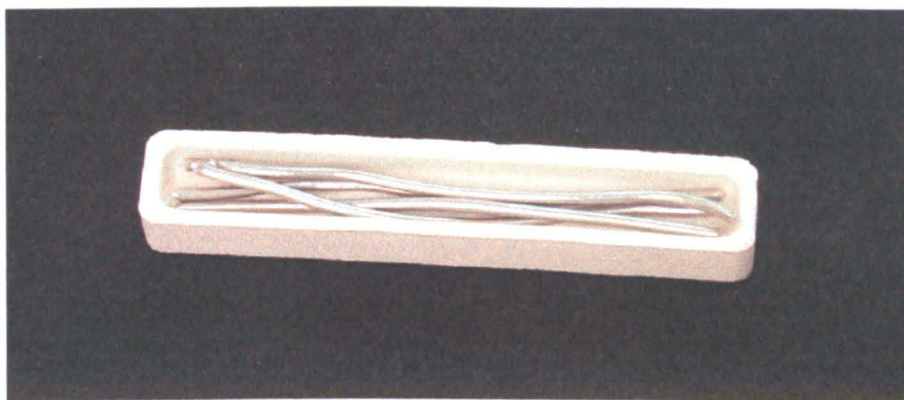
Plate 6.2 Original 'tin' crucible containing tin strips before test.
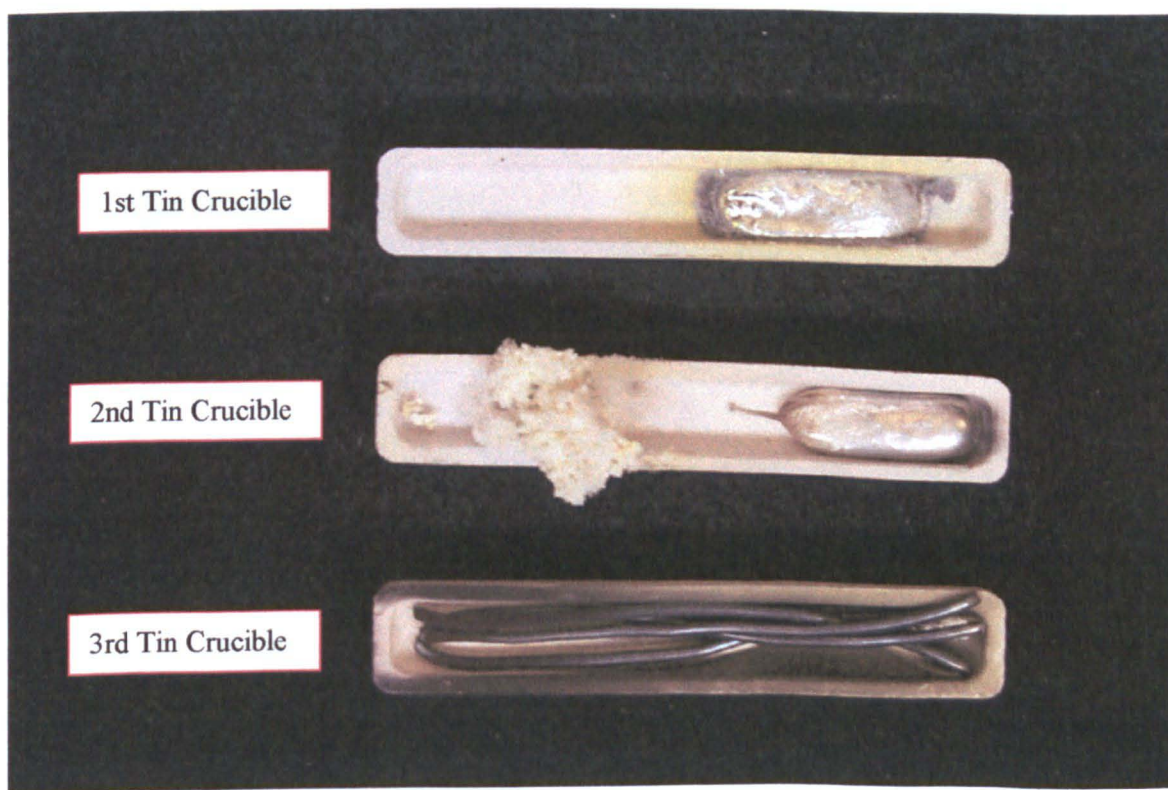
Plate 6.3 'Tin' crucibles after test.
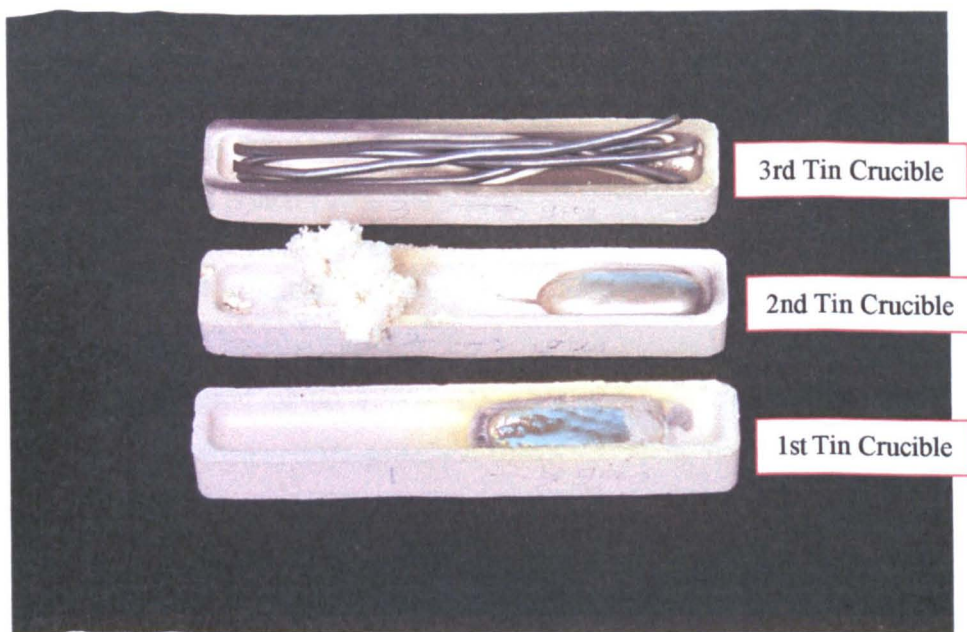
Plate 6.4 '*Tin' crucibles after test.*

Soft pale yellow deposit on inner wall of combustion tube.
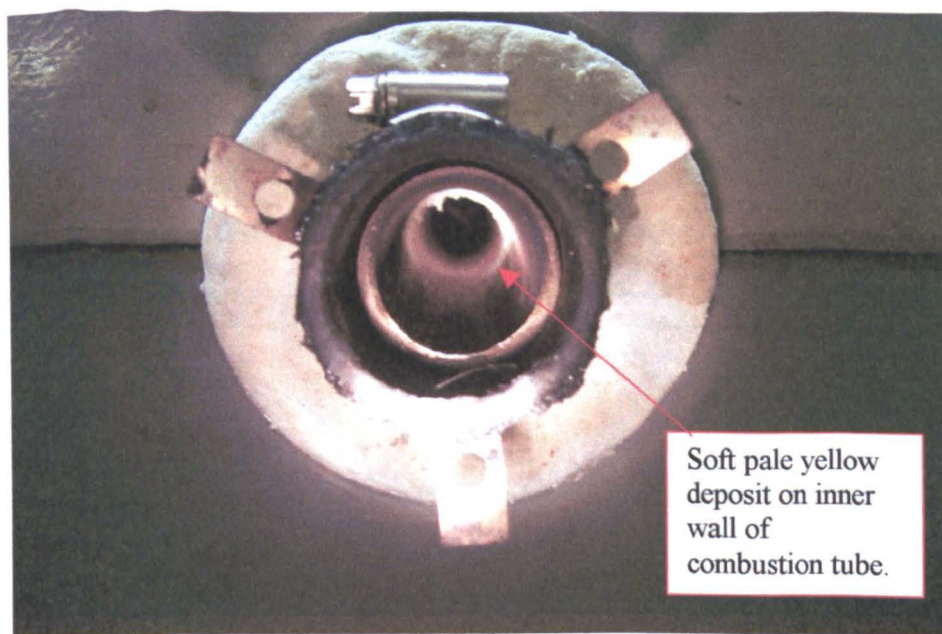
Plate 6.5 Residue in combustion tube.

The tin wires in the first 'tin' crucible were completely melted, and solidified into a lump. The tin lump settled at one end of the crucible in the direction of the gas flow and was fused to the bottom of the crucible. The surface of the lump was coated with traces of silver-white crystals. The sides of the tin lump were surrounded by a grey ash-like substance. The adjacent crucible walls have turned yellow on an originally white surface.

The tin wires in the second 'tin' crucible were also completely solidified into a lump, which settled at end of the crucible. However, the tin lump was detachable from the crucible, and its

silver-white surface was clean, free from any crystal or ash formation. A significant amount of soft pale yellow substance was deposited over the first half of the crucible, spilling over the crucible rim. Some of this substance was deposited on the adjacent combustion tube walls. The sides of the crucible in contact with the pale yellow substance have also turned yellow.

The tin wires in the third crucible were blackened but not melted. The sides of the crucible were blackened as well. This suggests that the temperature at the location of the last crucible was below the melting point of tin which is approximately 232°C (Iida and Guthrie, 1988). This is confirmed by the temperature profile of the combustion tube in the gasification furnace as illustrated in Figure 6.1, the furnace set point being 1200°C. It should be noted that the temperature profile shows the wall temperatures along the combustion tube as the temperatures were measured with the thermocouple touching the base of the tube. The actual temperatures of the crucible contents could be lower than the combustion tube wall temperatures. The inlet N_2/steam gas mixture temperature to the combustion tube during gasification ranged from 200°C to 250°C whilst the wet product gas temperature at the combustion tube outlet was surprisingly low at about 150°C to 200°C. The gas outlet temperature was measured outside the combustion tube, meaning that the gas had been cooled by the surroundings, which would explain the low outlet temperature.
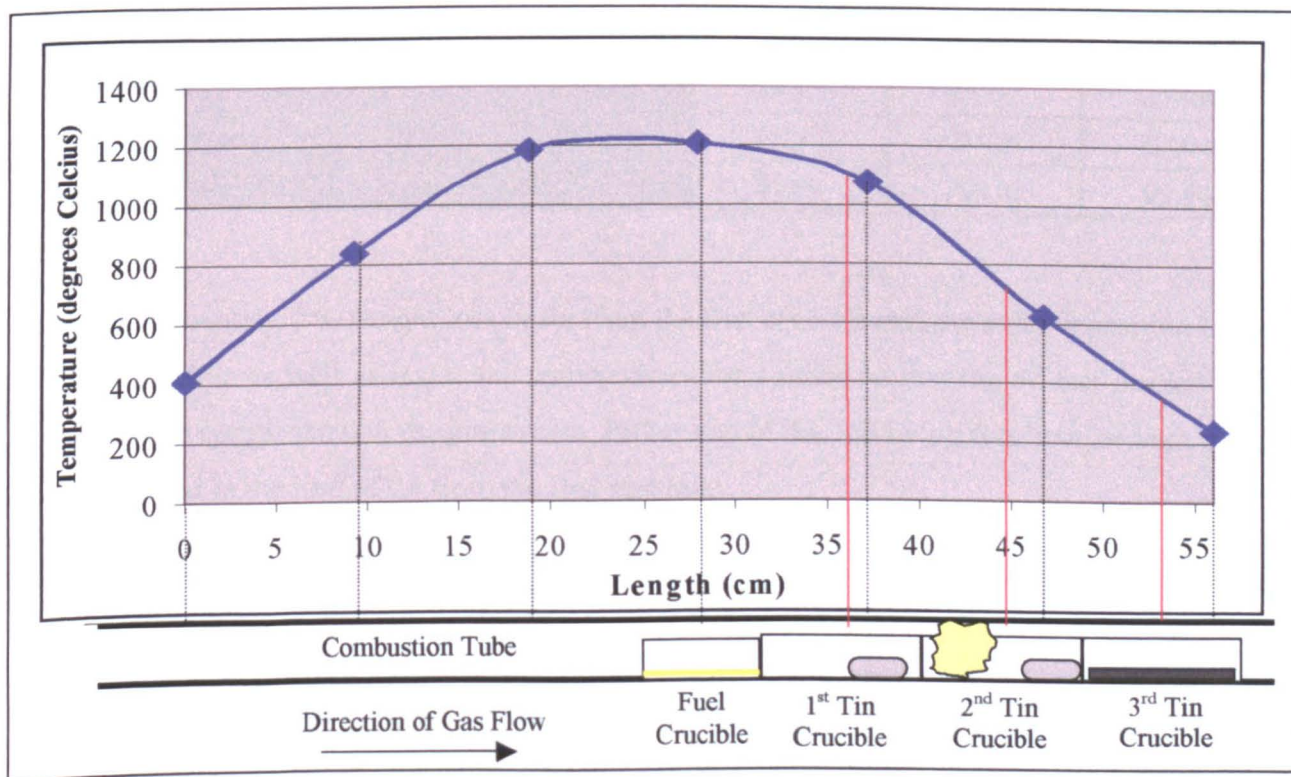
Figure 6.1 *Temperature profile of gasification furnace (set point = 1200°C) with position of crucibles and their contents along the combustion tube.*

The position where the pale yellow solid residue was deposited suggests that it was a product of reaction(s) between the product gas and the molten tin in the first 'tin' crucible. The temperature profile of the furnace indicates that the reaction occurred when the molten tin temperature was in the vicinity of 1000°C. However, the temperature of the gas-liquid interface where the reaction took place could have been lower than this considering the possibly lower temperature of the gas phase.

Although the tin in the second 'tin' crucible was also melted, no deposition occurred downstream. Also, the surface of the tin lump in the second crucible was clean and free from solid deposits unlike the first one. These observations suggest that the tin temperature in the region of 500°C was too low for any reaction with the product gas to take place. Again, the gas-liquid interface temperature could be lower than this considering the possibly lower gas phase temperature.

The mass of the tin strips before the test and the mass of the residues after the test are summarised in Table 6.3.

Table 6.3 *Mass of 'tin' crucible contents before and after test.*

	1ˢᵗ Crucible	2ⁿᵈ Crucible	3ʳᵈ Crucible
Mass of tin wires before test (g)	6.8840	6.7954	6.7908
Mass of residues after test (g)	6.7409	6.8217	6.7868
Mass loss(-)/gain(+) of contents (g)	- 0.1431	+ 0.0263	- 0.0040
Residues as weight % of original tin wires (%)	97.92	100.39	99.94

The approximately 2 % weight loss of tin from the first crucible and the solid deposition in the second crucible as well as inside the combustion tube confirmed that the tin has reacted with one or more components in the gas stream. Either one of the following reactions or both could have resulted in the loss of tin from the first crucible:

- Reaction of tin with H_2S to form SnS.
- Reaction of tin with steam and/or CO_2 to form SnO_2.

Reaction with steam ($Sn + 2H_2O \leftrightarrow SnO_2 + 2H_2$) was very likely due to the very large H_2O/H_2 ratio. The phase diagram in Figure 2.5 indicates that under such condition, SnO_2 formation from reaction of molten tin with steam is extremely favourable.

Reaction with CO_2 ($Sn + 2CO_2 \leftrightarrow SnO_2 + 2CO$) was also likely, as previous fuel gas analysis has shown that the amount of CO_2 emitted during gasification was about twice that of CO. The forward reaction would be possible in a temperature range of 350°C to 500°C as reported by Nielsen and Sigurdardottir (1993).

The colour of the solid deposit could help throw some light on its identification, hence giving an indication of the reaction that has taken place. Table 6.4 shows the physical properties of several tin compounds of interest.

Table 6.4 Physical properties of tin compounds of interest
(Nielsen and Sigurdardottir, 1993; Vogel, 1989; Samsanov, 1982).

Compound	Colour of solid	Specific gravity	Melting point (°C)	Boiling point (°C)
Sn	Silver-white	7.3	232	2623
SnO	Black	6.45	1050	1425
SnO_2	White	6.95	2000	2500
SnS	Brown	5.08	881	1210

Considering the pale-yellow colour of the solid deposit formed in the test and the possible reactions between tin with H_2S, steam and CO_2, the deposit could then be a mixture of mainly SnO_2 (white) with a small fraction of SnS (brown). For confirmation, the deposit was sent to SUMAC (Sheffield University Materials Analytical Centre) for elemental analysis.

At SUMAC, due to the very small amount of available sample, only tests on sulphur and tin were carried out. Sulphur content was determined by combustion analysis, but there was insufficient sample for a satisfactory test. The result for sulphur was found to be approximately 23 wt.%. The tin content was determined using inductively coupled plasma spectrometry. Likewise, the available sample weight was less than optimum and in addition, there was unsatisfactory dissolution of the sample for the tin analysis. The result for tin was found to be approximately 12 wt.%. The lack of sample material cancelled out the possibility of any preliminary investigation into the most suitable method for accurate analysis.

Although the lack of available sample might limit the accuracy of the quantitative determination of sulphur and tin contents, nevertheless the elemental analyses confirmed

qualitatively the presence of both sulphur and tin in the residue. This meant that the sulphur content in the fuel gas had indeed reacted with molten tin, most likely resulting in the formation of SnS. Also, the side reactions of molten tin with steam and CO_2 to form SnO_2 were highly possible.

Molten tin based gas desulphurisation in actual gasification conditions has never been carried out before. These small scale gasification studies have provided actual confirmation and evidence of the possibility of sulphur removal by molten tin in the gasification environment.

6.1.3 Analysis of Errors

❑ *Measured Quantities*

An instrument's sensitivity or smallest resolution is the minimum amount of change in the measured quantity that the instrument is capable of detecting or indicating (Massey, 1986). It affects the random errors of the reading, hence its precision. The smaller the random error, the greater is the precision.

The main error of concern in this study is that corresponding to the determination of the amount of sulphur captured in the gas washing bottles. The sensitivity of the apparatus and instruments used and the corresponding error in the measured quantities are summarised in the following table.

Table 6.5 Errors in measured quantities for sulphur determination.

Apparatus/ Instrument	Measured Quantity	Smallest Instrument Graduation or Sensitivity	Smallest Reading Obtainable	Absolute Error on Measured Quantity
Microbalance	Mass of crucible plus contents	0.0001 g	0.0001 g	±0.00005 g
Burette	Volume of $Na_2S_2O_3$ solution used in titration	0.1 ml	0.05 ml	±0.03 ml

❑ *Amount of Sulphur Collected*

The mass of petroleum coke sample used in each test run was determined from the difference in the mass of the empty crucible and the total mass of the crucible containing the fuel sample. Therefore the error associated with the mass of the fuel sample used is ±0.00007 g, calculated

as follows:

$$e_{fuel} = \pm \sqrt{0.00005^2 + 0.00005^2} \text{ g} = \underline{\pm 0.00007 \text{ g}} \qquad (6.4)$$

The volume of sodium thiosulphate ($Na_2S_2O_3$) solution used in each titration was obtained from the difference of the initial and final readings on the burette. Hence the error on both the measured quantities v_1 ($Na_2S_2O_3$ volume used for test solution) and v_2 ($Na_2S_2O_3$ volume used in the blank determination) is ± 0.04 ml, calculated as follows:

$$e(v_1) = e(v_2) = \pm \sqrt{0.03^2 + 0.03^2} = \underline{\pm 0.04 \text{ ml}} \qquad (6.5)$$

The total mass of sulphur collected was calculated from equation 6.3 and the corresponding error is ± 0.00009 g, as determined from equation 6.6:

$$\text{Total sulphur collected (g)} = (v_2 - v_1) \times 0.0016 \qquad (6.3)$$

$$e_{sulphur} = \sqrt{e(v_1)^2 + e(v_2)^2} \times 0.0016 = \sqrt{0.04^2 + 0.04^2} \times 0.0016 \text{ g} = \underline{\pm 0.00009 \text{ g}} \qquad (6.6)$$

Based on equation 6.7, the calculated percentage error associated with the mass of total sulphur collected from each test run is $\pm 0.1\%$, this being solely due to resolution limitations of the apparatus used. The actual error would be higher than this due to the inevitable loss in traces of ZnS precipitate when transferred from the Dreschel bottle to the final titration vessel.

$$\frac{e_{sulphur}}{sulphur} \times 100\% = \frac{\sqrt{e(v_1)^2 + e(v_2)^2}}{v_2 - v_1} \times 100\% \qquad (6.7)$$

The sulphur captured as weight % of petroleum coke sample was calculated from the mass ratio of sulphur collected to the fuel sample used. Therefore the percentage error associated with the sulphur captured expressed as the weight % of the fuel sample used is calculated following equation 6.8. For each test run, the percentage error is $\pm 0.1\%$. Again, the actual error would be higher than this figure due to the loss in ZnS precipitate during its transfer to the final titration vessel.

$$\% \text{ } e(\text{sulphur captured as wt. \% of fuel sample}) = \sqrt{\left(\frac{e_{sulphur}}{sulphur}\right)^2 + \left(\frac{e_{fuel}}{fuel}\right)^2} \times 100\% \qquad (6.8)$$

6.2   Cold Gas Scrubber Studies: Flow Visualisation

6.2.1   Experimental Observations

❑ *Droplet and Rivulet Formation*

It was observed that there were generally three types of spherical packing configurations which encouraged droplet formation. These are illustrated in Figure 6.2:
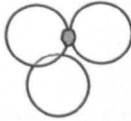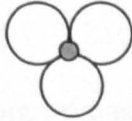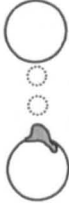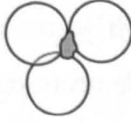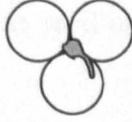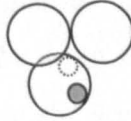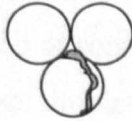
1. A Single Sphere With an immediate space below.	2. Two Contacting Spheres With an immediate bottom sphere. Example of droplet flow.	3. Three Contacting Spheres Example of rivulet flow.

Figure 6.2 Droplet and rivulet formation on spherical packing.

In the first configuration, water flows down a single sphere till it reaches the base of the spherical surface. The base of the sphere is free from contact with other spheres. A droplet starts to form at this bottom point, increasing in size as more water accumulates there. Once the droplet reaches a size of approximately 4 mm, it is displaced from the sphere. The displaced droplet falls freely through the empty space before hitting the sphere below, disintegrating into a rivulet.

In the second configuration, water droplet formation takes place at the intersection of two horizontally touching spheres. The water droplet grows in size as more water is held up at the intersection, the additional water flowing either from the top of the sphere (either as rivulet or droplet) or from within the packed bed. When the droplet size reaches approximately 4 mm, it is displaced downwards. If there is a free space between these spheres and the sphere below, the droplet will then fall freely before hitting the bottom sphere and disintegrates into a rivulet. However if the spheres touch an adjacent sphere below, whether or not the displaced droplet maintains its flow on the bottom sphere depends on the rate of water replenishment from the top spheres. At low water flowrates, a pulsating droplet flow is observed from the intersection point of the top spheres to the surface of the bottom sphere. At high water flowrates, the frequency of droplet formation becomes sufficiently high such that the individual droplets flow so close to one another that a rivulet flow of about 3 to 4 mm width is formed on the surface of the bottom sphere.

The final configuration consists of three adjacent spheres. Water flowing from either the top or from within the packed bed accumulates at the interstice formed by the three touching spheres. Again as the droplet size approaches 4 mm, it is displaced downwards. A droplet or rivulet flow is formed depending on the arrangement of the spheres below as well as on the water flowrates as described for the second configuration above.

❑ **_Static Droplets_**

The above observations describe the formation and displacement of mobile droplets. In addition, static droplets of approximately 2 mm in size were also noted at some intersections for both horizontally and vertically touching spheres. No clear, obvious droplets smaller than this size were observed on the packing surface.

❑ **_Droplet Velocity_**

An attempt was made to measure the velocity of mobile droplets. Video images were captured at selected locations where visible droplet formation took place. It was observed that a droplet formed at the apex of a sphere travelled downwards on the top hemisphere surface, picking up speed at the equator before dripping off. It then hit an adjacent sphere below before the next droplet was formed again at the apex of the top sphere. Based on this observation, two different assumptions were applied with regards to the distance travelled by the droplet while

calculating its velocity. In the first calculation, the droplet was assumed to travel strictly vertically i.e. the distance of one diameter of the sphere before dripping off. In the second calculation, the droplet was assumed to travel a distance of half a circular perimeter of the sphere (i.e. half a circumference of the projected circle) before dripping off. The actual droplet velocity should fall in between these two extreme values.

A sample calculation is shown as follows:

<u>1.5 litre/min water flowrate; 50 litre/min air flowrate; 10 mm waxed glass bead:</u>

Total number of droplets formed   = 38 droplets

Total elapsed time (from the total elapsed frames during droplet formation) = 10.22 s

First average velocity of droplet flow:

Distance travelled for each droplet   = 1 diameter of spherical bead = 10 mm

∴ Average velocity of droplet flow   = (38 × 10)/10.22   = 37 mm/s

Second average velocity of droplet flow:

Distance travelled for each droplet   = ½ one circular perimeter of sphere

$$= ½ × 10\pi \qquad = 5\pi \text{ mm}$$

∴ Average velocity of droplet flow   = (38 × 5π)/10.22   = 58 mm/s

The results are tabulated as follows:

Table 6.6   Velocity of droplet flow at a particular location.

Paraffin waxed glass beads (10 mm diameter); Water flowrate = 1.5 litre/min					
Air flowrate (litre/min)	Flow type	Total number of droplets	Total elapsed time (s)	1st Average velocity of droplet flow* (mm/s)	2nd Average velocity of droplet flow** (mm/s)
40	Droplet	5	3.20	16	25
50	Droplet	38	10.22	37	58
70	Droplet	19	9.46	20	32
95	Droplet	28	9.86	28	45
100	Droplet - Rivulet	-	-	-	-
110	Rivulet	-	-	-	-
120	Rivulet	-	-	-	-

* Distance per drop based on 1 diameter of sphere.
** Distance per drop based on ½ one circular perimeter of sphere.

Table 6.7 *Velocity of droplet flow at a particular location.*

Paraffin waxed glass beads (10 mm diameter); Water flowrate = 2.5 litre/min					
Air flowrate (liter/min)	Flow type	Total number of droplets	Total elapsed time (s)	1st Average velocity of droplet flow* (mm/s)	2nd Average velocity of droplet flow** (mm/s)
45	Droplet	37.5	10.22	37	58
50	Droplet	32	10.22	31	49
60	Droplet	24	10.22	23	37
70	Droplet	25	10.22	24	38
80	Droplet	28	10.22	27	43

* Distance per drop based on 1 diameter of sphere.
** Distance per drop based on ½ one circular perimeter of sphere.

Table 6.8 *Velocity of droplet flow at a particular location.*

Polyethylene beads (9.53 mm diameter); Water flowrate = 2.5 litre/min					
Air flowrate (liter/min)	Flow type	Total number of droplets	Total elapsed time (s)	1st Average velocity of droplet flow* (mm/s)	2nd Average velocity of droplet flow** (mm/s)
50	Droplet	9	8.58	10	16
60	Droplet	12	9.76	12	18
70	Droplet	10.75	10.22	10	16

* Distance per drop based on 1 diameter of sphere.
** Distance per drop based on ½ one circular perimeter of sphere.

□ ***Effect of Increasing Fluid Flowrates***

The results in Tables 6.6 to 6.8 showed that there was no definite trend in droplet velocity at a particular packing location with increasing air flowrate. It was noted however that as the air flowrate increased while maintaining a constant water flowrate, the droplet flow progressively changed into a continuous rivulet flow at a particular packed bed location. On the whole, the number of rivulets seen on the outer packing surface increased.

Comparing the images obtained at the same air flowrate but differing water flowrates, it was found that rivulet flow became very much prominent at a larger water throughput. The number of rivulets observable on the outer packing surface rose significantly. The effect was more prominent than that of increasing air flowrate.

Throughout the normal operating range of fluid flowrates i.e. before flooding, the mobile water droplets and rivulets observed were approximately the same size of about 4 mm diameter for the former and 3 to 4 mm width for the latter.

◻ *Comparison between Flow on Polyethylene and Glass Packings*

A more prominent droplet flow was observed for the waxed glass packed bed compared to the polyethylene one. This could be attributed to the difference in water-solid contact angles, which is 109° for paraffin wax surface (Craig *et al.*, 1960) and 95° for polyethylene surface (Adamson and Gast, 1997). The larger contact angle on the waxed glass surface results in higher tendencies for droplet flow.

It is to be noted that the observations documented in the preceeding paragraphs pertain to only water flow on the outer surface of the packed bed observable through the Perspex column wall. It does not refer to flow within the packed bed which was not visible from the outside.

6.2.2 Prediction of Maximum Liquid Droplet Size

The droplets hanging from the base of the spheres are examples of pendent (or hanging) droplets. The static equilibrium of the pendent droplet is governed by the balance between surface tension and the gravitational force.

Assume that the contact line of the water with the solid sphere surface is a circle of diameter $d_{contact}$ and that the contact angle is θ. Surface tension, σ_L is the force per unit length acting tangentially along the liquid-solid-gas contact line. The vertical component of the surface tension force acts upwards, holding the droplet against the packing surface. On the other hand, the gravitational force acting on the droplet i.e. its weight tends to pull the droplet downwards. Hence, for a droplet at static equilibrium, the force balance is:

Vertical component of surface tension force = Droplet weight

$$\sigma_L \pi d_{contact} \cos \theta = \rho_L g V \quad (6.9)$$

where σ_L = liquid surface tension (N/m)

$d_{contact}$ = diameter of contact circle between liquid and solid surface (m)

θ = contact angle between liquid droplet and solid surface

ρ_L = liquid density (kg/m^3)

g = gravitational acceleration (m/s^2)

V = volume of droplet (m^3)

As more water accumulates in the droplet, the droplet increases in volume. Its weight grows and eventually a maximum volume will be reached at which the weight overcomes the surface tension force holding the droplet against the solid sphere surface. At this point, the pendent droplet falls off the sphere. This was experimentally observed on the spherical packing, the water droplet increased in size till about 4 mm before it was displaced from surface of the spheres.

The liquid pendent droplet is elongated vertically by its weight i.e. gravitational force, forming a pearl-like shape. As illustrated in Figure 6.3, Andreas *et al.* (1938) defined an experimentally measurable shape dependent quantity, S for pendent drops:

$$S = \frac{d_s}{d_e} \tag{6.10}$$

d_e = equatorial diameter (m)
d_s = diameter measured from distance d_e up from the base of drop (m)
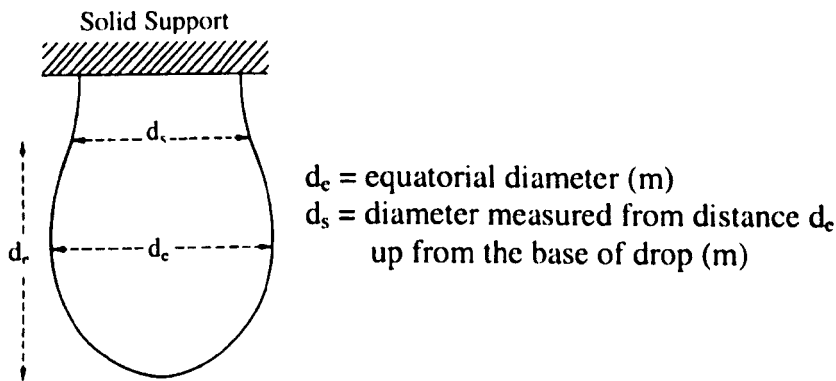
Figure 6.3 *Pendent (or hanging) drop.*

The surface tension of the liquid pendent drop is given by the following equation (Adamson, 1976):

$$\sigma_L = \frac{\Delta \rho g d_e^2}{H} \tag{6.11}$$

Rearranging:

$$H = \frac{\Delta \rho g d_e^2}{\sigma_L} \approx \frac{\rho_L g d_e^2}{\sigma_L} \tag{6.12}$$

where   H   = a shape dependent quantity (dimensionless)

     $\Delta \rho$ = density difference between liquid and gas phase (kg/m³)

     ρ_L = liquid density (kg/m³)

     g   = gravitational acceleration (m/s²)

For a hydrophobic surface, a pendent water droplet is expected to adopt a pearl-like shape i.e. with d_s less than d_e (see Figure 6.3). Since S equals d_s/d_e, S is expected to be less than 1. From the tables of 1/H versus S values tabulated by Niederhauser and Bartell (1950) (see Appendix

4), for an S value less than 1, the corresponding 1/H value has to be greater than 0.30586. Applying equation 6.12:

$$\frac{1}{H} > 0.30586 \qquad \text{hence} \qquad \frac{\sigma_L}{\rho_L g d_e^2} > 0.30586$$

$$\therefore d_e < \left(\frac{\sigma_L}{0.30586 \times \rho_L g} \right)^{\frac{1}{2}} \qquad\qquad (6.13)$$

Applying inequality 6.13 with physical properties of water at 15°C ($\sigma_L = 73.49 \times 10^{-3}$ N/m; $\rho_L = 1001.29$ kg/m³) and taking g as 9.81 m/s², the equatorial diameter d_e was worked out to be less than 4.9 mm. The experimentally observed maximum water droplet size on the spherical packings before falling off the solid surface is approximately 4 mm. This agrees with the calculated range of equatorial diameter of less than 4.9 mm.

6.2.3 Comparison with Wetting Flow

The work of Jesser and Elgin (1943) offers suitable comparison of liquid flow on a wettable packing of a similar geometry to the non-wettable spheres used in this study. They visually studied the flow of water through a glass column packed with 25.4 mm glass spheres having a voidage of 0.405. Water wets the glass surface, the contact angle of water on glass has been reported to be 14° (O'Brien, 1996). Jesser and Elgin described that at the lowest possible water rates, water collected at contact points between the spheres, forming a "doughnut" or a ring around each contact point (also noted by Turner and Hewitt, 1959). Upon increasing to a certain amount, water left the point flowing as fine rivulets between contact points, no film flow being evident at these low flow rates. As water rate increased, the ring enlarged and more contact points were formed, subsequently the packings began to be covered by water film. The fraction of surface wetted by the water film increased on further increase in water rates.

With the non-wettable spheres used in this investigation, water collected as droplets at contact points between the spheres. The droplet at a contact point increased in size as more water accumulated and subsequently dropped off as its weight overcame the surface tension force holding it to the sphere. It then rolled downwards, forming droplet flow on the packing. At higher water rates, the rate of droplet formation and detachment was sufficiently fast that adjacent droplets combined into rivulets, the rivulets becoming more prevalent as water rate increased. Under normal operation before flooding, no obvious film flow was observed.

The change in liquid flow pattern on wettable and non-wettable spherical packing as liquid rate increases is summarised as follows:

Table 6.9 Comparison between wetting and non-wetting flow on a spherical packing surface.

Relative Liquid Rate	Wetting Flow*	Non-Wetting Flow**
Low	Ring formation at contact point.	Droplet formation at contact point.
Moderate	Liquid leaves contact point as rivulet flow.	Droplet detaches from contact point, forming droplet flow.
High	Liquid film covers packing surface, forming film flow.	Droplets combine into rivulets, forming rivulet flow.

* Observations made by Jesser and Elgin (1943); ** Observations made in this study.

6.2.4 Comparison with Other Non-Wetting Flow

In this study, it was observed that for a packed bed of 9.53 mm (polyethylene beads) and 10 mm (paraffin waxed glass beads) hydrophobic spheres, droplet flow progressively changed into rivulet flow as fluid flowrates increased. Generally rivulet flow was more pronounced at higher gas and liquid flowrates, this is especially so for the latter. This observation agrees with that made by Mackey and Warner (1973) with regards to mercury flow on solid packing. The liquid metal was reported to flow as individual drops and rivulets in the packed bed, continuous rivulet flow becoming prominent as the liquid flowrate increased. In comparison, Tait (1998) reported that a transition point between droplet and rivulet flow did not exist for water flowing on a bed of 15 cm polypropylene spheres (average $\theta_{\text{water-polypropylene}}$ is 95° from Shimizu and Demarquette (1999)). Instead, both rivulets and droplets existed simultaneously. Tait's packed bed was made up of only eleven 15 cm spheres in total in a 39 cm diameter column. The column to packing diameter was 2.6 as opposed to 7.8 (paraffin waxed glass spheres) and 8.2 (polyethylene spheres) used in this work. The bigger spheres meant that Tait's packed bed would have greater voidage than the ones in this work. These factors i.e. comparatively bigger spheres, smaller column to packing diameter ratio, as well as greater voidage in Tait's system means that available water channels and hence droplet formation sites were significantly fewer compared to this work. Had there been more of these channels, the water flow would have been distributed more extensively and a prominent droplet to rivulet transition with increasing fluid flowrates would possibly have been observed.

However, this work agrees with the observation made by Tait (1998) with regards to the mobility of static holdup. As reported in section 6.2.1, droplets were formed at intersection points of spheres. As more water accumulated at these sites, droplets size increased until the droplets became unstable due to their weight and dropped downwards. This demonstrated the mobility of the static holdup due to the tendency of water to form droplets rather than film on the hydrophobic surface of polyethylene and paraffin waxed glass spheres.

Tait (1998) reported that in his packed bed of 15 cm spheres, the droplet size ranged from 2 to 9 mm with most of the droplets smaller than 6 mm. The mean droplet size was 4.4 mm and the mode was 5 mm. In comparison, the droplet size observed in this work with a bed of 9.53 and 10 mm spheres ranged from about 2 to 4 mm. The larger spheres (15 times bigger) used by Tait permitted larger droplets to be supported on the top hemisphere surface of the spheres.

Tait (1998) reported that the velocity of all the measured droplets was between 1 to 1.7 m/s (at 1.6 m/s air velocity, water velocity not mentioned) assuming that all droplets travelled vertically downwards. The velocity of droplets measured in this work assuming vertical movement only is significantly smaller, from 10 to 37 mm/s. One reason for this difference is that the vertical distance available for the droplet acceleration by gravity is 15 times bigger for Tait's spheres compared to the spheres used in this work. Another reason is presumably a larger water flowrate used by Tait, however the water flowrate applied was not mentioned.

6.2.5   Implication for Hot Scrubber

Compared to the cold model, droplet flow is expected to be more predominant for molten tin flow on ceramic alumina spheres in the hot scrubber. This is due to the significantly larger contact angle of molten tin on solid alumina surface, about 160° at 300°C (Nogi *et al.*, 1988).

Since the hot scrubber incorporates 9.53 mm spheres as packing with physical dimensions similar to the polyethylene and waxed glass beads, the drip tip at the base of the ceramic sphere would be dimensionally alike as well. The pendent droplet of molten tin at the base of the ceramic sphere would be expected to conform to inequality 6.13. At a typical operating temperature of 400°C, the surface tension of molten tin is 0.545 N/m while its density is 6878 kg/m^3 (Iida and Guthrie, 1988). Applying inequality 6.13, the equatorial diameter d_e was worked out to be less than 5.1 mm. Therefore, the estimated maximum molten tin droplet size in the packed bed of the hot scrubber would be approximately 5 mm. This information would be useful in the modelling of particulate capture by liquid tin droplets on the packing surface.

6.3   Cold Gas Scrubber Studies: Flooding

6.3.1   Bed Pressure Drop and Flooding Points

Pressure drop variation with air flowrate was obtained for the dry bed, and with water irrigation from 1.0 to 3.0 litre/min at 0.5 litre/min increments. Readings were obtained for both polyethylene and waxed glass packings. The experimental data is tabulated in Appendix 2.1.

□ *Experimental Observation*

As the air velocity was increased, there came a point when water started to accumulate at the packing support plate. On further increase in the air velocity, the water started to fill the column, eventually reaching the top surface of the bed and accompanied by severe water entrainment in the air outlet. The column was completely flooded at this point. For the polyethylene spheres which are less dense than water, an additional phenomena occurred: the bed tended to fluidise slightly as water started to fill the voids between the spheres. At the extreme end, the whole bed fluidised severely when the water level reached the top of the bed.

□ *Polyethylene Packing*

Figure 6.4 is the linear plot of bed pressure drop versus air volumetric flowrate whilst Figure 6.5 shows the log-log plot of bed pressure gradient versus air superficial mass velocity for the polyethylene packing. Physical properties of air and water were taken at 15°C and 1 atm.
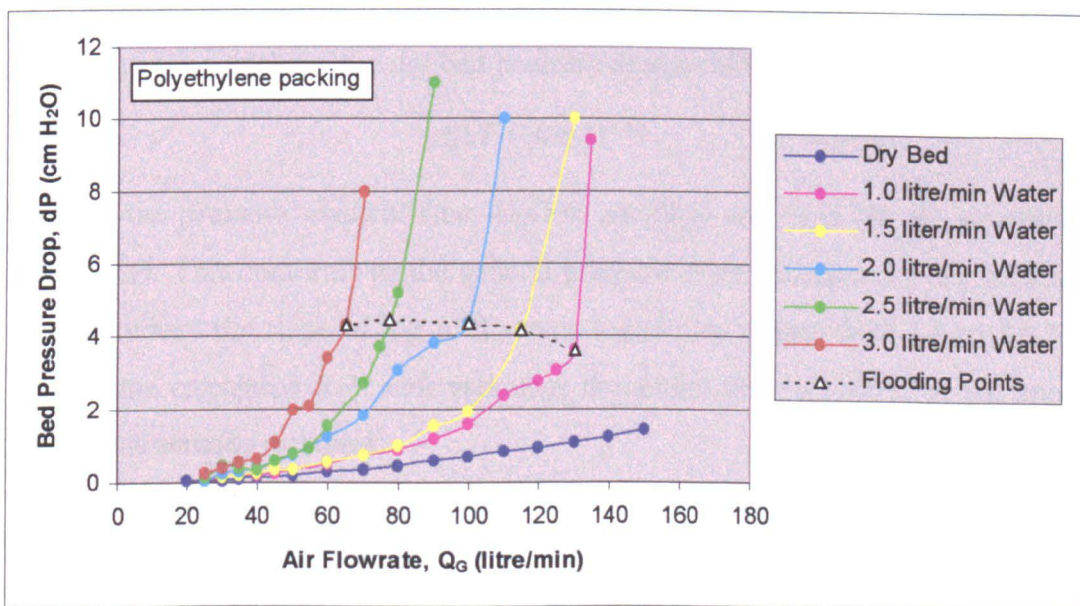
Figure 6.4 Variation of bed pressure drop with air volumetric flowrate for polyethylene packing.
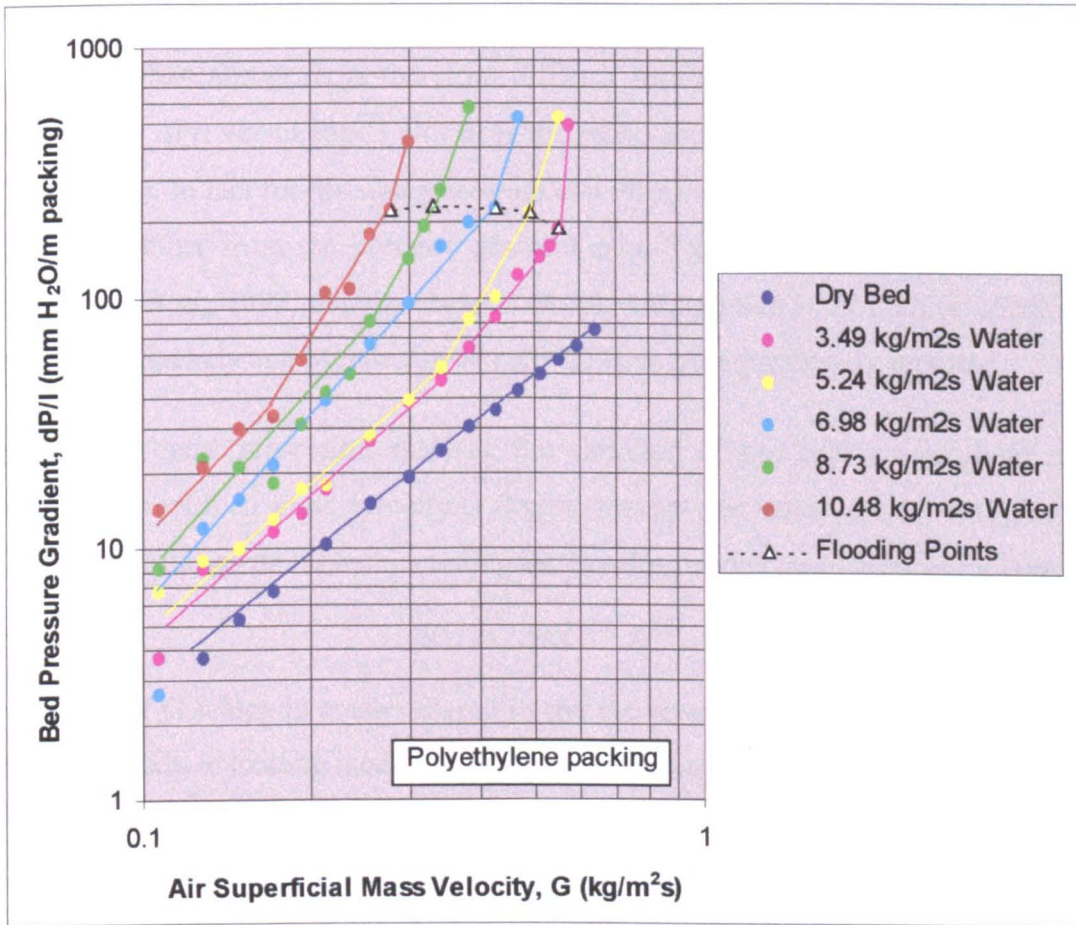
Figure 6.5 *Variation of bed pressure gradient with air mass velocity on logarithmic axes for polyethylene packing.*

The Reynolds number Re* (equation 3.4) for flow through the dry packed bed of polyethylene spheres was relatively low, ranging from 82 to 617, suggesting that the flow is in the transition regime i.e. between fully laminar (Re* < 1) and fully turbulent flows (Re* > 2000). However using linear regression analysis, the dry bed pressure drop could be described by the equation:

$$\Delta P/l = 180 \, G^{1.88} \qquad (R^2 = 1.00) \qquad (6.14)$$

where $\Delta P/l$ is the pressure gradient (mm H_2O/m packing) and G is the air superficial mass velocity (kg/m^{2}s). This conforms to the general pressure drop variation for dry packing under turbulent flow where the slope of log $\Delta P/l$ versus log G plot ranges from 1.8 to 2.0 (Treybal, 1980). Hence the calculated Re* underestimates the actual flow condition in the packed bed and the flow was actually turbulent.

The pressure gradient plots for the irrigated bed in Figure 6.5 become steeper as the air velocity increases. At the low end of the air velocity, their gradients approximate that of the dry packed bed. Although an attempt has been made in Figure 6.5 to represent the data points

in terms of segments of constant slopes where possible, it is clear that the rise in gradient is gradual rather than abrupt. It is therefore difficult to ascertain the loading point where the slope of the log $\Delta P/l$ versus log G plot rises distinctly above 2, following the definition given by White (1935). In fact for the water flowrate at 6.98 kg/m^{2}s, the lower break point seemed to be absent altogether from the pressure gradient plot. The difficulty of locating the loading point (McCabe *et al.*, 1993) and the absence of the loading point itself (White, 1935; Bain and Hougen, 1944; Szekely and Mendrykowski, 1972) have been previously reported.

Using multiple linear regression analysis, the variation of bed pressure gradient $\Delta P/l$ (mm H$_2$O/m packing) with air mass velocity G (kg/m^{2}s) and water mass velocity L (kg/m^{2}s) for all the air flowrate settings up till and including the flooding points was found as follows:

$$\Delta P/l = 134 \, G^{2.44} \, L^{1.31} \qquad (R^2 = 0.93) \qquad (6.15)$$

The exponent of G which is greater than 2 in the above equation suggests that in general, the system was already in loading mode up till the onset of flooding.

The nearly vertical rise in the slope of the pressure drop curve at the higher air velocity end marked the flooding point. These flooding air velocities were compared against experimental observations. Visual indicators of flooding during the experiments (i.e. water accumulation throughout the packed bed and wild pressure drop fluctuations) at these air velocities or in the vicinity further confirmed the onset of flooding. The pressure gradient at the flooding points ranges from 189 to 234 mm H$_2$O/m packing, agreeing with those reported in the literature i.e. 150 to 250 mm H$_2$O/m packing (McCabe *et al.*, 1993).

❑ *Waxed Glass Packing*

Figure 6.6 is the linear plot of bed pressure drop versus air volumetric flowrate whilst Figure 6.7 shows the log-log plot of bed pressure gradient versus air superficial mass velocity for the waxed glass packing. Physical properties of both air and water were taken at 15°C and 1 atm.

Linear regression gives the following equation for the pressure drop variation of the dry bed:

$$\Delta P/l = 158 \, G^{1.80} \qquad (R^2 = 1.00) \qquad (6.16)$$

Again, the exponent on G shows that the flow in the dry packed bed is turbulent, although the Reynolds number through the packed bed Re*, which ranges from 108 to 820 seems to indicate a transitional regime.
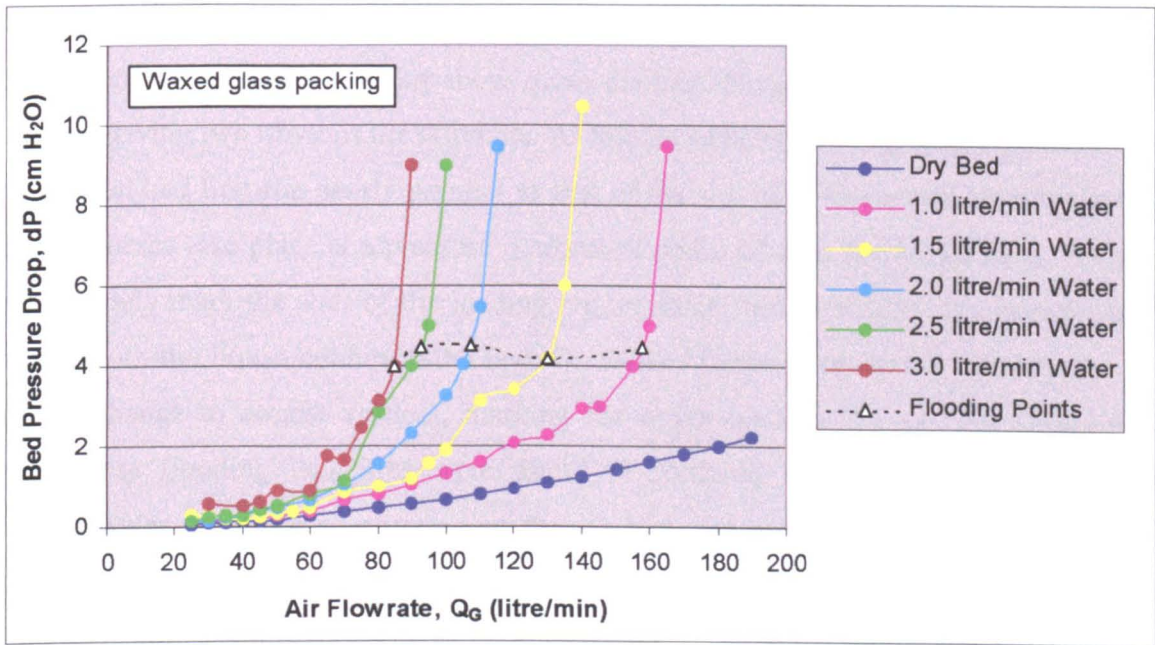
Figure 6.6 *Variation of bed pressure drop with air volumetric flowrate for waxed glass packing.*
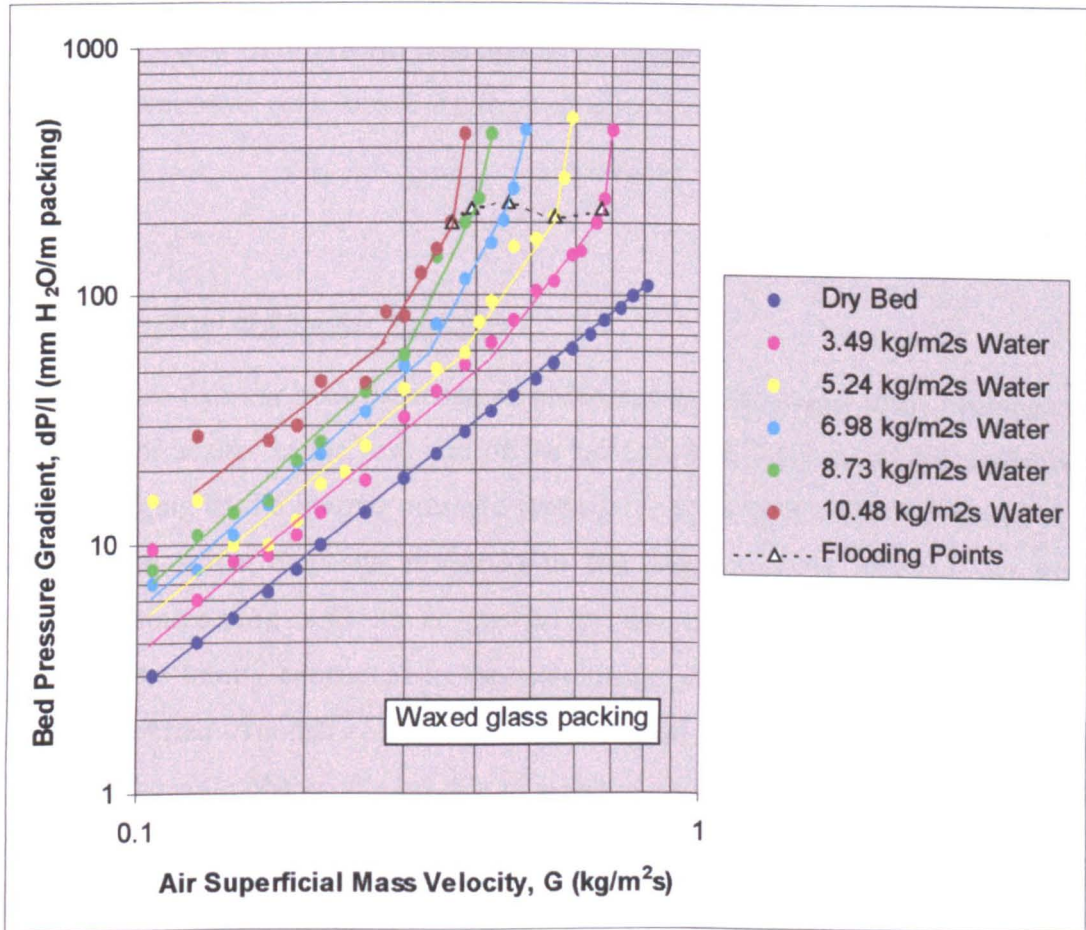
Figure 6.7 *Variation of bed pressure gradient with air mass velocity on logarithmic axes for waxed glass packing.*

Compared to the log $\Delta P/l$ versus log G plots of the irrigated polyethylene packing, the plots for the irrigated waxed glass packing show more distinct changes in slopes as the air velocity increases, giving two obvious break points. At low air velocities, the pressure gradient lines of the irrigated bed first run nearly parallel to that of the dry bed. The lower break point for the irrigated curves take place at a pressure gradient of about 60 mm H_2O/m packing. This would approximately mark the start of the loading region where the increasing gas velocity starts to interfere with the liquid holdup in the bed. On further increase of the air velocity, the curves abruptly change to almost vertical, marking the upper break point i.e. the flooding point. Again, these flooding velocities were found to coincide with experimental observations whereby water accumulated throughout the packed bed and bed pressure drop fluctuated widely at or near these gas velocities. The pressure gradient at the flooding points ranges from 200 to 239 mm H_2O/m packing which are nearly the same or slightly higher that those of the polyethylene packing (189 to 234 mm H_2O/m packing).

Multiple linear regression analysis gives the following equation for the variation in bed pressure gradient $\Delta P/l$ (mm H_2O/m packing) of the irrigated waxed glass packing with air G (kg/m^{2}s) and water mass velocities L (kg/m^{2}s) up till and including the flooding point:

$$\Delta P/l = 135\, G^{2.10}\, L^{0.89} \qquad (R^2 = 0.92) \qquad (6.17)$$

☐ *__Pressure Drop at Low Air Velocities__*

The pressure drop data for both the irrigated polyethylene and waxed glass packings shows a greater degree of scatter at the low end of the air flowrate. This could be attributed to the occasional plugging of the bottom pressure tapping by water that went undetected at low air velocities as the water blockage remained in the brass pressure tapping. At higher air velocities, the water plug tends to be pushed by the air pressure in the column into the transparent plastic tubing connected to the manometer; the water blockage was then visible and could be rectified. Another cause of this scatter could be attributed to noise from pressure fluctuations at the base of the column due to a changing flow pattern as the air stream alters direction as it enters through the air injector. The noise effect becomes more pronounced at very low bed pressure drop. In addition, the gas flow might not be completely turbulent at the low air flowrates, hence the slope at the lower end of the gas rate might be less than 2. This could be seen from the first few data points on the plots for 3.49, 5.24 and 10.48 kg/m^{2}s water rate on Figure 6.7 which tend to horizontal lines.

❏ *Flooding Conditions*

The table below summarises the flooding conditions obtained. The waxed glass packing exhibited higher flooding gas velocities than the polyethylene packing. This is attributed to the slightly higher degree of non-wettability of the former compared to the latter. The water-solid contact angle is 109° for paraffin wax surface (Craig *et al.*, 1960) and 95° for polyethylene surface (Adamson and Gast, 1997).

Table 6.10 *Flooding conditions for polyethylene packing and waxed glass packing.*

Polyethylene spherical packing					
Water flowrate		Air flooding flowrate		Pressure drop at flooding	
Q_L litre/min	L kg/m^{2}s	$Q_{G, flooding}$ litre/min	$G_{flooding}$ kg/m^{2}s	$\Delta P_{flooding}$ cm H_2O	$\Delta P/l_{flooding}$ mm H_2O/m packing
1.0	3.49	130	0.56	3.60	189
1.5	5.24	115	0.49	4.19	221
2.0	6.98	100	0.43	4.38	231
2.5	8.73	78	0.33	4.45	234
3.0	10.48	65	0.28	4.32	227
Waxed glass spherical packing					
Water flowrate		Air flooding flowrate		Pressure drop at flooding	
Q_L litre/min	L kg/m^{2}s	$Q_{G, flooding}$ litre/min	$G_{flooding}$ kg/m^{2}s	$\Delta P_{flooding}$ cm H_2O	$\Delta P/l_{flooding}$ mm H_2O/m packing
1.0	3.49	158	0.67	4.50	225
1.5	5.24	130	0.56	4.20	210
2.0	6.98	108	0.46	4.52	239
2.5	8.73	93	0.40	4.50	225
3.0	10.48	85	0.36	4.00	200

Physical properties of air and water were taken at 15°C and 1 atm.

❏ *Reproducibility of Flooding Points*

Good reproducibility of the flooding velocities was obtained as demonstrated in Figure 6.8 and Table 6.11 based on the waxed glass packing data. Although there tend to be some discrepancies between the bed pressure drop taken at the two different test runs, this is relatively unimportant in this case as the flooding points are the matter of concern in this study. The exact pressure drop values are not essential, instead it is the variation in the dependence of bed pressure drop with gas velocity which is the focus herein. As Figure 6.8

and Table 6.11 illustrate, the upper inflexion point on the pressure drop curve representing the flooding point for each water flowrate occurs at approximately the same air flowrate for both test runs.
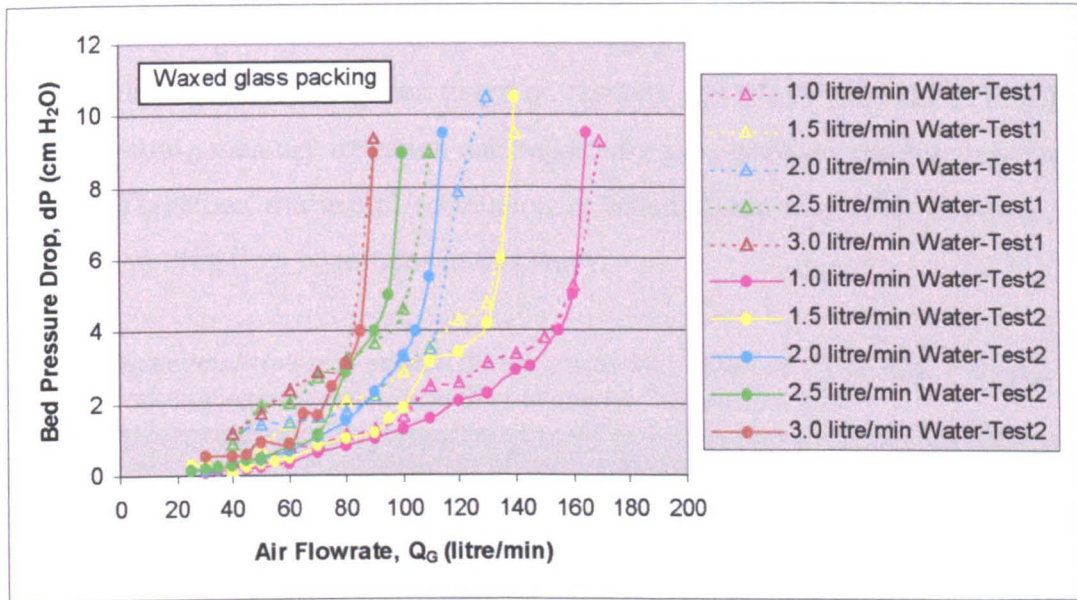
Figure 6.8 Pressure drop data for waxed glass packing obtained from two separate test runs.

Table 6.11 Flooding velocities for waxed glass packing obtained from two separate test runs.

Water flowrate, Q_L (litre/min)	Flooding air flowrate, $Q_{G, flooding}$ (litre/min)	
	Test 1	Test 2
1.0	155	158
1.5	130	130
2.0	110	108
2.5	95	93
3.0	80	85

6.3.2 Applicability of Piche *et al.*'s Neural Correlation

Piche *et al.* (2001a) compared the accuracy of their neural correlation in predicting flooding capacities and those of 14 other existing correlations against a wide collection of flooding data available in the literature. The three existing correlations demonstrating similar if not better predictive accuracies than the neural correlation were the semi-empirical correlations of Billet and Schultes (1995) and Mackowiak (1990), plus Kister and Gill's (1991) generalised pressure drop correlation. However it was not possible to test out these three correlations against the flooding data obtained from this study as they either require empirically determined packing factors or packing constants which are only available for conventional commercial packings,

and not for spherical packing as used in this study. On the other hand, Piche *et al.*'s neural correlation which is readily available as a spreadsheet of counter-current randomly packed bed simulator (Piche *et al.*, 2001c) is without the constraints of packing factors or packing constants. The packing effect is included in terms of the porosity, sphericity and the specific surface area of the packed bed which are all readily available for the spherical packing. Furthermore, the correlation has been tested on Szekely and Mendrykowski's (1972) flooding data on non-wetting mercury irrigation and reportedly gave average absolute relative error as low as 14%. Therefore, the neural correlation is tested herein to predict flooding velocities under the non-wetting flow conditions in this study.

Table 6.12 Comparison between predicted flooding velocities based on Piche et al.'s neural correlation against experimentally obtained flooding capacities.

Polyethylene spherical packing			
Water mass velocity L (kg/m^{2}s)	Experimental flooding air mass velocity $G_{flooding}$ (kg/m^{2}s)	Predicted flooding air mass velocity $G_{flooding}$ (kg/m^{2}s)	Absolute relative error (%)
3.49	0.56	0.46	17.9
5.24	0.49	0.34	30.6
6.98	0.43	0.25	41.9
8.73	0.33	0.17	48.5
10.48	0.28	0.11	60.7
			Average absolute relative error = 39.9 %
Waxed glass spherical packing			
Water mass velocity L (kg/m^{2}s)	Experimental flooding air mass velocity $G_{flooding}$ (kg/m^{2}s)	Predicted flooding air mass velocity $G_{flooding}$ (kg/m^{2}s)	Absolute relative error (%)
3.49	0.67	0.48	28.4
5.24	0.56	0.36	35.7
6.98	0.46	0.27	41.3
8.73	0.40	0.19	52.5
10.48	0.36	0.12	66.7
			Average absolute relative error = 44.9 %

Table 6.12 demonstrates that Piche *et al.*'s neural correlation gives poor prediction of the flooding capacities of the non-wettable packing used in this study. In all cases, the neural

correlation underestimates the flooding velocities, the error increasing as the water velocity increases. Although the neural correlation takes into consideration the liquid surface tension, it neglects the surface tension of the solid packing material. Both affect the degree of liquid wetting on the solid packing surface, and hence the amount of liquid held up in the bed which ultimately affects the flooding capacity of the packed bed. Liquid holdup has been mostly found to be higher for wettable packing rather than its non-wettable counterpart (Standish, 1968b; Coughlin, 1969; Van Swaij *et al.*, 1969; Andrieu, 1975; Gaston-Bonhomme *et al.*, 1980). Therefore the non-wettable packing would be expected to sustain a higher flooding velocity than wettable packing. The neural correlation's development was based on pre-existing flooding data mainly obtained from conventional wettable systems using aqueous and organic liquids. Hence although it gives remarkable accuracy in predicting the flooding capacities of conventional systems compared to other existing flooding correlations (Piche *et al.*, 2001a), the neural correlation's extension to non-wettable systems is still limited as demonstrated in Table 6.12.

6.3.3 Comparison of Flooding Points between Wetting and Non-Wetting Systems

The flooding points obtained for the water-irrigated packed bed of polyethylene spheres and paraffin waxed glass spheres are plotted in Figure 6.9. The earlier flooding data for other non-wetting systems available in the literature were plotted using the same axes as those first introduced in the classical generalised flooding correlation of Sherwood *et al.* (1938). Therefore for ease of comparison, Sherwood *et al.*'s axes have been employed as well herein. Sherwood *et al.*'s correlation itself has been included as the basis of comparing the flooding capacity of conventional wetting systems with those that are non-wetting.

The flooding points obtained in this investigation along with those of other non-wetting systems were clearly displaced above Sherwood *et al.*'s (1938) flooding line. Sherwood *et al.*'s graphical flooding correlation was developed using a packed bed of carbon Raschig rings irrigated by water and aqueous organic solutions i.e. essentially wetting systems. With the exception of the flooding data by Elliott *et al.* (1952) and Shavrin *et al.* (1962), the flooding data for the non-wetting systems shown in Figure 6.9 including those of liquid metal irrigated systems show good agreement, having fairly the same displacement above Sherwood *et al.*'s flooding line. The accord between the flooding data of the various non-wetting systems is very encouraging considering the possible scatter due to effects of differing method of packing the column, column diameter, bed height, and experimental technique. This demonstrates a clear

influence of non-wettability on the flooding capacity of packed columns. Even Elliott *et al.* and Shavrin *et al.'s* flooding data on average are located slightly above Sherwood *et al.*'s line, although displaced somewhat lower than the mean non-wetting flooding line.

The y-axis is labelled $\dfrac{G^2 S_B \mu_L^{0.2}}{\rho_G \rho_L g \varepsilon^3}$ with values 10, 1, 0.1, 0.01, 0.001. The x-axis is labelled $\dfrac{L}{G}\sqrt{\dfrac{\rho_G}{\rho_L}}$ with values 0.0001, 0.001, 0.01, 0.1, 1, 10.

Legend:
- This Work: Water irrigated 9.5 mm polyethylene spheres
- This Work: Water irrigated 10.0 mm paraffin waxed glass spheres
- Standish & Drinkwater (1972): Water irrigated waxed packing
- Extrapolation of Standish & Drinkwater (1972): Water irrigated waxed packing
- Sherwood et al. (1938): Water/Aqueous solution irrigated unwaxed packing
- Szekely & Mendrykowski (1972): Mercury irrigated glass & ceramic packing
- Kukarin & Kitaev (1962): Woods Metal irrigated graphite packing
- Elliott et al. (1952): Liquid wax irrigated glass packing
- Tait (1998): Water irrigated 20 mm paraffin waxed polypropylene spheres
- Shavrin et al. (1962): Molten slag irrigated packing

Figure 6.9 *Comparison of flooding capacity of non-wetting systems with the Sherwood et al.'s generalised flooding correlation.*

It is interesting to note that the flooding capacity of the water-irrigated systems could agree well with those of the liquid metal systems. This is despite the fact that the density and surface tension of water (1001 kg/m^3 and 0.073 N/m respectively at 15°C) are markedly lower than those of the liquid metals (13591 kg/m^3 and 0.488 N/m for mercury at 15°C). The one notable characteristic common to the various systems is that the liquid does not wet the solid surface as the contact angle of the liquid with the solid surface is greater than 90°. For example: water on polyethylene surface: 95° (averaged from Adamson and Gast, 1997); water on paraffin wax surface: 109° (Craig *et al.*, 1960); mercury on glass: 128° to 148° (Adamson and Gast,

1997). This implies that for a packed column operating under non-wetting conditions, the liquid-solid packing contact angle exerts a dominating influence on the flooding capacity, overriding the differences in liquid physical properties.

The higher flooding capacity of the non-wetting systems compared to the conventional wetting systems suggests that the amount of liquid held up within the column is lower for the former compared to the latter under the same conditions of fluid flowrates. This deduction is in accord with the observation made by previous investigators (Standish, 1968b; Coughlin, 1969; Van Swaij et al., 1969; Andrieu, 1975; Gaston-Bonhomme et al., 1980) that liquid holdup is mostly higher for wettable packing rather than its non-wettable counterpart. The ability of non-wetting systems to sustain higher fluid velocities than conventional wetting systems before the onset flooding allows a smaller column to be used for a particular set of fluid volume flowrates.

It can also be seen from Figure 6.9 that under the same experimental conditions and with similar packing geometry, the flooding capacity of the waxed glass beads is slightly higher than that of the polyethylene beads; in line with the somewhat larger water-solid contact angle on the paraffin surface (109°) compared to that for the polyethylene surface (95°).

6.3.4 Correlation of Flooding Capacity with Non-Wetting Tendency

Newton et al. (1952) added a surface tension correction factor $(\sigma_{water}/\sigma_L)^3$ to the abscissa of Sherwood et al.'s (1938) flooding correlation whilst Standish and Drinkwater (1972) added a nearly similar factor of $(\sigma_{water}/\sigma_L)^{2.5}$ to the abscissa to account for varying liquid surface tensions. The addition of these factors might help to reduce the scatter in the flooding data due to differing liquid systems provided that the same type of solid packing is used. However as demonstrated in Figure 6.9, the flooding capacity is evidently affected by the non-wettability of the system. The degree of non-wettability is not just influenced by the type of irrigating liquid, but by the type of solid packing surface as well i.e. its critical surface tension.

The critical surface tension of a solid σ_c determines the wetting or non-wetting tendency of a liquid on the solid surface. Liquids with surface tensions σ_L greater than σ_c will form discrete drops (i.e. non-wetting) whilst those with smaller surface tensions will spread on the solid surface (i.e. wetting).

To account for the non-wetting tendency of a particular solid-liquid system, an additional

factor $(\sigma_c/\sigma_L)^{0.53}$ has been added onto the ordinate of the flooding plot in Figure 6.10 which otherwise still retains the same parameters on the axes as that of Figure 6.9. The ratio σ_c/σ_L is less than unity for non-wetting systems. The greater the non-wetting tendency of the solid-liquid system, the larger the liquid surface tension will be compared to the solid critical surface tension and hence the smaller σ_c/σ_L will be. The decrease in the ratio σ_c/σ_L offsets the higher flooding velocity. This maintains the flooding points of the non-wetting system close to or exactly on the Sherwood *et al.*'s generalised flooding correlation as depicted in Figure 6.10. The scatter in the flooding points of the non-wetting systems has been slightly reduced by the introduction of the $(\sigma_c/\sigma_L)^{0.53}$ factor onto the ordinate.

The y-axis is labelled $\dfrac{G^2 S_B \mu_L^{0.2}}{\rho_G \rho_L g \varepsilon^3}\left(\dfrac{\sigma_c}{\sigma_L}\right)^{0.53}$ and the x-axis is labelled $\dfrac{L}{G}\sqrt{\dfrac{\rho_G}{\rho_L}}$

Legend:
- This Work: Water irrigated 9.5 mm polyethylene spheres
- This Work: Water irrigated 10.0 mm paraffin waxed glass spheres
- Standish & Drinkwater (1972): Water irrigated waxed packing
- Extrapolation of Standish & Drinkwater (1972): Water irrigated waxed packing
- Sherwood et al. (1938): Water/Aqueous solution irrigated unwaxed packing
- Szekely & Mendrykowski (1972): Mercury irrigated glass & ceramic packing
- Tait (1998): Water irrigated 20 mm paraffin waxed polypropylene spheres

Figure 6.10 Correlation of flooding capacity with the non-wetting tendency of solid-liquid system.

The values of surface tensions used for the different non-wetting systems are listed in Table 6.13. Only the flooding points of the non-wetting systems with available surface tension values have been included in Figure 6.10.

Table 6.13 Surface tension values used in Figure 6.10.

System	Solid Critical Surface Tension, σ_c (dynes/cm)	Liquid Surface Tension, σ_L (dynes/cm)	$\dfrac{\sigma_c}{\sigma_L}$	$\left(\dfrac{\sigma_c}{\sigma_L}\right)^{0.53}$
This Work: Water irrigated polyethylene spheres	Polyethylene 31[1]	Water 73[2]	0.42	0.64
This Work: Water irrigated paraffin waxed glass spheres	Paraffin 24[3]	Water 73	0.33	0.55
Standish & Drinkwater: Water irrigated waxed packing	Paraffin 24	Water 73	0.33	0.55
Extrapolation of Standish & Drinkwater: Water irrigated waxed packing	Paraffin 24	Water 73	0.33	0.55
Szekely & Mendrykowski: Mercury irrigated glass & ceramic packing	Glass 170[4]	Mercury 488[5]	0.35	0.57
Tait: Water irrigated paraffin waxed polypropylene spheres	Paraffin 24	Water 73	0.33	0.55

1. Osipow, 1962; Zisman, 1964; Clayfield *et al.*, 1985.
2. Lide (1999) at 15°C, 1 atm.
3. Average value of 22 to 26 dynes/cm from Lyman *et al.* (1965).
4. Lyman *et al.* (1965).
5. Lide (1999) at 15°C, 1 atm.

6.3.5 Implication for Hot Scrubber

The flooding capacity of the hot gas scrubber irrigated by molten tin can be estimated using the generalised flooding correlation in Figure 6.10. Knowing the critical surface tension of the packing material and the physical properties of the molten tin including its surface tension at the operating temperature of the scrubber, the gas flooding velocity at a particular liquid metal flowrate can be determined. A stable gas-liquid operating range can thus be obtained. In the event that the critical surface tension of the packing material is unavailable, then the average flooding line of the non-wetting systems in Figure 6.9 has to be used instead.

6.3.6 Analysis of Errors

❑ *Measured Quantities*

The sensitivity of instruments used in the flooding tests and the corresponding error in the measured quantities are summarised in Table 6.14.

Table 6.14 Errors in measured quantities for flooding tests.

Apparatus/ Instrument	Measured Quantity	Smallest Instrument Graduation or Sensitivity	Smallest Reading Obtainable	Absolute Error on Measured Quantity
Air rotameter	Air volumetric flowrate	5 litre/min	5 litre/min	±2.5 litre/min
Water rotameter	Water volumetric flowrate	0.1 cm Calibration chart average gradient = 5.8 cm/1.0 litre/min.	0.02 litre/min	±0.01 litre/min
Manometer ≥ 10 cm H$_2$O < 10 cm H$_2$O	Column pressure drop	0.1 cm H$_2$O	0.05 cm H$_2$O	±0.03 cm H$_2$O ±0.005 cm H$_2$O
Measuring tape	Packed bed height; Column diameter	0.1 cm	0.1 cm	±0.05 cm

The error of the column pressure drop reading was dependent on the manometer tube position. When the tube was in the vertical position, the manometer gave the actual pressure drop reading. However when the tube was in the bottom and top inclined positions, the apparent reading on the manometer must be multiplied by a factor of 0.1 and 0.2 respectively to give the actual reading. These conversion factors affect the absolute errors of the final pressure drop readings. At 10 cm H$_2$O and above, the vertical tube position was used. The errors of pressure drop readings were then within ±0.03 cm H$_2$O (rounded off from ±0.025 cm H$_2$O). Below 10 cm H$_2$O, the top inclined tube position was used. This meant that every apparent reading was multiplied by a factor of 0.2 to give the actual reading, yielding an equivalent error of ±0.005 cm H$_2$O (from ±0.025 cm H$_2$O × 0.2).

❏ *__Bed Pressure Gradient__*

The bed pressure gradient $\Delta P/l$ is the ratio of the measured quantities of bed pressure drop ΔP to the bed height l. Hence the percentage error on the bed pressure gradient is as follows:

$$\left(\frac{e_{\Delta P/l}}{\Delta P/l}\right) \times 100\% = \sqrt{\left(\frac{e_{\Delta P}}{\Delta P}\right)^2 + \left(\frac{e_l}{l}\right)^2} \times 100\% \qquad (6.18)$$

The percentage error on $\Delta P/l$ decreases as the air flowrate increases i.e. as the pressure drop increases. The contribution from the fractional error of bed height remains the same for the same packing. For the polyethylene packing, the calculated percentage error on $\Delta P/l$ ranges

from ±0.3% to ±10% whilst that of the waxed glass packing ranges from ±0.3% to ±8%, both for operation until flooding.

The ±0.3% error calculated for the bed pressure gradient at the high air flowrate end is overly optimistic. This is due to stark error in readings caused by pressure fluctuations during flooding at high air flowrates. The absolute error associated with the individual pressure drop reading from the manometer would be significantly greater than the figures listed in Table 6.14 in the presence of pressure fluctuations. The largest fluctuation magnitude was about 1.5 cm H_2O, giving an absolute error in ΔP readings of about 0.8 cm H_2O. Hence the actual error associated with the pressure gradient at the high air flowrate end during flooding is in the vicinity of ±10%.

❏ *Fluid Superficial Mass Velocities*

The superficial mass velocities of air G (kg/m²s) and water L (kg/m²s) were derived from the measured quantities of fluid volumetric flowrates Q_G, Q_L (litre/min) and the column diameter D_{col} (cm):

$$G \propto \frac{Q_G}{D_{col}^2} \quad \text{and} \quad L \propto \frac{Q_L}{D_{col}^2}$$

Hence the fractional errors on G and L are calculated as follows:

$$\frac{e_G}{G} = \sqrt{\left(\frac{e(Q_G)}{Q_G}\right)^2 + \left(2 \times \frac{e(D_{col})}{D_{col}}\right)^2} \quad \text{and} \quad \frac{e_L}{L} = \sqrt{\left(\frac{e(Q_L)}{Q_L}\right)^2 + \left(2 \times \frac{e(D_{col})}{D_{col}}\right)^2} \quad (6.19)$$

The percentage error on G and L decreases as the fluid flowrate increases. The contribution from the fractional error of column diameter is a constant. The percentage error on G ranges from ±2% to ±10% whilst that of L ranges from ±1% to ±2%.

The physical properties of the fluids were taken at 15°C and 1 atm. The highest recorded bottom pressure of the column within the operating fluid flowrates used was 16.8 cm H_2O gauge pressure which is just higher than atmospheric pressure by a factor of 0.016. Hence there is negligible error in taking the air density at 1 atm.

6.4   Cold Gas Scrubber Studies: Liquid Holdup

Static and dynamic liquid holdups were measured for the polyethylene packed bed with water flowrate ranging from 1.0 to 2.5 litre/min and air flowrate starting from 40 litre/min until flooding velocities were reached. The experimental data is tabulated in Appendix 2.2.

6.4.1   Static Holdup

❑ *Results and Analysis*

The results of the static holdup test are illustrated in Figure 6.11. The static holdup was independent of the air velocity, however there was a small but definite decrease in static holdup as water velocity increased. The static holdup decreased from an average value of 3.46 to 3.02 vol. % of packing as water velocity increased from 0.35 to 0.87 cm/s. The average static holdup $\bar{h}_s$ (vol. %) is related to the water superficial velocity u_L (m/s) as follows:

$$\bar{h}_s = 1.40 \; u_L^{-0.16} \qquad (R^2 = 0.93) \qquad (6.20)$$
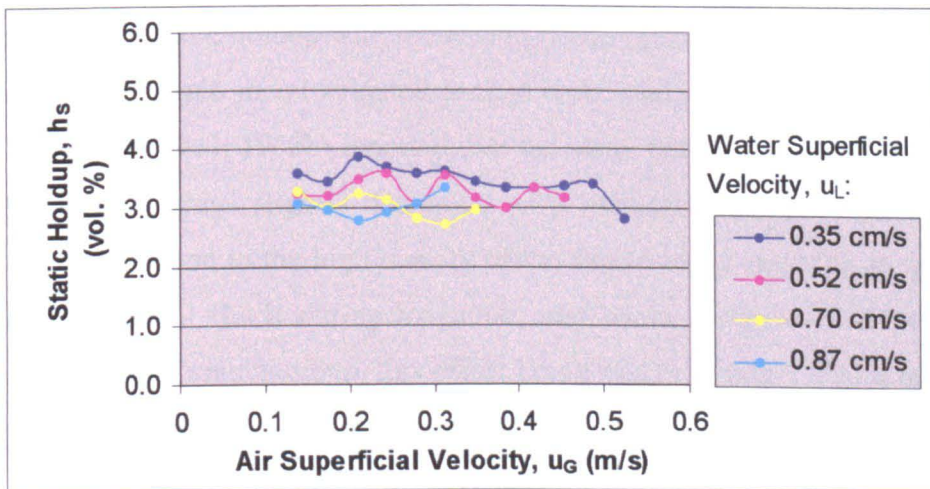
Figure 6.11 Variation of static holdup with air and water superficial velocities.

❑ *Comparison With Other Work*

The static holdup of conventional wetting systems (water irrigation of ceramic and carbon packings) has been reported to be independent of variations in gas and liquid flowrates but is a function of the nature of the packing and the liquid physical properties (Jesser and Elgin, 1943; Shulman *et al.*, 1955a, 1955b). Static holdup was thought to be made up of very stagnant pools protected in the packing interstices. The liquid in the static holdup rapidly

becomes equilibrated with the adjacent gas while it is only replaced very slowly by fresh liquid. It was therefore deduced that the semi-stagnant static holdup is relatively ineffective to mass transfer in an absorption process (Shulman *et al.*, 1955a).

In contrast, the results of this study show that the static holdup for a packed column operating under non-wetting flow conditions is affected by liquid flowrates, the static holdup decreasing slightly as water flowrate increases. The apparent decrease in static holdup with water flowrates demonstrates its actual mobility. This is attributed to the tendency of water to form discrete droplets rather than a spreading film on the hydrophobic surface of polyethylene spheres which encourages water turnover in static holdup sites. The water droplets held in the interstices of the non-wettable packed bed are more easily displaced at high water flowrates than the semi-stagnant pools formed in wetting flow conditions. This is supported by the observed mobility of droplets held at packing intersections from the high-speed video footage taken during the flow visualisation exercise. Therefore the static holdup in a non-wetting flow packed bed system provides a relatively more effective contribution to mass transfer in a gas absorption process than a conventional wetting system.

The slight decrease in static holdup with increasing liquid rate observed in this study has been similarly reported for liquid metal irrigated packed beds which are also non-wetting. Warner (1959a) and Standish (1963, 1968b) reported that the static holdup for mercury irrigated steel and porcelain Raschig rings slightly decreased with increasing mercury flowrates. Warner attributed this phenomenon to the high density of the liquid metal resulting in greater kinetic energy than conventional fluids during irrigation, and hence the greater ability to disperse semi-stagnant pockets of static holdup, this effect being higher at larger liquid rates. However similar observation in the present study using water irrigation with density vastly smaller than that of mercury (1001 kg/m^3 and 13591 kg/m^3 respectively at 15°C) suggests that the effect of liquid rate on static holdup more likely arises from the non-wetting flow condition in the packed bed common to both systems as discussed in the preceding paragraph.

The independence of the static holdup from the gas velocity in this study is in accord with the general observation made on static holdup for both conventional wetting systems (Jesser and Elgin, 1943; Shulman *et al.*, 1955a, 1955b) and other non-wetting system (Warner, 1959a).

The magnitude of the static holdup obtained from this study is compared with those of other non-wetting systems in Table 6.15 under a nearly similar liquid superficial velocity range.

Table 6.15 The influence of bed porosity on static holdup in non-wetting systems.

System	Dry Bed Porosity ε	Liquid Superficial Velocity u_L (cm/s)	Static Holdup h_S (vol. %)
This Work: Water irrigated 9.53 mm polyethylene spheres. Air flow.	0.45	0.35 – 0.87	3.46 – 3.02
Standish (1963): Mercury irrigated ¼ in. porcelain Raschig rings. Zero gas flow.	0.63	0.34 – 0.73	6.92 – 6.13
Standish (1963): Mercury irrigated ¼ in. steel Raschig rings. Zero gas flow.	0.72	0.31 – 0.69	10.83 – 10.06
Warner (1959a): Mercury irrigated ¼ in. steel Raschig rings. N_2 gas flow.	0.72	0.36 – 0.67	12.22 – 10.33
Warner (1959a): Mercury irrigated ¼ in. steel Raschig rings. H_2 gas flow.	0.72	0.32 – 0.73	10.57 – 9.72
Warner (1959a): Mercury irrigated ¼ in. steel Raschig rings. N_2 atmosphere.	0.72	0.28 – 0.57	12.86 – 11.86
Warner (1959a): Mercury irrigated ¼ in. steel Raschig rings. H_2 atmosphere.	0.72	0.40 – 0.72	11.22 – 10.85

It is evident that the relative magnitude of the static holdup is dependent on the bed porosity. The smallest porosity is that of the polyethylene spheres used in this study ($\varepsilon = 0.45$), resulting in a correspondingly lowest static holdup of about 3 to 3.5 vol. %. This is followed by the porcelain Raschig rings ($\varepsilon = 0.63$), its static holdup about 6 to 7 vol. %. The highest porosity is that of the steel Raschig rings ($\varepsilon = 0.72$), with the correspondingly largest static holdup ranging from 10 to 13 vol. %. Unlike Raschig rings, the rounded external surface coupled with the absence of open, internal surface on the spherical packing does not allow much potential for liquid accumulation except at points of contact between adjacent spheres.

6.4.2 Dynamic Holdup

❑ *Results and Analysis*

The dynamic holdup for the water irrigated polyethylene packing was found to increase with both the air and water rates, with a greater dependence on the liquid rate as depicted in Figures 6.12 and 6.13. Note that the dynamic holdup considered herein is the 'net' value after

deducting the contribution due to 'end effects' i.e. the water held up in the water distributor above the packed bed and the bottom reservoir below the packed bed.
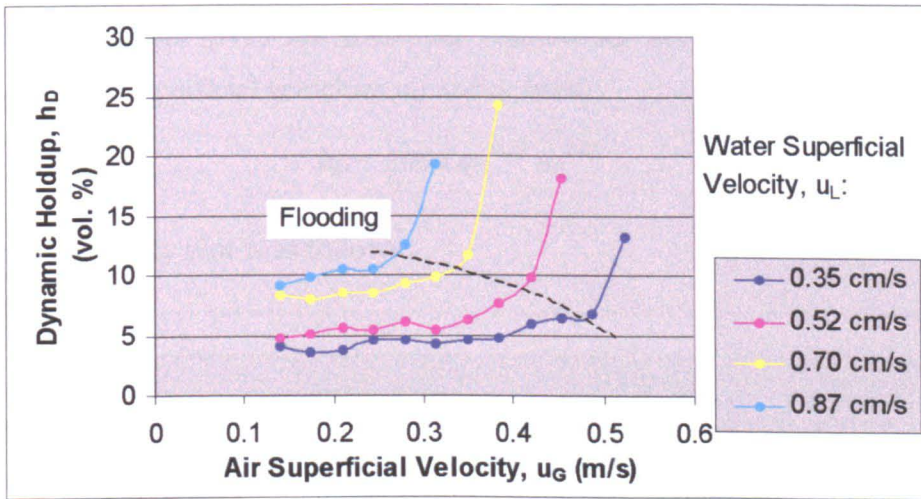
Figure 6.12 Variation of dynamic holdup with air and water superficial velocities.
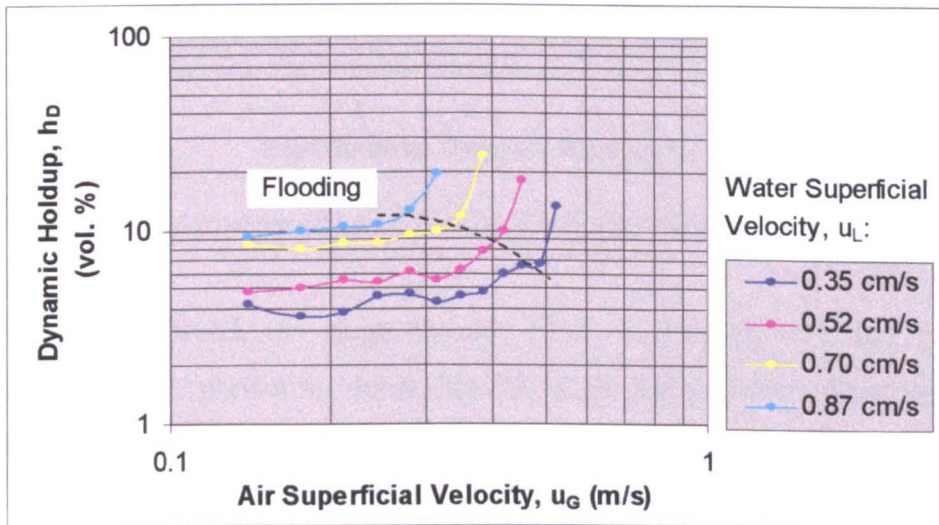
Figure 6.13 Variation of dynamic holdup with air and water superficial velocities, plotted on logarithmic axes.

At low air velocities, the dynamic holdup remains relatively unaffected by the air rates although it evidently increases with water rates. As the air velocity increases, the air flow becomes sufficiency high at one point such that it starts to interfere with the downward flow of the liquid. This is the loading region in which the dynamic holdup curve shows a more obvious rise with air velocity. On further increase in the air velocity, the liquid holdup increases rapidly, filling the interstices in the packed bed and finally giving rise to flooding of

the column. The sudden rapid rise in the dynamic holdup curve corresponds with visually observed flooding during the experimental study.

For operation at gas rate below the inflexion point (flooding point) on Figure 6.12, multiple linear regression analysis gives the following relationship between the dynamic holdup h_D (vol.%) and the fluid superficial velocities u_G and u_L (m/s):

$$h_D = 2000\, u_G^{0.33}\, u_L^{1.01} \qquad (R^2 = 0.90) \qquad (6.21)$$

The corresponding parity plot is as follows:
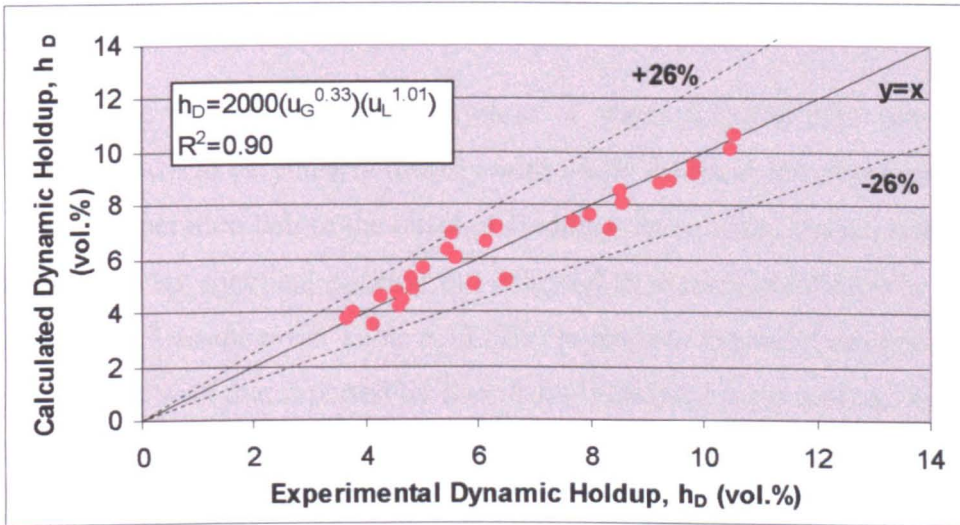
Figure 6.14 Parity plot of experimental and correlated values of dynamic holdup.

The gas velocities at which the slope abruptly rises on Figures 6.12 and 6.13 coincide extremely well with the previously determined flooding gas velocities determined from the upper break point on the bed pressure drop versus air rate plot in Figures 6.4 and 6.5 in Section 6.3.1. This is shown in Table 6.16. Again, this demonstrates the good reproducibility of the flooding velocities.

Table 6.16 Comparison of gas flowrate at inflexion point on dynamic holdup-gas rate plot with flooding gas flowrate determined from upper break point on bed pressure drop-gas rate plot for polyethylene packing.

Water flowrate Q_L (litre/min)	Air flowrate at inflexion point on h_D-gas rate plot (litre/min)	Air flowrate at flooding from ΔP-gas rate plot (litre/min)
1.0	135	130
1.5	115	115
2.0	95	100
2.5	75	78

❏ *<u>Comparison With Other Work</u>*

The dynamic holdup recorded in this investigation generally agrees with the dynamic holdup trend of wetting (Shulman *et al.*, 1955b) as well as non-wetting systems (Coughlin, 1969) in that it is mainly a function of liquid flowrate and the effect of gas rate becoming evident only beyond the loading point. The dynamic holdup of liquid metal irrigation has also been reported to increase with both liquid rate (Standish, 1968a) and gas rate (Warner, 1959a).

The break point in the log-log plot of dynamic holdup versus air velocity in Figure 6.13 coincided with visually observed flooding during the experimental study. This has also been documented by Elgin and Weiss (1939).

The dynamic holdup for the non-wetting system of water-irrigated 9.53 mm polyethylene spheres has been shown to vary nearly linearly with water flowrate, the exponent on the liquid rate being 1.01 for operation before the onset of flooding. In contrast, the exponent reported in the literature for similar spherical packing but irrigated at wetting conditions is lower, on the whole being about 0.7 as shown in Table 6.17. The liquid rate exponent obtained in this study is in close agreement with that reported by Standish (1968a) for rings and saddles irrigated by the liquid metals of cerrobend and mercury as well as non-wetting water. Standish documented that the dynamic holdup in his system varied as the 0.95 power of liquid rate.

Table 6.17 *The dependence of dynamic holdup on liquid rates for spherical packing under wetting conditions.*

System	Exponent B for $h_D \alpha$ (Liquid rate)[B]

Simmons and Osborne (1934):
    0.592 inch spheres
    0.726 inch spheres
	
	0.714
	0.727

Elgin and Weiss (1939): 0.5 inch spheres	 0.734

Jesser and Elgin (1943):
    0.5 inch spheres
    0.75 inch spheres
    1 inch spheres
	
	0.672
	0.654
	0.655

6.4.3 Total Holdup

The total liquid holdup h_T (vol.%) is the sum of both the static and dynamic holdups. It increased with both air velocity u_G (m/s) and water velocity u_L (m/s) with the latter exerting a

greater influence as described by the following correlation for operation below flooding:

$$h_T = 265 \, u_G^{0.18} \, u_L^{0.58} \qquad (R^2 = 0.88) \qquad (6.22)$$

6.4.4 Comparison with Liquid Metal Irrigation

Despite the pronounced differences in liquid density and surface tension, the liquid holdup trends found in this work for water irrigated polyethylene packing are generally in accordance with those reported for liquid metal irrigation. The notable similarities include the slight decrease in static holdup as liquid rate increases, and the nearly linear relationship between the dynamic holdup with liquid rate for operation before flooding. The accord in liquid holdup trends is attributed to similar non-wetting flow regimes present in the systems, characterised by discrete droplets and rivulets owing to the large liquid-solid contact angle (greater than 90°). The apparent mobility of the static holdup for the packed bed operating under non-wetting condition means that the effective liquid holdup for gas absorption would be expected to be that of the total liquid holdup, and not just limited to the dynamic holdup alone.

6.4.5 Prediction of Total Liquid Holdup

6.4.5.1 Warner's Empirical Correlation

Warner (1959a) put forward an empirical correlation which could be built from a simple packed bed model and then potentially used to estimate liquid holdups on the same packing for any other liquid system, using measurements of gas phase pressure drop, gas velocity and gas density (see Section 3.1.4.3). Based on the liquid holdup measured for a packed bed of ¼ inch steel Raschig rings irrigated by mercury countercurrent to hydrogen and nitrogen flow, an empirical correlation was derived and was reported to apply reasonably well to the holdup data from water irrigation of the same packing.

Warner's method of liquid holdup correlation is tested herein on the holdup data of this study, considering its potential for predicting liquid holdup for the more complex molten tin irrigated hot scrubber based on current hydrodynamics data available from the simpler water-based cold studies.

The derivation of the correlation begins from the Ergun equation describing single phase pressure drop in randomly packed granular beds (Ergun, 1952):

$$\frac{(\Delta P)}{l} = 150 \frac{\mu u}{d^2} \frac{(1-\varepsilon)^2}{\varepsilon^3} + 1.75 \frac{\rho u^2}{d} \frac{(1-\varepsilon)}{\varepsilon^3} \qquad (3.6)$$

laminar component   turbulent component

For high gas flow through the packed bed such that the flow is turbulent, the viscous energy losses can be neglected, hence simplifying the Ergun equation to this form:

$$\frac{(\Delta P)}{l} = \alpha u_G^2 \rho_G \qquad (3.7)$$

For single phase flow, α is a constant, its value depending on the dry bed porosity ε and packing size parameter d, equalling $1.75(1-\varepsilon)/d\varepsilon^3$ as given by the Ergun equation. However in a packed bed through which gas and liquid flow simultaneously, both the effective bed porosity ε_{eff} and the packing size parameter d vary according to the total liquid holdup. Therefore α now becomes a function of the total volumetric liquid holdup H_T (ml) in the packed bed. Also, the gas superficial velocity u_G is now replaced with the true gas velocity U_G taking into account the effective bed voidage ε_{eff}, which has been defined in equation 3.9.

$$U_G = \frac{u_G}{\varepsilon_{eff}} = \frac{u_G}{\varepsilon - h_T} \qquad (6.23)$$

Hence the relationship between the bed pressure drop and the total liquid holdup at a particular true gas velocity is given by the following equation:

$$\frac{(\Delta P)}{f(H_T)} = g(U_G^2 \rho_G) \qquad (6.24)$$

where $f(H_T)$ and $g(U_G^2\rho_G)$ are functions of H_T and $U_G^2\rho_G$ respectively.

For a given value of $U_G^2\rho_G$, let the irrigated bed pressure drop ΔP be the product of the dry bed pressure drop ΔP_{dry} with the function $f(H_T)$:

$$\Delta P = \Delta P_{dry} \times f(H_T) \qquad \text{i.e.} \qquad f(H_T) = \frac{\Delta P}{\Delta P_{dry}} \qquad (6.25)$$

Let $f(H_T) = a + bH_T^c$ where a, b, c are constants. Since $\Delta P = \Delta P_{dry}$ when $H_T = 0$, therefore $a = 1$ and:

$$f(H_T) = 1 + bH_T^c \qquad (6.26)$$

and hence:
$$\frac{\Delta P}{\Delta P_{dry}} = 1 + bH_T{}^c \qquad (6.27)$$

Warner demonstrated that the liquid holdup data from his investigation could be empirically correlated using equation 6.24 in the final form of a 2-parameter power function $y = Ax^B$ where A and B are constants giving a straight line on a log-log plot of $\Delta P/f(H_T)$ versus $U_G{}^2\rho_G$:

$$\frac{(\Delta P)}{1 + bH_T{}^c} = A(U_G{}^2 \rho_G)^B \qquad (6.28)$$

Warner's method of liquid holdup correlation is tested on the liquid holdup data of this study for operation before the onset of flooding. The hydrodynamics data for the polyethylene packing was used which include the irrigated bed pressure drop ΔP (cm H_2O), the dry bed pressure drop ΔP_{dry} (cm H_2O) and the total volumetric liquid holdup H_T (ml) at true gas velocity U_G (m/s). Equation 6.27 was found to take the following form:

$$\frac{\Delta P}{\Delta P_{dry}} = 1 + 9.388 \times 10^{-7} H_T{}^{3.23} \qquad (R^2 = 0.76) \qquad (6.29)$$

The application of equation 6.28 is justified as the gas flow through the polyethylene packed bed has been shown to be turbulent in Section 6.3.1. The final form of the correlation is as follows:

$$\frac{\Delta P}{1 + 9.388 \times 10^{-7} H_T{}^{3.23}} = 0.6563(U_G{}^2 \rho_G)^{1.03} \qquad (R^2 = 0.95) \qquad (6.30)$$
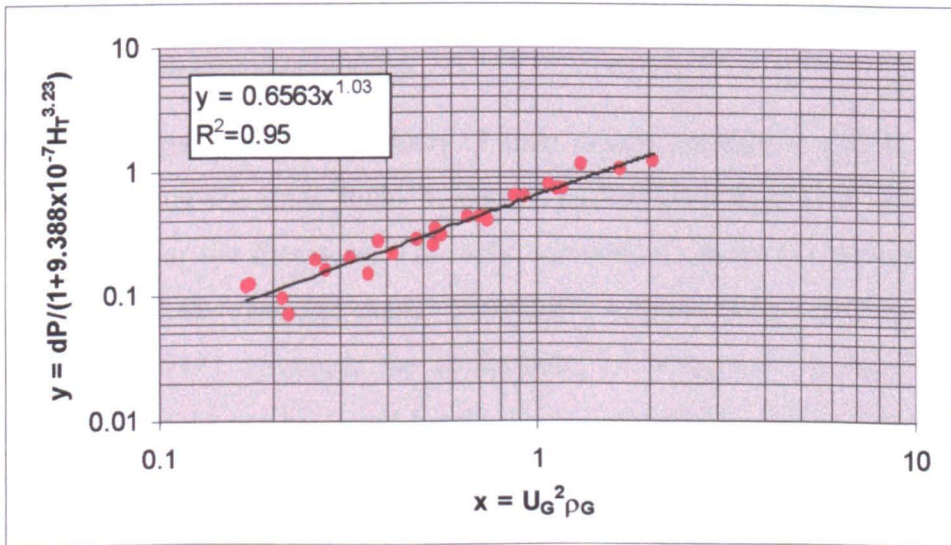
Figure 6.15 Empirical correlation of total liquid holdup data.

The corresponding parity plot is shown in Figure 6.16. All the predicted H_T values fall within ±17% of the experimentally measured values except for a single data point having a relative error of -25%. The average absolute relative error (AARE) of all the predicted H_T values is 7.2 % whilst the standard deviation on the error (s) is 6.1 %. Both the AARE and s are defined in Appendix 3.3. Figure 6.15 shows that the data points are more scattered towards the lower gas velocity end. The gas flow might not have been fully turbulent at these low gas velocities causing the data to deviate from equation 6.30 which assumes turbulent flow. Also, the bed pressure drops and the liquid holdups were measured on separate occasions. As Figure 6.8 in Section 6.3.1 illustrates, the bed pressure drop tends to differ slightly from test to test. These factors would collectively account for the scatter in the parity plot.
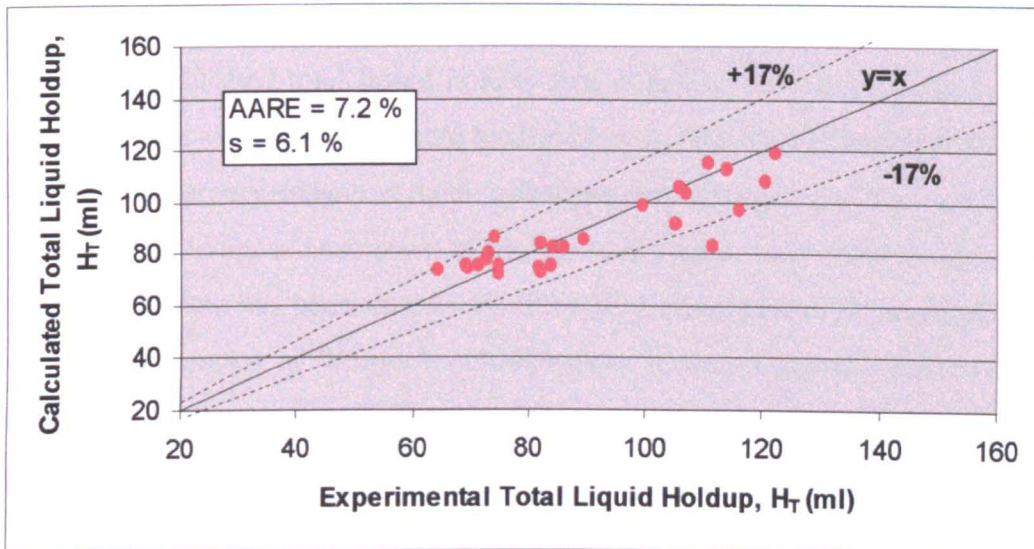
Figure 6.16 Parity plot of experimental and correlated values of total volumetric liquid holdup.

6.4.5.2 Piche et al.'s Neural Correlation

Piche *et al.* (2001b) compared the accuracy of their neural correlation and 11 other existing correlations in predicting the total liquid holdup in packed beds against a wide collection of liquid holdup data from the literature. The only correlation reportedly demonstrating better overall predictive accuracy than the neural correlation was the semi-empirical correlation of Billet and Schultes (1993). However the applicability of Billet and Schultes' correlation to non-wetting systems could not be tested herein due to unavailable packing constants required to apply the correlation. Experimental data on total liquid holdup of non-wetting systems are available from this study for water-irrigated 9.53 mm polyethylene spheres as well as Warner's (1959a) work on mercury irrigated ¼ inch Raschig rings.

On the other hand, Piche *et al.*'s (2001b) neural correlation is available as a spreadsheet of a counter-current randomly packed bed simulator (Piche *et al.*, 2001c) and is not constrained by packing factors or constants. The packing effect is accounted for in terms of the porosity, sphericity and the specific surface area of the packed bed which are all readily available for the spheres and ¼ inch Raschig rings. Furthermore, the neural correlation has been tested on Warner's (1959b) liquid holdup data for molten lead irrigated steel Raschig rings, reportedly yielding average absolute relative error (AARE) as low as 10.7% (Piche *et al.*, 2001b).

Using Piche *et al.*'s (2001c) packed bed simulator, the neural correlation was tested against the liquid holdup data from this study. A poor prediction was obtained. In all cases, the neural correlation overestimated the liquid holdup, the error ranging from 12% to as high as 48%. The average absolute relative error is 30.5% and the standard deviation on the error is 8.0%.

Only two sets of published total liquid holdup data based on molten metal-irrigated packed columns with counter-current gas flow are available in the literature. These are from Warner's (1959a) study on mercury irrigation with hydrogen and nitrogen gas flows, and Warner's (1959b) study of zinc vapour absorption in molten lead. Piche *et al.* (2001b) reported that the molten lead holdup data has been tested with the neural correlation with an AARE of 10.7%. However closer inspection of Warner's (1959b) paper revealed that the molten lead holdup was not experimentally measured, but was in fact estimated based on holdup data from mercury irrigation of the same packed bed in an earlier work (Warner, 1959a). Hence the neural correlation should really be tested on the mercury holdup data rather than the molten lead holdup data. Using Piche *et al.*'s (2001c) packed bed simulator, the neural correlation was tested against the mercury holdup data. A poor prediction was obtained with the neural correlation overestimating the mercury holdup in all cases, yielding an AARE of 52%.

Although the neural correlation considers the liquid surface tension, it ignores the surface tension of the solid packing material. Both factors influence the degree of liquid wetting on the solid packing surface, and therefore the amount of liquid held up in the packed bed. This would account for the failure of the neural correlation to adequately predict the liquid holdup in non-wetting systems. The neural correlation was developed based on pre-existing liquid holdup data mainly derived from conventional wettable systems of water, aqueous and organic liquids. Therefore its overestimation of the liquid holdup for non-wetting systems is consistent with previous findings that liquid holdup is generally higher for wettable packing rather than its non-wettable counterpart (Standish, 1968b; Coughlin, 1969; Van Swaij *et al.*, 1969;

181

Andrieu, 1975; Gaston-Bonhomme *et al.*, 1980). Summing up, although the neural correlation gives relatively good accuracy (relative to other existing liquid holdup correlations) in predicting the total liquid holdup of conventional systems (Piche *et al.*, 2001b), the neural correlation's applicability to non-wettable systems is unsatisfactory as demonstrated herein.

6.4.6   Implication for Hot Scrubber

Liquid holdup affects the gas pressure drop, the loading and flooding points in a countercurrent packed column. It influences the mass transfer efficiency in the packed column, affecting the volumetric mass transfer coefficients in the gas and liquid phases. Therefore it would be useful to be able to predict liquid holdup in the molten tin-irrigated packed bed scrubber where system complexities and experimental difficulties discourage direct measurement of the liquid holdup.

The only correlation method possible for application herein is that of Warner's (1959a). The good fit provided by the empirical correlation (equation 6.30) on total liquid holdup data from the water model following Warner's method is encouraging. Warner has shown that the same holdup correlation holds for both water and liquid metal irrigated systems using the same packing. In the absence of better proven liquid holdup predictive tools for non-wetting systems, the empirical correlation derived from the water model would provide the first approximation of the molten tin total holdup in the hot gas scrubber incorporating a packed bed of similar physical geometry to that of the cold model. The hot scrubber would feature an 8.0 cm inner diameter column filled with 9.53 mm alumina spheres as packing as detailed in Chapter 8. To estimate the static holdup for the liquid metal scrubber, the fluid flows are stopped and the bed drained after each test run, and then the gas flow is put back on and the column pressure drop read immediately. Using these column pressure drop and gas velocity readings together with the gas density, the static holdup can be estimated from the empirical holdup correlation. The difference between the total holdup estimated from pressure drop and gas velocity readings while the scrubber is in operation and the static holdup will give the dynamic holdup.

For the same liquid volumetric flowrate, the molten tin holdup in the hot scrubber is expected to be lower than that of the water holdup in the cold model. This is because both the liquid-solid contact angle and the liquid density are significantly higher for the hot system. Molten tin's contact angle on solid alumina surface is approximately 160° at 300°C (Nogi *et al.*, 1988)

while that of water on solid polyethylene is approximately 95° at 20 to 25°C (Adamson and Gast, 1997). The density of molten tin is 6980 kg/m³ at its melting point of 232°C as opposed to 1001 kg/m³ for water at 15°C. For large contact angles such as these, an increase in contact angle has been found to reduce liquid retention at the contact points of touching spheres under the effect of gravity (Saez and Carbonell, 1990). Since a larger contact angle enables easier liquid droplet displacement whilst a higher liquid density provides greater gravitational effect, the overall result would be improved bed drainage and the reduction in total liquid holdup for the molten tin system relative to the water model.

In the absorption process of hydrogen sulphide gas into molten tin in the hot scrubber, the effective liquid holdup is expected to be that of the total liquid holdup and not just limited to the dynamic holdup alone as in conventional wettable systems. This is attributed to the mobility and high turnover rate of liquid metal in the static holdup sites. Compared to the non-wetting water system, the static holdup of the molten tin irrigated bed is expected to exhibit an even higher rate of movement due to reasons already mentioned in the preceding paragraph.

6.4.7   Analysis of Errors

  ❑ *__Measured Quantities__*

The sensitivity of instruments used in the liquid holdup tests and the corresponding errors in measured quantities are summarised in the following table.

Table 6.18 Errors in measured quantities for liquid holdup tests.

Apparatus/ Instrument	Measured Quantity	Smallest Instrument Graduation or Sensitivity	Smallest Reading Obtainable	Absolute Error on Measured Quantity
Air rotameter	Air volumetric flowrate	5 litre/min	5 litre/min	±2.5 litre/min
Water rotameter	Water volumetric flowrate	0.1 cm Calibration chart average gradient = 5.8 cm/1.0 litre/min.	0.02 litre/min	±0.01 litre/min
Weighing balance	Mass of water collected	0.01 g	0.01 g	±0.005 g
Measuring tape	Packed bed height, Column diameter	0.1 cm	0.1 cm	±0.05 cm

❑ *__Static Holdup__*

The static holdup was determined from the difference in mass of the dry (m_{dry}) and wet packing (m_{wet}). The equivalent volume of water was evaluated knowing the water density, and when divided by the packed bed volume ($\pi D_{col}^2 l/4$) gives the static holdup h_S (vol.%):

$$m_{static} = m_{wet} - m_{dry} \qquad (6.31)$$

$$h_S (vol\%) = \frac{m_{static}}{\rho_L} \times \frac{4}{\pi D_{col}^2 l} \times 100\% \qquad (6.32)$$

where D_{col} and l are the column diameter and packed bed height respectively.

The absolute error on m_{static} is obtained as follows:

$$e(m_{static}) = \sqrt{e(m_{wet})^2 + e(m_{dry})^2} \qquad (6.33)$$

$$e(m_{static}) = \sqrt{0.005^2 + 0.005^2} = \mathbf{\pm 0.007\ g}$$

The percentage error on h_S is derived as follows:

$$\frac{e(h_S)}{h_S} \times 100\% = \sqrt{\left(\frac{e(m_{static})}{m_{static}}\right)^2 + \left(2 \times \frac{e(D_{col})}{D_{col}}\right)^2 + \left(\frac{e(l)}{l}\right)^2} \times 100\% \qquad (6.34)$$

The percentage error on h_S decreases with increase in the mass of water collected as the fractional error contributions from the column diameter and bed height measurements are constant using the same packed bed system. The percentage error on the static holdup h_S calculated in this way is approximately $\pm 1\%$ for all the data sets obtained.

In measuring the static holdup, care was taken to remove the wet spheres as gently as possible from the column and to ensure that the dislodged water from the bed of spheres was collected into the weighing container to determine the total weight of the wet spheres. However it was possible that some water could have been lost especially from the base of the packed bed in the process of transferring the wet spheres to the weighing container. This would render the percentage error on the static holdup to be higher than the calculated value of $\pm 1\%$.

□ *Dynamic Holdup*

The net mass of dynamic holdup $m_{dynamic}$ was obtained by deducting the mass of water which drained just from the top water distributor and the bottom reservoir constituting the 'end effects' m_{ends} from the water that drained from the whole packed column m_{gross}. The equivalent net volume of water was calculated knowing the water density and when divided by the packed bed volume ($\pi D_{col}^2 l/4$) gives the net dynamic holdup h_D (vol.%):

$$m_{dynamic} = m_{gross} - m_{ends} \tag{6.35}$$

$$h_D (vol\%) = \frac{m_{dynamic}}{\rho_L} \times \frac{4}{\pi D_{col}^2 l} \times 100\% \tag{6.36}$$

The error associated with $m_{dynamic}$ is determined as follows:

$$e(m_{dynamic}) = \sqrt{e(m_{gross})^2 + e(m_{ends})^2} \tag{6.37}$$

$$e(m_{dynamic}) = \sqrt{0.005^2 + 0.005^2} = \underline{\pm 0.007 \text{ g}}$$

The percentage error on h_D is derived as follows:

$$\frac{e(h_D)}{h_D} \times 100\% = \sqrt{\left(\frac{e(m_{dynamic})}{m_{dynamic}}\right)^2 + \left(2 \times \frac{e(D_{col})}{D_{col}}\right)^2 + \left(\frac{e(l)}{l}\right)^2} \times 100\% \tag{6.38}$$

Similar to h_S, the percentage error on h_D decreases with increase in the net mass of water collected due to the constant fractional error contributions from the column diameter and bed height measurements. The percentage error on the dynamic holdup h_D is approximately ±1% for all the data sets obtained.

□ *Total Holdup*

The total liquid holdup h_T is the sum of the static h_S and dynamic holdups h_D:

$$h_T = h_S + h_D \tag{6.39}$$

Therefore the absolute error associated with the total liquid holdup is:

$$e(h_T) = \sqrt{e(h_S)^2 + e(h_D)^2} \tag{6.40}$$

The percentage error on the calculated h_T is approximately ±1% for all the data sets obtained.

6.5   Cold Gas Scrubber Studies: Gas Lift

6.5.1   Experimental Observation

At low air rates, the water discharged intermittently at the top of the riser. The frequency of water discharge increased as air supply rate increased, until the water flow became nearly continuous at sufficiently high air rates. This intermittent discharge is attributed to the alternating gas and liquid slugs characterising the slug flow regime in two-phase vertical upward flow. When liquid slugs reached the top of the riser, water was discharged whilst only air was released when gas pockets reached the riser top. The slug velocities increased with increasing air rate, thereby increasing the frequency of water discharge at the top of the column.

6.5.2   Pump Operating Curves

At each air flow setting of the air lift pump, a total of two to three readings were taken from which the average water volumetric pumping rate was determined. The air lift experimental data is tabulated in Appendix 2.3. The air flowrates have been standardised to atmospheric pressure. The air lift pump operating curves obtained from Test 1 and Test 2 are compared in the following figure:
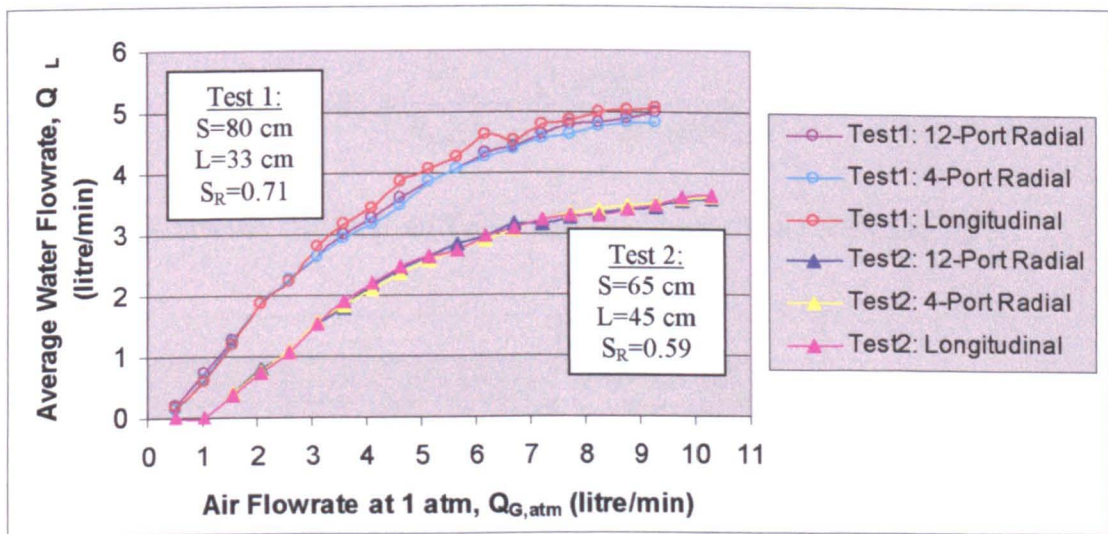
Figure 6.17 Air lift operating curves: Average water pumping rate versus injected air flowrate.

The water pumping rate rises with the air flow rate. The air lifts used in Test 1 and Test 2 are about the same total length, 113 cm for the former and 110 cm for the latter. The curves from Test 1 where the submergence ratio S_R is 0.71 are displaced higher than the curves from Test 2 where S_R is 0.59. The minimum possible air flowrate to effect pumping is less than 0.5 litre/min for the former and at 1.0 litre/min for the latter. The general shape of the operating curve and the

186

observation that higher submergence ratio brings about an earlier water flow initiation and an overall higher pumping rate are in accord with the findings of other investigators (Todoroki *et al.*, 1973; Kouremenos and Staicos, 1985; Lawniczak *et al.*, 1999; Khalil *et al.*, 1999). As the air flowrate increases, the air voidage in the riser increases and the corresponding liquid holdup decreases. This reduces further the overall density of the two-phase mixture relative to the single-phase water in the downcomer, hence increasing the driving force of the pump. The effect becomes more pronounced the greater the submergence as the total mass of the two-phase mixture in the riser becomes even smaller relative to the mass of water in the downcomer.

6.5.3 Pump Efficiency

The air lift pump efficiency η_p assuming isothermal expansion to atmospheric pressure P_{atm} (101325 Pa) at the top of the riser is given as follows:

$$\eta_p = \frac{Q_L \rho_L g L}{P_{atm} Q_{G,atm} \ln(P_o / P_{atm})} \tag{6.41}$$

The pressure at the air injector level P_o equals the atmospheric pressure P_{atm} plus the hydrostatic pressure due to the submergence height S, that is P_o equals ($P_{atm} + S\rho_L g$). Hence the air lift pump efficiency is evaluated using the following equation:

$$\eta_p = \frac{Q_L \rho_L g L}{P_{atm} Q_{G,atm} \ln(1 + S\rho_L g / P_{atm})} \tag{6.42}$$

The air lift pump efficiency curves from Test 1 and Test 2 are shown in Figure 6.18.
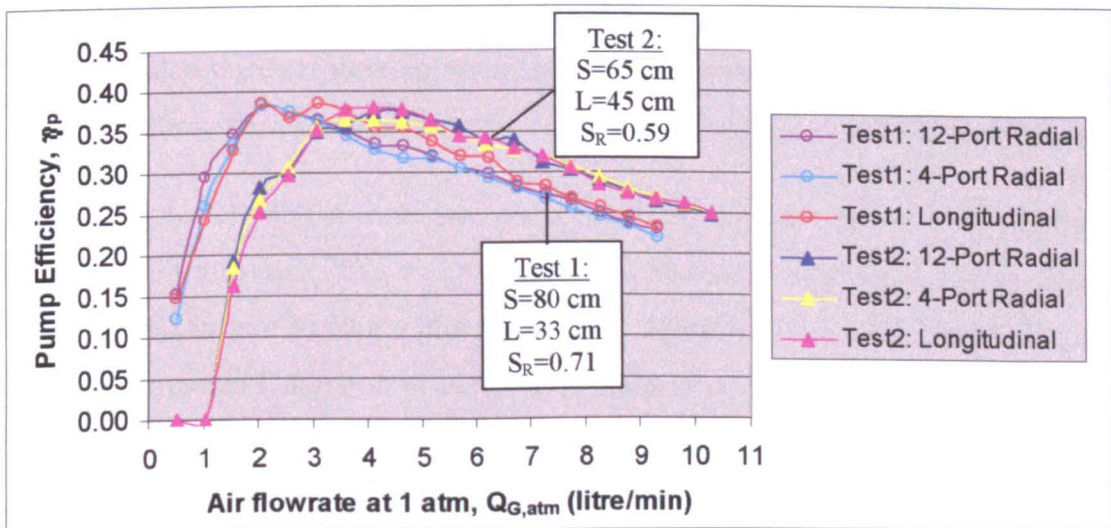
Figure 6.18 Air lift pumping efficiency versus injected air flowrate.

The efficiency curves rapidly rise to a maximum with increasing air flowrate and then decrease on further increase of air flowrate. The peaks are displaced to the lower end of the air flowrate. At very low air flowrates, the amount of injected air is insufficient to raise the water up the required lift height, hence the pump efficiency is zero. As the air flowrate increases, a higher proportion of water in the riser is raised up the required lift height and is discharged at the top of the riser. Frictional losses due to fluid velocities are small at this stage, therefore the pump efficiency increases with air flowrate to a peak value. The drop in efficiency from the peak value as the air rate is increased further could be attributed to firstly increased pipe wall frictional losses due to increased water velocity relative to the riser tube wall, and secondly excessive energy losses from increased water-air slip velocity as the air slugs rise faster up the tube. Also, entrance, exit and accelerative effects all become more pronounced at higher water velocities.

The average peak efficiency for Test 1 is slightly higher and occurs at a lower air flowrate than that of Test 2. For Test 1, the average peak efficiency is about 0.39 occurring at 2.1 litre/min air flowrate, whilst for Test 2, the efficiency peaks at approximately 0.38 occuring at about 4.1 litre/min air flowrate. These observations are similar to the pump efficiency plots of Lawniczak *et al.* (1999) and Khalil *et al.* (1999) as well as agreeing with the findings of Nicklin (1963) and Todoroki *et al.* (1973) in that the maximum pump efficiency increases with submergence ratio whilst the corresponding air flowrate at maximum efficiency decreases. Todoroki *et al.* found that the maximum pump efficiency increased with submergence ratio until a peak is reached at submergence ratios of about 0.7 to 0.8, after which it decreased.

6.5.4 Effect of Different Injectors

There is negligible difference in air lift performance using the different air injectors in Test 2. In Test 1, the two radial injectors gave approximately the same pumping performance, however the longitudinal injector gave slightly higher efficiencies in the region beyond the peak efficiency.

In this study, the size of each air hole was maintained the same for both the 4-port and 12-port injectors i.e. at 2.54 mm each. This means that the total cross-sectional area for air flow on the 12-port injector (60.80 mm^2) is three times that of the 4-port injector (20.27 mm^2). On the other hand, other investigators (Morrison *et al.*, 1987; Khalil *et al.*, 1999) who studied the effect of differing number of air ports on air lift pumping performance maintained the same total cross-sectional area of the air ports i.e. the size of the air ports were reduced the larger the number of holes used. The differences are summarised in the examples given in Tables 6.19 and 6.20:

Table 6.19 *Case A: Maintain same size of air port on multiport injectors.*

Air hole size (mm)	No. of holes	Area of 1 hole (mm^2)	Total area (mm^2)	Total gas rate (mm^3/s)	Gas rate/hole (mm^3/s)	Gas velocity/hole (mm/s)
2.54	1	5.07	5.07	100 (arbitrary)	100.00	19.74
2.54	4	5.07	20.27	100	25.00	4.93
2.54	12	5.07	60.80	100	8.33	1.64

Table 6.20 *Case B: Maintain same total cross-sectional area of air flow on multiport injectors.*

Air hole size (mm)	No. of holes	Area of 1 hole (mm^2)	Total area (mm^2)	Total gas rate (mm^3/s)	Gas rate/hole (mm^3/s)	Gas velocity/hole (mm/s)
2.54	1	5.07	5.07	100 (arbitrary)	100.00	19.74
1.27	4	1.27	5.07	100	25.00	19.74
0.73	12	0.42	5.07	100	8.33	19.74

Table 6.19 suggests that in this work which is similar to Case A, the gas velocity through each hole decreases as the number of holes on the air injector increases. This could potentially reduce the slip velocity between the air bubbles or slugs with the surrounding water, minimising energy loss associated with slip, hence improving the pump efficiency. However this is not the case, as shown by the pump efficiency curves in Figure 6.18. The effect of bubble size as dictated by the air hole size seems to be more influential on the pump efficiency as suggested from the work of Morrison *et al.* (1987) who showed that their 8-port injector gave consistently higher efficiency than their 4-port injector. Their system is similar to Case B in Table 6.20 wherein as the number of ports increase, the air holes become smaller producing smaller gas bubbles but the gas velocity through the air hole remains the same. However the work of Khalil *et al.* (1999) (similar to Case B) using nine different injectors with varying number of air holes showed that there was no consistent and definite increase in pump efficiency as the number of air ports increased.

Therefore although there is no doubt that entrance geometry and injector designs affect the two-phase upflow (initial bubble or slug size, velocity and distribution) in the riser, hence affecting friction and ultimately the air lift pump efficiency (Morrison *et al.*, 1987; Khalil *et al.*, 1999), there is no definite consistent relationship as yet between increasing the number of air ports on the injector with the air lift pumping performance. One thing is certain though, the results from this investigation show that increasing the number of air ports on the injector with no change to the air hole size has negligible effect on the air lift pump performance.

6.5.5 Prediction of Air Lift Pump Performance

Three published methods in the literature to predict air lift operating performance are tested against the actual experimental data obtained in this study. These are Zenz' (1993) generalised graphical correlation (as detailed in Section 3.2.2.2), and the theoretical design equations of Nicklin (1963) and Clark and Dabolt (1986) (as detailed in Section 3.2.2.1).

❑ *Zenz' (1993) Generalised Graphical Correlation*

Zenz' graphical correlation is straightforward to apply. The value of the abscissa was evaluated for each air flowrate at the discharge conditions i.e. atmospheric pressure and then the corresponding value of the ordinate was read off the plot. The water flowrate was then calculated knowing the physical dimensions of the air lift.

❑ *Nicklin's (1963) Theoretical Model*

In Nicklin's approach, the two-phase flow pressure gradient in the air lift riser consists of the hydrostatic head component and wall frictional loss. Accelerative, entrance and exit losses are neglected. The average pressure gradient along the riser equals the submergence ratio of the air lift:

$$\Delta P_H + \Delta P_W = S\rho_L g \tag{3.33}$$

The hydrostatic pressure change across the riser ΔP_H, the gas voidage fraction α, and the wall frictional pressure loss across the riser tube ΔP_W are defined by the model in equations 3.29 to 3.31 respectively. Both ΔP_H and ΔP_W consider only the liquid phase whilst ignoring the gas phase contribution in the two-phase flow.

$$\Delta P_H = (1-\alpha)\rho_L g(L+S) \tag{3.29}$$

$$\frac{W_G}{\alpha} = 1.2(W_G + W_L) + 0.35(gD)^{1/2} \tag{3.30}$$

$$\Delta P_W = (1-\alpha)\frac{f_L(S+L)}{D} \cdot \frac{\rho_L(W_G + W_L)^2}{2} \tag{3.31}$$

To determine ΔP_W, the Moody friction factor for the liquid phase f_L has to be determined. Although a friction factor chart (f versus Re) is readily available to determine f, this method is tedious and is impractical where an iterative procedure is required (in this case, the Goal Seek

function in Microsoft Excel) to determine the liquid velocity. Instead, the friction factor was evaluated directly from either one of the following equations (Miller, 1990), the first for laminar flow (Re < 3000) and the second for turbulent flow (Re > 3000):

$$f = \frac{64}{Re} \qquad (Re < 3000) \qquad (6.43)$$

$$f = \frac{0.25}{\left[\log\left(\dfrac{k}{3.7D} + \dfrac{5.74}{Re^{0.9}} \right) \right]^2} \qquad (Re > 3000) \qquad (6.44)$$

The pipe roughness k was 0.0025 mm as tabulated for smooth plastic pipes (Miller, 1990). The liquid Reynolds number Re_L was evaluated using the average velocity of the liquid slugs which according to Nicklin (1963) is equivalent to the total superficial velocity ($W_G + W_L$):

$$Re_L = \frac{\rho_L (W_G + W_L) D}{\mu_L} \qquad (6.45)$$

By using the above equations and knowing the physical geometry of the air lift (i.e. its lift L, submergence S and inner pipe diameter D), the water superficial velocity in the air lift W_L was evaluated for a particular air superficial velocity in the air lift W_G using the Goal Seek tool in Microsoft Excel. W_G was taken to be the air superficial velocity at the midpoint of the riser height whereby the pressure was the average of the discharge atmospheric pressure (P_{atm}) and the pressure at the gas injector level ($P_{atm} + S\rho_L g$).

□ *Clark and Dabolt's (1986) Theoretical Model*

In Clark and Dabolt's theoretical approach, the design equation (equation 3.40) was obtained by integrating the total differential pressure gradient in the air lift riser over its whole length. The total differential pressure gradient consists of hydrostatic and wall frictional loss terms. Accelerative, entrance and exit losses were neglected.

$$\frac{P_{atm} - P_0}{\rho_L g + F_s} - \left(\frac{1.5 F_s M - \rho_L g M}{(\rho_L g + F_s)^2 B'} \right) \log\left(\frac{A' + (\rho_L g + F_s) B' P_{atm}}{A' + (\rho_L g + F_s) B' P_o} \right) + (S + L) = 0 \qquad (3.40)$$

where A' $= 0.2\rho_L g M + 2.7 F_s M \ (kg^2/s^5 m^2)$

B' $= 1.2 W_L + 0.35(gD)^{1/2} \ (m/s)$

P_o $= P_{atm} + S\rho_L g \ (Pa)$

$$F_S \quad = \frac{f_L}{D} \cdot \frac{\rho_L W_L^2}{2} \ \text{(Pa/m)}$$

$$M \quad = \frac{G' P_{atm}}{A \rho_G} \ \text{(kg/s}^3\text{)}$$

The Moody friction factor for the single liquid phase f_L was determined in a similar manner to that outlined in the aforementioned Nicklin's method using equations 6.43 or 6.44.

The predicted pump performance using the three different methods: Zenz' graphical correlation, Nicklin's theoretical model and Clark and Dabolt's theoretical model are compared against the experimental data for Test 2 in the following figure:
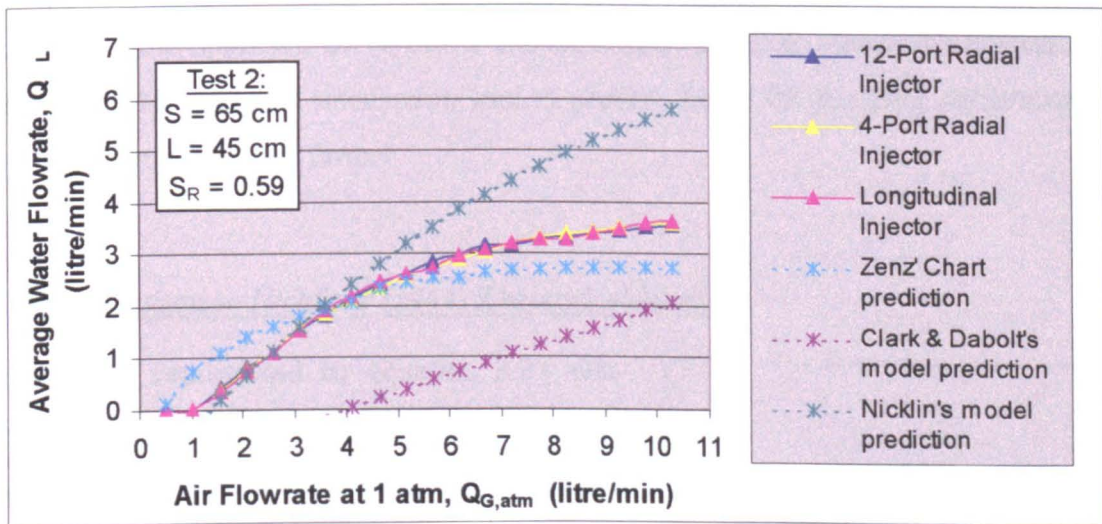
Figure 6.19 *Comparison of different air lift performance predictive methods against experimental data from Test 2.*

Figure 6.19 shows that on average, Zenz' graphical correlation seems to offer the best estimate of the air lift pumping performance. Zenz' correlation was based on published air-water lift data with lift heights ranging from 12.7 cm to 19.8 m and pipe diameters ranging from 1.27 to 38.10 cm. The dimensions of the air lift tested in this study are within these ranges. However no information was given on the entrance geometry of the riser and the air injector design used in the air lift data by Zenz. Both of these affect the frictional losses at the air lift entrance and thus could possibly explain the deviation of the estimated pump performance curve using Zenz' chart from the experimental data curve of this study.

Clark and Dabolt's theoretical model underestimates the air lift performance significantly. Nicklin's theoretical model provides a very close prediction of the water pumping rate at low air velocities, however the deviation increases as the air velocity increases. The entrance, exit and

accelerative losses have been omitted in both Nicklin's as well as Clark and Dabolt's models. In the case of Nicklin's model, the omission of these additional pressure losses could well explain the positive deviation of the predicted curve compared to the experimental curve especially at higher air velocities. As air velocity increases, the water velocity increases accordingly hence resulting in greater entrance and exit frictional losses. Also, the water slug velocity in the riser increases as the air velocity increases, accentuating the flow accelerative losses. For short air lift pumps such as those used in this investigation, the contribution of these additional pressure losses would be significant relative to the combined hydrostatic and riser wall frictional losses, hence cannot be ignored. This suggests that the prediction of the air lift performance by Nicklin's model can be potentially improved by including these additional losses. However in the case of Clark and Dabolt's model, the inclusion of these additional pressure losses would further displace the predicted curve below the experimental curve. Hence the theoretical model of Clark and Dabolt is not a satisfactory tool to predict the air lift pumping performance in this case and shall not be pursued further.

❑ *Modifications to Nicklin's (1963) Theoretical Model*

Nicklin's model represented by equation 3.33 was too simplified, ignoring several pressure terms. In this section, additional components are added to complete the pressure balance. The pressure balance between points 1 and 2 of the air lift system as illustrated in Figure 6.20 is described by the following equation:

$$\Delta P_H + \Delta P_W + \Delta P_D + \Delta P_A = S\rho_L g + P_{pump} \quad (6.46)$$

Both the hydrostatic pressure component ΔP_H (Pa) and the wall frictional pressure loss ΔP_W (Pa) across the riser height in Nicklin's model ignored the gas phase contribution, which has now been included as follows:

Figure 6.20 Air lift system in this study.

$$\Delta P_H = (1-\alpha)\rho_L g(L+S) + \alpha\rho_G g(L+S) \tag{6.47}$$

$$\Delta P_W = (1-\alpha)\frac{f_L(S+L)}{D} \cdot \frac{\rho_L(W_G+W_L)^2}{2} + \alpha\frac{f_G(S+L)}{D} \cdot \frac{\rho_G}{2} \cdot \left(\frac{W_G}{\alpha}\right)^2 \tag{6.48}$$

The gas slug velocity equals W_G/α (Nicklin *et al.*, 1962). Both ρ_G and W_G are evaluated at the mid-height of the riser. The Moody friction factor for the gas phase f_G is similarly determined from either equation 6.43 or 6.44 depending on the gas phase Reynolds number Re_G:

$$Re_G = \frac{\rho_G W_G D}{\mu_G \alpha} \tag{6.49}$$

ΔP_D (Pa) represents the U-tube downcomer frictional losses constituting the entrance effects of the air lift. The downcomer frictional losses include the wall friction losses as well as inlet (sudden contraction) and bend friction losses as a result of the single-phase liquid flow through the downcomer.

$$\Delta P_D = (f_L(L_1+L_2)/D + K_c + K_{b1} + K_{b2}) \times 0.5\rho_L W_L^2 \tag{6.50}$$

where f_L = Moody friction factor (derived using equations 6.43 or 6.44; the liquid Reynolds number Re_L based on single phase liquid superficial velocity W_L)

D = pipe inner diameter (m)

L_1, L_2 = lengths of vertical and horizontal sections of U-tube downcomer leg (m)

K_c = sudden contraction loss coefficient = 0.40 (approximated following McCabe *et al.* (1993)).

K_{b1}, K_{b2} = bend loss coefficient = 0.32, 0.42 respectively (approximated based on procedure provided by Miller (1990)).

W_L = liquid superficial velocity (m/s)

The fluid velocity increased from zero at point 1 to an average velocity of $(W_L + W_G)$ for the liquid slugs and a velocity of W_G/α for the gas slugs in the riser. Hence, the kinetic energy term or the accelerative pressure losses ΔP_A (Pa) is determined as follows:

$$\Delta P_A = 0.5\rho_L(W_L+W_G)^2 + 0.5\rho_G(W_G/\alpha)^2 \tag{6.51}$$

As a result of air expansion across the riser, pressure is developed by the pump P_{pump} (Pa) which is transferred to the two-phase flow mixture:

$$P_{pump} = \frac{P_{atm} V_{G,atm} \ln\left(\dfrac{P_{atm} + S\rho_L g}{P_{atm}}\right) \rho_{G,atm}}{\dfrac{W_G}{\alpha} A\rho_G + (W_L + W_G)A\rho_L}$$

(6.52)

where $V_{G,\,atm}$ = gas flowrate at atmospheric pressure (m^3/s)

$\rho_{G,\,atm}$ = gas density at atmospheric pressure (kg/m^3)

A   = cross-sectional area of riser (m^2)

Figure 6.21 depicts the predicted air lift pumping performance using the modified Nicklin's model with the various additional pressure terms. Plots following Zenz' Chart and Nicklin's original model are also included for comparison.
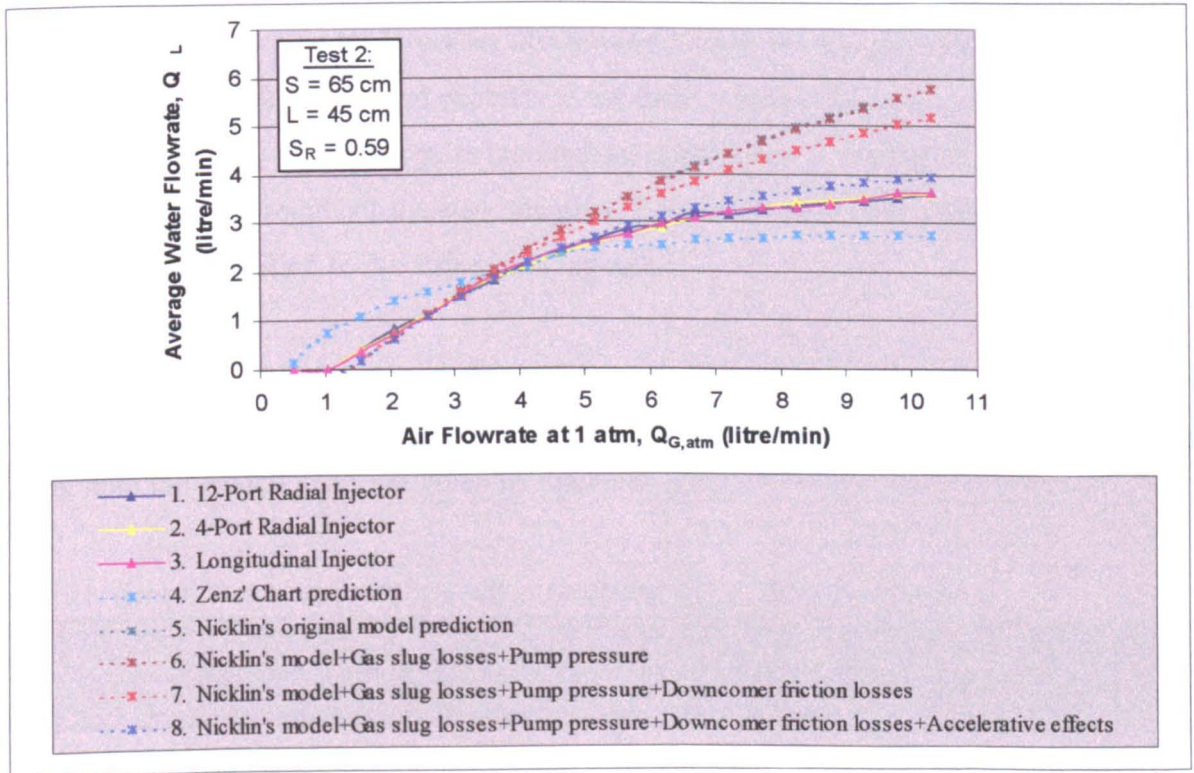
Figure 6.21 Comparison of air lift experimental data with the modified Nicklin's model.

The addition of the gas slug contribution to hydrostatic and wall friction losses across the riser as well as the pressure developed by the pump has negligible difference to Nicklin's original model, curves 5 and 6 being practically superimposed on one another. However the predicted air lift pump performance shows notable improvement over the higher air flowrate range upon addition

of the downcomer frictional losses (entrance effects) and the accelerative effects (kinetic energy changes) into Nicklin's model. The remaining positive deviation of curve 8 relative to the experimental curves could be attributed to additional losses occurring at the top of the air lift riser i.e. exit effects which have been neglected as marked by dotted lines in Figure 6.20. These include wall frictional losses, losses due to bends and sudden expansion in this section as the fluid leaves the air lift tubing. The complex two-phase flow of air-water mixture in this section means that the conventional method to estimate single-phase pipe losses could not be extended herein.

Nicklin's (1963) momentum balance of the two-phase flow in the air lift uses average point conditions, without provision for variation of gas volumetric flow rate over the riser. In this case, gas flowrate at the midpoint of the riser height was used in the calculations. For short risers, the gas volumetric flowrate will stay approximately constant along the tube, and hence the averaging will not affect the accuracy of the prediction significantly. This has been demonstrated herein by the close agreement between curve 8 with the experimental curves for the small air lift used in this investigation. However for larger air lifts having long risers, the gas volumetric flowrate will increase significantly as it rises and expands in the riser, varying the local gas voidage fraction as well. Nicklin's model will then require incremental application as the use of a single average gas volumetric flowrate throughout the riser length will be inadequate. The entrance and exit losses will become less important for air lifts with long risers.

Table 6.21 compares the average absolute relative error (AARE) and the corresponding standard deviation of the absolute relative error (s) of the different predictive methods. The equations defining both the AARE and s are given in Appendix 3.3.

Table 6.21 Comparison of different methods in predicting air lift pump performance.

Predictive Method	Average Absolute Relative Error, AARE (%)	Standard Deviation of Absolute Relative Error, s (%)
Zenz' Graphical Correlation	31.0	48.5
Clark and Dabolt's Theoretical Model	76.5	20.9
Nicklin's Theoretical Model	31.5	19.8
Nicklin's Model + gas slug losses + pump pressure	31.3	19.7
Nicklin's Model + gas slug losses + pump pressure + downcomer friction losses	23.4	15.4
Nicklin's Model + gas slug losses + pump pressure + downcomer friction + accelerative effects	8.9	11.6

6.5.6   Effect of Pipe Bend at Discharge

The two-phase mixture in the air lift discharges through a U-bend at the top of the riser as depicted in Figure 6.20. The U-bend facilitates the discharge of water into the top of the column. This raises the question regarding the 'true' lift of the riser, whether it should be length L or H.

The downward bend of length (L-H) could possibly exert a siphoning effect to the fluid at the top end of the riser, therefore increasing the water discharge rate. However to act as a siphon, a continuous 'rope' of water must exist throughout the U-bend, i.e. any complete break of the liquid phase across the tubing cross-section by say air pockets will break the siphon effect. Theoretical speculation alone could not provide a straightforward answer because whether or not the downward bend would affect the true lift would depend on the actual air-water flow in the horizontal and downward sections. The best and simplest way to determine the effect of the downward discharge tubing would be by experimentally comparing the performance of the air lift with and without the downward tubing, all else maintained the same.

This was carried out, the setups shown in Plate 6.6 and the resulting pump operating curves shown in Figure 6.22. The plots show that the U-bend at the top of the riser exerts negligible effect on the air lift performance. Therefore the use of L as the effective lift and the acceptance of water discharge level as marked by the horizontal tubing at the riser top in the preceeding calculations are justified.
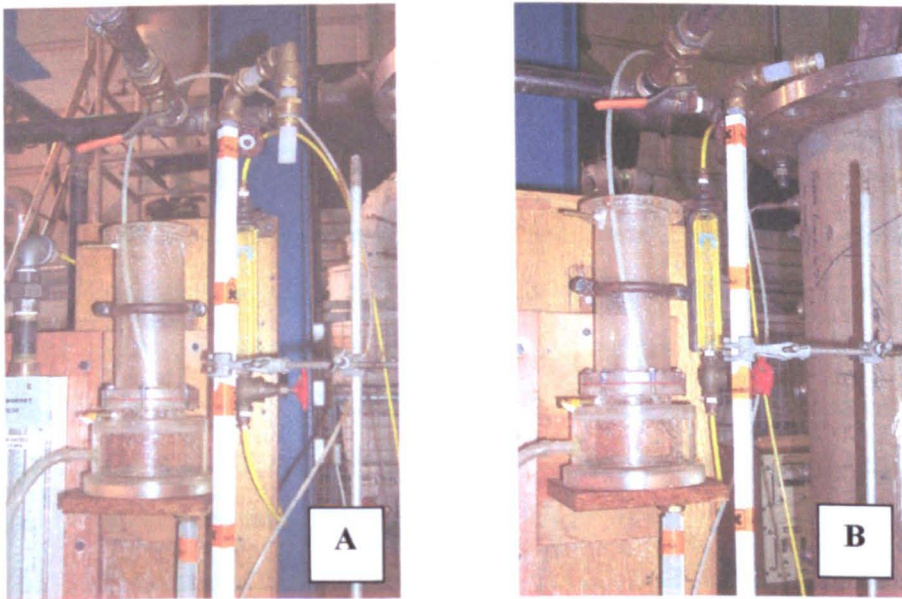
Plate 6.6 Air lift with (A) and without (B) downward bend at riser top.
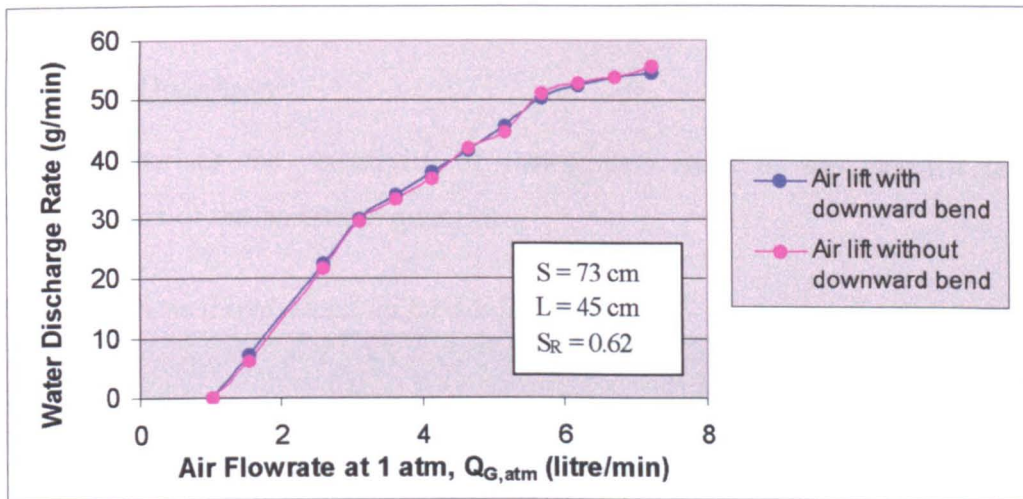
Figure 6.22 *Comparison between air lift performance with and without downward bend at discharge (using longitudinal gas injector).*

6.5.7 Implication for Hot Scrubber

The results of this investigation demonstrates that Nicklin's (1963) theoretical model when added with the necessary pressure changes to complete the momentum balance of the system (notably the downcomer friction losses and accelerative effects) gives the best prediction for the performance of a small air lift for water transport. However, although the equations in the model describing the hydrostatic component and wall frictional losses for the two-phase mixture in the riser have been proven to apply for air-water systems (Nicklin, 1963), the question remains whether it would extend adequately to liquid metal transport with vastly different physical properties. In this case, the liquid tin system of interest has a density of about 6.9 times and a surface tension that is approximately 7.5 times that of water. On the other hand, the standard equations describing the single phase liquid pressure changes should apply similarly well to the liquid metal.

The same concern applies to using Zenz' (1993) graphical correlation which has been developed based on data derived from air-water systems. Although Zenz' correlation includes fluid physical property correction factors to enable application to other fluids apart from water, it is still unknown whether it can be extended to pumping liquid metals. Although it has been tested on caustic solution with density approximately 1.5 times that of water and a good agreement was obtained (Zenz, 1993), it is not conclusive that the correlation will similarly apply satisfactorily to the liquid tin system with density about 6.9 times that of water.

Future gas lift data from the hot rig will help to establish the validity of extending the above mentioned predictive methods on gas lift performance to liquid metal systems.

6.5.8 Analysis of Errors

❑ *Measured Quantities*

Table 6.22 summarises the sensitivity of instruments used in the gas lift tests and the corresponding errors of the measured quantities.

Table 6.22 Errors in measured quantities for gas lift tests.

Apparatus/ Instrument	Measured Quantity	Smallest Instrument Graduation or Sensitivity	Smallest Reading Obtainable	Absolute Error on Measured Quantity
Air rotameter	Air volumetric flowrate	0.5 litre/min	0.5 litre/min	±0.25 litre/min
Weighing balance	Mass of collected water	0.01 g	0.01 g	±0.005 g
Digital stop clock	Duration of test run	0.01 s	0.01 s	±0.005 s
Measuring tape	Lift; Submergence	0.1 cm	0.1 cm	±0.05 cm

❑ *Water Volumetric Flowrate*

The water volumetric flowrate provided by the air lift pump was determined from the mean mass flowrate of water discharged at the top of the riser divided by the water density. Two to three sets of readings (mass of collected water, m and duration of test run, t) were obtained for each air flowrate. The individual mass flowrates M (where $M = m/t$) were averaged, giving the mean mass flowrate of water $\overline{M}$ at a particular air supply rate. The absolute error in the mean mass flowrate of water $e_{\overline{M}}$ equals the standard deviation of $\overline{M}$. Since the water volumetric flowrate Q_L (litre/min) was derived from the mean mass flowrate of water $\overline{M}$ (g/s), the percentage error on Q_L equals that on $\overline{M}$:

$$Q_L = B \times \overline{M} \tag{6.53}$$

$$\left(\frac{e_{Q_L}}{Q_L}\right) \times 100\% = \left(\frac{e_{\overline{M}}}{\overline{M}}\right) \times 100\% \tag{6.54}$$

B is the conversion factor. The percentage error on Q_L for the data sets in both Test 1 and Test 2 was found to range from ±0.01% to ±3%.

❑ *Pump Efficiency*

The air lift pump efficiency was evaluated using equation 6.42:

$$\eta_p = \frac{Q_L \rho_L g L}{P_{atm} Q_{G,atm} \ln(1 + S\rho_L g / P_{atm})} \tag{6.42}$$

L and S have errors of ±0.05 cm, or ±0.0005 m each. The determination of the error associated with Q_L has been shown previously. $Q_{G,atm}$ is obtained by adjusting the flowmeter reading Q_G to the equivalent flowrate at atmospheric pressure as in equation 6.55. Tests have shown that there is negligible difference between the static pressure measured by placing a pressure tapping at the air rotameter outlet and that calculated using $S\rho_L g$. The absolute error on $Q_{G,atm}$ is thus given by equation 6.56. The remaining quantities of ρ_L, g, P_{atm} are known, exact values.

$$Q_{G,atm} = \sqrt{\frac{P_{atm} + S\rho_L g}{P_{atm}}} \times Q_G \text{ (reading from rotameter)} \tag{6.55}$$

$$e(Q_{G,atm}) = \sqrt{\frac{P_{atm} + S\rho_L g}{P_{atm}}} \times e(Q_G) = \sqrt{\frac{P_{atm} + S\rho_L g}{P_{atm}}} \times \pm 0.25 \text{ litre/min} \tag{6.56}$$

From equation A3.11 in Appendix 3.1, the error on η_p is as follows:

$$e_{\eta_P} = \sqrt{\left(\frac{\partial \eta_p}{\partial Q_L} e_{Q_L}\right)^2 + \left(\frac{\partial \eta_p}{\partial L} e_L\right)^2 + \left(\frac{\partial \eta_p}{\partial Q_{G,atm}} e_{Q_{G,atm}}\right)^2 + \left(\frac{\partial \eta_p}{\partial S} e_S\right)^2} \tag{6.57}$$

where

$$\frac{\partial \eta_p}{\partial Q_L} = \frac{\rho_L g L}{P_{atm} Q_{G,atm} \ln(1 + S\rho_L g / P_{atm})}$$

$$\frac{\partial \eta_p}{\partial L} = \frac{Q_L \rho_L g}{P_{atm} Q_{G,atm} \ln(1 + S\rho_L g / P_{atm})}$$

$$\frac{\partial \eta_p}{\partial Q_{G,atm}} = \frac{-Q_L \rho_L g L}{P_{atm} Q_{G,atm}^2 \ln(1 + S\rho_L g / P_{atm})}$$

$$\frac{\partial \eta_p}{\partial S} = \frac{-Q_L \rho_L^2 g^2 L}{P_{atm}^2 Q_{G,atm} (1 + S\rho_L g / P_{atm})[\ln(1 + S\rho_L g / P_{atm})]^2}$$

The calculated percentage error associated with the pumping efficiency decreases rapidly as air injection rate increases. For Test 1, the percentage errors at 0.5 and 1.0 litre/min air supply rate $(Q_{G,atm})$ are ±50% and ±25% respectively. It then diminishes from ±17% to ±3% as the air rate increases from 1.6 litre/min to 9.3 litre/min. In the case of Test 2, there was no water discharge at 0.5 and 1.0 litre/min air rate. As the air injection rate rises from 1.5 litre/min to 10.3 litre/min, the percentage error on the pumping efficiency decreases from ±17% to ±3%.

6.6   Cold Gas Scrubber Studies: Particulate Removal

6.6.1   Particle Size Distribution of Glass Powder

The suspension of glass powder in distilled water was found to contain particles ranging from 0.5 to 35 μm. Comparison of the average number % distribution of the glass powder suspension and the distilled water alone suggested that particles smaller than 1.5 μm in the glass powder suspension were mostly contributed by the distilled water, shown in Figure 6.23.
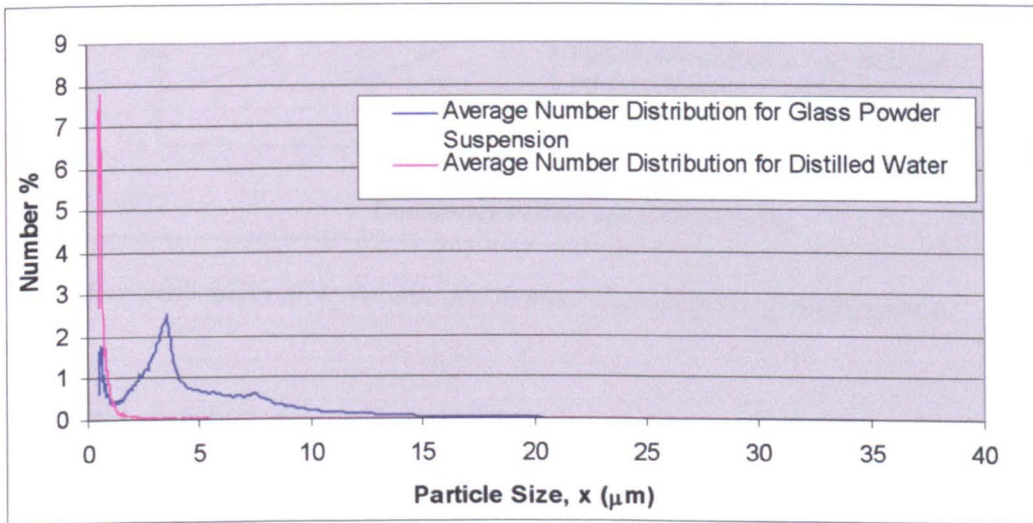
Figure 6.23 *Comparison of number distribution for glass powder suspension and that of the distilled water dispersant.*

To omit the background solid particles contributed by the distilled water, the particle size range for the glass dust was taken to be ranging from 1.5 to 35 μm. The particle size distribution of the glass powder sample was then determined as follows:

The average number % distribution was evaluated from results obtained from three dust samplings for a particle size range of 0.5 to 35 μm. The average number % distribution was then adjusted for a particle size range of 1.5 to 35 μm. The average volume % distribution was evaluated from the adjusted average number % distribution (for 1.5 to 35 μm particle size range) considering that the glass powder particles were spherical.

The log-probability plots of cumulative number and volume distributions of the glass dust in Figure 6.24 showed that the sample resembled very closely a log-normal distribution.
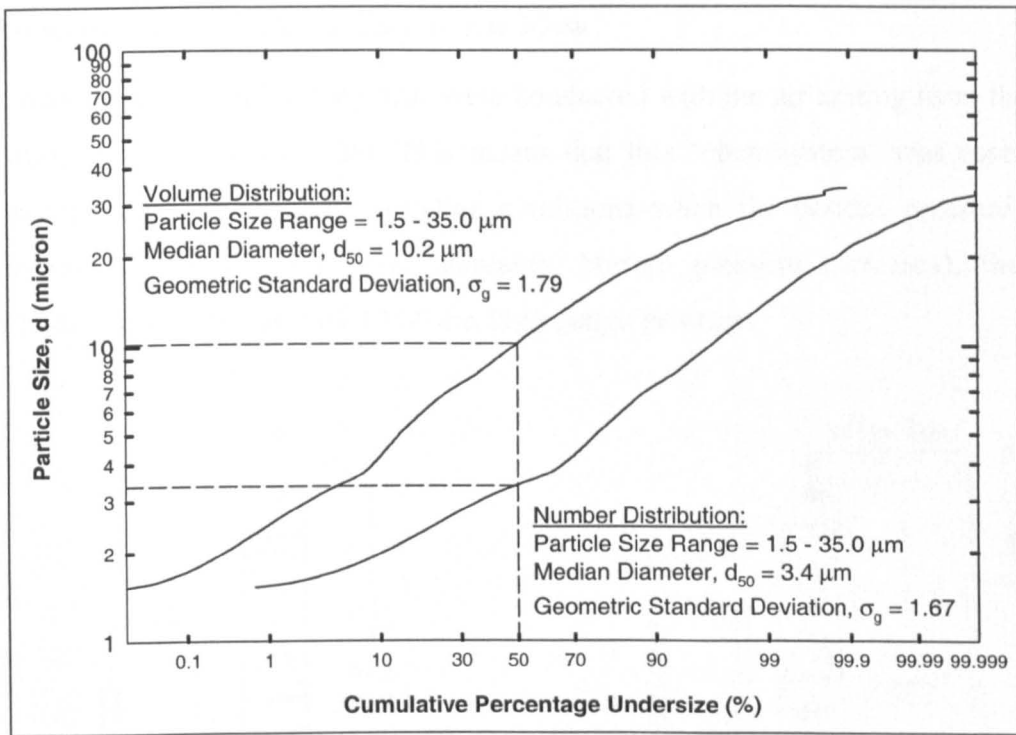
Figure 6.24 Log-probability plot: Volume and number distributions of glass powder.

The log-normal distribution is fully defined by two parameters: the median diameter d_{50} that defines the location of the distribution; and the geometric standard deviation σ_g which defines its spread. The median diameter is the 50% size on the cumulative distribution i.e. the size which splits the distribution into two equal parts as marked in Figure 6.24. The standard deviation is determined from the particle diameters corresponding to 84% and 16% cumulative distribution:

$$\sigma_g = \left(\frac{d_{84\%}}{d_{16\%}} \right)^{1/2} \tag{6.58}$$

The particle size distribution on volume and number bases is summarised in Table 6.23. Since the glass dust was of uniform particle density regardless of particle size, the volume distribution was identical to the mass distribution.

Table 6.23 Particle size distribution of glass powder.

	Median Diameter (μm), d_{50}	Geometric Standard Deviation, σ_g
Volume Distribution	10.2	1.79
Number Distribution	3.4	1.67

6.6.2 Effect of Additional Resistance to Air Flow

Previous flooding and liquid holdup tests were conducted with the air exiting from the column straight into open air (Figure 6.25). This meant that this 'open system' was essentially at atmospheric pressure. Even under flooding conditions when the bottom pressure is at its maximum (as column pressure drop increases, bottom pressure increases), the highest recorded bottom pressure was only 13.50 cm H_2O gauge pressure.
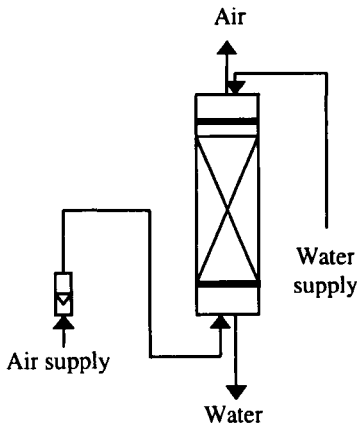
Figure 6.25 *'Open' system used for flooding and liquid holdup tests.*
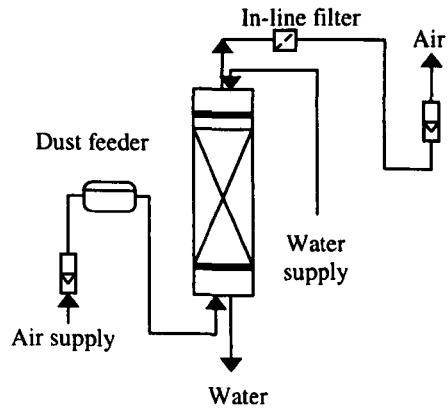
Figure 6.26 *Particulate removal system.*

In the particulate removal experiments (Figure 6.26), the resistance in the air line increased significantly compared to the open system. The extra resistance was due to the following additional apparatus in the air line: dust feeder, in-line filter and rotameter downstream of column. The marked increased in resistance to air flow meant that the air inlet flowrate as indicated by the air rotameter (calibrated at atmospheric pressure) before the dust feeder gave readings which were lower than those that should have been obtained at atmospheric pressure. Therefore an additional air rotameter was placed at the end of the air line downstream of the in-line filter. This measured the exit air volumetric flowrate at atmospheric pressure.

6.6.3 Total Efficiency of Particulate Removal

There are essentially three material streams containing the dust particles pertaining to the gas scrubber: the feed air stream with the challenging dust particles, the outlet air stream carrying the unseparated or penetrating dust particles, and the outlet water stream that washes out the separated dust particles. There is also accumulation of dust particles within the packed bed that is not washed out by the water. The material balance about the scrubber is as follows:

$$(M_{in})(\omega_{in,\,x}) = (M_c)(\omega_{c,\,x}) + (M_f)(\omega_{f,\,x}) \tag{4.3}$$

M_{in} (kg/s) corresponds to the dust in the feed air stream; M_c (kg/s) corresponds to the sum of dust in the outlet water stream as well as the dust retained within the packed bed. M_f (kg/s) corresponds to the dust in the exiting air stream. ω_x is the mass fraction of particles at size x.

The total efficiency E_T is defined by the following equation based on the mass flowrate of the feed dust M_{in} (kg/s) and the unseparated dust in the exit air stream M_f (kg/s):

$$E_T = 1 - \frac{M_f}{M_{in}} \tag{4.4}$$

Herein, the total efficiency of the scrubber is determined gravimetrically as follows:

$$E_T = 1 - \frac{m_{out}}{m_{in}} \tag{6.59}$$

where m_{out} = mass of unseparated dust in exit air retained on filter (g)

  m_{in} = mass of dust fed into scrubber (g)

m_{out} was obtained from the increase in total weight of the dried and cooled plastic weighing container holding the filter tube and cotton bud. m_{in} was determined from the decrease in weight of the glass powder contained within the paper boat in the dust feeder after a test run.

The inlet dust concentration C_p (ppmw) was calculated as follows:

$$C_p = \frac{\Delta m}{t} \times \frac{1}{V_G \rho_G} \times 1000 \tag{6.60}$$

where Δm = decrease in mass of paper boat containing feed glass powder (g)

  t = duration of test run (s)

  V_G = air volumetric flowrate measured by outlet air rotameter downstream of in-line filter at atmospheric pressure (m^3/s)

  ρ_G = air density at 15°C and 1 atm (kg/m^3)

The dust feed rate was adjusted at each air flowrate to give an average inlet dust concentration mainly within the range of 500 to 4500 ppmw. The operating air superficial velocity ranged from 11.2 to 29.6 cm/s (measured downstream of the in-line filter at atmospheric pressure) while the water superficial velocity ranged from 0.35 to 0.87 cm/s. Fluid physical properties were taken at 15°C and 1 atm. The experimental data is tabulated in Appendix 2.4.

❑   *Effect of Fluid Flowrates and Solids Loading*

The water-irrigated packed bed scrubber demonstrated very good particulate removal performance with total separation efficiencies ranging from 95.5 to 99.6%. The variation of total efficiency with air flowrate, water flowrate and solids loading are shown in the following figures:
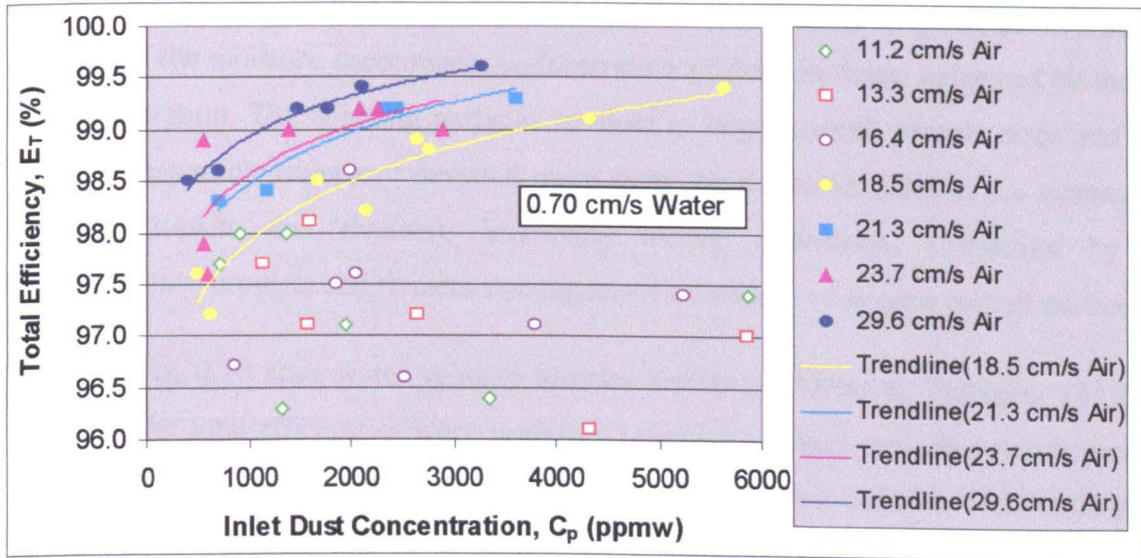
Figure 6.27 *Variation of total efficiency with inlet dust concentration and air flowrate.*
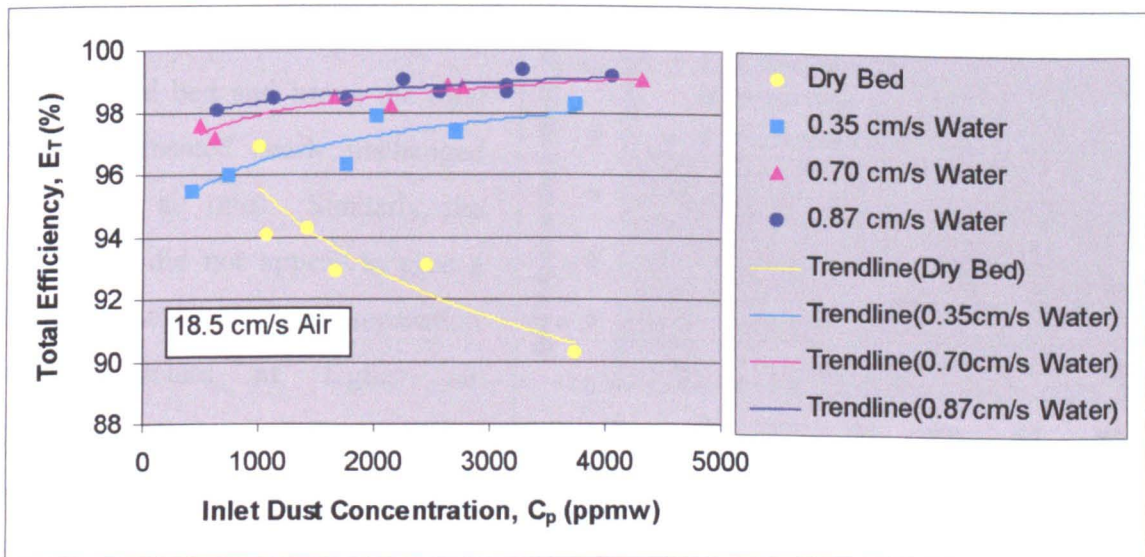
Figure 6.28 *Variation of total efficiency with inlet dust concentration and water flowrate.*

At air velocities of 18.5 cm/s and higher, the total efficiency E_T increased with air and water flowrates as well as inlet dust concentration. The total liquid holdup in the packed bed increased with increasing air and water flowrates as demonstrated earlier in the liquid holdup

tests. The droplets and rivulets in the bed functioned as particulate collectors. Their number increased with increasing liquid holdup, therefore improving the deposition of solid particulates through inertial capture and direct interception. In the packed bed scrubber, inertial deposition was expected to be the main particle collection mechanism whilst Brownian diffusional capture was negligible as the dust particle size was greater than 1.5 μm.

High dust loading gave better overall dust separation in the water irrigated packed bed. This was because the moisture encouraged agglomeration of dust particles, enhanced by increasing dust concentration. The adhering particles resulted in larger overall particle sizes and inertia. The resulting particle trajectory deviated more from the gas streamlines in the vicinity of the collector (droplets and rivulets), improving inertial deposition. Collection by direct interception onto droplets and rivulets also improved as a result of greater overall particle size.

Figure 6.27 for 0.70 cm/s water velocity showed that at the lower air velocities (11.2, 13.3, 16.4 cm/s), the total efficiencies were randomly scattered without any clear trends, averaging at about 97% to 97.5%. Nevertheless they were evidently lower than the total efficiencies at 18.5 cm/s air velocity and higher. At these lower air rates, the air rate exerted negligible effect on the liquid holdup in the packed bed, as suggested by the bed pressure drop at 0.70 cm/s water velocity in Figure 6.29. Therefore the dust retention capacity of the packed bed and hence the total efficiency remained nearly unchanged at these low air rates. Similarly, the dust loading did not appear to give a definite influence on the separation efficiency unlike at higher air velocities, suggesting negligible change in dust agglomeration effect due to constant liquid holdup.
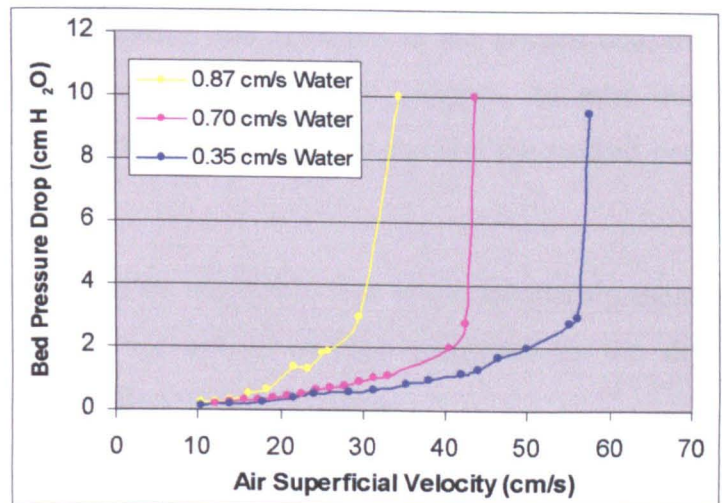
Figure 6.29 *Bed pressure drop for particulate removal experimental setup.*

❑ *Dry Bed*

The importance of the presence of water in the packed bed to prevent re-entrainment of dust particles back into the air stream is demonstrated by the data curve at zero water flowrate in

Figure 6.28. At the dry bed condition, dust separation decreased with increasing dust concentration. At the start, the dust introduced into the bed would stick to the clean packing surfaces mainly due to electrostatic force generated between the dry dust and the polyethylene spheres. The potential for electrostatics buildup was high due to the relative positions of glass and polyethylene in the triboelectric series. The triboelectric series is the rating of substances according to their natural tendency to lose or gain electrons. The higher the position of the material in the triboelectric series, the stronger is the tendency to lose electrons, hence becoming positively charged during frictional contact with another material. Conversely, the lower the position of a material in the triboelectric series, the stronger is its affinity for electrons, hence becoming negatively charged. Since glass is located significantly higher than polyethylene in the triboelectric series, the contact and separation of the dry glass powder with the polyethylene spheres at medium to high speeds would result in the loss of electrons from the glass powder to the polyethylene spheres. The glass powder would become positively charged whilst the plastic packings become negatively charged, producing an electrostatic force of attraction, pulling the glass particles towards the packing surface.

However, the dry bed has a limited dust retention capacity, depending on the available clean surface area of packing and column wall. This declined rapidly as more dust entered the column. Having found no clear surface for deposition and retention in the packed bed, the additional dust was swept along with the air stream out of the column. As inlet dust concentration increased, a higher proportion of dust penetrated and escaped the packed bed, reducing the overall separation efficiency.

With water irrigation, electrostatics effects would be negligible due to the moisture present. The humid environment reduces the capacity for energy storage compared to the dry environment. The static charges leak into the air, dissipating the charge.

◻ *Influence of Packed Bed Height*

The bulk of solids removal occurred at the bottom section of the packed bed, near the packing support plate. Dust retention visibly built up over time near the base of the packed bed. Similar observation has been noted in the literature for packed bed wet scrubbers (MacDonald, 1977).

The variation of total efficiency with packed bed heights at the same fluid flowrates is shown in Figure 6.30. It is clear that the bulk of dust in the air stream was removed near the base of

the packed bed. The air stream laden with dust entered the column via the air injector positioned below the packing support plate. Some solids were removed from the air stream even prior to the air stream reaching the packed bed. In the space below the packing support plate, some of the feed dust directly impinged on the surface of water in the bottom reservoir or was collected by the water spray below the packing support plate. Dust particles that remain entrained in the air stream then entered the packed bed where further entrapment occurred.
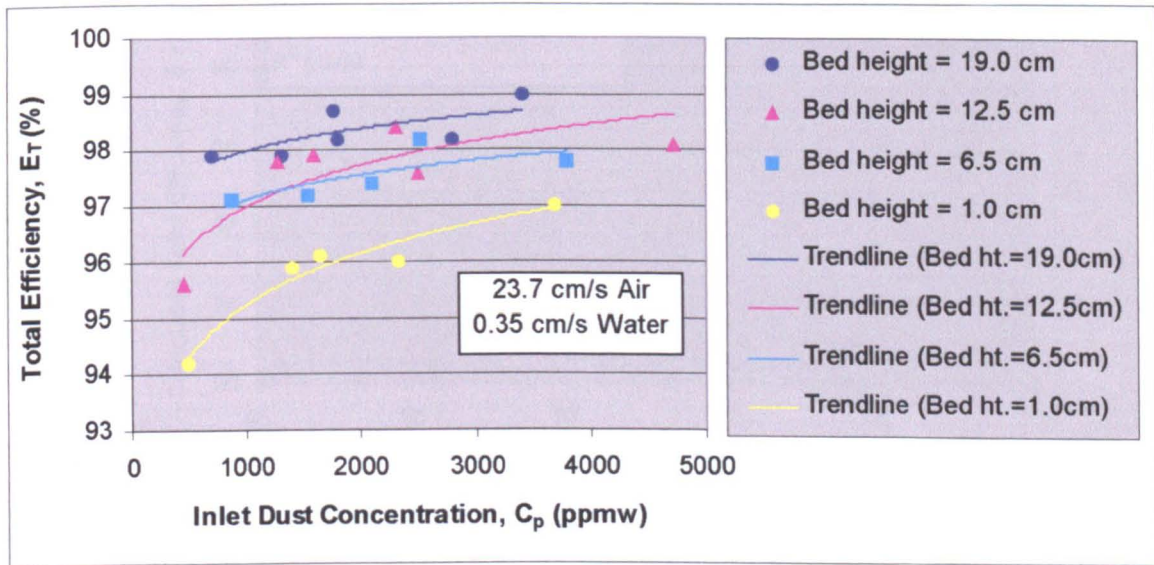
Figure 6.30 Variation of total efficiency with packed bed height.

For satisfactory long-term operation, the packing has to be removed so that the accumulated solids can be washed off to prevent blinding of the packing support plate and the initial depth of the packed bed. Rapid plugging of the bottom section of the fixed bed scrubber means that pre-removal of coarse particulates would be necessary or its operation restricted to low dust loading. This highlights the importance of ultimately having a moving bed in the gas scrubber, where the packing elements are withdrawn from the column and deposited solids are either mechanically scrapped off or shaken off with a vibrating mechanism in the external circulating loop before returning the packing elements back into the column.

❑ *Correlation of Separation Efficiency with Operating Parameters*

Using multiple linear regression analysis, the total efficiency was correlated against the operating fluid flowrates and solids loading. The corresponding value of the coefficient of determination, R^2 for the correlation is 0.80. The correlation predicts the total efficiency to within ±1.3%. The parity plot is shown in Figure 6.31.

$$E_T = 103.20(u_G^{0.025})(u_L^{0.013})(C_p^{0.008}) \qquad (R^2 = 0.80) \qquad (6.61)$$

where E_T = total efficiency (weight %)

u_G = air superficial velocity (m/s) [0.185 to 0.296 m/s]

u_L = water superficial velocity (m/s) [0.0035 to 0.0087 m/s]

C_p = inlet dust concentration (ppmw) [400 to 5614 ppmw]
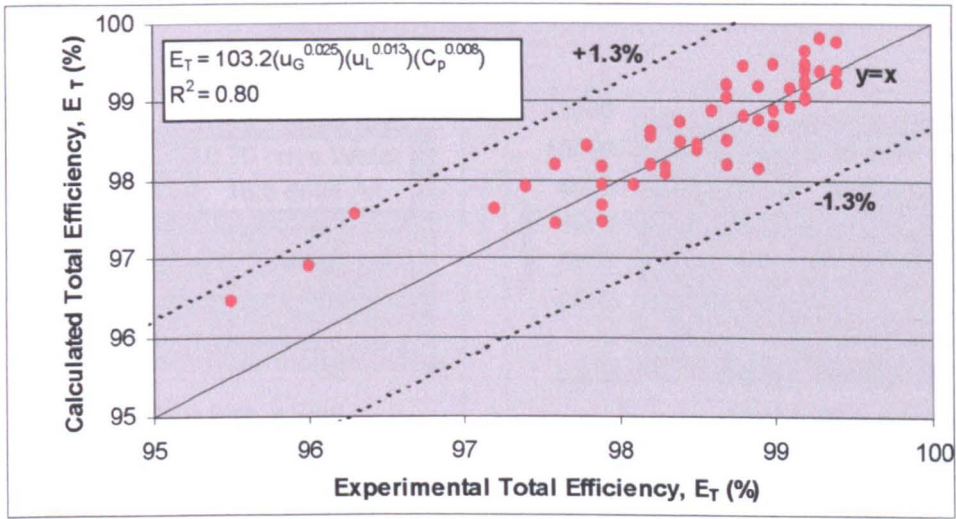
Figure 6.31 Parity plot of experimental and correlated values of total efficiency.

Alternatively, the separation efficiency was expressed in terms of number of transfer units, N_t which was similarly correlated against the same operating parameters as that for E_T and using the same data points. The correlation predicts the number of transfer units to within ±12%.

$$N_t = 7.62(u_G^{0.37})(u_L^{0.18})(C_p^{0.12}) \qquad (R^2 = 0.84) \qquad (6.62)$$
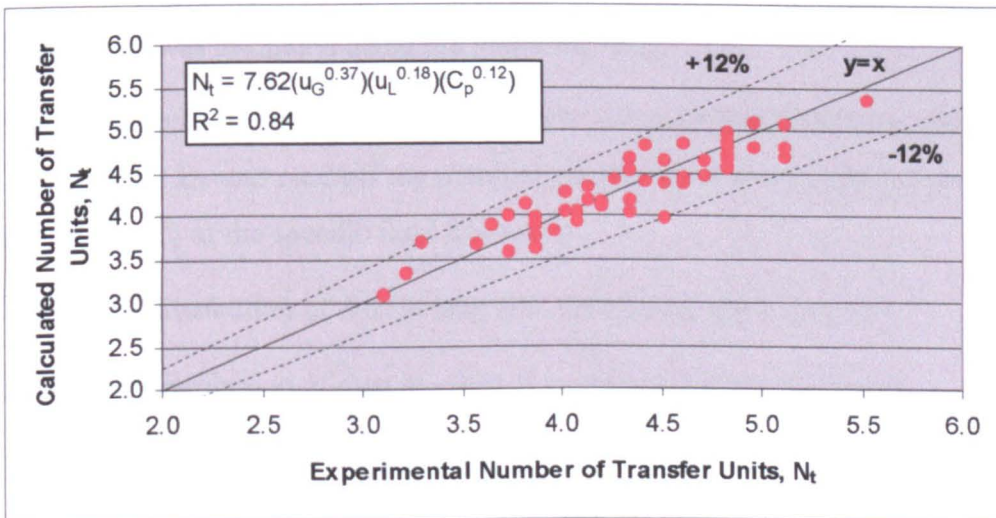
Figure 6.32 Parity plot of experimental and correlated number of transfer units.

6.6.4   Grade Efficiency

❑ *Dust Collection Into Impinger*

Preliminary tests were carried out using two impingers in series to collect the solids exiting the column. The following figure showed that the amount of solids collected in the second impinger was negligible. Hence it was sufficient to use only one impinger to collect the solids in the exit air stream for particle size analysis.
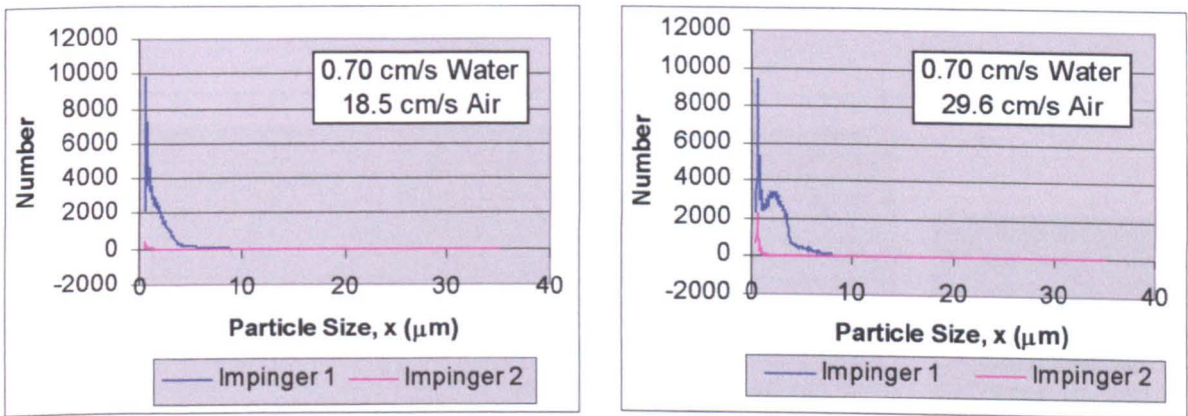
Figure 6.33 *Number distributions for solid particles collected in equal volumes of water from impingers 1 and 2 (uncorrected for background particles).*

❑ *Determination of Grade Efficiency*

The dust exiting the scrubber was collected for three sets of operating fluid flowrates: 53 litre/min (18.5 cm/s), 61 litre/min (21.3 cm/s) and 85 litre/min (29.6 cm/s) air flowrate as measured by the outlet air rotameter, and all at 2 litre/min (0.70 cm/s) water flowrate.

The grade efficiency was evaluated using the following data:

- Total collection efficiency E_T corresponding to the same fluid flowrates and inlet dust concentration. E_T was read off the trendline passing through the data points on the plot of E_T versus C_p at the specific fluid flowrates.

- Particle size distribution of dust at inlet (i.e. the original glass powder)

- Particle size distribution of dust at outlet (i.e. collected in the impinger)

The grade efficiency was calculated using the following equation:

$$G(x) = 1 - (1 - E_T) \frac{\omega_{out,x}}{\omega_{in,x}}$$ (6.63)

where $\omega_{in,x}$ = mass fraction of dust fed into scrubber at particle size x

$\omega_{out,x}$ = mass fraction of unseparated dust in exit air retained in impinger at particle size x

Figure 6.34 shows the grade efficiency curves obtained for the three sets of operating fluid flowrates. Key data from the grade efficiency curves is summarised in Table 6.24.
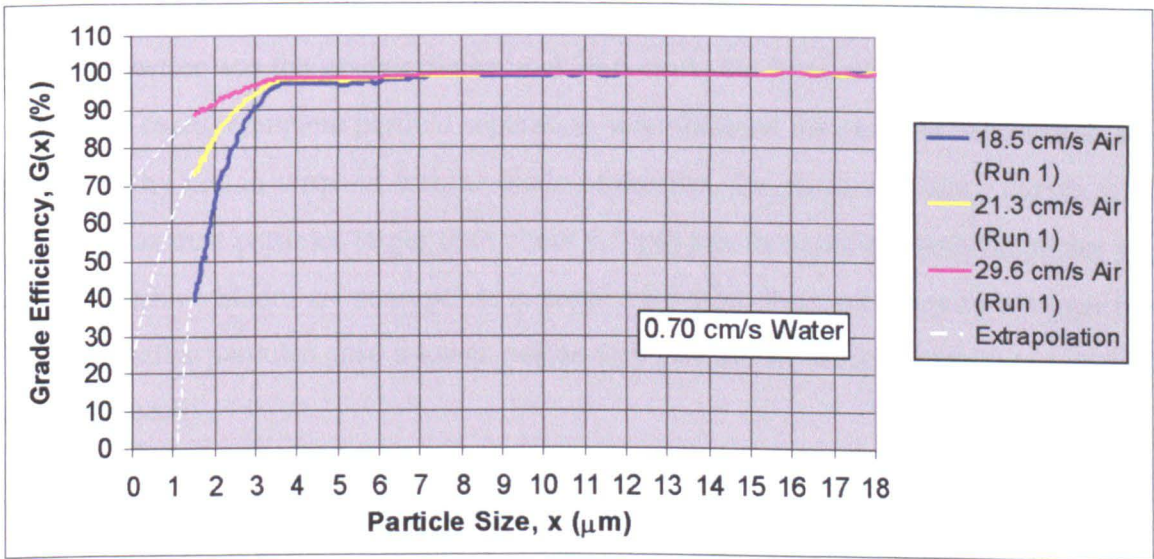
Figure 6.34 Grade efficiency curves at varying air flowrates.

Reproducibility of the grade efficiency curves is excellent, an example is shown herein:
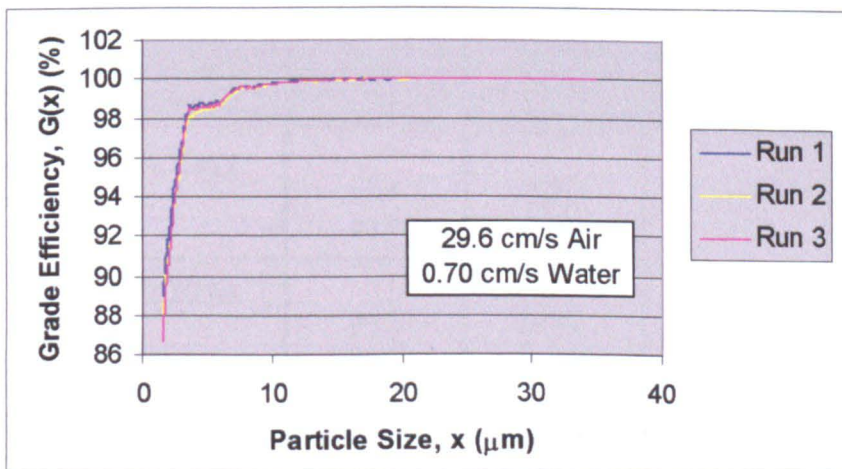
Figure 6.35 Grade efficiency curves for three separate runs at the same operating fluid flowrates.

Table 6.24 *Key data on the grade efficiency curves (Water superficial velocity = 0.70 cm/s).*

Air superficial velocity (cm/s)	y where $G(x) \geq y$ for $x \geq 1.53 \, \mu m$ (%)	Cut Size, x_{50} (μm)	Approximate Limit of Separation, x_{98} (μm)	Limit of Separation, x_{max} (μm)
18.5	39.81	1.71	6.40	16.03
21.3	73.39	0.7 (extrapolated)	3.63	15.60
29.6	88.97	Not applicable ($G(x) \geq 70\%$)	3.44	16.03

Impressive cut sizes were obtained. The cut size decreased with increasing air velocity. Extrapolation of the grade efficiency curve at 21.3 cm/s yields a cut size in the submicron range. Even better was the grade efficiency at 29.6 cm/s, the smallest extrapolated value being 70%. For all cases, complete particle separation was obtained for particles larger than 16 μm. It is noteworthy that in terms of turbine blade protection, the grade efficiency curves are very encouraging as dust particles larger than about 6.5 μm can be separated to efficiencies greater than 98%. Turbine blades are susceptible to erosion by these large particles with bigger inertia, whilst the smaller particles pose a lower risk as they can follow the gas streamlines around the blades more easily.

The grade efficiency curves are expressed as a function of the particle diameter x (μm), in line with the general form first proposed by Calvert (1977a; 1977b) for scrubbers where the inertial collection mechanism is dominant. A' and B are the dimensionless empirical constants:

$$G(x) = 1 - exp(-A'x^B) \tag{4.18}$$

Table 6.25 *Correlation of grade efficiency against particle diameter.*

Experimental Run	Total Efficiency E_T (%)	Empirical Constant A'	Empirical Constant B	Coefficient of Determination R^2
18.5 cm/s Air; 0.70 cm/s Water				
Run 1	98.5	0.219	2.187	0.992
Run 2	98.7	0.232	2.278	0.989
21.3 cm/s Air; 0.70 cm/s Water				
Run 1	99.1	0.792	1.153	0.992
Run 2	99.0	0.766	1.163	0.991
29.6 cm/s Air; 0.70 cm/s Water				
Run 1	99.5	1.621	0.650	0.989
Run 2	99.3	1.565	0.637	0.991
Run 3	99.4	1.457	0.716	0.990

As expected, A' varies with the operating variables, herein being the air superficial velocity. According to Calvert (1977a; 1977b), B equals 2 for packed columns. However the results here show that B is about 2 only at 18.5 cm/s air velocity, decreasing as the air velocity increases. This suggests a dependency of B on the air velocity as well.

6.6.5   Dust Separation Efficiency of 'Open' System

In the particulate removal experimental setup, the added resistance in the air line (as outlined in Section 6.6.2) reduced the column pressure drop and increased the column bottom pressure compared to the open system at the same atmospheric volumetric flowrate of air. This means the fluid flow conditions through the column at the same fluid flowrates would be different for the particulate removal experiments compared to the earlier flooding and liquid holdup tests. This difference is demonstrated by comparing the pressure drops across the column as follows, the air superficial velocity being measured at atmospheric pressure:
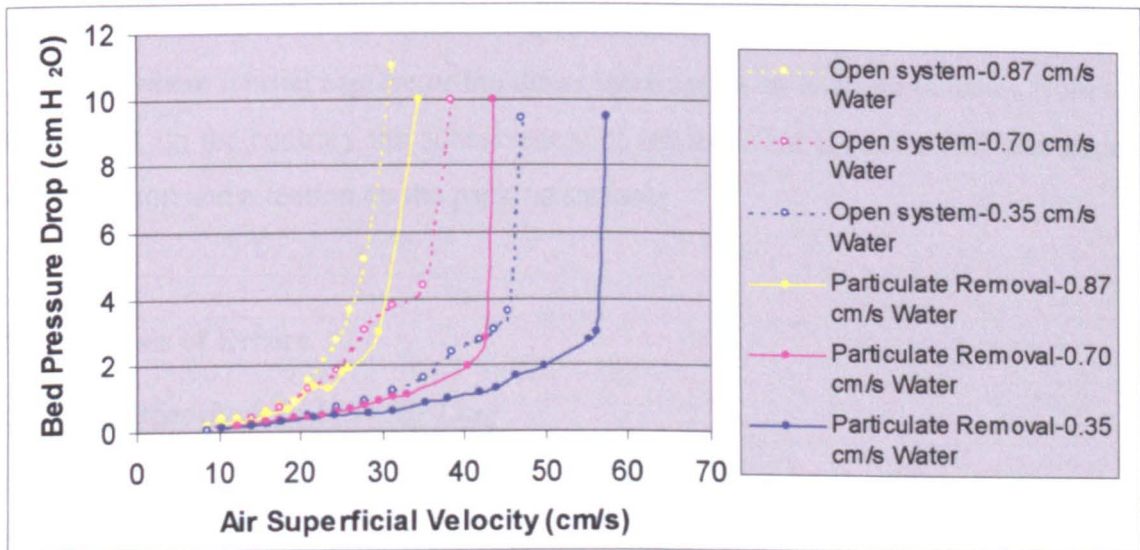
Figure 6.36 *Column pressure drops for open system and particulate removal system.*

The pressure drop curves obtained for the particulate removal system are displaced lower and to the right of the pressure drop curves for the open system. For the same fluid flowrates, a lower column pressure drop was observed for the particulate removal system. Flooding occurred at a higher gas flowrate but at a lower column pressure drop for the particulate removal test setup. This suggests that liquid holdup at the same fluid flowrates would be less compared to the open system. Due to higher column pressure drop hence larger liquid holdups for the open system, dust collection efficiency is expected to be higher for the open system at

the same fluid flowrates than that obtained using the particulate removal setup. Also, a smaller cut diameter would be expected of the open system at the same fluid flowrates because cut diameter decreases with increasing column pressure drop (Calvert, 1977a).

6.6.6 Implication for Hot Scrubber

The molten tin irrigated hot scrubber has the potential for an even better dust removal performance than the cold scrubber. In the cold model, the water droplets and rivulets were essentially the particle collectors whilst the packing elements served as turbulence promoters and to disperse the water flow. However in the hot scrubber, the packing elements would be expected to take a relatively more active role in particle collection by exploiting the inherent sticky nature of ash and char at elevated temperatures. The resulting plastic deformation that occurs when a partially fused ash or char particle collides with the solid packing surface will help dissipate the particle's impacting kinetic energy, aiding adhesion upon impact. An existing sticky layer on the packing surface would encourage further solids retention from the gas stream. This means that the collection sites are not only limited to the molten tin droplets and rivulets (where inertial capture or the direct interception of solid particulates from the gas stream occur), on the contrary the adhesiveness of ash and char particles will also encourage solids deposition and retention on the packing surfaces.

6.6.7 Analysis of Errors

❑ *Dust Deposition in Inlet Air Line*

Preliminary tests were carried out to ensure that all or nearly all the glass powder fed by the dust feeder entered the column instead of being deposited in the piping leading to the column. Solids deposition in the inlet piping would reduce the actual amount of solids that entered the column i.e. giving smaller solids loading in the inlet air.

The air injector was disconnected from the column and then connected to a tubing instead. The open end of the tubing was sealed with a Vacspare™ dust bag. The metal piping connecting the dust feeder to the air injector as well as the brass air injector itself were earthed; static charges were drawn and dissipated through a connected wire to the ground. The air supply was turned on and glass powder was fed from the dust feeder into the metal piping, through to the air injector, tubing and dust bag sequentially. The powder captured in the dust bag was

weighed and then compared to the amount of glass powder fed by the feeder. It was found that about 95% of the dust fed into the system was collected by the dust bag. Hence the amount of powder that left the dust feeder hopper was a reasonably good representation of the amount of solids that actually entered the column, having an error of approximately 5%.

❑ **_Measured Quantities_**

The sensitivity of instruments used in the particulate removal tests and the corresponding errors in the measured quantities are summarised in the following table:

Table 6.26 Errors in measured quantities for particulate removal tests.

Apparatus/ Instrument	Measured Quantity	Smallest Instrument Graduation or Sensitivity	Smallest Reading Obtainable	Absolute Error on Measured Quantity
Air outlet rotameter	Air volumetric flowrate	2 litre/min	1 litre/min	±0.5 litre/min
Water rotameter	Water volumetric flowrate	0.1 cm Calibration chart average gradient = 5.8 cm/1.0 litre/min.	0.02 litre/min	±0.01 litre/min
Manometer ≥ 10 cm H_2O < 10 cm H_2O	Column pressure drop	0.1 cm H_2O	0.05 cm H_2O	±0.03 cm H_2O ±0.005 cm H_2O
Microbalance	Mass of glass powder in paper boat; Mass of weighing container + contents	0.0001 g	0.0001 g	±0.00005 g
Digital stop clock	Duration of test run	0.01 s	0.01 s	±0.005 s

The error on the column pressure drop reading was dependent on the position of the manometer tube and has been previously discussed in Section 6.3.6.

❑ **_Total Efficiency_**

The total efficiency, E_T was calculated from the following equation:

$$E_T = 1 - \frac{m_{out}}{m_{in}} \tag{6.59}$$

where $\qquad\qquad m_{out} = m2 - m1 \qquad$ and $\qquad m_{in} = m3 - m4 \tag{6.64}$

m1   = mass of weighing container + filter tube + cotton bud before test run (g)

m2   = mass of weighing container + filter tube + cotton bud after test run (g)

m3   = mass of paper boat + glass powder before test run (g)

m4   = mass of paper boat + glass powder after test run (g)

The absolute error on E_T equals the absolute error on (m_{out}/m_{in}). The absolute errors on m_{out} and m_{in} are determined from the absolute errors on m1, m2, m3 and m4 as follows:

$$e(m_{out}) = \sqrt{e_{m2}{}^2 + e_{m1}{}^2} \quad \text{and} \quad e(m_{in}) = \sqrt{e_{m3}{}^2 + e_{m4}{}^2} \tag{6.65}$$

Since both e_{m1} and e_{m2} equal ±0.00005 g, $e(m_{out})$ is then ±0.00007 g. Similarly since e_{m3} and e_{m4} each equals ±0.00005 g, $e(m_{in})$ would apparently be ±0.00007 g.

The absolute error on E_T is then:

$$e(E_T) = e(m_{out} / m_{in}) = \sqrt{\left(\frac{e(m_{out})}{m_{out}} \right)^2 + \left(\frac{e(m_{in})}{m_{in}} \right)^2} \times \frac{m_{out}}{m_{in}} \tag{6.66}$$

Taking $e(m_{out})$ and $e(m_{in})$ to be ±0.00007 g, the maximum percentage error on m_{out} is ±0.7% whilst that on m_{in} is apparently a mere ±0.01% for all data points obtained under both irrigated and dry bed conditions. However besides the error due to equipment resolution, another major source of error on m_{in} is due to the deposition of some glass powder in the air inlet piping prior to entering the column. This additional error was estimated to be about 5%, rendering the error contribution from the equipment resolution to be negligible in comparison. Therefore the percentage error on m_{in} is approximately ±5%. The absolute error on E_T was small relative to the large figures obtained for E_T itself (above 0.9), resulting in the percentage error on E_T to be smaller than 1%.

❏ *Grade Efficiency*

The use of the single particle counting and sizing method by the AccuSizer gives reproducible particle size distributions that are of good accuracy and high resolution. The AccuSizer makes no assumptions about the shape of the size distribution, instead the particle size distribution is built one particle at a time, hence providing the true particle size determination. Accurate particle size distribution minimises errors in the grade efficiency determination. Random

errors in experimental measurement would lead to scatter in the final results, which would be revealed in the grade efficiency plots. To this end, the very good reproducibility of the grade efficiency curves as demonstrated in Figure 6.35 suggests minimal random errors in the determination of particle size distribution. The grade efficiency was calculated using the following equation:

$$G(x) = 1 - (1 - E_T) \frac{\omega_{out,x}}{\omega_{in,x}}$$ (6.63)

The absolute error on G(x) equals the absolute error on $(1-E_T)(\omega_{out,x}/\omega_{in,x})$. Since good accuracy of the particle size distributions is expected, the error on G(x) would be mainly attributed by the error on the total efficiency E_T. Assuming negligible error associated with $(\omega_{out,x}/\omega_{in,x})$, the absolute error on G(x) is calculated using the following equation:

$$e(G(x)) = e(E_T) \times \frac{\omega_{out,x}}{\omega_{in,x}}$$ (6.67)

The percentage error associated with G(x) at 18.5 cm/s air velocity decreases from 30% to zero as G(x) rises from 40% to 100%. At 21.3 cm/s, the percentage error diminishes from 12% to zero as G(x) increases from 73% to 100%. Finally at 29.6 cm/s, the percentage error associated with G(x) dropped from 7% to zero as G(x) rises from 89% to 100%.

❑ *Inlet Dust Concentration*

The solids mass flowrate was obtained by averaging the mass of glass powder which left the dust feeder hopper m_{in} over the period of the test run t. The ratio of the solids mass flowrate to the air mass flowrate gave the inlet dust concentration C_p. C_p being derived from an averaged quantity is actually not constant with time. In fact the feed gates on the sample hopper were occasionally blocked and the powder has to be slightly probed to loosen the blockage. C_p was calculated using the following equation:

$$C_p = B \times \frac{m_{in}}{t} \times \frac{1}{Q_G \rho_G}$$ (6.68)

B is the conversion factor, i.e. a constant. Q_G is the measured air flowrate. The air density ρ_G was taken at 15°C and 1 atm. The percentage error on C_p is determined as follows:

$$\frac{e_{Cp}}{C_p} \times 100\% = \sqrt{\left(\frac{e(m_{in})}{m_{in}}\right)^2 + \left(\frac{e_t}{t}\right)^2 + \left(\frac{e_{Q_G}}{Q_G}\right)^2} \times 100\%$$ (6.69)

e_t equals ± 0.005 s and $e(Q_G)$ equals ± 0.5 litre/min. The percentage error on m_{in} is 5% as previously discussed. For all the data points under both irrigated and dry bed conditions, the percentage error on C_p was found to be dominated by that of m_{in} i.e. being $\pm 5\%$.

□ *__Penetrating Dust__*

Although effort was made to transfer the solids deposited on the internal surface of the filter unit and the air outlet tubing to the total mass of solids collected on the filter tube, there were bound to be solids that remained on these surfaces especially on the tubing. This would render the overall collection efficiency to be slightly higher than it actually was although this could not be quantified.

□ *__Air Volumetric Flowrate__*

The air volumetric flowrate was read off from the outlet air rotameter, just before the air line opened to the atmosphere. This meant that the air flow through this rotameter was essentially at atmospheric pressure. Hence direct reading of air flowrates from this rotameter that was calibrated at atmospheric conditions was justified.

The highest recorded bottom pressure of the column within the operating fluid flowrates was 68.3 cm H_2O gauge, obtained at 85 litre/min (29.6 cm/s) air flowrate and 2 litre/min (0.70 cm/s) water flowrate. Rounding that to 70 cm H_2O gauge or approximately 1.07 atm absolute, the air density is 1.308 kg/m^3 as opposed to 1.225 kg/m^3 at 1 atm absolute (both at 15°C). This means that the largest percentage deviation of the air volumetric flowrate through the column to that measured by the outlet air rotameter is approximately +7%, obtained as follows:

For air mass flowrate M kg/s, the apparent volumetric flowrate is obtained at air density 1.225 kg/m^3. However the actual air volumetric flowrate through the column really should be determined at 1.308 kg/m^3. Therefore the percentage error in the air volumetric flowrate is given by:

$$\frac{V_G(apparent) - V_G(actual)}{V_G(actual)} \times 100\% = \frac{\dfrac{M}{1.225} - \dfrac{M}{1.308}}{\dfrac{M}{1.308}} \times 100\% \approx \underline{+7\%} \qquad (6.70)$$

6.7 Cold Gas Scrubber Studies: Gas Absorption

6.7.1 Determination of Overall Mass Transfer Efficiency

The mass transfer process of ammonia gas absorption from air/ammonia gas mixture into water in a packed bed of non-wetting spheres was investigated. The absorption of ammonia into water is a known gas film controlled process, with about 80 to 95% of resistance to mass transfer lying in the gas phase (Sherwood *et al.*, 1975; Coulson *et al.*, 1991; McCabe *et al.*, 1993; Knudsen *et al.*, 1997).

The mass transfer efficiency of the packed bed of polyethylene spheres irrigated by water was determined from the measured ammonia gas concentrations in the inlet and outlet gas streams. Measurements were carried out at 1 and 2 litre/min (3.49 and 6.97 kg/m²s) water flowrate, at increasing gas flowrates till before flooding sets in. The experimental data and the corresponding mass transfer efficiency figures are tabulated in Appendix 2.5.

As the ammonia concentrations involved were small (less than 0.1% in the gas), only small amounts of solute were transferred between the gas and liquid phases producing dilute solutions. This meant that both the operating and equilibrium lines for the system are essentially linear. The equilibrium relationship for the dilute solution could be described using Henry's Law. In view of these considerations, the efficiency of mass transfer could be determined as follows:

The number of overall gas phase transfer units:

$$N_{OG} = \frac{y_B - y_T}{(y - y^*)_{lm}} \tag{4.53}$$

The height of an overall gas phase transfer unit:

$$H_{OG} = \frac{Z}{N_{OG}} = Z \frac{(y - y^*)_{lm}}{y_B - y_T} \quad \text{(m)} \tag{6.71}$$

The volumetric overall gas phase mass transfer coefficient:

$$K'_G \, a = \frac{G'}{H_{OG}} = \frac{G'}{Z} \frac{(y_B - y_T)}{(y - y^*)_{lm}} \quad \text{(kmol/m}^3\text{s)} \tag{6.72}$$

where G' = molar flowrate of air per unit cross-sectional area of column (kmol/m²s)

   Z = packed bed height (m)

   y_B = ammonia gas concentration at the bottom of the column (mol/mol)

   y_T = ammonia gas concentration at the top of the column (mol/mol)

$(y-y^*)_{lm}$ is the logarithmic mean of the driving forces at the ends of the column represented by $(y-y^*)_B$ and $(y-y^*)_T$:

$$(y - y^*)_{lm} = \frac{(y - y^*)_B - (y - y^*)_T}{\ln \dfrac{(y - y^*)_B}{(y - y^*)_T}} \qquad (6.73)$$

Since the concentration of dissolved ammonia in the incoming water at the top of the column is zero (i.e. $x_T = 0$), the corresponding equilibrium gas concentration y_T^* is zero as well. This simplifies equation 6.73 to:

$$(y - y^*)_{lm} = \frac{y_B - y_B{}^* - y_T}{\ln\left(\dfrac{y_B - y_B{}^*}{y_T}\right)} \qquad (6.74)$$

To find out the equilibrium gas concentration at the bottom of the column y_B^*, the concentration of dissolved solute in the exiting water x_B needs to be determined by carrying out a material balance over the column:

$$L'(x_B - x_T) = G'\ (y_B - y_T) \qquad (6.75)$$

where   L'   = molar flowrate of water per unit cross-sectional area of column (kmol/m²s)

  x_B = dissolved ammonia concentration in water at bottom of the column (mol/mol)

  x_T = dissolved ammonia concentration in water at top of the column (mol/mol)

Since $x_T = 0$,

$$x_B = \frac{G'}{L'}(y_B - y_T) \qquad (6.76)$$

y_B^* was then evaluated from Henry's Law which describes the gas-liquid equilibrium for the dilute solution:

$$p_B^* = H\,x_B \qquad (6.77)$$

The Henry's Law constant H was obtained from tabulated gas-liquid equilibrium data for dilute ammonia solutions (Liley *et al.*, 1997), corrected to the water temperature exiting the column. The temperature correction factor was determined based on ammonia solubility data tabulated by Sherwood (1928). Taking the total pressure at 1 atm, y_B^* could then be determined.

6.7.2   Correction for End Effects

The H_{OG} and $K'_{G}a$ given by equations 6.71 and 6.72 are apparent values, suggesting higher mass transfer efficiency of the packed bed than the true values. This apparent higher mass transfer

efficiency is due to end effects i.e. additional mass transfer occurring beyond the packed bed region. End effects to mass transfer were expected to be significant due to the short packed bed used. The main source of end effect would be the additional mass transfer occurring in the spray of water below the packing support plate. Another source would be due to gas absorption at the free liquid surface in the bottom reservoir. At this end, the water level in the reservoir was maintained at approximately 0.5 cm in all test runs to minimise changes in end effects below the packed bed. The other possible end effect contributor was the water shower above the packed bed, however this has been minimised by positioning the opening of the gas sampling tube directly above the packed bed.

The gas absorption tests were conducted at two different packed bed heights to assess the magnitude of end effects. The bed height equivalent to the end effects Z_{end} was determined by plotting the number of overall gas phase transfer units N_{OG} (at the same gas and liquid flowrates) against the packed bed height, Z and extrapolating the resulting line to zero bed height, illustrated as in Figure 6.37.
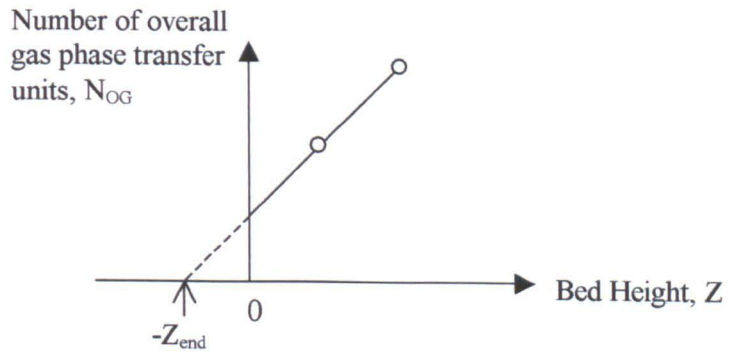
Figure 6.37 *Determination of end effects.*

N_{OG} obtained from tests using 8.5 cm and 19.0 cm packed bed heights were plotted against Z as depicted in Figure 6.38.
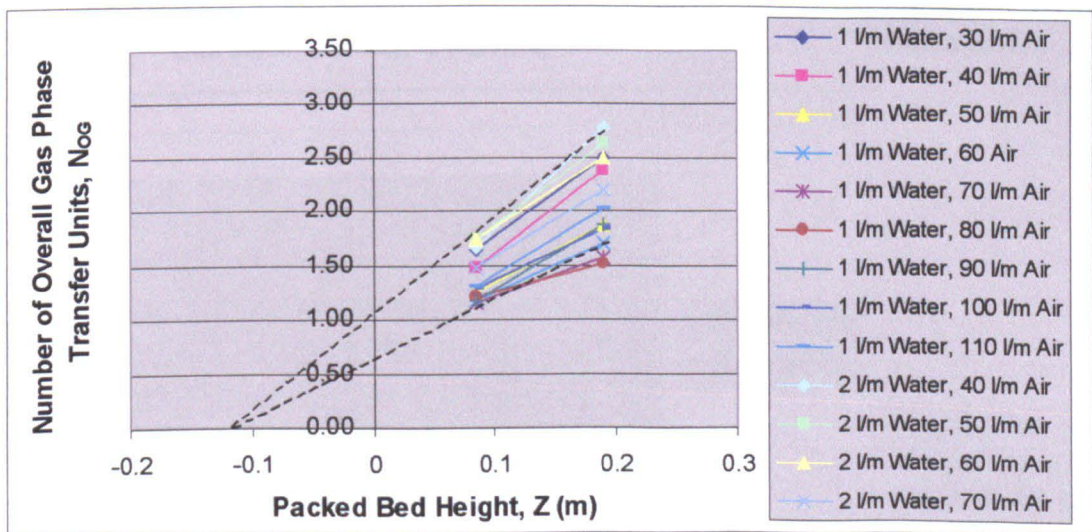
Figure 6.38 *N_{OG} versus Bed Height, Z.*

As only two data points were available for each combination of fluid flowrates, the use of an average value of Z_{end} for all fluid flowrates seemed more practical than individual Z_{end} at different fluid flowrates as the random errors would be averaged out by the former method. The average Z_{end} was taken to be 12 cm as shown in Figure 6.38. The true height of an overall gas phase transfer unit H_{OG} was then determined from the packed bed height (Z) and the equivalent height of the end effects (Z_{end} = 12 cm) as follows:

$$H_{OG}(true) = \frac{Z + Z_{end}}{N_{OG}} \tag{6.78}$$

The correct Z_{end} should result in true values of H_{OG} independent of the packed bed height. Hence the data from both the 8.5 cm and 19.0 cm packed bed heights should yield equivalent true values of H_{OG} at the same gas and liquid flowrates. Linear regression analysis suggested that the apparent values of H_{OG} are proportional to $L^{-0.33}$ where L is the liquid mass velocity (kg/m^{2}s). Graphs of $H_{OG} L^{0.33}$ versus the gas mass velocity G (kg/m^{2}s) based on data from both packed bed heights should then superimpose one another when sufficiently corrected for the end effects. Figure 6.39 shows the uncorrected data whilst Figure 6.40 shows the corrected version using an average Z_{end} of 12 cm.
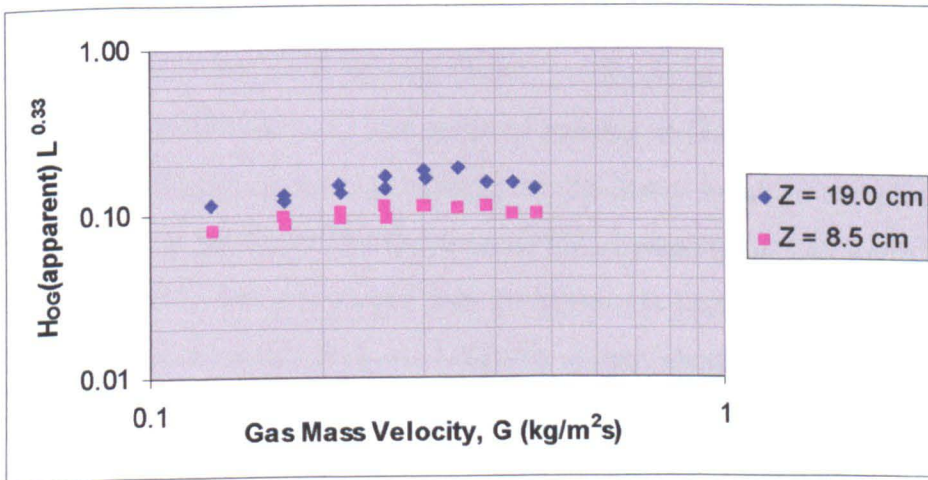
Figure 6.39
End effects in apparent values of H_{OG}.
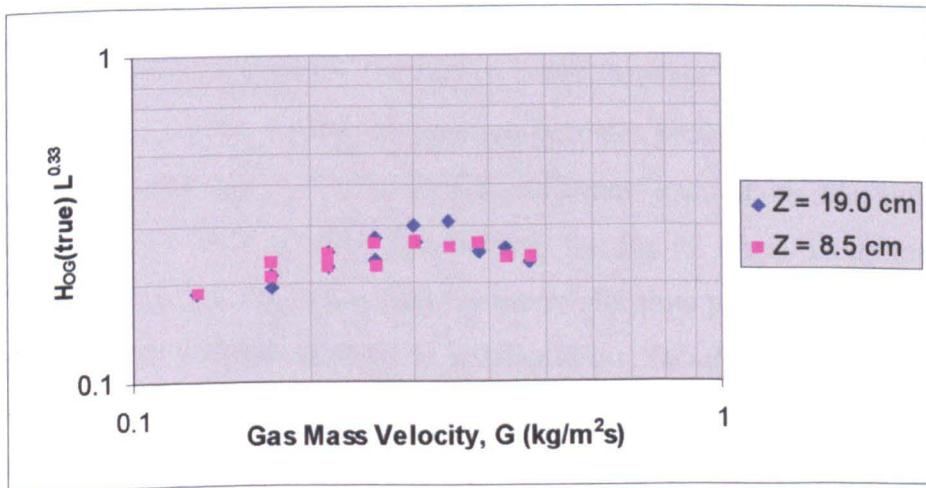
Figure 6.40
True values of H_{OG}, corrected for end effects equivalent bed height of 12 cm.

222

Multiple linear regression analysis yields the following correlation between the overall volumetric gas phase mass transfer coefficient (true values) with the liquid and gas mass velocities up till before the flooding point (till 0.51 kg/m^{2}s air at 3.49 kg/m^{2}s water; till 0.39 kg/m^{2}s air at 6.97 kg/m^{2}s water). The main resistance to mass transfer for ammonia absorption into water resides in the gas phase. The exponents on the liquid and gas mass velocities are in accord with those documented by Strigle (1994) for gas film controlled processes.

$$K'_{G}a = 0.127 \, L^{0.22} \, G^{0.79} \qquad (R^2 = 0.87) \qquad (6.79)$$

where $K'_{G}a$ = overall volumetric gas phase mass transfer coefficient (kmol/m^{3}s)

  L   = liquid mass velocity (kg/m^{2}s)

  G   = gas mass velocity (kg/m^{2}s)

The variation of true values of H_{OG} with gas mass velocity, G is depicted in Figure 6.41. At a liquid mass velocity L of 3.49 kg/m^{2}s, H_{OG} increases with G until a maximum is reached at 0.34 kg/m^{2}s which marks the onset of loading. Beyond this point, the mass transfer efficiency (as in $K'_{G}a$) markedly rises rapidly with G, producing a corresponding drop in H_{OG}. This is attributed to more effective wetting of the packing as the gas flow becomes sufficiently high such that it interferes with the downflowing liquid, producing an increase in liquid holdup and hence the gas-liquid interfacial area. The onset of loading at G equals 0.34 kg/m^{2}s herein coincided with the apparent loading point as marked by the lower break in the plot of log $\Delta P/l$ versus log G (Figure 6.5 in Section 6.3.1) at the same liquid velocity of 3.49 kg/m^{2}s. However, the data for L at 6.97 kg/m^{2}s seems to imply that the system is just approaching the loading point, although experimental observation showed that the system should already be in the loading region by the time G reaches 0.39 kg/m^{2}s at the very least, as flooding set in at 0.43 kg/m^{2}s air flowrate. The corresponding plot of true values of $K'_{G}a$ versus G is shown in Figure 6.42. A change in liquid flow pattern could explain the apparent suppression in $K'_{G}a$ as G increases and hence the 'missing' loading point for the higher water flowrate. Flow visualisation studies (Section 6.2) have shown that the rivulet flow pattern becomes predominant over droplet flow at both higher liquid and gas rates, with a greater influence exerted by the liquid rate. From observed differences in heat transfer coefficients for liquid metal irrigation, Standish (1968c) has concluded that the interfacial area for the rivulet flow pattern is lower than that of droplet flow. Therefore the possible decrease in gas-liquid interfacial area as water flowed mainly as rivulets rather than droplets at the higher water flowrate (L at 6.97 kg/m^{2}s) could explain the apparent suppression of mass transfer efficiency.
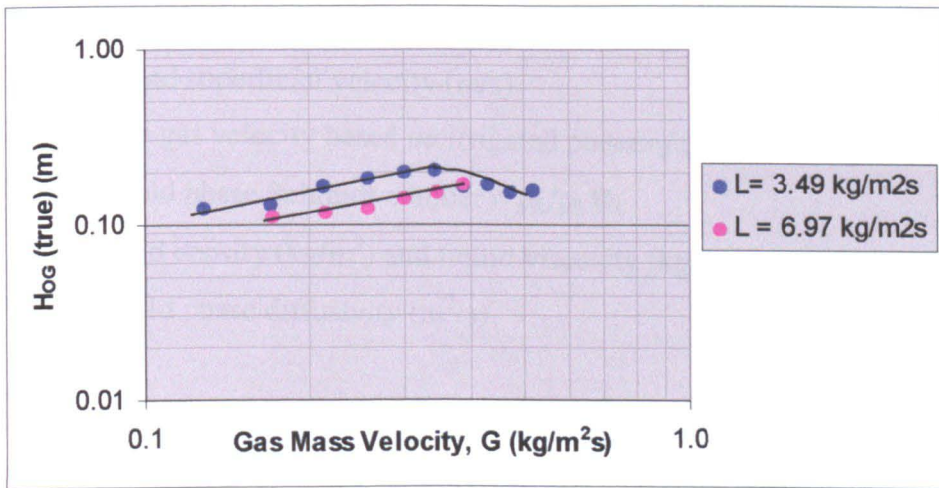
Figure 6.41 *Variation of H_{OG} with gas mass velocity, G.*
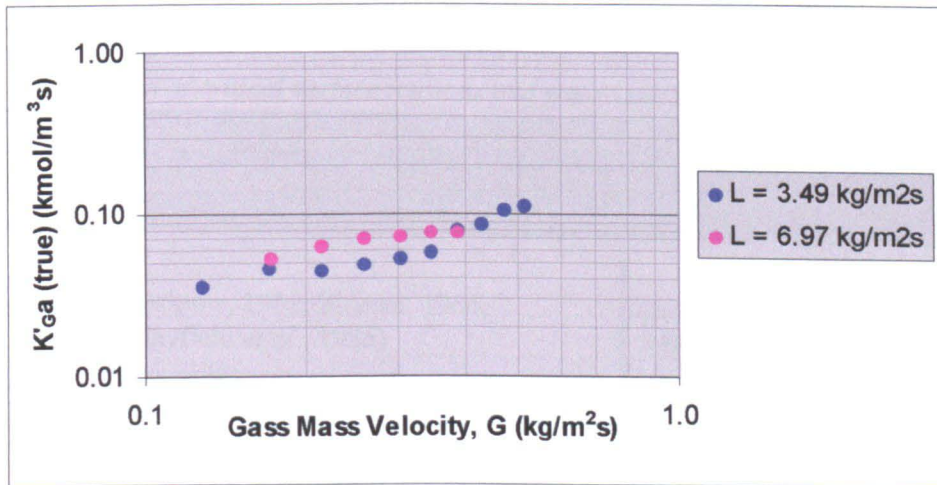
Figure 6.42 *Variation of $K'_{G}a$ with gas mass velocity, G.*

6.7.3 Determination of Gas Film Mass Transfer Efficiency

In order to determine the height of the gas film transfer unit H_G, the mass transfer resistance exerted by the liquid film needs to be subtracted from the overall resistance. To find the height of the liquid film transfer unit H_L for the water-ammonia system, Tait's (1998) H_L data based on oxygen desorption from water into air where the resistance is entirely in the liquid film, was used. Tait measured H_L for 45 and 20 mm waxed polypropylene spheres as well as 45 mm untreated polypropylene spheres and correlated H_L as follows for data up till the loading point (mistakenly viewed by Tait as the flooding point):

$$H_L = \beta' \, (Re_L)^c \, (U_G)^d \, Sc_L^{0.5} \tag{6.80}$$

where H_L = height of a liquid film transfer unit (m)

224

Re_L = liquid phase Reynolds number = $\rho_L u_L d / \mu_L$

u_L = liquid superficial velocity (m/s)

U_G = true gas velocity based on irrigated porosity (m/s)

Sc_L = liquid phase Schmidt number = $\mu_L / \rho_L D_L$

ρ_L, μ_L = liquid density (kg/m^3) and liquid viscosity (kg/ms) respectively

D_L = liquid phase diffusivity (m^2/s)

In terms of non-wetting behaviour, the untreated polypropylene spheres rather than the waxed spheres would resemble much more closely the polyethylene spheres used in this work, as suggested by Table 6.27. Therefore Tait's correlation for the untreated polypropylene packing was used to estimate the liquid film resistance in this study.

Table 6.27 Comparison of critical surface tensions and water-solid contact angles.

Solid Surface	Solid Critical Surface Tension σ_c (dynes/cm)	Water-Solid Contact Angle θ
Polyethylene	31 (Osipow, 1962; Zisman, 1964; Clayfield *et al.*, 1985)	95° (Averaged from Adamson and Gast, 1997)
Polypropylene	31 (Clayfield *et al.*, 1985)	95° (Averaged from Shimizu and Demarquette, 1999)
Paraffin (wax)	24 (Averaged from Lyman *et al.*, 1965)	109° (Craig *et al.*, 1960)

However the correlation derived by Tait for the untreated polypropylene packing was based on data obtained for 45 mm spheres. This has to be corrected to the size of the spheres used in this study i.e. 9.53 mm. An inspection of the H_L data by Tait for the 45 and 20 mm waxed spheres suggested that the both sets of data could be brought to a fairly close agreement by dividing H_L with a factor of $d^{0.2}$ where d is the packing size. It is not unreasonable to assume that the same packing size dependency should apply to the untreated packing as well, having similar spherical geometry and comparable dimension as the waxed spheres. Therefore a packing size correction factor $(9.53/45)^{0.2}$ is added to Tait's H_L correlation for the 45 mm untreated spheres (equation 6.81), giving the equation to estimate H_L for 9.53 mm spheres used in this study (equation 6.82).

For untreated 45 mm spheres (Tait, 1998):

$$H_L = 0.015 \, Re_L^{0.33} \, U_G^{0.14} \, Sc_L^{0.5} \qquad (6.81)$$

For untreated 9.53 mm spheres:

$$H_L \text{ (9.53 mm spheres)} = H_L \text{ (45 mm spheres)} \times \left(\frac{9.53}{45}\right)^{0.2}$$

$$\therefore \; H_L = 0.011 \, Re_L^{0.33} \, U_G^{0.14} \, Sc_L^{0.5} \qquad (6.82)$$

The ammonia absorption in this study is a gas film controlled process involving dilute solutions. Therefore the height of the gas film transfer unit, H_G could be determined using equation 6.83, deducting the liquid film resistance from the overall mass transfer resistance:

$$H_G = H_{OG} - \frac{mG'}{L'} H_L \qquad (6.83)$$

H_G was found to vary from approximately 90% of H_{OG} at a low air rate of 0.13 kg/m^{2}s to about 80% at 0.39 kg/m^{2}s. Therefore about 10% to 20% of the resistance to mass transfer resided in the liquid phase.

6.7.4 Correlation of H_G with Re_G and u_L

The height of the gas film transfer unit obtained in this study is correlated against the gas phase Reynolds number Re_G and the liquid superficial velocity u_L (m/s) as shown in equation 6.84. The true gas velocity U_G in Re_G is based on the effective irrigated bed voidage after deducting the total liquid holdup from the dry bed voidage. To allow for other diffusing species, the gas phase Schmidt number Sc_G is added in equation 6.85, the corresponding plot is shown in Figure 6.43. The exponent of 0.5 on Sc_G is used in line with its general acceptance over the value of 2/3 (Sherwood *et al.*, 1975; Knudsen *et al.*, 1997). The correlations are based on data up till the apparent onset of loading as depicted in Figure 6.41 (G up till 0.34 kg/m^{2}s at L = 3.49 kg/m^{2}s; G up till 0.39 kg/m^{2}s at L = 6.97 kg/m^{2}s).

$$H_G = 0.0011 \, Re_G^{0.39} \, u_L^{-0.46} \qquad (R^2 = 0.92) \qquad (6.84)$$

$$H_G = 0.0013 \, Re_G^{0.39} \, u_L^{-0.46} \, Sc_G^{0.5} \qquad (R^2 = 0.92) \qquad (6.85)$$

where Re_G = gas phase Reynolds number = $\rho_L U_G d / \mu_L$

U_G = true gas velocity based on irrigated porosity = $\dfrac{u_G}{\varepsilon - h_T}$ (m/s)

d = packing diameter (m)
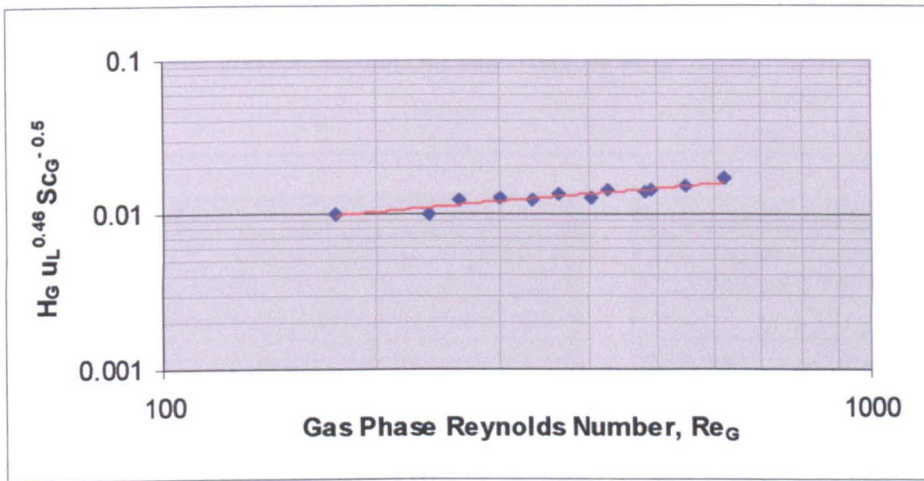
Figure 6.43 *Correlation of H_G with Re_G and u_L.*

The correlation obtained from this study and similar correlations for H_G of non-wetting systems incorporating spherical packing by other investigators are tabulated in Table 6.28. The vast majority of published mass transfer data (both wetting and non-wetting systems) were based on Raschig ring packing. On the other hand, mass transfer data for spherical packing is relatively less, the few available sources on non-wetting spherical packing systems are tabulated herein.

Table 6.28 *H_G correlations based on non-wetting systems (β = empirical constant).*

System	Re_G	u_L (m/s)	H_G
This Work: 9.53 mm polyethylene spheres. Ammonia absorption into water.	$170 \leq Re_G \leq 630$	$0.0035 \leq u_L \leq 0.0070$	$H_G = \beta\,Re_G^{0.39}\,u_L^{-0.46}$
Mackey and Warner (1973): 10 mm glass spheres. Mercury vaporisation into air.	$400 \leq Re_G \leq 3400$	$0.000085 \leq u_L \leq 0.0025$	$H_G = \beta\,Re_G^{0.37}\,u_L^{-0.35}$
Tait (1998): 45 mm paraffin waxed polypropylene spheres. Water vaporisation into air.	$230 \leq Re_G \leq 5000$	$0.00021 \leq u_L \leq 0.0034$	$H_G = \beta\,Re_G^{0.31}\,u_L^{-0.20}$
Tait (1998): 45 mm polypropylene spheres. Water vaporisation into air.	$600 \leq Re_G \leq 5500$	$0.00021 \leq u_L \leq 0.0034$	$H_G = \beta\,Re_G^{0.16}\,u_L^{-0.24}$

Using multiple linear regression analysis, the best fitting exponent on u_L common to all the H_G data from the various sources in Table 6.28 was found to be -0.30. Variation of (H_G $u_L^{0.30}$ $Sc_G^{-0.5}$) with Re_G for the various non-wetting systems are then compared in Figure 6.44. The gas phase Schmidt number Sc_G is added to allow for different diffusing species. The exponent of 0.5 was found to give a slightly better overall fit than an exponent of 2/3.
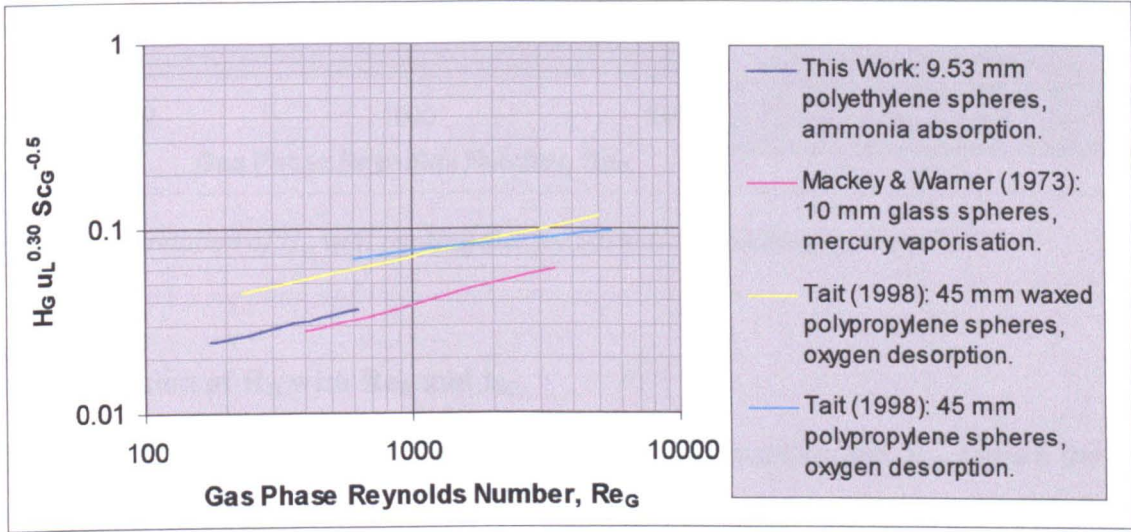
Figure 6.44 Comparison of H_G from various non-wetting systems.

There is an obvious dependence of H_G on the size of the spherical packing. Both the 9.53 mm and 10 mm spheres give higher mass transfer efficiency, the H_G plots being displaced significantly lower than the plots for the 45 mm spheres. The specific surface area of a sphere is inversely proportional to its diameter. Hence smaller spheres have greater specific surface area and form packed beds of greater surface area per unit bed volume. Therefore for a given packed bed volume, smaller spheres would provide greater liquid-gas interfacial area for more efficient mass transfer. The displacement between the plots in Figure 6.44 can be reduced significantly by introducing a packing size factor d (m). Multiple linear regression gives the best general fit for all the data when H_G is correlated against $u_L^{-0.27}$ $d^{0.40}$ as shown in Figure 6.45 and the corresponding relationship shown by equation 6.86. The correlation is remarkable considering that the data is from different sources based on various physical systems and mass transfer processes. The decrease in H_G with packing size has also been noted by Mackey and Warner (1973) for mercury vaporisation and ammonia absorption involving beds of Raschig rings (the latter using non-wettable waxed packing).

$$H_G = \beta \, Re_G^{0.27} \, u_L^{-0.27} \, d^{0.40} \, Sc_G^{0.5} \qquad (6.86)$$
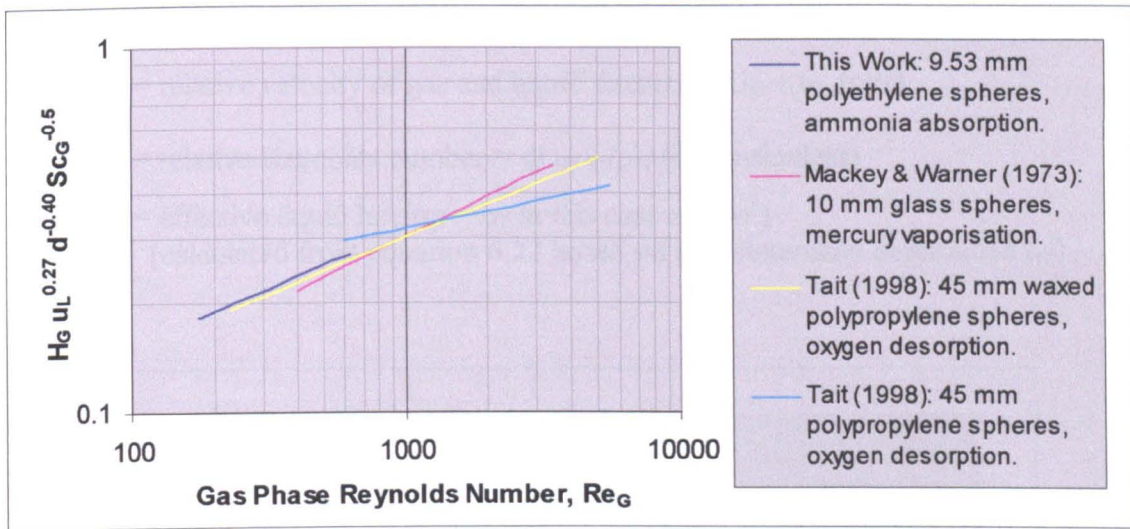
Figure 6.45 Correlation of H_G with packing size for various non-wetting systems.

6.7.5   Correlation of H_G with Re_R and h_E

Warner (1959b) first correlated the height of the gas film transfer unit H_G against the relative velocity of gas and liquid streams U_R, the relative Reynolds number Re_R, and the effective liquid holdup h_E. h_E is the holdup which is effective for the mass transfer process. For conventional aqueous and organic liquid systems, only the dynamic holdup is considered the active contributor in gas absorption as the static holdup is made up of relatively stagnant liquid pools held in the packing interstices, becoming easily saturated with the solute which renders it ineffective to solute transfer (Shulman *et al.*, 1955a). However the mobility and higher turnover rate of liquid at static holdup sites have been observed for non-wetting systems such as those for liquid metals (Warner, 1959a; Standish, 1963, 1968b) as well as in the present study involving water irrigation on a polyethylene surface. Therefore the total holdup would be effective in these non-wetting systems.

Using the same form of correlation as proposed by Warner (1959b), the mass transfer data obtained from this study is correlated as follows, the effective holdup being equivalent to the total holdup. Again, the correlations are based on data up till the onset of loading.

$$H_G = 0.0008 \left(\frac{U_G}{U_R} \right) (\text{Re}_R)^{0.53} (h_E)^{-0.82} \qquad (R^2 = 0.91) \qquad (6.87)$$

$$H_G = 0.001 \left(\frac{U_G}{U_R} \right) (\text{Re}_R)^{0.53} (h_E)^{-0.82} (Sc_G)^{0.5} \qquad (R^2 = 0.91) \qquad (6.88)$$

where U_G = true gas velocity based on irrigated bed porosity (m/s)

U_R = relative velocity of gas and liquid streams = $U_G + u_L$ (m/s)

Re_R = relative Reynolds number = $dU_R\rho_G/\mu_G$ (dimensionless)

h_E = effective liquid holdup = h_T in this case (m^3/m^3)
(calculated from equation 6.22 based on experimentally determined h_T)
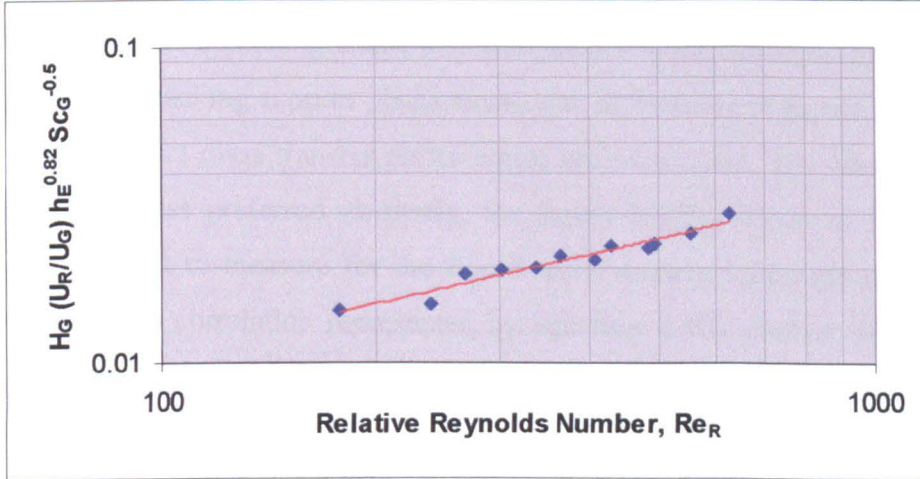
Figure 6.46 *Correlation of H_G with effective liquid holdup h_E.*

In comparison to the exponent of –0.82 for h_E in equations 6.87 and 6.88, Tait (1998) found that the exponent on h_E is –0.29 for 45 mm waxed spheres, -0.16 for 20 mm waxed spheres and –0.21 for 45 mm untreated polypropylene spheres. However, Tait used the measured dynamic holdup as h_E as the static holdup could not be determined in his study, although it was acknowledged that the effective holdup should in fact equal the total holdup in the water vaporisation studies. Regression analysis using data from this study based on dynamic holdup as the correlating parameter rather than the total holdup give the exponent on the holdup term to be –0.48, which is closer now to those of Tait's.

6.7.6   Implication for Hot Scrubber

In the case of H_2S gas absorption into molten tin in the high temperature gas scrubber, the process rate is dependent on the physical diffusion within the gas and liquid phases as well as the chemical reaction between H_2S and tin in the liquid phase. In other words, the rate of absorption is influenced by both the resistance to diffusion and by the finite velocity of the reaction.

The chemical reaction in the liquid phase does not influence the gas film mass transfer coefficient. Hence the gas phase diffusional resistance to mass transfer could be estimated using equation 6.85 derived from ammonia absorption in the analogous non-wetting water system. As the same sphere diameter of 9.53 mm is used in both systems, no correction for packing size is required. As demonstrated in Figure 6.45, the form of correlation given in equation 6.86 (similar form to equation 6.85) holds well for mass transfer in both non-wetting water and liquid metal systems. In addition, hydrodynamic similarities between the packed beds in the cold model and the hot scrubber (identical packing shape and size, nearly identical column dimensions, similar liquid distributor and packing support plate) meant that differences in liquid distribution and end effects which may affect mass transfer performance are minimised. The correlation represented by equation 6.88 is less preferred as firstly, the liquid holdup needs to be known which is experimentally difficult to measure for the liquid metal system (although it may be estimated from the liquid holdup correlation represented by equation 6.30), and secondly it has not been verified to apply simultaneously to both aqueous and liquid metal irrigated spherical packed beds.

The liquid film mass transfer coefficient k'_L will depend on the reaction rate between dissolved H_2S and tin. Favourable kinetics conditions such as higher temperatures (as noted by Schürmann, 1984) will increase k'_L. If coupled with a large excess of unreacted tin such that equilibrium back pressure of H_2S over the molten tin and hence m (the liquid-gas equilibrium constant) are negligible, the resulting liquid phase resistance m/k'_L will be insignificant. The absorption process is then governed nearly completely by the diffusional resistance in the gas phase. In this case, the gas absorption rate may be estimated from k'_G which will approximate K'_G, or H_G which can be estimated from equation 6.85 will approximate H_{OG}. Conversely, the liquid phase resistance becomes predominant when chemical kinetics is slow and/or when high gas rates are used together with very low liquid tin rates. The liquid film mass transfer coefficient in the presence of a chemical reaction as in this case will differ from that for a physical absorption. Therefore equations to predict k'_L or H_L based on a purely physical absorption process such as equation 6.80 will not be applicable.

Summing up, the liquid phase contribution to the overall mass exchange resistance and hence the relative proportion of resistance in the gas and liquid phases for the H_2S absorption process will be dictated by experimental conditions such as operating temperature as well as gas and liquid rates used. As H_G can be approximated from equation 6.85, H_L for the hot system can be found as the difference between the experimentally determined H_{OG} and the calculated H_G.

6.7.7   Analysis of Errors

❑ *Measured Quantities*

The sensitivity of instruments used in the gas absorption tests and the corresponding errors in the measured quantities are summarised in the following table.

Table 6.29 *Errors in measured quantities for gas absorption tests.*

Apparatus/ Instrument	Measured Quantity	Smallest Instrument Graduation or Sensitivity	Smallest Reading Obtainable	Absolute Error on Measured Quantity
Air rotameter	Air volumetric flowrate	5 litre/min	5 litre/min	±2.5 litre/min
Water rotameter	Water volumetric flowrate	0.1 cm Calibration chart average gradient = 5.8 cm/1.0 litre/min.	0.02 litre/min	±0.01 litre/min
NH_3 rotameter	NH_3 volumetric flowrate	5 cm^3/min	1 cm^3/min	±0.5 cm^3/min
NH_3 gas analyser	NH_3 concentration in outlet gas	1 ppmv	1 ppmv	±20 ppmv (due to reading fluctuations)
Thermometer	Fluid temperature	0.1°C	0.1°C	±0.05°C
Photometer	Dissolved NH_4 ions concentration in outlet water	0.1 mg/litre	0.1 mg/litre	±0.05 mg/litre
Measuring tape	Packed bed height; Column diameter	0.1 cm	0.1 cm	±0.05 cm

❑ *NH_3 Gas Concentration*

Due to fluctuations in the gas analyser readings, the absolute error associated with the measured NH_3 gas concentration is estimated to be ±20 ppmv. The resulting percentage error on the values of y i.e. the mol fraction of NH_3 in the gas phase increases as y decreases. It ranges from ±7% to ±30% for NH_3 concentrations at the gas outlet (y_T), whilst the NH_3 concentration at the gas inlet (y_B) has an associated percentage error of about ±2%.

❑ *Dissolved NH_3 Concentration in Liquid Phase*

The concentration of dissolved ammonia in the outlet water, x_B was calculated from the material balance represented by the following equation:

$$x_B = \frac{G'}{L'}(y_B - y_T) \tag{6.76}$$

The percentage error associated with x_B is then:

$$\frac{e_{xB}}{x_B} \times 100\% = \sqrt{\left(\frac{e_{G'}}{G'}\right)^2 + \left(\frac{e_{L'}}{L'}\right)^2 + \left(\frac{e(y_B - y_T)}{y_B - y_T}\right)^2} \times 100\% \tag{6.89}$$

where
$$e(y_B - y_T) = \sqrt{e_{yB}^2 + e_{yT}^2} = \pm\sqrt{20^2 + 20^2} = \underline{\pm 30 \text{ ppmv}} \tag{6.90}$$

And since $G' \propto \dfrac{Q_G}{D_{col}^2}$ and $L' \propto \dfrac{Q_L}{D_{col}^2}$ where Q = measured volumetric flowrate (litre/min) and

D_{col} = column diameter, the fractional errors on G' and L' are calculated as follows:

$$\frac{e_{G'}}{G'} = \sqrt{\left(\frac{e(Q_G)}{Q_G}\right)^2 + \left(2 \times \frac{e(D_{col})}{D_{col}}\right)^2} \quad \text{and} \quad \frac{e_{L'}}{L'} = \sqrt{\left(\frac{e(Q_L)}{Q_L}\right)^2 + \left(2 \times \frac{e(D_{col})}{D_{col}}\right)^2} \tag{6.91}$$

Based on all the data sets up till before flooding, the percentage error on x_B was found to range from about ±5% to ±10%.

For a random selection of the test runs (not all due to insufficient cuvettes), analyses for the ammonium content were made on the water stream leaving at the bottom of the column. The difference between the measured ammonia concentration in the exit water stream and the concentration calculated from the material balance over the column (equation 6.76) averages at approximately 10% higher for the former. This figure coincides fairly with the range of the preceding calculated percentage error on x_B.

❑ *Logarithmic Mean Driving Force*

The logarithmic driving force is calculated using the following equation with 'g' and 'f' representing the numerator and denominator respectively:

$$(y - y^*)_{lm} = \frac{y_B - y_B^* - y_T}{\ln\left(\dfrac{y_B - y_B^*}{y_T}\right)} = \frac{g}{f} \tag{6.92}$$

The error associated with 'g' is determined as follows ($y*_B = m \times x_B$):

$$e_g = \sqrt{e_{yB}^2 + e_{yB*}^2 + e_{yT}^2} = \sqrt{e_{yB}^2 + (m \times e_{xB})^2 + e_{yT}^2} \qquad (6.93)$$

From equation A3.11 in Appendix 3.1, the error associated with 'f' is as follows:

$$e_f = \sqrt{\left(\frac{\partial f}{\partial y_B} \cdot e_{yB}\right)^2 + \left(\frac{\partial f}{\partial y_B *} \cdot e_{yB*}\right)^2 + \left(\frac{\partial f}{\partial y_T} \cdot e_{yT}\right)^2} \qquad (6.94)$$

$$e_f = \sqrt{\left(\frac{e_{yB}}{y_B - y*_B}\right)^2 + \left(\frac{e_{y*B}}{y*_B - y_B}\right)^2 + \left(\frac{e_{yT}}{-y_T}\right)^2} \qquad (6.95)$$

The percentage error associated with the logarithmic driving force $(y-y*)_{lm}$ was calculated as follows and was found to range from ±8% to ±13% based on all data sets up till before the onset of flooding.

$$\frac{e(y - y*)_{lm}}{(y - y*)_{lm}} \times 100\% = \sqrt{\left(\frac{e_g}{g}\right)^2 + \left(\frac{e_f}{f}\right)^2} \times 100\% \qquad (6.96)$$

❏ *True Height of an Overall Gas Phase Transfer Unit*

The true value of H_{OG} corrected for end effects and its corresponding percentage error were calculated as follows:

$$H_{OG} = \frac{Z + Z_{end}}{N_{OG}} = (Z + Z_{end}) \times \frac{(y - y*)_{lm}}{y_B - y_T} \qquad (6.97)$$

$$\frac{e(H_{OG})}{H_{OG}} \times 100\% = \sqrt{\left(\frac{e(Z + Z_{end})}{Z + Z_{end}}\right)^2 + \left(\frac{e(y - y*)_{lm}}{(y - y*)_{lm}}\right)^2 + \left(\frac{e(y_B - y_T)}{y_B - y_T}\right)^2} \times 100\%$$

Both $e(y - y*)_{lm}$ and $e(y_B - y_T)$ have been previously determined, which leaves only $e(Z + Z_{end})$ to be ascertained. The error associated with the measured height of the packed bed Z is simply ±0.05 cm as shown in Table 6.29. A best average Z_{end} value of 12 cm was applied to all the mass transfer data. Inspection of Figure 6.40 shows that this average value did not fully correct the end effects for some of the data points. The error between the best fitting Z_{end} for a particular combination of gas and liquid rates with the employed value of 12 cm averages at approximately

±20% i.e. ±2.4 cm. Therefore, the final calculated percentage error on true values of H_{OG} ranges from ±12 to 15% for all data points up till before flooding.

□ *True Overall Volumetric Gas Phase Mass Transfer Coefficient*

True values of $K'_G a$ were calculated as follows, based on true values of H_{OG}:

$$K'_G a = \frac{G'}{H_{OG}} \tag{6.98}$$

The percentage error on $K'_G a$ is then based on the following equation, and was found to range from ±12% to ±16%.

$$\left(\frac{e(K'_G a)}{K'_G a} \right) \times 100\% = \sqrt{\left(\frac{e(G')}{G'} \right)^2 + \left(\frac{e(H_{OG})}{H_{OG}} \right)^2} \times 100\% \tag{6.99}$$

□ *Height of a Gas Film Transfer Unit*

H_G was determined from the following equation, using the experimentally determined H_{OG} with H_L predicted from the empirical equation given by Tait (1998) and corrected for difference in packing size.

$$H_G = H_{OG} - \frac{mG'}{L'} H_L \tag{6.83}$$

The error associated with H_G is determined as follows. The error on H_L that was determined from equation 6.82 was approximately ±15% (Tait, 1998).

$$e(H_G) = \sqrt{e(H_{OG})^2 + e\left(\frac{mG'}{L'} H_L \right)^2} \tag{6.100}$$

where
$$\frac{e\left(\frac{mG'}{L'} H_L \right)}{\frac{mG'}{L'} H_L} = \sqrt{\left(\frac{e(G')}{G'} \right)^2 + \left(\frac{e(L')}{L'} \right)^2 + \left(\frac{e(H_L)}{H_L} \right)^2} \tag{6.101}$$

The calculated percentage error on H_G ranges from ±12% to ±15%.

6.8   Summary

❏ *Preliminary Gasification Studies*

Small-scale gasification of petroleum coke samples was carried out in an electrically heated horizontal furnace using a steam/nitrogen mixture as the gasifying medium. Gasification was performed with and without the presence of tin. The amounts of H_2S sampled from the product gas stream in both occasions were compared. There was roughly 10% reduction in the sampled H_2S upon tin addition. The reduction was small as any reaction involving the tin was limited by the small surface area of the tin available for contact with the gas stream. At a temperature of about 1000°C, the molten tin reacted with the product gas depositing a solid residue. However at a temperature in the region of 500°C (could be lower due to possibly lower gas phase temperature), the kinetics were too slow for similar reaction(s) between the fuel gas and the molten tin to take place. The solid residue was most likely a mixture of mainly SnO_2 from the reaction of molten tin with steam and CO_2 with a small fraction of SnS contributed by the reaction of molten tin with H_2S. Combustion analysis of the residue detected the presence of sulphur while inductive coupled plasma spectrometry detected the presence of tin, hence confirming that the H_2S in the product gas has indeed reacted with molten tin. The small-scale gasification studies have provided actual confirmation and evidence of the possibility of sulphur removal by molten tin under the gasification environment.

❏ *Cold Gas Scrubber Studies: Flow Visualisation*

The water flow on the surface of polyethylene and paraffin-waxed glass spheres were visually observed, aided by high-speed digital imaging for motion analysis of droplets and rivulets. Droplet formation sites were identified. These were generally sites having either a single packing sphere with an immediate space below it or sites at which two or three spheres contacted one another. At these locations, the water droplet grew to about 4 mm in size as more water accumulated before becoming unstable and being displaced. The mobility of static holdup is demonstrated herein due to the tendency of water to form droplets rather than film on the hydrophobic packing surface. Either a droplet flow or rivulet flow was formed from the displaced droplet depending on the configuration of the bottom spheres and the water flowrate. At high water flowrates, the frequency of droplet formation was sufficiently high such that individual droplets flow so close to one another merging into rivulets about 3 to 4 mm width. Static droplets about 2 mm in size were also noted at some packing intersections. The droplet

velocity at a particular packing location showed no definite trend with increasing air rate. The droplet velocity measured assuming only vertical downward motion ranged from 10 to 37 mm/s. Rivulet flow generally became more pronounced at higher gas and liquid rates, the latter exerting a much greater effect, agreeing with that documented for liquid metal flow. A more prominent droplet flow was observed for the waxed glass packing compared to the polyethylene packing, this being attributed to the larger water-glass contact angle.

In this study using non-wetting spheres, droplets initiated at packing contact points formed droplet flow and then rivulet flow as liquid rate increased. In comparison, for a reported wetting spherical packed bed system, liquid rings were produced at the contact points, forming rivulet flow and then film flow as liquid rate increased.

The water droplets hanging from the base of the spheres are similar to pendent droplets, their static equilibrium being governed by surface tension and gravitational force. The pendent droplet is expected to adopt a pearl-like shape on a non-wetting solid surface, and it was shown from force balance that the maximum possible equatorial diameter of the water droplet could be predicted from the water surface tension and density. The maximum molten tin droplet size in the packed bed of the hot gas scrubber was estimated in this way to be about 5 mm. Droplet flow is expected to be more prevalent in the hot scrubber compared to the cold model due to significantly larger contact angle of molten tin on the alumina packing surface.

❑ *Cold Gas Scrubber Studies: Flooding*

Pressure drop variation with air flowrate was measured for dry and water-irrigated packed beds of polyethylene and waxed glass spheres. The gas flow through the packed beds was turbulent. The bed pressure gradient varied with the gas velocity to an exponent of at least 1.8. The pressure drop of the polyethylene packing showed a larger dependence on the gas and liquid rates compared to the waxed glass packing. It was difficult to locate the loading point from the log-log plot of pressure gradient versus gas mass velocity for the polyethylene packing. For the waxed glass packing, the loading points were more obvious occurring at a pressure gradient of about 60 mm H_2O/m packing. The flooding points were easier to ascertain, marked by sudden nearly vertical rise in graph gradient. The flooding velocities determined in this manner coincided well with visual flooding indicators during the experiments. The pressure gradient at flooding ranges from 189 to 234 mm H_2O/m and 200 to 239 mm H_2O/m for the polyethylene and waxed glass packings respectively. The waxed glass packing exhibited higher flooding gas

velocities than the polyethylene packing, this being attributed to the slightly higher degree of non-wettability of the former compared to the latter.

Piche *et al.*'s (2001a, 2001c) neural correlation, reportedly one of the best estimators of flooding capacities for randomly packed columns poorly predicted the flooding gas velocities of this study. The flooding velocities were all underpredicted (AARE of 40 to 45%), the error increasing with increasing water velocity. The correlation's failure to extend adequately to the non-wetting system is attributed to its neglect of the surface tension of the solid packing material, a key factor affecting the degree of liquid wetting on the packing surface.

The flooding points from this study along with those of other non-wetting systems were compared graphically with Sherwood *et al.*'s (1938) generalised flooding correlation based on conventional wetting packed columns. The non-wetting flooding points were all clearly displaced above Sherwood *et al.*'s flooding line, demonstrating a clear influence of non-wettability on flooding capacity. The higher flooding capacity of non-wetting systems means a smaller column can be used for a set of fluid volume flowrates. The good agreement in flooding capacities between water-irrigated non-wettable systems with those involving liquid metals implies that under a non-wetting condition, liquid-solid packing contact angle exerts a dominating influence on the maximum hydraulic capacity of packed beds, overriding differences in liquid physical properties. The flooding capacities of non-wetting systems were correlated against their non-wetting tendencies by introducing an additional $(\sigma_c/\sigma_L)^{0.53}$ factor onto the ordinate of the generalised flooding plot. This places the flooding points of the non-wetting system close to or exactly on the Sherwood *et al.*'s generalised flooding line. The scatter in the flooding points of the non-wetting systems was also slightly reduced. The generalised flooding correlation with the inclusion of the non-wetting tendency factor could be used to predict the flooding capacity of the molten tin irrigated hot gas scrubber, allowing a stable gas-liquid operating range to be determined.

❑ *Cold Gas Scrubber Studies: Liquid Holdup*

Static and dynamic holdups were measured for the water-irrigated packed bed of polyethylene spheres. The static holdup was independent of the air velocity, but slightly decreased as water velocity increased. This phenomenon which has been similarly reported for liquid metal irrigation demonstrates the actual mobility of static holdup in non-wetting systems due to the tendency of liquid to form discrete droplets rather than a spreading film. The static holdup in a

non-wetting packed bed would be relatively more effective to mass transfer in a gas absorption process than a conventional wetting system. Static holdup increases with bed porosity. The dynamic holdup increased with both air and water rates, but the air rate effect was evident only beyond the loading point. These dynamic holdup trends are in line with those reported for wetting and other non-wetting systems including liquid metal ones. The gas velocities at which the dynamic holdup showed a sudden rapid rise coincide with previously determined flooding velocities. The dynamic holdup was correlated against the air and water velocities. It varied nearly linearly with water rate before flooding, similar to liquid metal irrigation. In comparison, the exponent on the liquid rate is reported to be less than unity for dynamic holdup of spherical packing at wetting conditions. Total liquid holdup was correlated against the air and water velocities. It increased with both fluid velocities with the latter exerting a greater influence. The agreement in liquid holdup trends between the water irrigated polyethylene packing in this study with those reported for liquid metal irrigation despite vastly different liquid densities and surface tensions is attributed to the similar non-wetting flow regime in both systems.

The total volumetric liquid holdup was empirically correlated following Warner's (1959a) method against bed pressure drop, true gas velocity and gas density. An AARE of 7.2% was obtained. Piche *et al.*'s (2001b, 2001c) neural correlation, reportedly one of the best estimators of liquid holdup in packed columns overestimated the water holdup of this study (AARE 30.5%) and Warner's (1959a) mercury holdup (AARE 52%). The neural correlation's inadequacy where non-wetting systems are concerned is attributed to its neglect of the surface tension of the solid packing material, a key factor affecting the degree of wetting.

The empirical total holdup correlation derived from the cold model based on Warner's method would provide the first approximation of molten tin holdup in the hot scrubber with a packed bed of similar physical geometry to the cold model. The molten tin holdup is expected to be lower than the water holdup due to larger liquid-solid contact angle and liquid density. The total holdup would be effective for H_2S absorption into tin due to mobility of the static holdup.

□ *Cold Gas Scrubber Studies: Gas Lift*

The performance of a small air lift in transporting water has been investigated. Tests were carried out on two different submergence ratios of 0.71 and 0.59. The total length of the air lift was slightly over a metre in both cases. The pumping rate increased with increasing air injection rate. The air lift with the larger submergence ratio gave a higher water discharge rate than the

one with smaller submergence ratio for the same air supply rate. Pumping was initiated at a lower gas injection rate for the former compared to the latter. As the submergence ratio increases, the total mass of the two-phase mixture in the riser becomes progressively smaller relative to the mass of water in the downcomer, therefore increasing the driving force of the pump. The pump efficiency curves exhibited maximum points as air flowrate increased, the peaks being displaced to the lower end of the air flowrate. The drop in efficiency at higher air rates was attributed to more pronounced frictional and air-water slip losses at higher fluid velocities. The peak efficiency was slightly higher for the larger submergence ratio and occurred at a lower air injection rate compared to the smaller submergence ratio.

The various gas injectors tested (longitudinal, 4-port radial, 12-port radial) gave nearly identical pumping performance. The air holes on the radial injectors were all of the same size. Therefore increasing the number of air ports on the injector with no change to the air hole dimension was shown to have negligible effect on the air lift pump performance.

Three available methods to predict air lift pump performance were tested against the experimental data in this study: Zenz' (1993) empirical generalised graphical correlation, and the theoretical models of Nicklin (1963) and Clark and Dabolt (1986). The agreement between Nicklin's model and the experimental data was improved significantly especially over the higher air flowrates by including additional pressure losses, notably the downcomer friction and accelerative effects, giving it the smallest average absolute relative error (AARE) of 9%. Zenz' graphical correlation gave moderate agreement with the experimental data (AARE 31%) whilst Clark and Dabolt's model yielded very poor prediction (AARE 77%).

The best available method to estimate the gas lift performance in transporting molten tin in the hot scrubber would be Nicklin's (1963) model, to which is added other necessary pressure changes within the system particularly the accelerative and downcomer friction losses to complete the momentum balance. However the uncertainty over the extension of two-phase flow equations in the model to liquid metal system remains.

❏ *Cold Gas Scrubber Studies: Particulate Removal*

Particulate removal performance of the water-irrigated packed bed of polyethylene spheres was investigated using a glass dust laden air stream. The particle size distribution of the glass dust resembles a log-normal distribution with mass median diameter of 10.2 μm and geometric

standard deviation of 1.8. The non-wetting packed bed gas scrubber demonstrated very good particulate removal performance with total separation efficiencies ranging from 95.5 to 99.6%. At high air velocities, the total efficiency E_T increased with air and water flowrates as well as inlet dust concentration. Improvement of E_T with fluid flowrates was due to increasing total liquid holdup, resulting in a larger number of droplet and rivulet particulate collectors. Higher dust loading encouraged agglomeration of dust particles in the presence of moisture in the packed bed. The resulting larger overall solids sizes and inertia improved particulate collection via inertial deposition and direct interception mechanisms. In the packed bed gas scrubber, inertial deposition was expected to be the main collection mechanism. At low air velocities, the total efficiencies were randomly scattered without any clear trends. This was attributed to negligible effect of air rate on liquid holdup, hence unchanged dust retention capacity. Similarly, dust loading did not appear to give a definite influence on the separation efficiency at low air velocities, suggesting negligible change in dust agglomeration effect due to constant liquid holdup. At dry bed conditions, dust separation decreased with increasing dust loading due to limited dust retention capacity of the dry bed. The available clean surface area for dust deposition via the electrostatics effect declined rapidly as more dust entered the column, reducing the overall efficiency. The total particulate removal efficiency and the corresponding number of transfer units were correlated against the operating fluid flowrates and solids loading.

Rapid buildup of solids at the bottom section of the fixed bed highlighted the importance of ultimately having a moving bed in the gas scrubber.

The resulting grade efficiency curves demonstrated impressive cut sizes, approaching the submicron range. The cut size decreased with increasing air velocity. The grade efficiency curves were very encouraging in terms of turbine blade protection as dust particles larger than about 6.5 μm can be separated to efficiencies greater than 98%. For all cases, complete particle separation was achieved for particles larger than 16 μm. The grade efficiency was correlated against the particle size, following the form proposed by Calvert (1977a; 1977b).

The molten tin irrigated hot scrubber can potentially achieve better solids removal efficiency than the cold scrubber. Besides the tin droplets and rivulets acting as particle collectors in the hot scrubber, the packing elements would also play a part by exploiting the inherent sticky nature of ash and char at elevated temperatures. The adhesiveness of ash and char particles will encourage solids deposition and retention on the packing surfaces.

❑ *Cold Gas Scrubber Studies: Gas Absorption*

The mass transfer efficiency of ammonia absorption into water has been experimentally determined in the non-wetting cold gas scrubber. End effects have been accounted for, giving the true height of overall gas phase transfer unit H_{OG} and the true volumetric overall gas phase mass transfer coefficient K'_{Ga}. K'_{Ga} was found to be proportional to $L^{0.22}$ and $G^{0.79}$, the exponents on the fluid rates were in agreement with those documented for gas film controlled processes. A more predominant rivulet flow pattern over droplet flow might explain the apparent suppression in K'_{Ga} as gas rate increased and hence the 'missing' loading point at high water rate. It has been previously shown that a rivulet flow pattern has lower interfacial area than droplet flow.

The height of the gas film transfer unit H_G was determined by subtracting the liquid film resistance (estimated from a published correlation on similar packing) from the overall mass transfer resistance. H_G obtained in this study for fluid rates up till the apparent onset of loading was correlated against the gas phase Reynolds number and the liquid superficial velocity. A comparison was made with existing published H_G data based on other non-wetting spherical packing systems including liquid metal irrigated packed beds. The various H_G data showed a strong dependence on packing size, H_G decreases as packing size decreases. This was attributed to the increase in gas-liquid interfacial area as packing size diminishes, hence improving mass transfer. The H_G data based on the various non-wetting spherical packed beds could be correlated with good agreement against the gas phase Reynolds number $Re_G^{0.27}$, the liquid superficial velocity $u_L^{-0.27}$ and the packing size $d^{0.40}$. H_G was also correlated against the relative Reynolds number and effective liquid holdup, the latter being the total liquid holdup due to observed mobility of the static holdup in this study.

The rate of H_2S gas absorption into molten tin in the high temperature gas scrubber will be dependent on both physical diffusion within the fluid phases as well as the chemical reaction between H_2S and tin in the liquid phase. Experimental conditions will influence the extent of liquid phase contribution to the overall mass transfer resistance. The H_G correlation derived from the cold study as a function of gas phase Reynolds number and liquid superficial velocity will provide the means of estimating the gas side resistance whilst the liquid side resistance can be found as the difference between the experimentally determined overall mass transfer resistance and the calculated gas side resistance.

Chapter Seven

Computational Fluid Dynamics Modelling: Particulate Removal In A Packed Bed

This chapter presents the computational fluid dynamics (CFD) modelling of particulate removal in a non-wetting packed bed of spheres. Grid generation pre-processing was carried out on GAMBIT whilst mathematical calculations were performed using the CFD solver on FLUENT 5. Simulation results are compared with the experimental findings from particulate removal studies performed on the water-irrigated cold gas scrubber.

7.1   Problem Definition and Geometry Assumptions

The removal of particulates from a gas stream flowing through a packed bed of spheres under non-wetting liquid flow conditions is to be simulated and the modelling results compared to the experimental findings. In the actual packed bed gas scrubber, liquid flows downwards counter-currently to the upward flowing gas stream laden with dust particles. Under non-wetting conditions, the liquid flows as discrete droplets and rivulets on the packing surface.

In the CFD simulations, it is assumed that only droplets are present on the packing surface. The gas stream sees the liquid flow as fixed droplets on the solid spheres. This is a reasonable assumption as in the experimental studies on particulate removal in the actual packed bed scrubber, the gas velocity was typically 25 to 45 times that of the water velocity. Flow visualisation studies have shown that the water droplets could attain a maximum size of approximately 4 mm before becoming unstable and be displaced off the packing surface. It is hence assumed in the simulations that all the droplets have a uniform size of about 3 mm each.

In the actual system, the solid spheres are randomly packed within the column. However a systematic type of spherical packing is assumed in the CFD simulations. Graton and Fraser (1935) discussed several systematic packings of spheres. These systematic assemblages are made up of either square

Square Layer   Simple Rhombic Layer
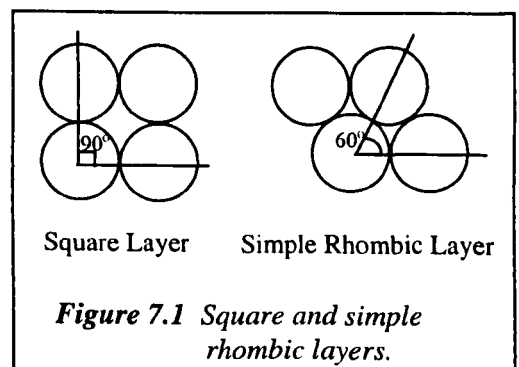
Figure 7.1 *Square and simple rhombic layers.*

or simple rhombic layers (Figure 7.1), or a combination of both types of layers. The square and simple rhombic layers form four major types of systematic packings listed in Table 7.1. In each type of systematic packing, every sphere is arranged identically with respect to every other sphere, and each sphere is identified by the same co-ordination number i.e. the number of adjacent spheres which are in contact with a selected sphere (Gray, 1968). There is a characteristic porosity associated with each systematic packing type.

Table 7.1 Systematic assemblages of spheres (Graton and Fraser, 1935).

Systematic Packing Type	Porosity (%)	Co-ordination Number
Cubic	47.6	6
Ortho-rhombic	39.5	8
Tetragonal	30.2	10
Rhombohedral	26.0	12

The porosity of the packed bed of 9.53 mm polyethylene spheres is 45%. Based on the porosity, the packed bed most closely resembles a cubic type of systematic packing as suggested by the figures in Table 7.1. Therefore a cubic arrangement of spheres is adopted to model the packed bed. This consists of square layers aligned directly on top of one another.

7.2   Geometry Setup and Grid Generation

The number of droplets per unit volume of the packed bed depends on the total liquid holdup and the volume of each droplet. The total liquid holdup is dependent on both the air and water flowrates. At 53 litre/min air flowrate (atmospheric pressure) and 2 litre/min water flowrate (particulate removal experimental setup), the experimentally measured volumetric total liquid holdup is 93.18 cm^3. The total volume of the packed bed (bed height 19 cm, column diameter 7.8 cm) is 907.89 cm^3.

The packing in the model is made up of 10 mm spheres, each sphere occupying a 10×10×10 mm^3 cube. Assuming equal distribution of liquid holdup per unit volume of bed, the volume of liquid in the 10×10×10 mm^3 cubic space is $\frac{1000}{907890} \times 93180$ mm^3 i.e. 102.63 mm^3. Assuming that all the liquid in the packed bed is present as droplets on the spherical packing surface and none exists in the free space between the packing elements, this means that the total volume of liquid droplets on a single solid sphere is 102.63 mm^3.

Each liquid droplet is a 3 mm sphere 'merged' with the 10 mm solid packing sphere such that the angle of contact between the two spheres is about 95° (measured from within the droplet) i.e. the contact angle of water on a polyethylene packing surface. The droplet volume is then obtained by deducting the common volume of intersection between the two spheres from the volume of the droplet sphere, this being illustrated in Figure 7.2.

Figure 7.2 *Intersecting droplet and solid spherical packing.*
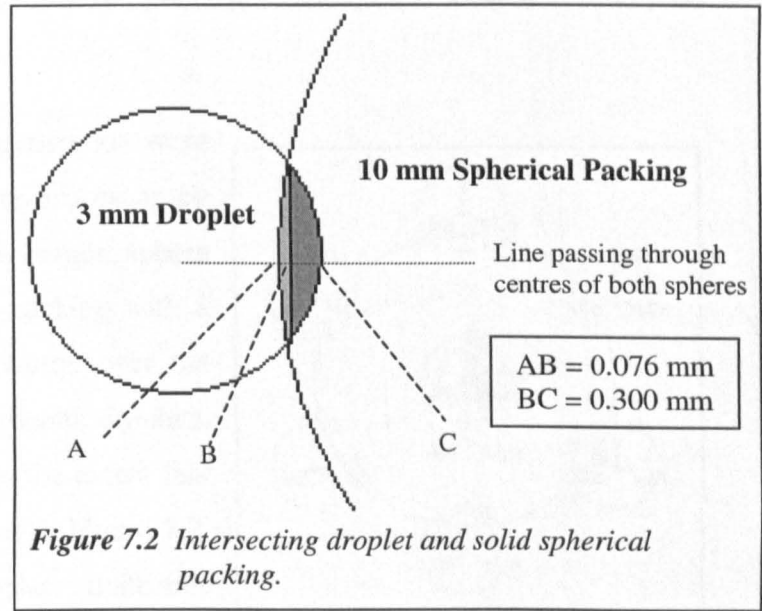
A cap of height h on a sphere having a radius r as depicted in Figure 7.3 has a volume given by the following equation:

$$\text{Volume} = \pi h^2 \left(r - \frac{h}{3} \right) \qquad (7.1)$$

Figure 7.3 *Volume of sphere cap.*
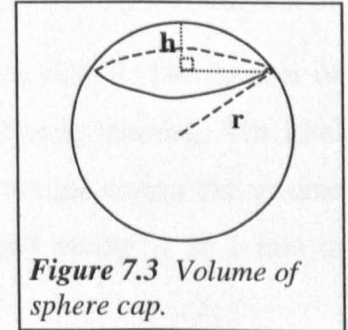
Therefore the volume of the cap on the 3 mm droplet sphere as represented by the black shaded area in Figure 7.2 is:

$$= \pi [BC]^2 \left(1.5 - \frac{[BC]}{3} \right) = \pi (0.300)^2 \left(1.5 - \frac{0.300}{3} \right) = 0.1260\pi \text{ mm}^3 \qquad (7.2)$$

Similarly, the volume of the cap on the 10 mm spherical packing as represented by the grey shaded area in Figure 7.2 is:

$$= \pi [AB]^2 \left(5 - \frac{[AB]}{3} \right) = \pi (0.076)^2 \left(5 - \frac{0.076}{3} \right) = 0.0287\pi \text{ mm}^3 \qquad (7.3)$$

$\therefore$ Total volume of intersection $\quad = 0.1260\pi + 0.0287\pi = 0.155\pi \text{ mm}^3$

$\therefore$ Actual volume of 1 liquid droplet $=$ Volume of complete sphere $-$ Volume of intersection

$$= 4/3 \times \pi (1.5)^3 - 0.155\pi$$

$$= 13.65 \text{ mm}^3$$

Since the total volume of droplets on a single solid sphere is 102.63 mm³, the number of droplets on the sphere is 102.63/13.65 i.e. approximately 8. The 8 droplets on each solid

sphere are assumed distributed uniformly over the packing surface, each located centrally on each of the 8 face quadrants of the sphere.

3-dimensional geometry setup and grid generation were performed using the GAMBIT CFD Pre-processor by Fluent Inc. Figure 7.4 depicts the basic single sphere volume representing the solid spherical packing with 8 smaller sphere volumes uniformly distributed over the larger sphere surface representing the liquid droplets. The 8 droplets are identical in size and in the extent that they intersect the solid sphere as depicted in Figure 7.2. The single solid sphere with 8 droplets uniformly distributed on its surface forms the basic unit of the packed bed. The final 3-dimensional packed bed
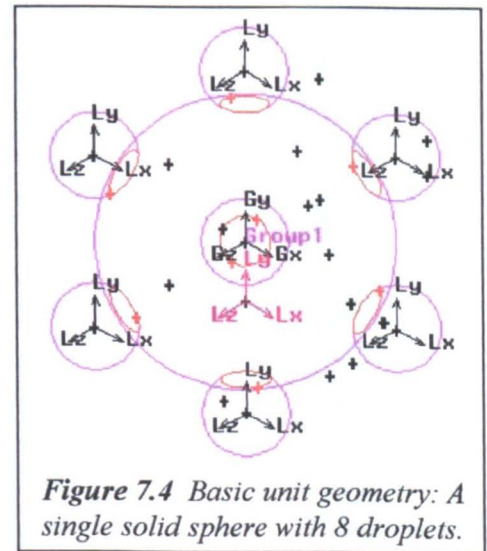
Figure 7.4 *Basic unit geometry: A single solid sphere with 8 droplets.*

geometry is constructed from 2 × 2 × 5 basic units contained within a cuboid. The number of basic units in the packed bed model is limited by computer memory during meshing. The total volume of the 2 × 2 × 5 basic units is subtracted from the cuboid volume giving the volume occupied by the gas phase. The cuboid representing the packed bed model is 20.1 mm in width, 20.1 mm in length and 55.2 mm in height.

The grid of the gas phase volume was generated using the Tet/Hybrid meshing elements in conjunction with the Tgrid meshing scheme. With this selection, all faces are meshed with irregular triangular mesh elements following the Tri-Pave face meshing scheme whilst the grid volume is meshed with tetrahedral mesh elements. This choice was made as the rounded surface of the spheres and the sharp corners of the intersecting spheres were deemed most easily built from tetrahedral mesh elements having tapered corners. The node spacing was such that the interval size between adjacent nodes on an edge is 0.5 mm. This results in the interval size on the shortest edge existing in the entire model being 9.5% of the edge length. It was not possible to generate finer meshes with interval size smaller than 0.5 mm.

Figure 7.5 gives the packed bed model represented by a 20.1 mm × 20.1 mm × 55.2 mm cuboid which houses 5 layers of 2 × 2 solid spheres, each solid sphere having 8 droplets uniformly distributed on its surface. The gas phase volume in between the solid spheres and droplets has been completely meshed. The final grid consists of 572025 cells. The grid face (filled grid) display of the spheres and droplets are depicted in Figure 7.6.
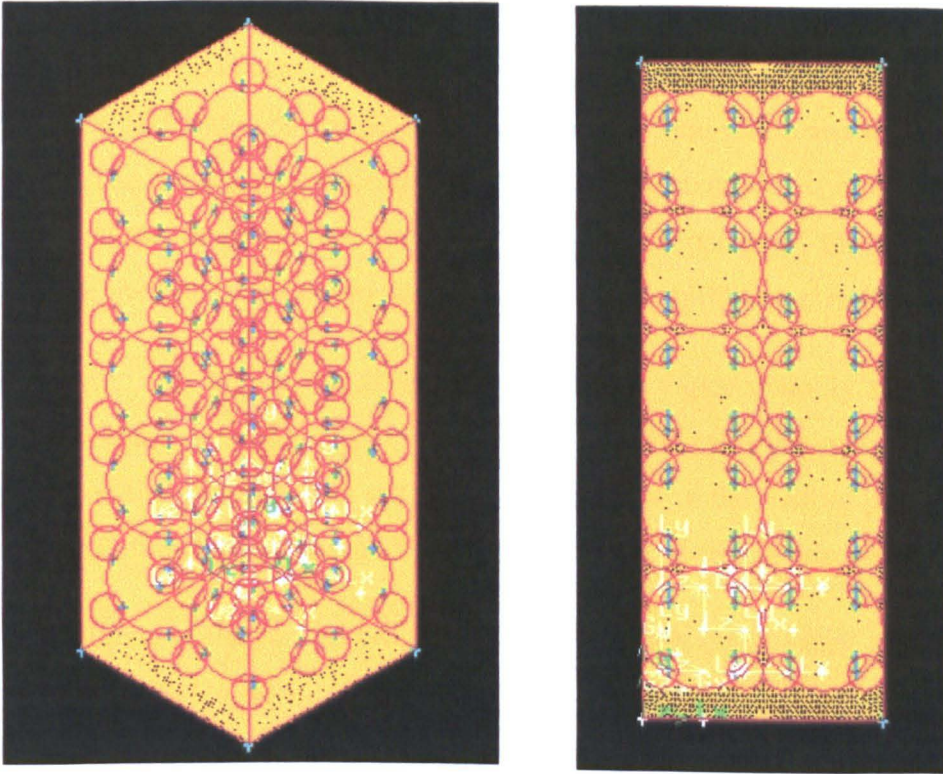
Figure 7.5 Isometric and side views of meshed packed bed model.
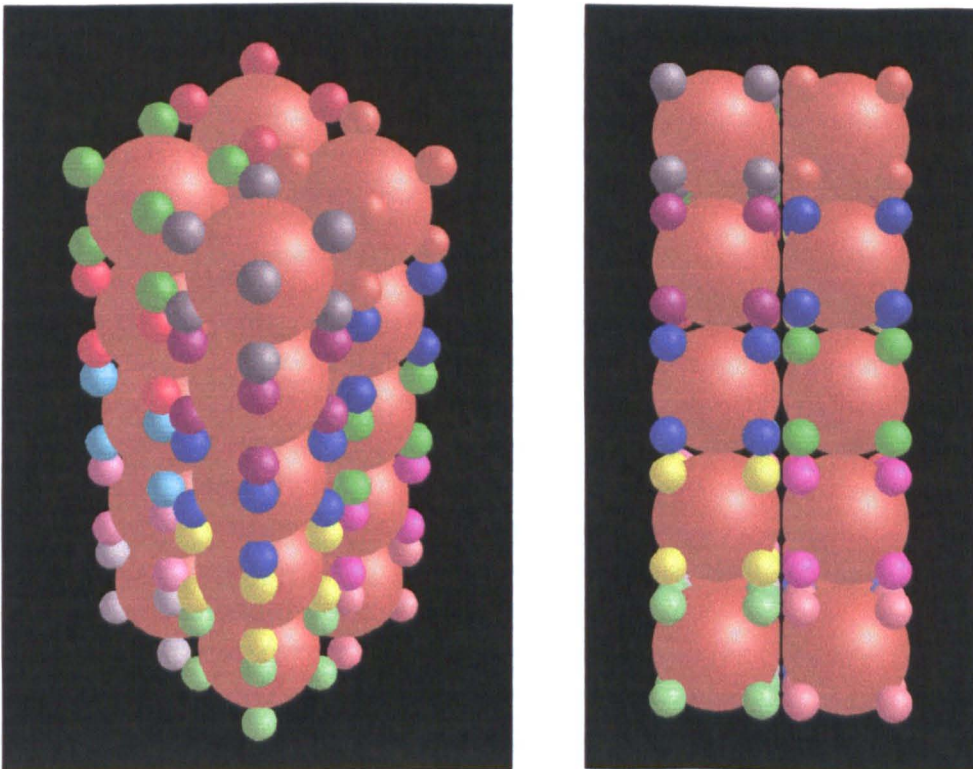
Figure 7.6 Isometric and side views of grid face of packing spheres and droplets.

7.3 Material Properties, Operating and Boundary Conditions

The fully meshed packed bed model was exported to Fluent Inc.'s FLUENT 5 for subsequent processing. The specified materials are air for the continuous fluid phase and inert particle for the discrete phase. The density and viscosity of air are the constant values at 15°C and at the pressure experimentally measured via the bottom pressure tapping of the water irrigated packed column. The inert particle density is varied from 400 to 1800 kg/m³ in the simulations.

The operating pressure P_{op} equals the absolute value of the experimentally measured static pressure via the bottom pressure tapping of the packed column. The reference pressure location for this operating pressure was set at the central point of the bottom plane surface of the 'cuboid'. A gravitational acceleration of -9.81 m/s² in the y-direction was specified.

The boundary conditions of the packed bed model housed within the 'cuboid' are summarised in Table 7.2.

Table 7.2 Boundary conditions of packed bed model.

Regions	Boundary Conditions and Inputs	
Solid spheres	**Wall face boundary:**	*Discrete phase* = reflect.
Droplets on solid spheres	**Wall face boundary:**	*Discrete phase* = trap.
Bottom plane surface of cuboid	**Mass Flow Inlet face boundary:** *Mass flow rate of continuous gas phase, M_G* = (varied). *Total temperature, T* = 288 K. *Initial gauge pressure, P_g* = static pressure relative to operating pressure, P_{op} = 0. *Turbulent intensity, I* = u'/$\overline{u}$ ≈ 0.16 $Re_{Dh}^{-1/8}$ (varied) where u' = root-mean-square of velocity fluctuations; $\overline{u}$ = mean flow velocity; Re_{Dh} = Reynolds number based on hydraulic diameter. *Hydraulic diameter, D_h* = Column diameter = 78 mm. *Discrete phase* = escape.	
Top plane surface of cuboid	**Outflow face boundary:**	*Flow rate weighting* = 1. *Discrete phase* = escape.
Vertical sides of cuboid	**Symmetry face boundary:**	No input required.
Interior of cuboid unoccupied by solid spheres and droplets	**Interior face boundary:** **Fluid cell zones:**	No input required. *Material* = Air.

Two different sets of continuous gas phase were solved, the inputs as in Table 7.3. The first one replicates the particulate removal experimental conditions at 53 litre/min air flowrate (1 atm) and 2 litre/min water flowrate. The packed bed model geometry has been set up following the experimentally obtained liquid holdup data at these fluid flowrates (section 7.2).

The second continuous gas phase was solved following the experimental conditions at 85 litre/min air flowrate (1 atm) and 2 litre/min water flowrate. To save time, the same mesh as that obtained earlier based on the lower air flowrate was applied. As the total liquid holdup at 85 litre/min air is 90.19 cm^3 whilst that obtained at 53 litre/min is 93.18 cm^3, the error involved in the total volume of the droplets is about 3% in this case.

Table 7.3 The different inputs used to solve the continuous gas phases.

Inputs	53 litre/min (0.185 m/s) air flowrate at 1 atm or 0.179 m/s at base of packed bed	85 litre/min (0.296 m/s) air flowrate at 1 atm or 0.278 m/s at base of packed bed
Operating pressure, P_{op} (Pa)	104460	108034
Gas density (kg/m^3)	1.263	1.307
Gas viscosity (kg/ms)	1.8066×10^{-5}	1.8066×10^{-5}
Gas mass flowrate at Mass Flow Inlet, M_G (kg/s)	9.14×10^{-5}	1.47×10^{-4}
Turbulent Intensity at Mass Flow Inlet, I (%)	7	6

7.4   Mathematical Models

The steady-state continuous gas phase flow field is first solved using the RNG k-ε turbulence model. Discrete phase particle trajectories are then computed for particles injected from the Mass Flow Inlet face boundary into the flow domain.

7.4.1   Continuity and Momentum Equations

The conservation equations of mass and momentum are solved by FLUENT for all flows. The conservation of mass or continuity in the i-direction for the continuous phase is represented by equation 7.4. The source term S_m is zero in this case as there is no mass transfer into and out of the continuous gas phase.

$$\frac{\partial \rho}{\partial t} + \frac{\partial}{\partial x_i}(\rho u_i) = S_m \tag{7.4}$$

The conservation of momentum in the i-direction is described by the general equation:

$$\frac{\partial}{\partial t}(\rho u_i) + \frac{\partial}{\partial x_j}(\rho u_i u_j) = -\frac{\partial p}{\partial x_i} + \frac{\partial \tau_{ij}}{\partial x_j} + \rho g_i + F_i \tag{7.5}$$

p is the static pressure, τ_{ij} is the stress tensor, ρg_i is the gravitational body force while F_i represents any external body forces impacting the continuous phase. F_i is zero in this case.

7.4.2 Turbulence Model

The RNG (renormalisation group) k-ε model is used to model the turbulence in the continuous gas flow field. It uses the Reynolds-averaged approach whereby instantaneous solution variables consist of the mean and fluctuating components. For the velocity components:

$$u_i = \overline{u}_i + u'_i \tag{7.6}$$

where $\overline{u}_i$ and u'_i are the mean and instantaneous velocity components ($i = 1,2,3$). The same applies for scalar quantities such as pressure or energy. The turbulence model includes the ensemble-averaged momentum equations containing the Reynolds stresses which represent the effects of turbulence, modelled using the Boussinesq hypothesis. Besides the continuity and momentum equations, additional transport equations describing the turbulent kinetic energy k (equals $\frac{1}{2}\overline{u'_i}^2$ for a unit mass) and the turbulence dissipation rate ε are solved. The turbulent viscosity μ_t is computed as a function of k and ε.

The main reason for selecting the RNG k-ε model is that it provides an option to use a differential formula for effective viscosity to account for low Reynolds number effects, a feature which is absent from the standard k-ε model. This inclusion is necessary as the calculated Reynolds number for gas flow through the packed bed Re* during the experiments was found to be low and within the transition regime (although the approximately quadratic variation of measured pressure drop with gas velocity suggests that the flow is turbulent). The low Reynolds number effects are enabled by activating the Differential Viscosity Model option.

The flow through the packed bed is affected significantly by the wall boundaries of the solid spheres and the liquid droplets. To account for wall-bounded flows, the Two-Layer Zonal Model is incorporated. In this near-wall treatment approach, the whole domain is divided into viscosity-affected zones and fully turbulent zones, determined by the wall-distance-based, turbulent Reynolds number Re_y where $Re_y = \rho\sqrt{k}\,y/\mu$. y is the normal distance to the nearest wall measured at the cell centres and μ is the laminar viscosity. The solution of the viscosity-affected near-wall region ($Re_y < 200$) differs from that of the fully turbulent region ($Re_y > 200$ where the usual RNG k-ε model is employed) in the computation of the turbulent viscosity μ_t and ε. However, the same momentum equations and k equation are retained.

7.4.3   Discrete Phase Model

A discrete second phase of spherical particles dispersed in the continuous gas phase is introduced to represent the solid dust particles in the gas stream. The particle trajectories are computed via uncoupled calculations between the discrete and continuous phases. While the continuous phase always impacts the discrete phase, in the uncoupled approach the discrete phase does not affect the continuous phase flow field. The highest solids concentration used in the simulations herein is 4500 ppmw or 0.45 wt.% and the particles are injected at the same velocity as the gas phase at the inlet to the flow domain. For such low mass and momentum loading of particles, the use of uncoupled calculations is deemed reasonable.

The discrete phase trajectory is computed via stepwise integration of the force balance on the particle over discrete time steps. The particle inertia is equated to the hydrodynamic drag, the gravitational force and other additional forces acting on the particle. For steady flow in the x-direction in Cartesian coordinates:

$$\frac{du_p}{dt} = F_D(u - u_p) + \frac{g_x(\rho_p - \rho)}{\rho_p} + F_x \qquad (7.7)$$

where $F_D(u - u_p)$ is the drag force per unit particle mass; F_D equals $18\mu C_D Re/24\rho_p d^2$; u and u_p are the velocities of the gas phase and particle respectively; μ is the gas phase molecular viscosity; ρ and ρ_p are the gas phase and particle densities respectively; d is the particle diameter; Re is the relative Reynolds number which is defined as $\rho_G d|u_p - u|/\mu$ and C_D is the drag coefficient. F_x represents additional forces acting on the particle such as the force required to accelerate the fluid surrounding the particle and the force arising from the pressure gradient in the fluid. Integration in time of equation 7.7 gives the particle velocity u_p at each point along the trajectory and the trajectory itself is computed from:

$$\frac{dx}{dt} = u_p \qquad (7.8)$$

The time integration of the particle trajectory equations is controlled using two parameters:

* The Maximum Number of Time Steps allowed for integration of equations 7.7 and 7.8 before aborting trajectory computations when the particle does not exit the flow domain. This was set at 100 000. The trajectory fate is "incomplete" when trajectory calculation is abandoned.

* The Length Scale used to set the time step size for integration. This was set at 0.05 mm.

For turbulent flow, the impact of turbulent eddies present in the continuous phase on particle dispersion is incorporated via the stochastic tracking or the discrete random walk model. The model considers the effect of instantaneous turbulent velocity fluctuations on the particle trajectories. The gas phase velocity u is the sum of the mean gas phase velocity $\bar{u}$ and the instantaneous value of the gas flow velocity fluctuations u' from the stochastic model.

$$u = \bar{u} + u' \tag{7.9}$$

The random effects of turbulence on the particle dispersion is accounted for by turning on the Stochastic Model and setting a total of five computations (i.e. "number of tries") for each particle trajectory. The Random Eddy Lifetime option was included to set the characteristic lifetime of the turbulent eddy to be random. Particle interaction with the fluid phase eddy occurs over this eddy lifetime.

The particles are released from the Mass Flow Inlet boundary surface. The individual mass flowrate of injected particle streams are scaled according to the area of the face from which they are released. The initial conditions set for the particle stream are listed as follows, whilst the particle density is varied from 400 to 1800 kg/m^3 in the Materials panel.

- Particle type = Inert i.e. particle undergoes no physical or chemical changes.
- Particle velocity = 0.179 m/s and 0.278 m/s in y-direction. Initial particle velocity is assumed to equal the gas velocity i.e. zero slip. Zero velocities in x- and z-directions.
- Particle diameter = Varies from 1 μm to 80 μm.
- Particle temperature = 288 K.
- Total mass flowrate of particles = Set such that solids loading varies from 500 to 4500 ppmw (following the particulate removal experimental inlet dust loading).

The fate of a particle at a boundary zone is set as follows:
- Escapes through Mass Flow Inlet and Outflow boundaries.
- Reflects via a fully elastic collision at Wall boundaries of packing spheres and Symmetry boundaries (default).
- Trapped at Wall boundaries of liquid droplets.
- Passes through Interior boundary zone (default).

The fate of a particle trajectory is reported as either "escaped" at flow boundaries, "trapped" at flow boundaries, "incomplete" when the Maximum Number of Time Steps is exceeded, or "aborted" for incomplete trajectories due to round-off reasons.

7.5 Results and Discussion

7.5.1 Continuous Gas Phase

Figures 7.7 to 7.10 show the CFD derived contours describing the continuous gas phase flow field for gas mass flowrate M_G of 9.14×10^{-5} kg/s (simulating experimental conditions at 53 litre/min air flowrate at 1 atm). The grids of the packing spheres and droplets are superimposed to indicate their locations, though partially blocked by the contours. The pressure drop across the simulated packed bed made up of 5 cm of packing is 1.87 Pa/cm packing. This is slightly lower than the experimentally measured bed pressure drop of 2.06 Pa/cm packing. The contours of velocity magnitude (Figure 7.8) show that the gas flow is at its highest velocity in the space between the discrete droplets and the spherical packing surface, and in between adjacent droplets. The discrete droplets help to accelerate the gas flow as suggested by the higher velocity contours surrounding the droplets compared to the lower velocity contours in the space between adjacent packing spheres. Due to the closely packed spheres and hence significant wall effects, highly viscous flow predominates throughout the flow domain as shown by the small magnitudes of wall-distance-based, turbulent Reynolds number Re_y of less than 10 (Figure 7.10). The viscosity-affected near-wall region occurs at Re_y less than 200 whilst the fully turbulent region is marked by

Figure 7.7 Contours of Absolute Pressure (Pa) {$M_G = 9.14 \times 10^{-5}$ kg/s}.
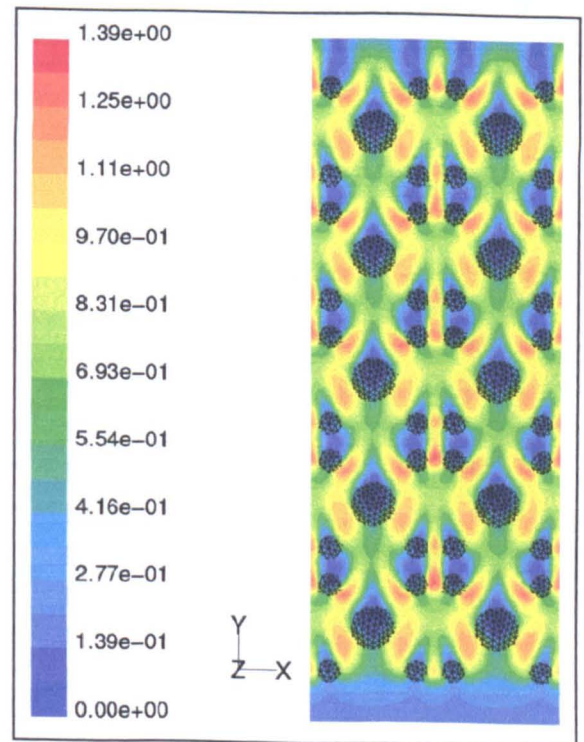
Figure 7.8 Contours of Velocity Magnitude (m/s) {$M_G = 9.14 \times 10^{-5}$ kg/s}.

Re_y greater than 200. The turbulent kinetic energy k (Figure 7.9) and Re_y are quickly dampened as soon as the gas flow hits the first layer of packing spheres. k at the bottom surface of the first layer spheres diminishes by about 3 times its original magnitude of

0.000241 m²/s² at the inlet to the flow domain. Beyond the first layer spheres, k drops by a factor of 10 compared to the inlet. Within the bed, k is as low as 1×10^{-10} m²/s². The sharp drop in k suggests that the assigned turbulence intensity at the flow inlet was rather high.
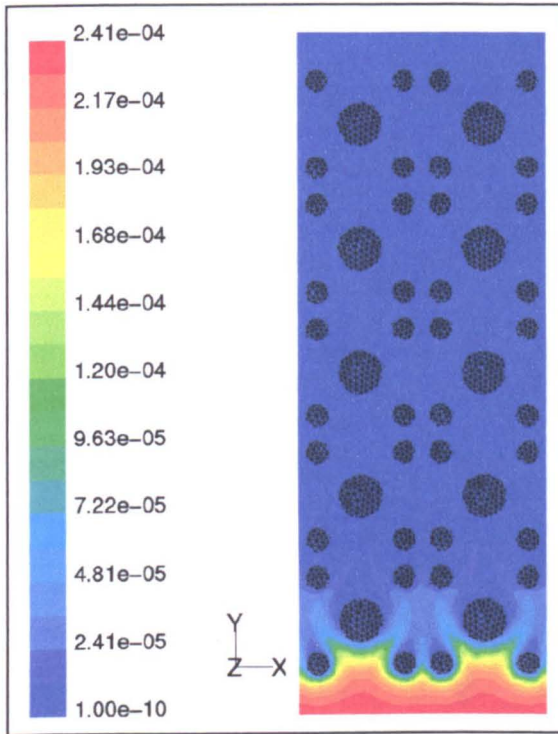
Figure 7.9 Contours of Turbulent Kinetic Energy, k (m²/s²) {$M_G = 9.14 \times 10^{-5}$ kg/s}.
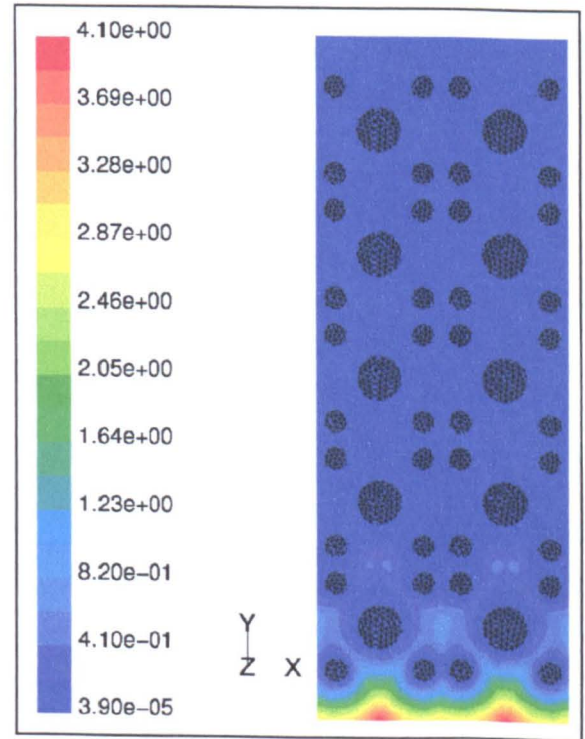
Figure 7.10 Contours of Turbulent Reynolds No., Re_y {$M_G = 9.14 \times 10^{-5}$ kg/s}.

Figures 7.11 to 7.13 describe the continuous gas phase flow field for gas mass flowrate M_G of 1.47×10^{-4} kg/s (simulating experimental conditions at 85 litre/min air flowrate at 1 atm). Closely similar contours to those at 9.14×10^{-5} kg/s air rate are obtained. The pressure drop is 3.80 Pa/cm packing for the simulated packed bed whilst the experimentally measured bed pressure drop is 4.75 Pa/cm packing. The velocity is higher herein as expected, the maximum value being 2.02 m/s compared to 1.39 m/s for the lower air rate. The maximum turbulent kinetic energy k and the maximum wall-distance-based, turbulent
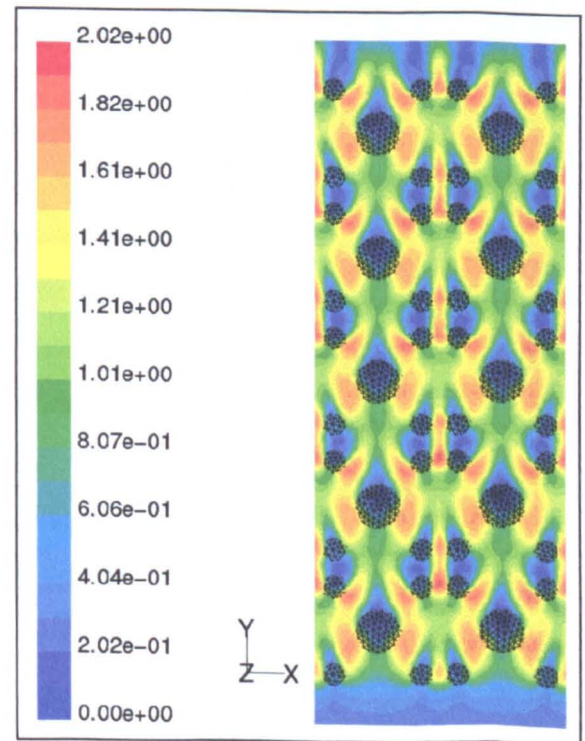
Figure 7.11 Contours of Velocity Magnitude (m/s) {$M_G = 1.47 \times 10^{-4}$ kg/s}.

254

Reynolds number Re$_y$ are about 80% and 40% higher respectively than those obtained for the lower air rate. Nevertheless, the gas flow through the packed bed is still highly viscous (Re$_y$ << 200). Both k and Re$_y$ quickly diminished beyond the first layer of packing.
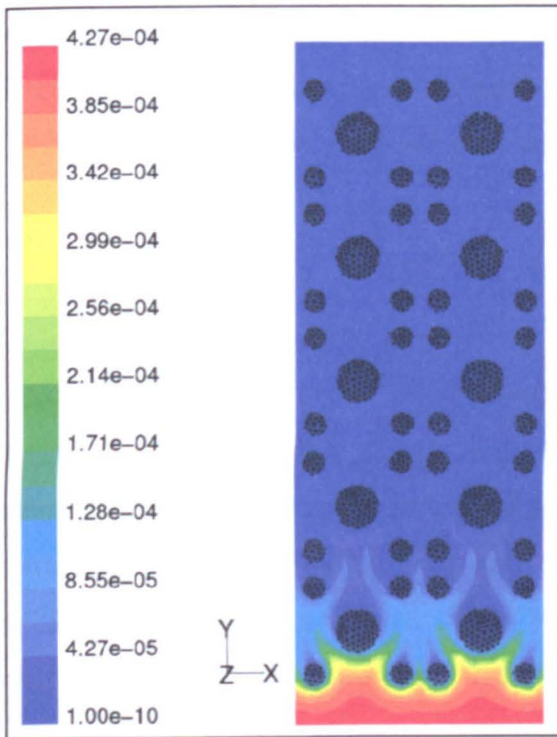
Figure 7.12 *Contours of Turbulent Kinetic Energy, k (m²/s²) {M$_G$ = 1.47 × 10⁻⁴ kg/s}.*
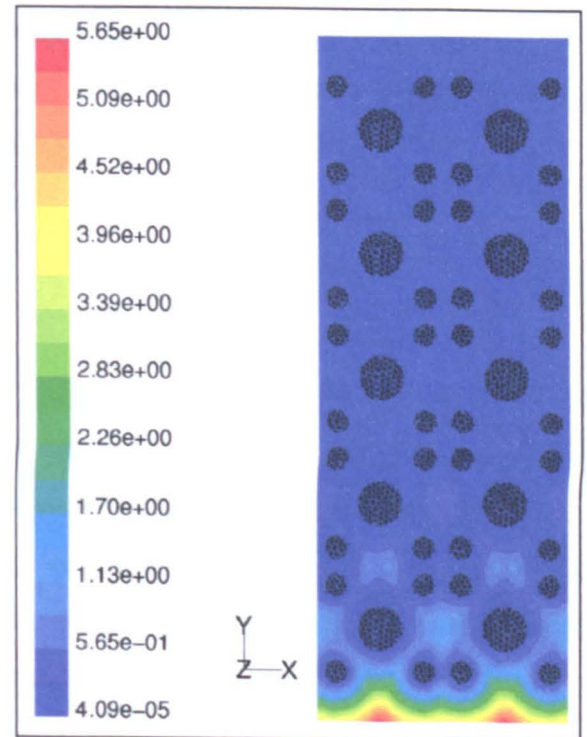
Figure 7.13 *Contours of Turbulent Reynolds No., Re$_y$ {M$_G$ = 1.47 × 10⁻⁴ kg/s}.*

7.5.2 Particle Separation

The particle separation efficiency is determined as the ratio of the "trapped" particles to the total "trapped" and "escaped" particles. The "incomplete" and "aborted" particles are ignored. The total height of the packed bed (minus the free space above and below the spheres) in the model is 5 cm. To afford comparison with the actual experimental packed bed of spheres of 19 cm in height, the separation efficiency obtained for the 5 cm model packed bed is used to estimate the equivalent efficiency for a packed bed of 20 cm in height (20 cm and not 19 cm for ease of estimation), shown as follows:
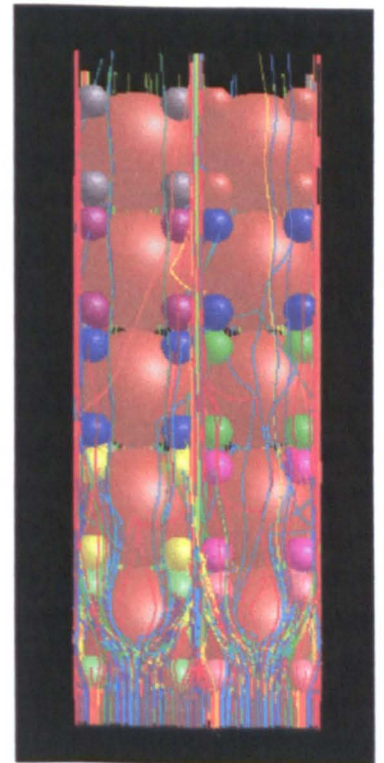
Figure 7.14 *Simulated particle trajectories.*

Let x be the total number of particles injected into the flow domain. Assume that the particle separation efficiency of the packed bed model of 5 cm depth is E%. Therefore the number of particles escaping the 5 cm packed bed is x(1-E/100). Let this x(1-E/100) number of particles enter the next 5 cm of the bed. Assuming the same particle separation efficiency of E%, the number of particles exiting the total 10 cm depth of the bed is x(1-E/100)(1-E/100). Ultimately, the number of particles exiting a packed bed of depth 20 cm is x(1-E/100)^4. Hence the overall particle separation efficiency of the 20 cm packed bed is:

$$E_{total} = \frac{x - x\left(1 - \frac{E}{100}\right)^4}{x} \times 100\% = \left[1 - \left(1 - \frac{E}{100}\right)^4\right] \times 100\% \qquad (7.10)$$

For air flowrate at 9.14×10^{-5} kg/s (18.5 cm/s at 1 atm), the overall particle separation efficiency E_{total} was obtained for varying particle size, particle density and injected particle concentration. All the data was derived using stochastic tracking of the particles. In addition, non-stochastic particle tracking was also carried out whilst varying the particle size and injected particle concentration, so that comparisons can be made with the results of the stochastic tracking approach. The results are illustrated in Figures 7.15 to 7.18.
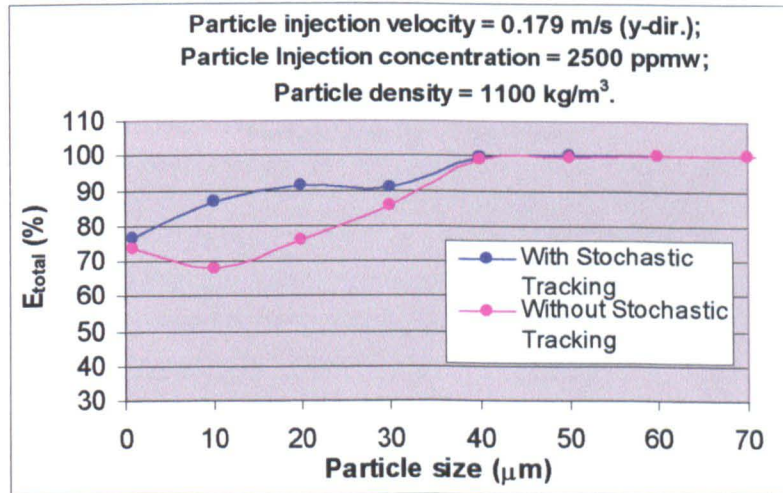
Figure 7.15 Variation of E_{total} with particle size.

The variation of E_{total} with particle size is essentially the grade efficiency curve (Figure 7.15). E_{total} increases with particle size. Direct interception of particles onto the "trapping" droplets is enhanced with larger particles. Also as particle size increases, its mass and hence its inertia increase as well. This improves inertial deposition of the particle i.e. there is a greater tendency for it to deviate from the gas streamlines and impact on the collector droplets. Larger particles also have higher probability of colliding with the packing spheres. The elastic

collisions increase the randomness of the particle trajectories hence improving the chances of particle entrapment by the droplets. For both stochastic and non-stochastic tracking methods, efficiencies above 98% are obtained for particles 40 μm and larger (i.e. 40 μm is the approximate limit of separation, x_{98}). Below 40 μm, stochastic tracking provides higher efficiencies as the particle trajectories are impacted by the instantaneous turbulent velocity fluctuations of the continuous gas phase.

Figure 7.16 graph: Particle injection velocity = 0.179 m/s (y-dir.); Particle injection concentration = 2500 ppmw; Particle size = 10 μm. Y-axis: E_{total} (%); X-axis: Particle Density (kg/m^3).
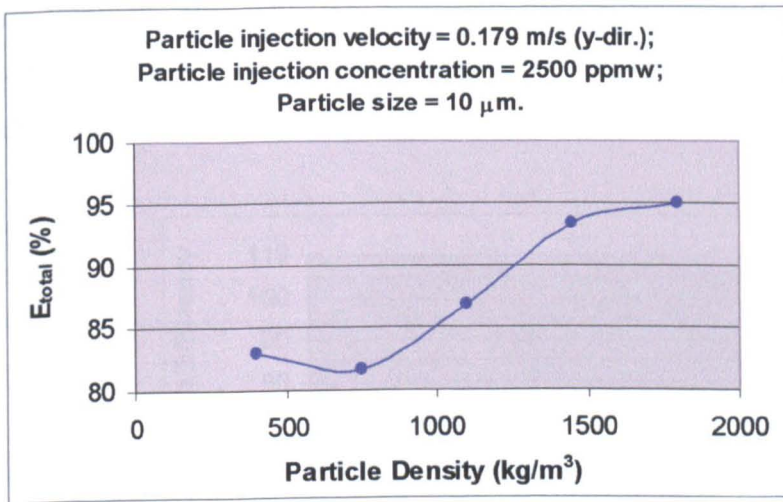
E_{total} increases with particle density (Figure 7.16). This is due to the effect of greater particle inertia as described in the preceding paragraph.

Figure 7.16 *Variation of E_{total} with particle density.*

Figure 7.17 graph: Particle injection velocity = 0.179 m/s (y-dir); Particle size = 10 μm; Particle density = 1100 kg/m^3. Y-axis: E_{total} (%); X-axis: Particle Injection Concentration (ppmw). Legend: With Stochastic Tracking; Without Stochastic Tracking.
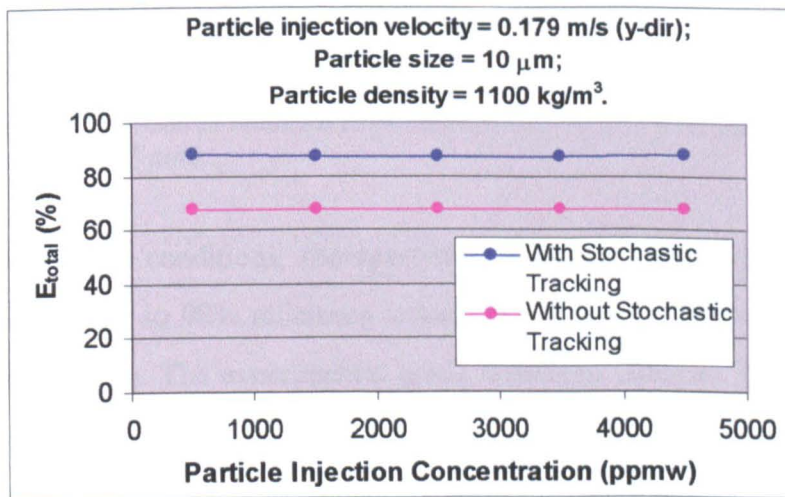
Figure 7.17 *Variation of E_{total} with injected particle concentration.*

The inlet particle concentration has negligible effect on E_{total} (Figure 7.17). In comparison, particle separation improves with increasing dust loading under actual experimental conditions (curve for 18.5 cm/s (1 atm) air velocity in Figure 6.27). In the actual water-irrigated packed bed scrubber, higher dust concentrations encouraged the agglomeration of the dust particles in the wet environment. The resulting solid agglomerates are easier to be separated than the

individual particles, therefore improving dust separation. This feature is absent from the simulated packed bed model. Incorporation of the stochastic particle tracking improves E_{total} due to particle interaction with the instantaneous velocity fluctuations of the gas phase.

For air flowrate at 1.47×10^{-4} kg/s (29.6 cm/s at 1 atm), only the data on variation of E_{total} with particle size is obtained using the stochastic particle tracking method. The resulting grade efficiency curve is compared with the curve obtained at 9.14×10^{-5} kg/s (18.5 cm/s at 1 atm) air flowrate, also with the stochastic particle tracking in Figure 7.18. The experimentally obtained grade efficiency curves at the same air velocities and at 2 litre/min water flowrate are also included for comparison.
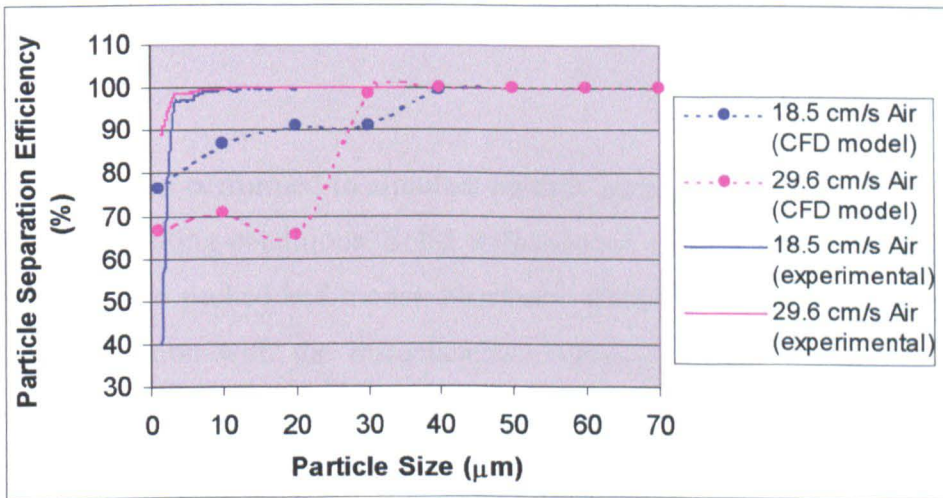
Figure 7.18 *Grade efficiency curves obtained from CFD modelling and experimental studies (air velocity at 1 atm).*

Under actual experimental conditions, the approximate limit of separation, x_{98} which is the particle size corresponding to 98% efficiency is less than 10 μm. However in the simulations, x_{98} is approximately 40 μm. The experimental grade efficiency curve at 29.6 cm/s air velocity is consistently higher throughout the tested particle size range than that of the lower air velocity until complete separation is achieved. On the other hand, the simulated curve at 29.6 cm/s air velocity starts off lower but then overtakes the curve at 18.5 cm/s air velocity at about 27 μm particle size.

Several factors are identified which could account for the differences observed between the experimentally obtained and CFD derived grade efficiency curves. Firstly, the CFD model assumes a cubic type of systematic packing when in reality, the packed bed is randomly filled with the solid spheres. Secondly, the liquid is assumed to exist only as fixed, identical discrete

droplets on the spherical packing surface in the model. In the actual packed bed scrubber, the liquid is distributed on the packing surface as droplets and rivulets of various sizes, with some free-falling in between the solid spheres. Thirdly, the dust particles in the actual packed bed are in various stages of agglomeration altering the effective particle size, this feature is absent from the simulated packed bed. Also, additional solid separation occurs below the packing support plate in the actual scrubber, which is outside the packed bed domain. This additional particle removal zone is altogether absent from the CFD model which is only restricted to the packed bed. Finally, solid wall-induced viscous effects are significant and the simulated gas flow is predominantly laminar throughout the packed bed model. On the other hand, the gas flow under actual experimental conditions is turbulent. These factors would collectively account for the discrepancies between the experimentally obtained and CFD derived curves.

7.6   Summary

CFD modelling has been performed to simulate particle removal in a packed bed of spheres operating under non-wetting conditions. Solid wall-induced viscous effects are significant in the gas flow through the packed bed model. Stochastic tracking improves particle separation due to particle interaction with the instantaneous velocity fluctuations of the gas phase. Particle separation efficiency increases with particle size due to better capture by direct interception and inertial impaction mechanisms as well as increased randomness of particle trajectories from elastic collisions with the solid spheres. Efficiencies above 98% are predicted for particles 40 μm and larger. Particle separation improves with particle density due to the effects of greater particle inertia. The separation efficiency is unaffected by the inlet particle concentration in the CFD model even though it actually improves with increasing dust loading under actual experimental conditions. This is attributed to the agglomeration of dust particles in wet conditions during the experiments, a feature which is absent from the CFD model. Under actual experimental conditions, the approximate limit of separation (x_{98}) is smaller than 10 μm, but is approximately 40 μm in the CFD model. The differences between the experimental and CFD derived grade efficiency curves are attributed to the assumptions made regarding the packing arrangement and liquid distribution in the modelled packed bed; the dust agglomeration within the actual scrubber which changes the effective particle size; the additional particle removal occurring beyond the packed bed domain in the actual scrubber; and the predominantly laminar gas flow through the CFD model as opposed to turbulent flow in the actual packed bed.

Chapter Eight

Hot Gas Scrubbing System

This chapter sets out the design and construction of the hot gas scrubbing system. The selection of the material of construction is first discussed. The design of the main gas scrubber unit is then presented which includes the column and its packing, the packing support plate, the liquid distributor and the column gas injector. This is followed by the design of the gas lift for molten tin transport through the column. Other aspects documented include provisions for loading and removal of tin from the scrubber, tin level indicators, system heating and insulation, temperature measurement and control as well as system operating parameters. The system operating procedure for a typical hot gas desulphurisation test run is outlined at the close of the chapter.

8.1   Material of Construction

The high-temperature gas scrubber has to be constructed from a material which can withstand high temperatures of at least 400°C and is resistant to attack by both hydrogen sulphide gas and corrosive molten tin. The range of materials that can be used in this combination of harsh environments is limited, the more obvious choice being ceramics such as high-purity alumina which is stable to molten metals and has excellent resistance to both oxidising and reducing atmospheres at high temperatures (ASM, 1991). However due to higher mechanical strength, easier and cheaper fabrication and construction with metals and alloys rather than ceramics, it was decided that an appropriate metal or alloy would be used; the economics being a major decisive factor of the final choice.

Molten tin is chemically corrosive to most refractory metals and alloys. Tungsten is resistant to attack by tin but its cost and fabrication difficulties have deterred its use. Similar to other molten metals, the reaction of molten tin with stainless steels or heat resisting alloys can involve dissolution of one or more elements from the latter into the liquid metal, or diffusion of the liquid phase into the solid material. Neither phenomenon is desirable as it results in chemical modifications to the molten tin. Also, intermetallic phases may form, leading to embrittlement of the solid material. (Tooley, 1984; American Society for Metals, 1980; Lacombe, 1993).

Consultations with AvestaPolarit (Willfor, 2001) and the British Stainless Steel Association (2001) yielded some key information. Nickel and nickel-based alloys are not suitable for

handling molten tin due to relatively high solubilities of nickel in molten tin. As a rough rule of thumb, where contact with low melting metals is concerned, the lower nickel alloys or the ferritic stainless steels are preferred. Both the high-chromium ferritic stainless steel Type 446 (23-27% Cr, 0% Ni) and the austenitic stainless steel Type 253 MA (20-22% Cr, 10-12% Ni) have been reportedly used to construct side shields in the tin float process of plate glass manufacture. However, ferritic grades with a chromium content higher than about 15% are sensitive to the '475°C embrittlement' when operating in the temperature range of 400 to 550°C. The austenitic stainless steel Type 304 (18-20% Cr, 8-10.5% Ni) is usable in molten tin's environment but operating temperatures should be kept below 400°C for minimal corrosion rate.

However, a check with the suppliers revealed that the aforementioned stainless steel Types 446, 253MA, and 304, (notably the first two) were not common grades and as such, the necessary parts to construct the hot scrubber were not available "off the shelf" and instead have to be specially fabricated and this would incur exorbitant costs. Therefore an alternative, more affordable stainless steel grade was sought with which the necessary parts required for the hot scrubber could be readily available.

The final choice for the construction material was the austenitic stainless steel Type 316 (16-18% Cr, 10-14% Ni, 2% Mn, 1% Si, 0.08% C, 0.045% P, 0.03% S). This grade is superior to the Type 304 in corrosion resistance, the recommended maximum working temperature being 870°C (ASM, 1991). The Type 316 stainless steel was one of the materials tested up to 800 hours in a study in Finland to test the long-term corrosion resistance of commercial metal filters under a simulated gasification environment with 300 ppmv H_2S at 400°C and 500°C. Good corrosion resistance was demonstrated at both temperatures (Mitchell, 1997). However there remains the issue of stainless steel corrosion by molten tin, with the dissolution of some of the nickel content into the liquid metal. As each test run involving the irrigation of molten tin through the hot gas scrubber is anticipated to be relatively short in duration, typically less than 30 minutes, coupled with the use of fresh tin for each test run, the degree of molten tin's contamination by dissolved nickel from the steel is expected to be minimal. Thus, the relatively short operating time for each test run should keep the corrosion of the stainless steel by the molten tin to a minimum level.

8.2   Design of Main Scrubber Unit

8.2.1   Column and Packing

To afford comparison with the water-irrigated cold model scrubber and to enable the use of

hydrodynamics correlations derived from the cold system, the physical geometry and dimensions of the Perspex column along with its packing have been closely followed herein on the hot scrubber. The close hydrodynamic similarities between both scrubbers include identical packing shape and size, nearly identical column size, similar packing support plate and liquid distributor.

9.53 mm (3/8 inch) high-purity ceramic alumina (Al_2O_3) spheres provided by the Precision Ball and Gauge Company are used as packing material. As previously mentioned, high-purity alumina has excellent resistance to molten metals and reducing atmospheres at elevated temperatures (ASM, 1991). Details on the packing are summarised as follows:

Table 8.1   Characteristics of the alumina packing used.

Diameter d (mm)	9.53
Column to packing diameter ratio (m/m)	8.4
Packing element specific surface area $S = 6/d$ (m^2/m^3)	630
Packed bed porosity ε (m^3/m^3)	0.45*
Packed bed specific surface area $S_B = S(1-\varepsilon)$ (m^2/m^3)	346
Packing specific gravity (dimensionless)	4.0
Alumina critical surface tension σ_c (dyne/cm)	Data unavailable
Molten tin-alumina contact angle θ (degree)	$\approx 160\text{-}140°$ at $300\text{-}1130°C$**

*   Assumed same as that for 9.53 mm polyethylene spheres.   ** Nogi *et al.*, 1988.

The whole body of the hot gas scrubber including the column is constructed with Type 316 stainless steel. To prevent the possible preferential wetting of molten tin on the stainless steel wall compared to the alumina ceramic packing, an alumina combustion tube 8 cm in internal diameter and 9.5 cm in outer diameter is used to line the interior of the stainless steel column. The stainless steel column is sized such as to just fit the alumina tube. The alumina tube is 23 cm in length allowing an approximately 20 cm packed bed depth.

A limitation imposed by using solid metal in constructing the column was the inability to visually observe the molten tin flow through the packed bed. The possibility of using glass to fabricate the column had been previously considered but was ruled out due to unfavourable economics and the undesirable fragility of glass. At temperatures as high as 400°C, fused quartz (pure silica glass) would have to be used which is an extremely costly material. Also, sealing difficulties between metal and glass would require that not only the column, but the complete gas scrubber unit be fabricated from fused quartz. External glass expertise would have to be sought to construct the hot scrubber. In addition, the glass setup would be susceptible to breakage, this being hazardous as the operator will be exposed to hot liquid metal should a breakage occur.

Summing up, it would not be economically and practically feasible to utilise glass for the column fabrication. The use of a glass window as a viewing port has also been considered but was deemed impractical. The viewing port would have to be extended from the column wall to outside the heated compartment. This would require a relatively long extension. Without any light source within the column, it would be too dark to observe the column interior via the protruding viewing window.

8.2.2 Packing Support Plate

Similar to the cold model, the packed bed of alumina spheres is supported on a simple stainless steel sieve-type of packing support plate with evenly-spaced 5 mm perforations, sufficiently small to prevent the spheres from falling through. The total fractional free area of the packing support plate is about 0.48. This is slightly smaller than the one used in the Perspex column as the perforations directly above the bottom pressure tapping have been omitted. This is to minimise plugging of the tapping by splashing liquid droplets, which was encountered in the cold tests.

8.2.3 Liquid Distributor

Like the cold model, a stainless steel orifice type of liquid distributor is employed, providing separate paths for gas and liquid flows. The gas flows up through risers whilst the liquid tin flows down through orifices on the distributor floor. The design of the liquid distributor has to fulfil two key criteria (Fadel, 1984). Firstly, the riser height must be higher than the liquid head corresponding to maximum liquid rate to prevent liquid overflow at high liquid rates, thus avoiding liquid maldistribution at the top of the bed. Secondly, the liquid head at minimum liquid rate must be higher than the gas pressure drop through the riser, preventing local flooding at the distributor which will eventually lead to flooding of the whole packed bed. Using equations 5.4 to 5.7 (Fadel, 1984; Chen, 1984) in Section 5.2.1, suitable geometry and dimensions for the liquid distributor were determined.

Table 8.2 demonstrates that the design criteria have been fulfilled for the anticipated extremes of operating fluid flowrates.

- Riser   :   Total = 6; Height = 4.0 cm; Internal diameter = 1.5 cm;
                 Total flow area = 21% of column cross-sectional area
- Orifice :   Total = 6; Diameter = 7.6 mm

Table 8.2 Checking liquid distributor geometry against design criteria.

---

1. Riser height (4.0 cm) must be higher than liquid head h_L:

Worst case scenario: Maximum h_L i.e. highest operating liquid rate:

Highest operating molten tin rate = 5 litre/min = 114.03 kg/m²s

Corresponding h_L from equation 5.4 (Fadel, 1984) = 12.69 mm of water
Corresponding h_L from equation 5.6 (Chen, 1984) = 10.21 mm of water

∴ In both equations by Fadel and Chen respectively, h_L < riser height (40 mm).

---

2. Liquid head h_L must be higher than gas pressure drop through riser ΔP:

Worst case scenario: Smallest h_L i.e. smallest operating liquid rate and highest ΔP i.e. highest operating gas rate:

Smallest operating molten tin rate = 3 litre/min   = 68.42 kg/m²s
Highest operating N_2 gas rate   = 300 litre/min = 0.50 kg/m²s

Corresponding h_L from equation 5.4 (Fadel, 1984) = 4.57 mm of water
Corresponding ΔP from equation 5.5 (Fadel, 1984) = 0.13 mm of water

Corresponding h_L from equation 5.6 (Chen, 1984) = 3.68 mm of water
Corresponding ΔP from equation 5.7 (Chen, 1984) = 0.21 mm of water

∴ In both sets of equations by Fadel and Chen respectively, h_L > ΔP.

Note: All fluid physical properties taken at 400°C. ρ(Sn(l), 400°C) = 6878 kg/m³ (Iida and Guthrie, 1988). ρ(N_2, 400°C) = 0.507 kg/m³.

8.2.4   Column Gas Injector

Gas enters the column via an injector which is made from an 11 mm internal diameter stainless steel pipe with 4 ports distributed at its side at one end. This end is capped, shielding the gas ports from the falling liquid stream.

8.3   Design of Gas Lift

The irrigation of molten tin through the packed bed scrubber is achieved by a nitrogen U-tube gas lift constructed from a 22 mm inner diameter (D) and 25 mm outer diameter stainless steel pipe. The submergence (S) is 61 cm while the lift (L) is 46 cm, giving a total height of just over 1 metre and a submergence ratio (S_R) of 0.57.

Various factors were taken into consideration when deciding the size of the gas lift. Firstly the liquid supply rate must meet the minimum packing wetting rate, this being 0.00035 to 0.0014

m^3/sm^2 for random packing (Kister, 1992) which works out to be 0.11 to 0.42 litre/min for the 8 cm column of the hot scrubber. If S_R is too small as given by a short submergence (the lift height is fixed by the column height), the pump efficiency is reduced and a higher gas consumption will be required for the same liquid discharge rate. This will incur a higher running cost as more compressed nitrogen will be required which also means a larger heating requirement. This is also undesirable as the larger the volume of gas exiting the top of the riser, the more interference that will be incurred on the upflowing process gas from the column. On the other hand, if S_R is too big, i.e. a longer submergence, an even larger heating requirement will be needed to melt the additional tin required and to maintain the extra tin at the operating temperature. The overall consequence is both higher material and running costs. Todoroki *et al.* (1963) found that the maximum pump efficiency increased with submergence ratio until a peak is reached at submergence ratios of about 0.7 to 0.8 after which it decreased, and that there is adequate submergence for ordinary gas lift operation if S_R is greater than 0.5. Considering these various factors, a submergence ratio of 0.57 was deemed sufficient to ensure normal gas lift operation without incurring excessive costs of tin and heating.

A simple longitudinal gas injector is incorporated, fabricated from a 5 mm stainless steel pipe. This follows from previous findings of the air lift in Section 6.5.4 that there is negligible or minimal difference in the pumping performance using either the radial or longitudinal injectors. Therefore the simplest one is selected, this being the longitudinal injector. Nitrogen gas was used as the pumping agent as a replacement for air to prevent oxidation of the molten tin.
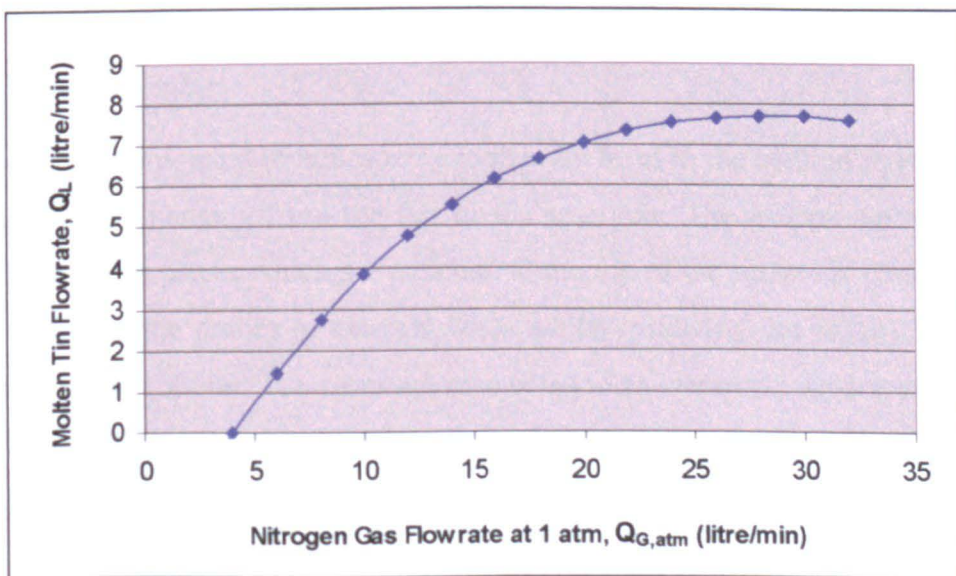

Figure 8.1 *Gas lift operating curve predicted using Nicklin's (1963) theoretical model coupled with gas slug losses, pump pressure, downcomer friction and accelerative effects.*

It was deduced from Section 6.5.5 that Nicklin's (1963) theoretical model would give the best available prediction for the pumping performance of the gas lift, provided that the necessary pressure changes are added to complete the momentum balance, notably that of downcomer friction and accelerative effects. Taking the physical properties of both molten tin and nitrogen gas at 400°C and accounting for the necessary additional pressure change terms, the operating curve of the nitrogen gas lift in pumping molten tin is obtained as in Figure 8.1.

8.4   Loading and Removal of Tin

A vessel with a removable lid is provided in which solid tin pellets are loaded before each test run. It is positioned at the top of the column such as to minimise the overall cross-sectional area of the space that needs to be heated. An overall compact unit helps to minimise the heating surface area requirement and also reduces heat loss. Once melted, the molten tin flows from the top vessel down through a downcomer pipe that connects to the side of the bottom reservoir of the column. From the reservoir, the tin then flows down through the downcomer of the gas lift, thus filling both the downcomer and the riser legs of the gas lift.

The provision of a bottom vessel positioned below the gas lift allows molten tin to be drained and thus removed from the system at the end of each test run. The vessel is provided with a detachable lid so that the solidified tin ingot can be removed. The interior of the vessel is lined with Kaowool paper prior to its use. Earlier tests using small amounts of tin strips showed that molten tin when solidified fused onto the wall of a bare stainless steel crucible, but the solid tin ingot was easily removed when the crucible was lined with Kaowool paper.

8.5   Tin Level Indicator

Level sensors are incorporated to indicate the molten tin level in the column reservoir. These are stainless steel probes hanging from the top of the reservoir. The probes are inserted through small ceramic alumina pieces which are attached to the top of the reservoir. The ceramic pieces enable connection of the probes to external wires whilst insulating the probes from contacting the metal body of the column. The wires are connected to an electronic system controller. When the molten tin in the reservoir rises sufficiently high such that it touches the tip of the hanging probe, an electrical contact is made between the system controller, the tin and the metal rig. Since both the control panel and the metal rig are earthed, a complete electrical circuit is achieved, hence an electrical signal is produced and displayed on the control panel as the tin level in the column reservoir. Three stainless steel probes are used with varying lengths to

provide a low (L1 = 2 cm), moderate (L2 = 3 cm) and high (L3 = 4 cm) level indication of the molten tin in the reservoir. At the start of each test run, a constant level of tin in the reservoir would indicate complete tin drainage from the top supply vessel, while at the end of the test run, the dropping tin level would confirm the initiation of tin removal from the gas lift into the bottom vessel. In addition, more accurate lift and submergence heights can be deduced by actually knowing the surface level of the tin in the reservoir.

8.6   System Heating and Insulation

Six semi-cylindrical ceramic radiant heaters model CRWS-1215/240-A (3400 watts, 240 volts) supplied by Omega® are used to heat the hot gas scrubber. The radiant heater is made from low mass, vacuum formed ceramic fibre with helically wound iron-chrome-aluminium wire elements embedded into the fibre. It provides the convenience of a combined heating element and insulation in a single unit. Each heater is 12 inches in length, 19 inches in external diameter and 15 inches in internal diameter. The six semi-cylindrical radiant heaters are stacked one on top of another, forming a compact semi-cylindrical compartment in which the column, gas lift, top and bottom vessels are fitted.

The main gas that enter the base of the column is preheated by a series of three in-line gas heaters model AHP-7562 (750 watts, 240 volts) with a heated length of 14 cm each, supplied by Omega®. The nitrogen gas to the gas lift is preheated by a single in-line gas heater model AHP-5052 (400 watts, 240 volts) with a heated length of 11 cm supplied by Omega®.

Kaowool boards and blankets are used for system insulation. The front of the semi-cylindrical heated compartment is covered by Kaowool boards. The interior of the heated compartment is partitioned by Kaowool blankets into a top and bottom section to help retain the heat. Initial tests without partitioning showed that the bottom part below the column was much cooler than the top segment as the hot air from the bottom escaped to the top. This problem was overcome with the partition in place.

8.7   Temperature Measurement and Control

K-type thermocouple probes with inconel sheath (temperature range 0-1100°C) and magnesium oxide insulation are used for temperature measurement in the high temperature gas scrubbing system. Their individual locations are listed in Table 8.3.

Table 8.3 *Temperature measurement locations.*

Thermocouple No.	Location
T1c	Downstream of series of in-line gas heaters, before main gas enters column base. Sets target temperature for series of in-line gas heaters.
T2c	Downstream of in-line gas heater, before lift gas enters gas lift base. Sets target temperature for in-line gas heater.
T3c	Molten tin in column reservoir. Sets target temperature for radiant heaters.
T1	Within heated compartment enclosed by radiant heaters.
T2	Gas outlet at top of column.
T3	Molten tin inlet to column at top of gas lift riser.
T4	Main gas inlet to gas injector at column base.
T5	Lift gas inlet to gas injector at gas lift base.

Thermocouples T1c, T2c and T3c are connected to the electronic system controller. Their set points dictate the extent of heating by the in-line gas heaters and the radiant heaters, controlling the preheated main gas and lift gas temperatures as well as temperature of the molten tin in the column reservoir respectively. The heaters are cut off once the target temperatures are reached. Thermocouples T1 to T5 are connected to a digital thermometer for temperature display.

Low pressure switches P1 and P2 prevent overheating of the in-line gas heaters by cutting off the heaters once the gas pressure falls below 3.8 cm H_2O (g). These are indicated on the control panel.

8.8 Gas Supply

The N_2 gas to both the main column and the gas lift is supplied from separate gas cylinders. H_2S in N_2 mixture is supplied from another gas cylinder for the gas desulphurisation studies.

8.9 Operating Parameters

The anticipated typical operating liquid tin flowrates, and the corresponding nitrogen flooding gas velocities are tabulated in Table 8.4. As the critical surface tension data for alumina was unavailable, the generalised graphical flooding correlation with the relative surface tension factor $(\sigma_c/\sigma_L)^{0.53}$ in Figure 6.10 (Section 6.3.4) could not be applied. Instead the gas flooding velocities were predicted from the average flooding line for non-wetting systems depicted in Figure 6.9 (Section 6.3.3).

Table 8.4 *Typical operating molten tin flowrates and the corresponding nitrogen gas flooding velocities at 400°C.*

Molten Tin Flowrate		Nitrogen Gas Flowrate	
Q_L (litre/min)	L (kg/m^{2}s)	$Q_{G, flooding}$ (litre/min)	$G_{flooding}$ (kg/m^{2}s)
3	68.42	325	0.55
4	91.22	240	0.40
5	114.03	165	0.28

Operating temperatures are anticipated to be at least 400°C due to kinetics limitation at lower temperatures as identified from the preliminary gasification tests as well as noted by Schürmann (1984). As the test gas is arranged to be a mixture of H_2S in nitrogen, there is no serious concern over SnO_2 formation. However if a simulated fuel gas with a high water vapour content is used, the scrubber has to be operated at temperatures above 500°C to avoid SnO_2 dross formation. There should be no problem over the volatility of either molten tin or SnS at temperatures of around 500°C, the boiling points being 2272°C for tin and 1210°C for SnS.

Figure 8.2 illustrates the orifice type liquid distributor used. The dimensions of the column, gas lift, top and bottom vessels are detailed in Figure 8.3. The schematic diagram in Figure 8.4 illustrates the overall high-temperature gas scrubbing system. A series of photographs of the hot gas scrubbing system are shown in Plates 8.1 to 8.4.
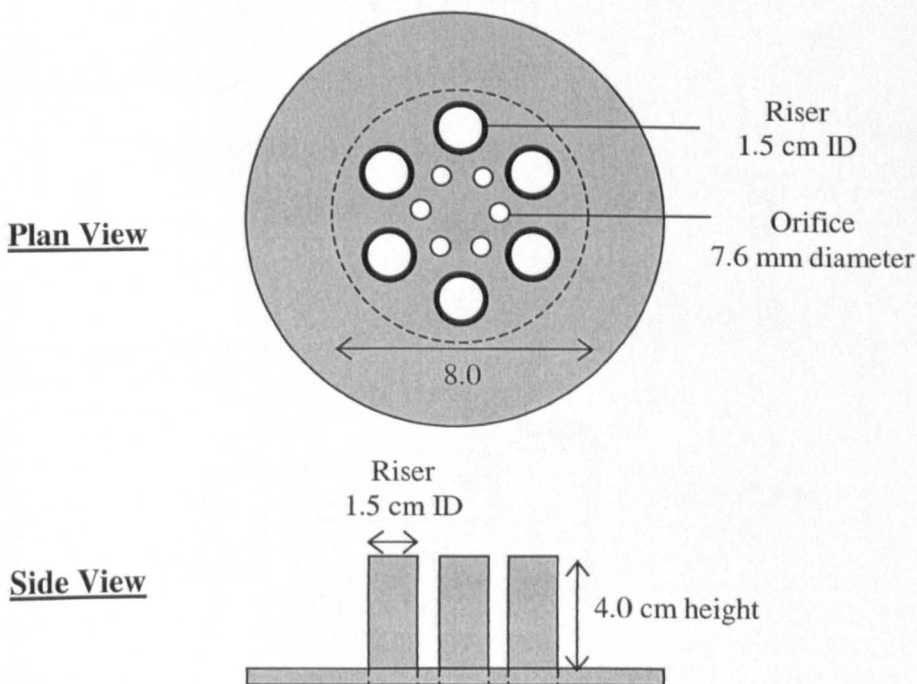
Figure 8.2 *Orifice type liquid distributor with dimensions.*
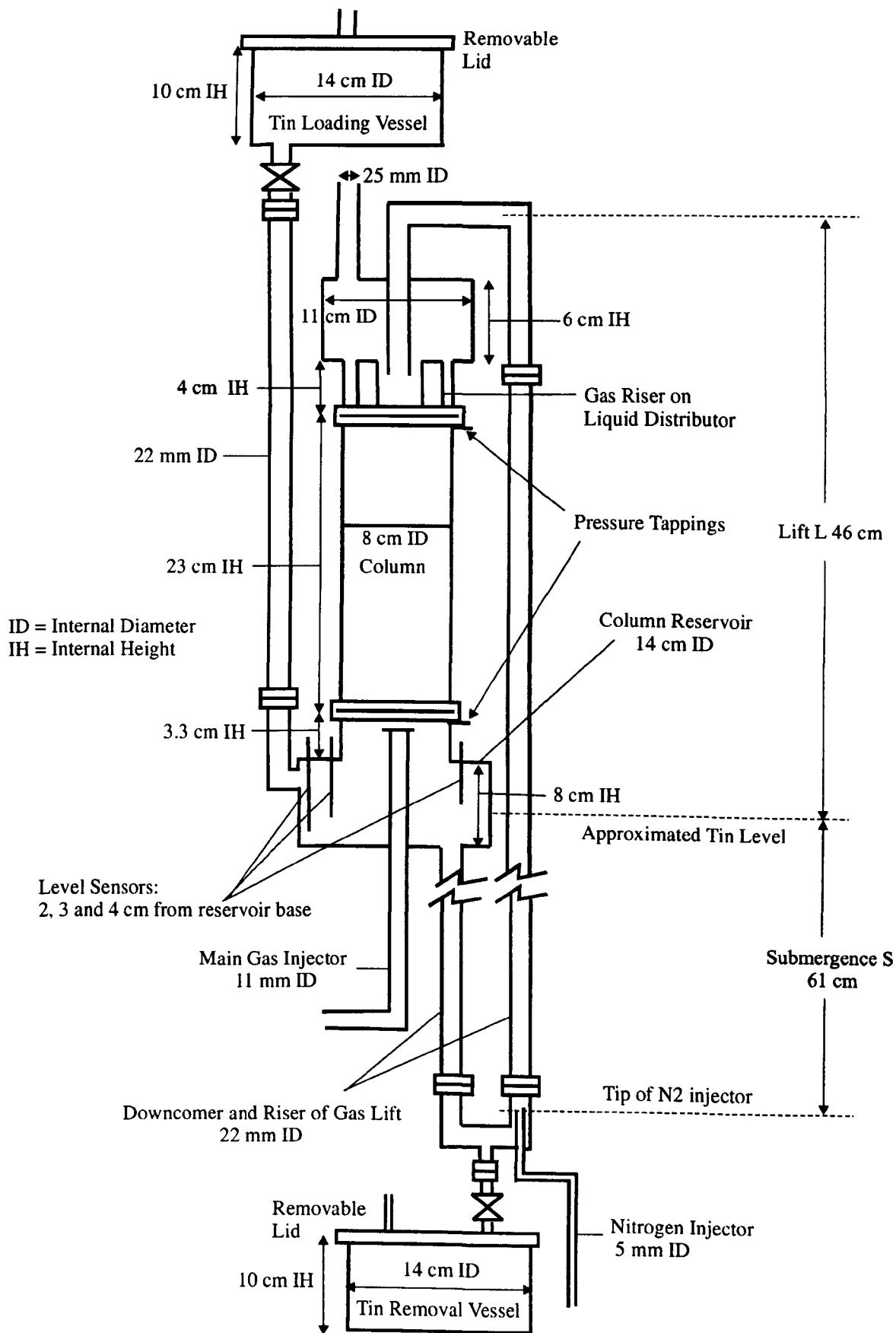
Figure 8.3 *Dimensions of hot gas scrubber.*

270
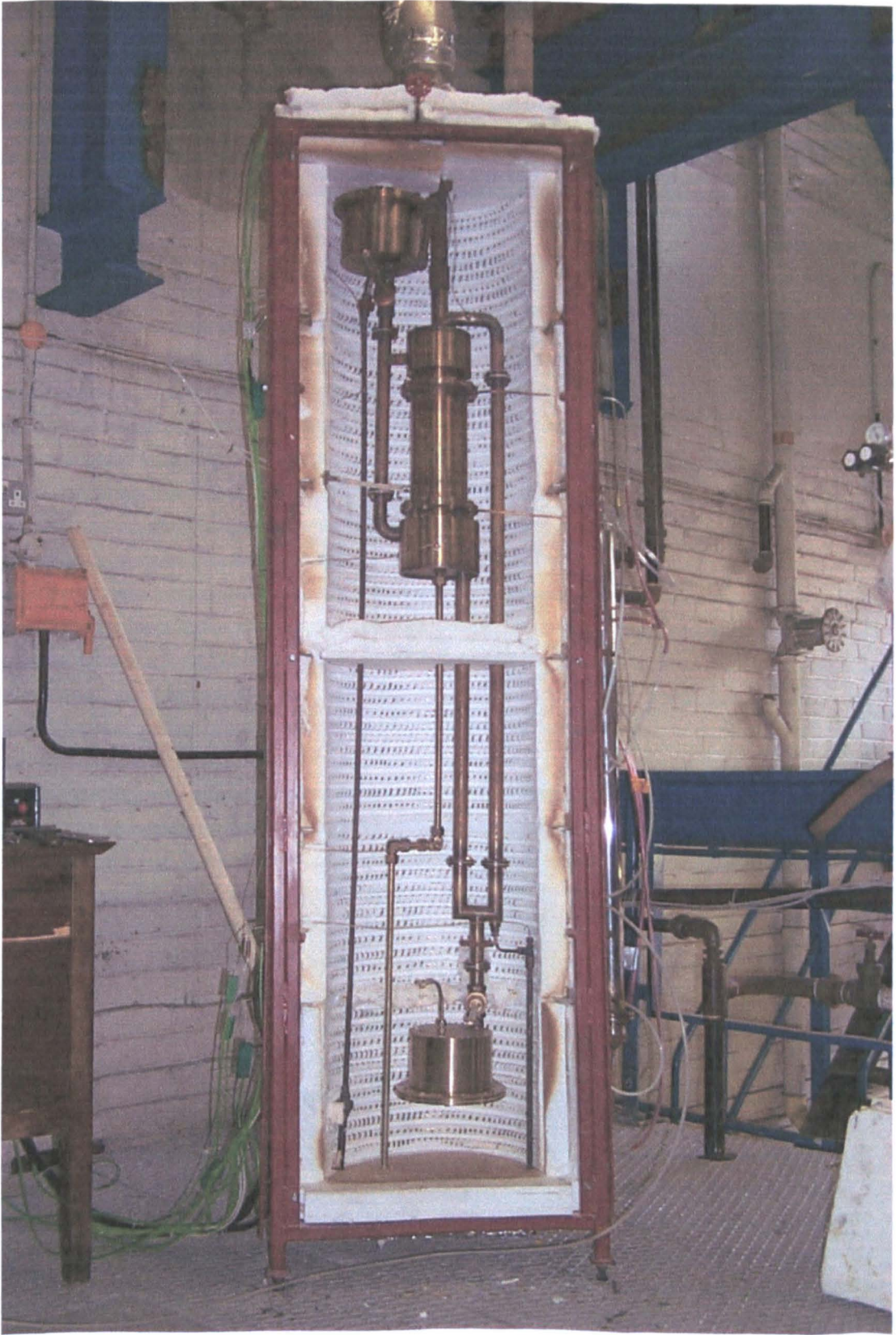
Plate 8.1 Hot gas scrubber enclosed by ceramic radiant heaters.
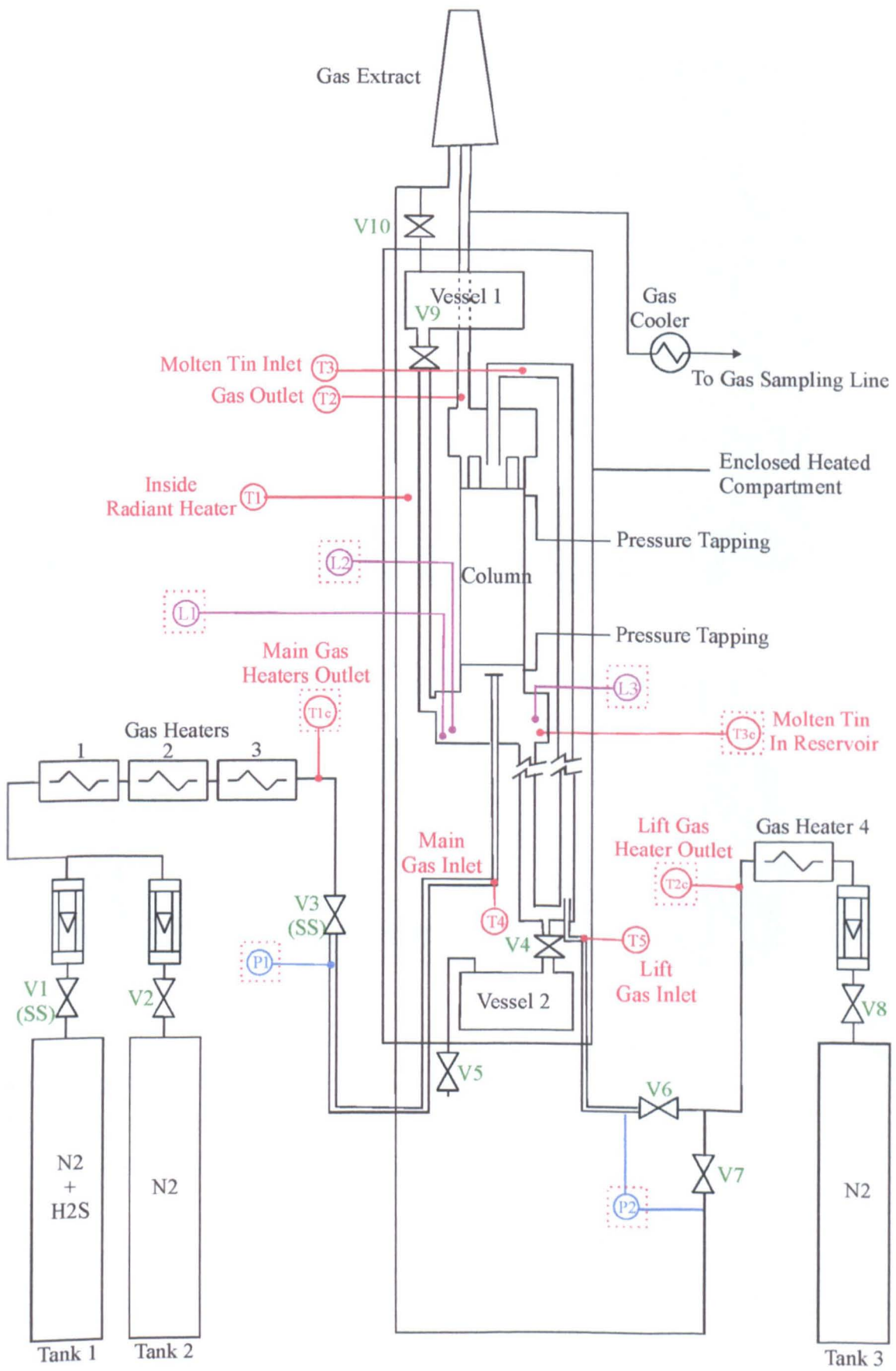
Figure 8.4 Overall hot gas scrubbing system.

Plate 8.2
Overall hot gas
scrubbing
system.
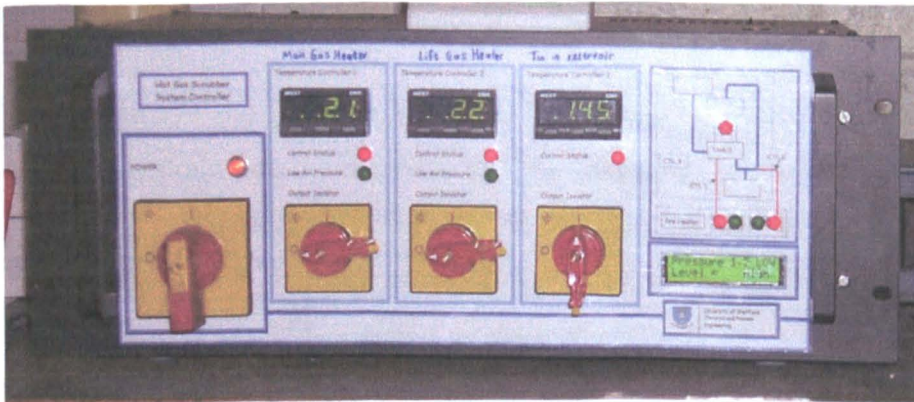
Plate 8.3
Electronic system
controller.

8.10   Operating Procedure

The system operating procedure for a typical hot gas desulphurisation test run is documented herein.

8.10.1 Start-Up Procedure

Plate 8.4 Alumina spherical packing in alumina-lined column.

- Tin Loading: The Kaowool outer insulating boards are removed from the rig to gain access to Vessel 1. Tin pellets of known weight are loaded into Vessel 1 which is then closed and secured.

- <u>Vessel 2 Lining</u>: The interior of Vessel 2 is lined with Kaowool paper and then secured back onto the rig. The Kaowool boards are put back onto the rig and the metal cage door secured.

- <u>Ventilation, Gas Sampling Line and Cooling Water</u>: The room ventilation fans and extract system are turned on, the extract gate is left semi-open to conserve heat. The water supply to the gas cooler (cold finger) is turned on. The necessary sampling equipment is put in place at the end of the gas sampling line.

- <u>System Controller On</u>: The circuit breaker (i.e. electrical supply to the rig) is switched on. The electronic system controller is turned on and the desired temperatures set.

- <u>System Purging</u>: (All valves are initially closed.) Valves V4, V5, V9, V10 and valves V3, V7 are fully opened. Valves V2 and V8 are opened and N_2 gas is fed into the system from tanks 2 and 3 respectively to purge the system of air. Valves V2 and V8 are adjusted to minimal flow to conserve the N_2 gas. After a short while, valve V5 followed by V4 are closed.

- <u>Radiant Heaters On</u>: The radiant heaters are turned on from the system control panel. The minimal N_2 gas flow from tanks 2 and 3 are maintained to ensure an inert atmosphere within the scrubber to prevent tin oxidation while the system heats up.

- <u>Full Tin Drainage and Full Gas Flow</u>: Sufficient time is allowed for the tin from vessel 1 to melt and fully drain into the reservoir and gas lift limbs. This is achieved when level sensors L1, L2 and L3 show constant readings. At this point, valves V9 and V10 are closed. Valve V7 and V8 are closed, shutting off the N_2 supply from Tank 3. The molten tin in the reservoir (T3c) is allowed to reach the desired set point temperature.

- <u>Main N_2 Gas at Operating Flow and Heaters On</u>: The extract gate is fully opened. Valve V2 is adjusted to increase the N_2 flow from Tank 2 to the desired gas flowrate i.e. the same flowrate as the N_2/H_2S gas mixture which is to be introduced later. Gas heaters 1,2 and 3 are turned on from the system control panel.

- <u>N_2 Lift at Operating Flow and Heater On</u>: Once the main gas inlet temperature (T4) reaches the desired value, gas heater 4 is turned on from the system control panel. Valve V6 is opened fully and Valve V8 is opened to the gas lift operating flow. This allows N_2 gas from Tank 3 into the gas lift riser, initiating the molten tin circulation through the packed column.

- <u>H_2S Flow Initiation and Gas Sampling</u>: Once the gas lift inlet temperature (T5) reaches the desired value, V2 is closed and V1 opened to allow the N_2/H_2S mixture from tank 1 into the system at the same flowrate as the initial N_2 gas flow from tank 2. Gas sampling is initiated.

8.10.2 Normal Shut-Down Procedure

- The gas sampling line is clamped. The gas sampling equipment is switched off and disconnected.

- Valve V6 is closed followed straightaway by V1, stopping the molten tin circulation and the H_2S gas flow through the scrubber respectively. Valve V8 is then fully shut.

- All the gas heaters and the radiant heaters are switched off from the system control panel. The circuit breaker is turned off.

- Valve V2 is opened to allow N_2 gas into the system, maintaining an inert atmosphere.

- Valve V4 is opened fully to allow the molten tin to drain into Vessel 2. Valve V5 is opened slightly to aid tin drainage.

- Sufficient time is allowed for the solidified tin as well as all the gas heaters to cool down to room temperature before turning off the N_2 gas supply from Tank 2. The front metal cage is removed followed by the Kaowool boards to gain access to Vessel 2. Vessel 2 lid is opened and the solidified tin is removed.

- Water supply to the gas cooler, ventilation fans and exhaust system are turned off.

8.10.3 Emergency Shut-Down Procedure

- All the gas heaters and the radiant heaters are switched off from the system control panel. The circuit breaker is turned off.

- Valve V6 is closed followed straightaway by V1, stopping the molten tin circulation and the H_2S gas flow through the scrubber respectively. Valve V8 is then fully shut.

- Valve V2 is opened to allow N_2 gas into the system, maintaining an inert atmosphere.

- Valve V4 is opened fully to allow the molten tin to drain into Vessel 2.

- Sufficient time is allowed for the solidified tin as well as all the gas heaters to cool down to room temperature before turning off the N_2 gas supply from Tank 2.

Summing up, the design of the hot gas scrubber has been investigated, fulfilling the final project objective. Further to this, a pilot unit of the liquid metal based scrubber has been constructed. The high temperature gas scrubbing facility is ready for commissioning.

Chapter Nine

Conclusions and Recommendations for Future Work

The conclusions derived from the various studies of this PhD programme are presented in this chapter. Areas where further development are necessary are identified and suggestions are put forward for possible future work.

9.1   Conclusions

9.1.1   Preliminary Gasification Studies

- H_2S in fuel gas produced from small-scale gasification of petroleum coke samples by a steam/nitrogen mixture was found to react with molten tin at a temperature of approximately $1000°C$, depositing a solid residue containing both sulphur and tin.

- Besides its reaction with H_2S, the molten tin most likely reacted with steam and CO_2 in the product gas as well under the experimental conditions involved.

- These studies have provided actual experimental evidence of the possibility of sulphur removal by molten tin in a gasification environment.

9.1.2   Cold Gas Scrubber Studies

An extensive series of experimental studies has been carried out on a small-scale water model scrubber operating under non-wetting flow conditions and serving as a liquid metal based gas scrubber analogue.

❑ *Flow Visualisation*

- Droplet formation sites have been identified for a packed bed of solid spheres irrigated by water under non-wetting flow conditions. These were generally sites having either a single packing sphere with an immediate empty space below it or sites at which two or three spheres touched one another. The maximum water droplet size attainable before being displaced from these locations was about 4 mm. Due to larger liquid-solid contact angle,

droplet flow was more prominent on waxed glass packing compared to polyethylene packing.

- Similar to liquid metal flows, higher gas and liquid rates were found to encourage rivulet formation (about 3 to 4 mm width), the effect by the liquid rate being more prominent.

- It was demonstrated from the balance of surface tension and gravitational forces that the maximum possible equatorial diameter of a liquid droplet hanging from a non-wetting spherical solid surface could be predicted from the liquid surface tension and density.

- The mobility of static holdup has been demonstrated herein due to the tendency of water to flow as discrete droplets rather than spreading films.

□ *Flooding*

- Flooding points have been determined for the water-irrigated packed beds of polyethylene and waxed glass spheres under non-wetting flow conditions. The waxed glass packing exhibited higher flooding gas velocities than the polyethylene packing, this being attributed to the slightly higher degree of non-wettability of the former.

- Flooding correlations that apply well on conventional wetting packed beds were shown to be inadequate where non-wetting aqueous and metallic liquid systems are concerned, underestimating the actual flooding capacities of these non-wetting packed beds. Non-wettability increases the maximum hydraulic capacity of a packed bed.

- The flooding capacities of the various non-wetting systems including that of liquid metals were correlated against their non-wetting tendencies by introducing an additional $(\sigma_c/\sigma_L)^{0.53}$ factor onto the ordinate of the generalised flooding plot originally used by Sherwood *et al.* (1938) for conventional wetting systems. The addition of the $(\sigma_c/\sigma_L)^{0.53}$ factor closes the gap between the flooding lines of wetting and non-wetting systems and reduced slightly the scatter in the flooding points between the non-wetting systems. This allows the flooding points of non-wetting systems to be predicted from Sherwood *et al.*'s flooding line.

□ *Liquid Holdup*

- Static and dynamic liquid holdups have been determined for the packed bed of polyethylene spheres irrigated by water under non-wetting flow conditions.

- Similar to that documented for liquid metal irrigation, the static holdup was found to be unaffected by gas velocity but slightly decreased with increasing liquid velocity. This

demonstrates the mobility of static holdup in non-wetting systems due to the tendency for liquid droplet rather than film formation. For the non-wetting packed beds, the static holdup would be relatively more effective to mass transfer during a gas absorption process compared to conventional wetting systems. Static holdup increases with bed porosity.

- The dynamic holdup increased with rising air and water velocities but the influence of the air rate was evident only beyond the loading point, these trends being in accord with those reported for wetting and other non-wetting packed beds including liquid metal systems. The dynamic holdup was correlated against operating air and water velocities. It varied nearly linearly with water rate before flooding, similar to liquid metal irrigation.

- Total liquid holdup increased with both air and water velocities with the latter exerting a greater influence. The total liquid holdup was correlated against the fluid velocities.

- A liquid holdup correlation that applies well on conventional wetting packed beds failed to give satisfactory predictions when tested against holdup data of non-wetting systems. In all cases, the liquid holdup was overestimated.

- Following Warner's (1959a) empirical method, the total volumetric liquid holdup obtained in this study was well correlated against bed pressure drop, true gas velocity and gas density, giving an average absolute relative error of 7.2%.

The hydrodynamics of the water-irrigated packed bed in these studies showed good similarities when compared with those irrigated by liquid metals. This suggest that for irrigated packed bed systems operating under non-wetting flow conditions, the liquid-solid contact angle exerts a dominating influence over the hydrodynamics, over-riding differences in liquid physical properties such as density and surface tension.

❑ *Gas Lift*

- The performance of a small air lift to transport water has been investigated. The pumping rate improved with increasing air injection rate and submergence ratio. The pump efficiency increased with air injection rate until a maximum was reached, after which it decreased. The peak was displaced to the lower end of the air flowrate. A larger submergence ratio gave a slightly higher peak efficiency, occurring at a lower air injection rate.

- Various gas injectors were tested (longitudinal, 4-port radial, 12-port radial), all having the same sized gas ports. Nearly identical pumping performance was obtained in each case, showing that increasing the number of gas ports on the injector with no change to the hole size has negligible effect on the air lift pump.

- Available empirical graphical correlation and theoretical models using two-phase flow theory for air lift pumps were tested against the data of the small air lift used in this study. At best, the average absolute error between the predicted and actual experimental data was 31%. However by including additional pressure losses, notably the downcomer friction and accelerative effects into the momentum balance originally in Nicklin's (1963) theoretical model, a very good prediction was obtained giving the smallest average absolute relative error of 9%. The error between the predicted and actual data at the higher air flowrates was vastly reduced showing that frictional losses in the downcomer of the U-tube air lift and the kinetic energy changes are significant for a small air lift and cannot be ignored.

□ *Particulate Removal*

- The particulate removal performance of the water-irrigated packed bed of polyethylene spheres under non-wetting flow conditions was investigated using a glass dust laden air stream. Good total separation efficiencies were obtained, ranging from 95.5 to 99.6%.

- At sufficiently high air velocities, the total efficiency increased with air and water flowrates as well as with inlet dust concentration. Higher fluid flowrates give greater total liquid holdup and hence a larger number of droplet and rivulet particulate collectors, whilst higher dust loading encouraged dust agglomeration in the presence of moisture which aids separation. However at low air velocities, the total efficiencies were randomly scattered showing no clear trends with either fluid rates or dust loading. This was attributed to nearly constant liquid holdup and hence unchanged dust retention capacity of the packed bed.

- At dry bed condition, dust separation deteriorated with increasing dust loading due to limited dust retention capacity of the dry bed. This demonstrates the importance of irrigating liquid to maintain the dust retention capacity of the packed bed and to prevent re-entrainment of dust particles back into the gas stream.

- The total particulate removal efficiency and the corresponding number of transfer units were correlated against the operating fluid flowrates and solids loading.

279

- Rapid buildup of solids at the bottom section of the fixed bed highlighted the importance of ultimately having a moving bed in the gas scrubber.

- Impressive cut sizes approaching the submicron range were demonstrated by the resulting grade efficiency curves, the cut size decreasing with increasing air velocity. In terms of turbine blade protection, the grade efficiency curves were very encouraging as dust particles larger than about 6.5 μm can be separated to efficiencies greater than 98%. Complete particle separation was achieved in all cases for particles larger than 16 μm.

□ *Gas Absorption*

- The mass transfer efficiency of ammonia absorption into water has been determined on the packed bed of polyethylene spheres operating under non-wetting flow conditions. The volumetric overall gas phase mass transfer coefficient K'_{Ga}, corrected for end effects, varied with the 0.22 power of the liquid mass velocity and the 0.79 power of the gas mass velocity.

- The height of the gas film transfer unit H_G at fluid rates up till the apparent onset of loading was correlated against the gas phase Reynolds number and the liquid superficial velocity. When compared with H_G data of other non-wetting spherical packing systems including those involving liquid metals, the various H_G data showed a strong dependency on packing size. H_G diminishes as packing size decreases, this being due to larger gas-liquid interfacial area of smaller packings which improves mass transfer. A good agreement was achieved when the H_G data of the various non-wetting spherical packed bed systems was correlated against the 0.27 power of the gas phase Reynolds number, the –0.27 power of the liquid superficial velocity and the 0.40 power of the packing diameter.

- H_G from this study was also correlated against the relative Reynolds number and the effective liquid holdup, i.e. the total liquid holdup in this case due to the observed mobility of the static holdup.

□ *Implication for Hot Gas Scrubber*

Results of the cold gas scrubber studies have provided insight into the workings of the liquid metal packed bed gas scrubber. Findings and correlations derived from the water model studies, occasionally complemented by data from other non-wetting systems, provide the means to predict the hydrodynamics, particulate removal capability and mass transfer performance of the liquid metal scrubber:

- From the force balance on the liquid pendent droplet, the maximum molten tin droplet size in the packed bed of the hot gas scrubber is expected to be about 5 mm. The significantly larger contact angle of molten tin on the alumina ceramic packing surface would provide a much more prominent droplet flow in the liquid metal irrigated packed bed compared to the cold scrubber.

- The flooding capacity of the molten tin scrubber could be estimated from the generalised flooding correlation for non-wetting systems which uses the non-wetting tendency factor, ensuring that operation is within a stable gas-liquid operating range. In the absence of the critical surface tension value of the packing material, the average generalised flooding line of non-wetting systems on conventional Sherwood *et al.*'s (1938) axes could be used instead.

- The molten tin holdup in the hot scrubber having a packed bed with similar physical geometry to the water model could be approximated by applying the bed pressure drop, true gas velocity and gas density to the empirical total holdup correlation derived based on the cold model following Warner's (1959a) empirical method. Compared to the water holdup in the water model, the molten tin holdup is expected to be lower as a result of the larger liquid-solid contact angle and liquid density. The total holdup would be effective for H_2S absorption into tin due to mobility of the liquid metal held at the static holdup sites.

- The performance of the gas lift in transporting molten tin in the hot scrubber is best estimated using momentum balance originating from Nicklin's (1963) model, to which has been added other necessary pressure changes within the system particularly the accelerative and downcomer friction losses to complete the momentum equation.

- The hot scrubber can potentially achieve better solids removal efficiency than that demonstrated by the cold model. In addition to primary particulate collection on tin droplets and rivulets, the sticky nature of ash and char particles at elevated temperatures will also encourage secondary solids deposition and retention on the packing surfaces.

- The gas side resistance of the H_2S absorption process into molten tin can be estimated from the H_G correlation derived from the cold study using the gas phase Reynolds number and liquid superficial velocity. The difference between the experimentally determined overall mass transfer resistance and the calculated gas side resistance will then provide the liquid side resistance.

9.1.3 CFD Modelling: Particulate Removal In A Packed Bed

- The ability to simulate particle removal in a packed bed of spheres under non-wetting flow conditions via computational fluid dynamics modelling has been demonstrated using FLUENT 5. Simulation results have shown that particle separation efficiency increases with particle size and particle density but is independent of initial injection concentration.

- The approximate limit of separation (x_{98}) is about 40 μm in the CFD model compared to less than 10 μm in the actual water-irrigated scrubber. The differences between the experimental and simulation results are attributed to the assumptions made regarding the packing arrangement and liquid distribution in the CFD model; the dust agglomeration which alters the effective particle size in the actual scrubber; the additional particle removal beyond the packed bed domain in the actual scrubber; and the predominantly laminar gas flow through the CFD model as opposed to turbulent flow in the actual packed bed.

9.1.4 Hot Gas Scrubber

- The series of experimental studies carried out on the water model scrubber have provided insight and understanding to the design and development of the final molten tin based hot gas scrubber. The physical geometry and dimensions of the cold scrubber's packed column have been closely followed on the hot scrubber, allowing hydrodynamics and mass transfer correlations derived from the cold studies to be extended to the high temperature system.

- The pilot unit of the liquid metal based hot gas scrubber has been fully constructed. The high temperature gas scrubbing facility is ready for commissioning.

9.2 Recommendations for Future Work

- The physical dimensions of the packed bed incorporated in the hot gas scrubber resemble closely those of the cold model. This negates scale-up concerns with respect to the application of the correlations derived from the cold model. However, before extending the derived correlations to larger systems, the consequences of scale-up need to be considered. This is best determined by conducting similar cold studies on a larger room-temperature packed column using the same packing material but of a larger size. The size of the larger cold system will have to be within the means of available resources and laboratory space. Comparison between the large and small systems will reveal the scale-up effects on the performance of the non-wetting gas scrubber.

- The momentum balance approach has been demonstrated to apply extremely well on the prediction of air lift performance for water transport. The theoretical model uses two-phase flow equations which have been proven on the air-water system. But the question remains over the validity of their extension to liquid metal systems. Similar gas lift tests can be performed, this time on transporting mercury to test the validity of the theoretical model on liquid metals. Mercury being a liquid at room temperature negates the need for a heated system, reducing the complexities and safety issues with regards to the experimental setup required.

- Future tests based on the now completed hot gas scrubber are suggested as follows:

$\Rightarrow$ The very core of these hot tests will be the removal of H_2S from a simulated fuel gas by the molten tin in the hot scrubber. H_2S in nitrogen mixture will be introduced into the gas scrubber, flowing counter-currently to the molten tin irrigating the packed bed. The circulation of molten tin through the packed bed will be effected by the nitrogen gas lift. Gas samples will be collected at the scrubber gas outlet to monitor the H_2S concentrations whilst samples of the reacted tin could be analysed to identify the compounds present and the amount of dissolved sulphur. Factors affecting the H_2S absorption such as operating temperature, gas and liquid flowrates, as well as inlet gas concentrations will be investigated. The same tests should be conducted on the removal of COS as well.

$\Rightarrow$ Once the studies on H_2S and COS removal in an inert gas like nitrogen have been accomplished, the effects of other gasification fuel gas constituents on the sulphur removal can be investigated. The main gas components of interest are CO, H_2, CO_2 and H_2O (where steam gasification is employed). The effect of impurities in the fuel gas such as NH_3 and HCl are also worth investigating.

$\Rightarrow$ Experimental studies on particulate removal by the molten tin irrigated hot gas scrubber will also be performed. Effects of gas and liquid flowrates, solids loading, particulate size and operating temperature on the separation efficiency will be the main areas of interest in this investigation.

$\Rightarrow$ Once sufficient knowledge and understanding of the fixed packed bed scrubber has been achieved, the system can progress towards a moving bed configuration whereby the spherical packing elements are withdrawn from the packed bed and are then entrained in the molten tin circulation effected by the gas lift. External cleaning of the packings to remove deposited solids must be studied.

References

1. Adamson, A.W. (1976) *Physical Chemistry of Surfaces*. 3rd edition. New York, John Wiley & Sons.

2. Adamson, A.W. and Gast, A.P. (1997) *Physical Chemistry of Surfaces*. 6th edition. New York, John Wiley & Sons, Inc.

3. Andreas, J.M. (1938) *J. Phys. Chem.*, 42, 1001. Cited in: Middleman, S. (1995) *Modeling axisymmetric flows: Dynamics of films, jets and drops*. London, Academic Press, Inc.

4. Andrieu, J. (1975) Influence of wettability on liquid phase texture in a countercurrently irrigated packing. *Chemical Engineering Science*, 30, 217-220.

5. ASM (1980) *Metals Handbook, Volume 3: Properties and Selection: Stainless steels, tool materials and special-purpose metals*. 9th edition. Ohio, American Society for Metals.

6. ASM (1981) *Metals Handbook, Volume 4: Heat Treating*. 9th edition. Ohio, American Society for Metals.

7. ASM (1984) *Metals Handbook, Volume 7: Powder Metallurgy*. 9th Edition. Ohio, American Society for Metals.

8. ASM (1991) *ASM Handbook, Volume 4: Heat Treating*. 10th edition. Ohio, ASM International.

9. Bain, W.A. and Hougen, O.A. (1944) Flooding velocities in packed columns. *Transactions of the American Institute of Chemical Engineers*, 40, 29-44.

10. Beard, K.V. (1976) *J. Atmos. Sci.*, 33, 851-864. Cited in: Seville, J.P.K. and Clift, R. (1997a) Gas cleaning at high temperatures: gas and particle properties. *In:* Seville, J.P.K. (ed) *Gas cleaning in demanding applications*. London, Blackie Academic & Professional. p.170-192.

11. Billet, R. and Schultes, M. (1993) A physical model for the prediction of liquid hold-up in two-phase countercurrent columns. *Chemical Engineering and Technology*, 16, 370-375.

12. Billet, R. and Schultes, M. (1995) Fluid dynamics and mass transfer in the total capacity range of packed columns up to the flood point. *Chemical and Engineering Technology*, 18, 371-379.

13. Bolles, W.L. and Fair, J.R. (1982) Chemical Engineering, 89(14), 109. Cited in: Strigle, R.F. (1994) *Packed Tower Design and Applications. Random and Structured Packings*. 2nd edition. Houston, Gulf Publishing Company.

14. British Stainless Steel Association: Stainless Steel Advisory Service (2001) *Private communication.*

15. British Standard (1968) *BS 3156: Part 2: 1968 British Standard Methods for The Analysis of Fuel Gases – Part 2: Special Determinations - Section 2.2: Hydrogen Sulphide in Crude Gas.*

16. British Standard (1977) *BS 1016: Part 6: 1977 British Standard Methods for Analysis and Testing of Coal and Coke - Ultimate Analysis of Coal.*

17. British Standard (1977) *BS 1016: Part 8: 1977 British Standard Methods for Analysis and Testing of Coal and Coke - Chlorine in Coal and Coke.*

18. Burke, S.P. and Plummer, W.B. (1928) Gas flow through packed columns. *Industrial and Engineering Chemistry*, 20(11), 1196-1200.

19. Calvert, S. *et al.* (1972) *Scrubber Handbook*. National Technical Information Service, Springfield, VA. Cited in: Svarovsky, L. (1981) Solid-gas separation. Amsterdam, Elsevier Scientific Publishing Company.

20. Calvert, S. (1977a) How to choose a particulate scrubber. *Chemical Engineering*, 84(18), 54-68.

21. Calvert, S. (1977b) Scrubbing. *In:* Stern, A.C. (ed) *Air pollution. Volume IV Engineering control of air pollution*. 3rd edition.. New York, Academic Press. p.257-291.

22. Carman, P.C. (1937) Fluid flow through granular beds. *Trans. Inst. Chem. Eng.*, 15, 150-166. Cited in: Coulson, J.M. *et al.* (1991) *Chemical Engineering, Volume 2, Particle technology and separation processes*. 4th edition. Oxford, Pergamon Press.

23. Charpentier, J.C. *et al.* (1968) Étude de la rétention de liquide dans une colonne à garnissage arrosé à co-courant et à contre-courant de gas-liquide. Chimie et Industrie Génie Chimique, 99(6), 803-826. Cited in: Saez, A. E and Carbonell, R.G. (1985) Hydrodynamic parameters for gas-liquid cocurrent flow in packed beds. *American Institute of Chemical Engineering Journal*, 31(1), 52-60.

24. Chen, G.K. (1984) Packed column internals. Chemical Engineering, 91(5), 40-51.

25. Chilton, T.H. and Colburn, A.P. (1934) Mass transfer (absorption) coefficients. Prediction from data on heat transfer and fluid friction. *Industrial and Engineering Chemistry*, 26, 1183-1187.

26. Chilton, T.H. and Colburn, A.P. (1935) Distillation and absorption in packed columns. A convenient design and correlation method. *Industrial and Engineering Chemistry*, 27(3), 255-260.

27. Clark, N.N. and Dabolt, R.J. (1986) A general design equation for air lift pumps operating in slug flow. *AIChE Journal*, 32(1), 56-64.

28. Clayfield, E.J. *et al.* (1985) The coalescence of secondary dispersions. I. The effect of wettability and surface energy. *Journal of Colloid and Interface Science,* 104 (2), 500-511.

29. Clift, R. (1997) Inertial separators: basic principles. *In:* Seville, J.P.K. (ed) *Gas cleaning in demanding applications.* London, Blackie Academic & Professional. p. 41-52.

30. Colburn, A.P. (1939) The simplified calculation of diffusional processes, general consideration of two-film resistances. *Transactions of American Institute of Chemical Engineers,* 35, 211-231.

31. Cornell, D. *et al.* (1960) Mass transfer efficiency-packed columns-part 1. *Chemical Engineering Progress,* 56(7), 68-74.

32. Coughlin, R.W. (1969) Effect of liquid-packing surface interaction on gas absorption and flooding in a packed column. *AiChE Journal,* 15(5), 654-659.

33. Coulson, J.M. *et al.* (1991) *Chemical Engineering, Volume 2, Particle technology and separation processes.* 4th edition. Oxford, Pergamon Press.

34. Coulson, J.M. *et al.* (1996) *Chemical Engineering, Volume 1, Fluid Flow, Heat Transfer and Mass Transfer.* 5th edition. Oxford, Butterworth-Heinemann Ltd.

35. Coury, J.R. *et al.* (1987) Capture and rebound of dust in granular bed gas filters. *Powder Technology,* 50, 253-265.

36. Craig, R.C. *et al.* (1960) Wetting of poly-(methyl methacrylate) and polystyrene by water and saliva. *Journal of Physical Chemistry,* 64, 541-543.

37. Danckwerts, P.V. (1951) Significance of liquid-film coefficients in gas absorption. *Industrial and Engineering Chemistry,* 43(6), 1460-1467.

38. Davies, C.N. (1945) *Proc. Phys. Soc.,*57, 259-270. Cited in: Seville, J.P.K. and Clift, R. (1997a) Gas cleaning at high temperatures: gas and particle properties. *In:* Seville, J.P.K. (ed) *Gas cleaning in demanding applications.* London, Blackie Academic & Professional. p.170-192.

39. Dunson, J.B. (1997) Gas-solid operations and equipment. In: Perry, R.H. and Green, D.W. (eds) *Perry's Chemical Engineers' Handbook.* 7th edition. New York, McGraw-Hill. p. 17-19 - 17-59.

40. Eckert, J.S. (1961) Design techniques for sizing packed towers. *Chemical Engineering Progress,* 57(9), 54-58.

41. Eckert, J.S. *et al.* (1966) What affects packing performance. *Chemical Engineering Progress,* 62(1), 59-66.

42. Eckert, J.S. (1970) Selecting the proper distillation column packing. *Chemical Engineering Progress,* 66(3), 39-44.

43. Elgin, J.C. and Weiss, F.B. (1939) *Liquid holdup and flooding in packed towers.* Industrial and Engineering Chemistry, 31(1), 435-445.

44. Elliott, J.F. *et al.* (1952) Physical conditions in the combustion and smelting zones of a blast furnace. *Transactions of the American Institute of Mining and Metallurgical Engineers,* 194, 709-717.

45. Ergun, S. (1952) Fluid flow through packed columns. *Chemical Engineering Progress,* 48(2), 89-94.

46. ETSU (1998) *Hot gas chemical cleanup.* TSR 006. Harwell, Energy Technology Support Unit. Cited in: Mitchell, S.C. (1998) *Hot gas cleanup of sulphur, nitrogen, minor and trace elements.* CCC/12. London, IEA Coal Research.

47. Fadel, T.M. (1984) Selecting packed-column auxiliaries. *Chemical Engineering,* 91(2), 71-76.

48. Fair, J.R. *et al.* (1997) Gas absorption and gas-liquid system design. *In:* Perry, R.H. and Green, D.W. (eds) (1997) *Perry's chemical engineers' handbook.* 7th edition. New York, McGraw-Hill. p. 14-1 - 14-98.

49. Fantom. I.R. (1997) *Hot gas desulphurisation for advanced power generation system.* COAL R090, UK DTI's Coal Research and Development Programme. Harwell, Energy Technology Support Unit.

50. Fick, A. (1855) Ueber Diffusion. *Ann. Phys.* 94, 59. Cited in: Coulson, J.M. *et al.* (1996) *Chemical Engineering, Volume 1, Fluid Flow, Heat Transfer and Mass Transfer.* 5th edition. Oxford, Butterworth-Heinemann Ltd.

51. Fluent Inc. (1998a) *FLUENT 5 User's Guide Volume 1.* Lebanon, Fluent Inc.

52. Fluent Inc. (1998b) *FLUENT 5 User's Guide Volume 2.* Lebanon, Fluent Inc.

53. Fluent Inc. (1998c) *FLUENT 5 User's Guide Volume 3.* Lebanon, Fluent Inc.

54. Fluent Inc. (1999) *GAMBIT Modeling Guide.* Lebanon, Fluent Inc.

55. Focht, G.D *et al.* (1988) High-temperature desulfurization using zinc ferrite: reduction and sulfidation kinetics. *Chemical Engineering Science*, 43(11), 3005-3013.

56. Focht, G.D *et al.* (1989) High-temperature desulfurization using zinc ferrite: regeneration kinetics and mulitcycle testing. *Chemical Engineering Science*, 44(12), 2919-2926.

57. Gangwal, S.K. *et al.* (1995) Hot-gas cleanup - sulfur recovery: technical, environmental, and economic issues. *Heat Recovery Systems and CHP*, 15(2), 205-214.

58. Gardner, G.C. (1956) Hold-up and pressure drop for water irrigating non-wettable coke. *Chemical Engineering Science*, 5(3), 101-114.

59. Gaston-Bonhomme, Y. *et al.* (1980) Influence of non-wetted fluored polymer packings in distillation columns-I Hydrodynamics. *Chemical Engineering Science*, 35, 1163-1169.

60. Genereaux, R.P. *et al.* (1973) Transport and Storage of Fluids. *In*: Perry, R.H. and Chilton, C.H. (eds) *Chemical Engineers' Handbook.* New York, McGraw-Hill. p. 6-14, 6-15.

61. Graton, L.C. and Fraser, H.J. (1935) *J. Geol.*, 43, 785. Cited in: Gray, W. A. (1968) *The Packing of Solid Particles.* London, Chapman & Hall Ltd.

62. Gray, W. A. (1968) *The Packing of Solid Particles.* London, Chapman & Hall Ltd.

63. Haupt, G. *et al.* (1995) Can hot gas cleanup improve IGCC efficiency today? *In: Power-Gen Europe '95*, Amsterdam, Netherlands, 16-18 May 1995. Cited in: Mitchell, S.C. (1998) *Hot gas cleanup of sulphur, nitrogen, minor and trace elements.* CCC/12. London, IEA Coal Research.

64. Haupt, G. (1997) Erlangen, Germany, Siemens/KWU. personal communication. Cited in: Mitchell, S.C. (1998) Hot gas cleanup of sulphur, nitrogen, minor and trace elements. CCC/12. London, IEA Coal Research.

65. Hedden, K. et al. (1986) Desulfurization of manufactured gases with liquid metals. *In: Proceedings of the 1986 International Gas Research Conference held at Toronto, Ont, Canada.*

66. Hedges, E.S. (ed) (1960) *Tin and Its Alloys.* London, Edward Arnold Ltd.

67. Herman, F.M. *et al.* (eds) (1985) *Encyclopedia of polymer science and engineering.* 2nd edition. Volume 1. New York, John Wiley & Sons.

68. Higbie, R. (1935) The rate of absorption of pure gas into a still liquid during short periods of exposure. *Transactions of AiChE*, 31, 365. Cited in: Coulson, J.M. *et al.* (1996) *Chemical Engineering, Volume 1, (Fluid Flow, Heat Transfer and Mass Transfer).* 5th edition. Oxford, Butterworth-Heinemann Ltd.

69. Horner, G. (1985) How to select internals for packed columns. *Process Engineering*, 66(5), 79-81.

70. IChemE (1999) IChemE Foresight Programme-Contribution on Energy. Document No. 71. Rugby, Institution of Chemical Engineers.

71. IEA (2000) *World Energy Outlook 2000 – Highlights* [online]. Paris, International Energy Agency. Available from: http://www.iea.org/weo/highlights.htm [Accessed 14 June 2002].

72. IEA Coal Research (1998) *The clean coal compendium.* London, IEA Coal Research. Cited in: Mitchell, S.C. (1998) *Hot gas cleanup of sulphur, nitrogen, minor and trace elements.* CCC/12. London, IEA Coal Research.

73. IEA Coal Research (2002) *Clean coal technologies (CCTs) and air pollution control technologies* [online]. London, IEA Coal Research. Available from: http://www.iea-coal.org.uk/iea1.htm [Accessed 11 April 2002].

74. Iida, T. and Guthrie, R.I.L. (1988) *The Physical Properties of Liquid Metals.* Oxford, Clarendon Press.

75. Jackson, S. and Calvert, S. (1966) Entrained particle collection in packed beds. *AIChE Journal*, 12(6), 1075-1078.

76. Jesser, B.W. and Elgin, J.C. (1943) Studies of liquid holdup in packed towers. *Transactions American Institute of Chemical Engineers*, 39, 277-298.

77. Khalil, M.F. *et al.* (1999) Effect of air injection method on the performance of an air lift pump. *International Journal of Heat and Fluid Flow*, 20, 598-604.

78. Kister, H.Z. and Gill, D.R. (1991) Predict flood point and pressure drop for modern random packings. *Chemical Engineering Progress*, 87(2), 32-42.

79. Kister, H.Z. (1992) *Distillation design.* New York, McGraw-Hill. Cited in: Sinnott, R.K. (1991) *Chemical Engineering, Volume 6, Chemical engineering design.* 2nd edition. Oxford, Butterworth-Heinemann.

80. Knudsen, J.G. *et al.* (1997) Heat and mass transfer. *In*: Perry, R.H. and Green, D.W. (eds) (1997) *Perry's Chemical Engineers' Handbook.* 7th edition. New York, McGraw-Hill. p. 5-1 - 5-79.

81. Kouremenos, D.A. and Staicos, J. (1985) Performance of a small air lift pump. *The International Journal of Heat and Fluid Flow*, 6(3), 217-222.

82. Kozeny, J. (1933) Uber bodendurchlassigkeit. *Z. Pfl.-Ernahr. Dung. Bodenk*, 28A, 54-56. Cited in: Coulson, J.M. *et al.* (1991) *Chemical Engineering, Volume 2, Particle technology and separation processes.* 4th edition. Oxford, Pergamon Press.

83. Kukarin, A.S. and Kitaev, B.I. (1962) *Izv. V.U.Z.Chern. Met.*, 12, 20. Cited in: Standish, N. (1973) On the flooding criteria for liquid metals. *Chemical Engineering Science*, 28, 1906-1907.

84. Lacombe, P. *et al.* (eds) (1993) *Stainless Steels.* France, Les Editions de Physique Les Ulis.

85. Lawniczak, F. *et al.* (1999) The efficiency of short airlift pumps operating at low submergence ratios. *The Canadian Journal of Chemical Engineering*, 77(1), 3-10.

86. Leva, M. (1954) Flow through irrigated dumped packings. Pressure drop, loading, flooding. *Chemical Engineering Progress Symposium Series*, 50(10), 51-59.

87. Lew, S. *et al.* (1989) High-temperature H$_2$S removal from fuel gases by regenerable zinc oxide-titanium dioxide sorbents. *Industrial and Engineering Chemistry Research*, 28(1), 535-541.

88. Lide, D.R. (ed) (1999) *CRC Handbook of Chemistry and Physics.* 80th edition. CRC Press.

89. Liengme, B.V. (2000) *A guide to Microsoft Excel for scientists and engineers.* 2nd edition. Oxford, Butterworth-Heinemann.

90. Liley, P.E. *et al.* (1997) Physical and chemical data. *In*: Perry, R.H. *et al.* (eds) *Perry's Chemical Engineers' Handbook.* 7th edition. New York, McGraw-Hill. p.2-125.

91. Lippert, T.E. and Newby, R.A. (1995) High-temperature particulate control. *In:* Alvarez, C.M. and Anthony, E.J. (eds) *Pressurized fluidised bed combustion.* Glasgow, Blackie Academic & Professional. p. 211-256.

92. Lobo, W.E. *et al.* (1945) Limiting capacity of dumped tower packings. *Transactions of the American Institute of Chemical Engineers*, 41, 693-710.

93. Lockhart, R.W. and Martinelli, R.C. (1949) Proposed correlation of data for isothermal two-phase, two-component flow in pipes. *Chemical Engineering Progress*, 45, 39. Cited in: Clark, N.N. and Dabolt, R.J. (1986) A general design equation for air lift pumps operating in slug flow. *AIChE Journal*, 32(1), 56-64.

94. Lyman, D.J. *et al.* (1965) The effect of chemical structure and surface properties of polymers on the coagulation of blood. I. Surface free energy effects. *Transactions of Americal Society for Artificial Internal Organs.* 11, 301-306.

95. Lyons, L. (1991) *A practical guide to data analysis for physical science students.* Cambridge, Cambridge University Press.

96. MacDonald, J.W. (1977) Packed wet scrubbers. *In:* Cheremisinoff, P.N. and Young, R.A (eds) *Air pollution control and design handbook. Part 2.* New York, Marcel Dekker.

97. Mackey, P.J. and Warner, N.A. (1973) Studies in the vaporization of mercury in irrigated packed bed. *Chemical Engineering Science*, 28, 2141-2154.

98. Mackowiak, J. (1990) Determination of flooding gas velocity and liquid hold-up at flooding in packed columns for gas/liquid systems. *Chemical Engineering Technology*, 13, 184-196.

99. Massey, B.S. (1986) *Measures in science and engineering: Their expression, relation and interpretation.* Chichester, Ellis Horwood Ltd.

100. McCabe, W.L. *et al.* (1993) *Unit operations of chemical engineering.* 5th edition. New York, McGraw-Hill.

101. McConville, A. (1997) *Emission standards handbook.* IEACR/96. London, IEA Coal Research.

102. Meissner, H.P. (1976) *Removal of hydrogen sulfide from reducing gases.* Institute of Gas Technology, US Patent US3954938.

103. Meissner, H.P. and Shora, F.C. (1981) High temperature pollutant removal from gas streams. Institute of Gas Technology, US Patent US4308037.

104. Middleman, S. (1995) Modeling axisymmetric flows: Dynamics of films, jets and drops. London, Academic Press, Inc.

105. Miller, D.S. (1990) *Internal flow systems.* 2nd edition. Bedford, BHRA (Information Services).

106. Mitchell, S.C. (1997) *Hot gas particulate filtration.* IEACR/95. London, IEA Coal Research.

107. Mitchell, S.C. (1998) *Hot gas cleanup of sulphur, nitrogen, minor and trace elements.* CCC/12. London, IEA Coal Research.

108. Mojtahedi, W. *et al.* (1994) Desulphurization of hot coal gas in fluidized bed with regenerable zinc titanate sorbents. *Fuel Processing Technology,* 37(1), 53-65.

109. Morris, G.A. and Jackson, J. (1953) *Absorption Towers.* Butterworths. Cited in: Coulson, J.M. *et al.* (1991) *Chemical Engineering, Volume 2, Particle technology and separation processes.* 4th edition. Oxford, Pergamon Press.

110. Morrison, G.L. *et al.* (1987) Experimental analysis of the mechanics of reverse circulation air lift pump. *Industrial and Engineering Chemistry Research,* 26, 387-391.

111. Newton, W.M. *et al.* (1952) How surface tension affects flooding in packed columns. *Petroleum Refiner,* 31(10), 141-143.

112. Nicklin, D.J. *et al.* (1962) Two-phase flow in vertical tubes. *Transactions of the Institution of Chemical Engineers,* 40, 61-68.

113. Nicklin, D.J. (1963) The air-lift pump: theory and optimisation. *Transactions of the Institution of Chemical Engineers,* 41, 29-39.

114. Niederhauser, D.O. and Bartell, F.E. (1950) *Report of Progress — Fundamental Research on the Occurrence and Recovery of Petroleum.* Baltimore, American Petroleum Institute, The Lord Baltimore Press. Cited in: Adamson, A.W. (1976) *Physical Chemistry of Surfaces.* 3rd edition. New York, John Wiley & Sons.

115. Nielsen, P.E.H and Sigurdardottir, I.D. (1993) Development and characterization of steam regenerable sorbents for hot gas desulphurization in coal gasification based combined cycle plant. *In*: Clift, R. and Seville, J.P.K. (eds) *Gas Cleaning At High Temperatures.* Glasgow, Blackie Academic & Professional.

116. Nogi, K. *et al.* (1988) Wettability of solid oxides by liquid pure metals. *Journal of Japan Institute of Metals,* 52(1), 72-78.

117. O'Brien, W.J. (1996) *Biomaterials properties database. Contact angle (liquid phase)* [online]. Michigan, University of Michigan School of Dentistry. Available from: http://www.lib.umich.edu/dentlib/Dental_tables/Contangle.html [Accessed 25th July 2002].

118. Osipow, L.I. (1962) *Surface chemistry theory and industrial applications.* New York, Reinhold Publishing Corporation.

119. Particle Sizing Systems (No date) *AccuSizer 780/SPOS Single Particle Optical Sizer* [online]. Santa Barbara, Particle Sizing Systems. Available from http://www.pssnicomp.com/780spos.htm. [Accessed 20 November 2001].

120. Peukert, W. (1995) Design criteria for high temperature filters. *In:* Chiang, S.H. (ed) *Proceedings, 12th annual international Pittsburgh coal conference.* Pittsburgh 11-15 September 1995. Pittsburgh, Pittsburgh Coal Conference, Vol 1, p. 373-378. Cited in: Mitchell, S.C. (1997) *Hot gas particulate filtration.* IEACR/95. London, IEA Coal Research.

121. Piche, S. *et al.* (2001a) Flooding capacity in packed towers: Database, correlations and analysis. *Industrial and Engineering Chemistry Research,* 40(1), 476-487.

122. Piche, S. *et al.* (2001b) Improved liquid hold-up correlation for randomly packed towers. Chemical Engineering Research and Design, 79, Part A, 71-80.

123. Piche, S. *et al.* (2001c) Counter-current randomly packed bed: Hydrodynamics and mass transfer simulator [online]. Quebec, Laval University. Available from: http://www.gch.ulaval.ca/~flarachi. *[Accessed 17 December 2001].*

124. Reitz, F. (1985) *Selective desulfurization of hot reducing gases by liquid tin and lead.* Dr.-Ing. dissertation, University of Karlsruhe. Cited in: Hedden, K. *et al.* (1986) Desulfurization of manufactured gases with liquid metals. *In: Proceedings of the 1986 International Gas Research Conference held at Toronto, Ont, Canada.*

125. Rennolds, P.J., S.M. (1939) S.M. Thesis in Chemical Engineering, M.I.T. Cited in: Sherwood, T.K. and Holloway, F.A.L. (1940) Performance of packed towers-experimental studies of absorption and desorption. *Transactions of AmIChE*, 36, 21-36.

126. Rhodes, M. (1998) *Introduction to particle technology.* Chichester, John Wiley and Sons.

127. Rutkowski, M., et al. (1993) IGCC database and hot gas cleanup systems studies. Proceedings of the Coal-Fired Power Systems 93 - Advances in IGCC and PFBC Review Meeting. DOE/METC-93/6131 (DE93000289). p.359-369.

128. Saez, A. E and Carbonell, R.G. (1985) Hydrodynamic parameters for gas-liquid cocurrent flow in packed beds. *American Institute of Chemical Engineering Journal*, 31(1), 52-60.

129. Saez, A.E. and Carbonell, R.G. (1990) The equilibrium and stability of menisci between touching spheres under the effect of gravity. *Journal of Colloid and Interface Science*, 140(2), 408-418.

130. Samsanov, G.V. (ed) (1982) *The Oxide Handbook.* 2nd Edition. New York, Plenum Data Co.

131. Schlegel Systems (2002) *An Engineer's Guide to Static Electricity* [online]. New York, Schlegel Systems. Available from: http://www.schlegel.com/education/Electricity.asp [Accesssed 4th September 2002].

132. Schürmann, B. (1984) Untersuchungen über die Gasreinigung durch geschmolzene Stoffe und Entwicklung eines entsprechnenden Verfahrens (Studies of gas purification by molten materials and development of an appropriate method). *Fortschritt-Berichte der VDI-Zeitschriften Reihe 3: Verfahrenstechnik*, 85.

133. Semrau, K.T. (1960) Correlation of dust scrubber efficiency. *Journal of the Air Pollution Control Association*, 10(3), 200-207.

134. Seville, J.P.K. (1996) *Hot gas particulate clean-up: current technological and commercial status.* COAL R092, UK DTI's Coal Research and Development Programme. Harwell, Energy Technology Support Unit.

135. Seville, J.P.K. *et al.* (1996) Recent advances in particulate removal from hot process gases. *In:* Schmidt, E. *et al.*(eds) *High temperature gas cleaning.* Universitat Karlsruhe, Institut fur Mechanische Verfahrenstechnik und Mechanik. p. 3-25.

136. Seville, J.P.K. (1997) Rigid ceramic filters. *In:* Seville, J.P.K. (ed) *Gas cleaning in demanding applications.* London, Blackie Academic & Professional. p. 96-129.

137. Seville, J.P.K. and Clift, R. (1997a) Gas cleaning at high temperatures: gas and particle properties. *In:* Seville, J.P.K. (ed) *Gas cleaning in demanding applications.* London, Blackie Academic & Professional. p.170-192.

138. Seville, J.P.K. and Clift, R. (1997b) Granular bed filters. *In:* Seville, J.P.K. (ed) *Gas cleaning in demanding applications.* London, Blackie Academic & Professional. p.170-192.

139. Shavrin, S.V. *et al.* (1962) *Izv. V.u.z., Chern.Met.,* 9, 54. Cited in: Szekely, J. and Mendrykowski, J. (1972) On the flooding criteria for liquids with high density and high interfacial tension. *Chemical Engineering Science*, 27, 959-963.

140. Shell The Royal Dutch Shell Group of Companies (2000) Coal [online]. Royal Dutch/Shell Group of Companies. Available from: http://134.146.1.138/royal-en/content/0.5028.25615-51271,00.html [Accessed 7 August 2000].

141. Sherwood, T.K. (1928) Solubilities of sulfur dioxide and ammonia in water. *Industrial and Engineering Chemistry*, 17(7), 745-747.

142. Sherwood, T.K. *et al.* (1938) Flooding velocities in packed columns. *Industrial Engineering Chemistry*, 30(7), 765-769.

143. Sherwood, T.K. and Holloway, F.A.L. (1940a) Performance of packed towers-experimental studies of absorption and desorption. *Transactions of AmIChE*, 36, 21-36.

144. Sherwood, T.K. and Holloway, F.A.L. (1940b) Performance of packed towers-liquid film data for several packings. *Transactions of AmIChE*, 36, 39.

145. Sherwood, T.K. *et al.* (1975) *Mass Transfer*. New York, McGraw-Hill.

146. Shimizu, R.N. and Dermarquette, N.R. (1999) Evaluation of surface energy of solid polymers using different models. *Journal of Applied Polymer Science*, 76, 1831-1845.

147. Shulman, H.L. *et al.* (1955a) Performance of packed columns 1. Total, static and operating holdups. *Journal of the American Institute of Chemical Engineers*, 1(2), 247-253.

148. Shulman, H.L. *et al.* (1955b) Performance of packed columns III. Holdup for aqueous and nonaqueous systems. *Journal of the American Institute of Chemical Engineers*, 1(2), 259-264.

149. Simmons, C.W. and Osborn, H.B., Jr. (1934) *Ibid.*, 26, 529. Cited in: Jesser, B.W. and Elgin, J.C. (1943) Studies of liquid holdup in packed towers. *Transactions American Institute of Chemical Engineers*, 39, 277-298.

150. Standish, N. (1963) Liquid metal hold-up in packed beds. *New Zealand Journal of Science*, 6, 215-228.

151. Standish, N. (1968a) Dynamic hold-up in liquid metal irrigated packed bed. *Chemical Engineering Science*, 23, 51-56.

152. Standish, N. (1968b) Some observations on the static hold-up of aqueous solutions and liquid metals in packed bed. *Chemical Engineering Science*, 23, 945-947.

153. Standish, N. (1968c) Heat transfer in liquid metal irrigated packed beds countercurrent to gases. *Transactions of the Metallurgical Society of AIME*, 242, 1733-1740.

154. Standish, N. and Drinkwater, J.B. (1972) Reducing blast furnace hang-ups. *Journal of Metals*, 24, 43-45.

155. Standish, N. (1973) On the flooding criteria for liquid metals. *Chemical Engineering Science*, 28, 1906-1907.

156. Strigle, R.F. (1994) *Packed Tower Designs and Applications. Random and Structured Packings*. 2nd edition. Houston, Gulf Publishing Company.

157. Svarovsky, L. (1981) Solid-gas separation. Amsterdam, Elsevier Scientific Publishing Company.

158. Svarovsky, L (1990) Solid-gas separation. *In:* Rhodes, M.J. (ed) *Principles of powder technology*. Chichester, John Wiley & Sons. p. 171-192.

159. Szekely, J. and Mendrykowski, J. (1972) On the flooding criteria for liquids with high density and high interfacial tension. *Chemical Engineering Science*, 27, 959-963.

160. Tait, P.M. (1998) *Cost effective cleaner technology for upgrading zinc quality*. PhD thesis, University of Birmingham.

161. Taylor, J.R. (1997) *An introduction to error analysis: The study of uncertainties in physical measurements*. 2nd edition. Sausalito, University Science Books.

162. Thambimuthu, K.V. (1993) *Gas cleaning for advanced coal-based power generation*. London, IEA Coal Research.

163. Todoroki, I. *et al.* (1973) Performance of air-lift pump. *Bulletin of Japan Society of Mechanical Engineers*, 16(94), 733-741.

164. Tooley, F.V. (1984) *The Handbook of Glass Manufacture: A book of reference for the plant executive, technologist and engineer, Volume II*. 3rd edition. New York, Ashlee Publishing Co.

165. Toor, H.L. and Marchello, J.M. (1958) Film-penetration model for mass and heat transfer. *AIChE Journal*, 4(1), 97-101.

166. Tramba, A. *et al.* (1995) Visual study of an airlift pump operating at low submergence ratios. *The Canadian Journal of Chemical Engineering*, 73, 755-764.

167. Treybal, R.E. (1980) *Mass-transfer operations*. 3rd edition. New York, McGraw-Hill.

168. Turner, G.A. and Hewitt, G.F. (1959) The amount of liquid held at the point of contact of spheres and the static liquid holdup in packed beds. *Transactions of the Institution of Chemical Engineers*, 37, 329-334.

169. UK DTI (1998a) *UK capabilities: Hot gas cleaning technologies for coal-based power generation.* UK DTI's Cleaner Coal Technology Programme.

170. UK DTI (1998b) *Technology status report-gasification of solid and liquid fuels for power generation.* UK DTI's Cleaner Coal Technology Programme.

171. UK DTI (2002) *The UK Cleaner Coal Technology Programme* [online]. London, UK Department of Trade and Industry. Available from: http://www.dti.gov.uk/cct/index.htm [Accessed 10th June 2002).

172. US DOE Office of Fossil Energy Communications (2000) *Fossil Energy: Integrated gasification combined cycle: Program summary* [online]. Washington, US Department of Energy. Available from: http://www.fe.doe.gov/coal_power/igcc/igcc_sum.html [Accessed 27 April 2000].

173. US EPA (no date) *EPA Inorganic Chemical Industry Notebook Section IVb* [online]. US Environmental Protection Agency. Available from: http://www.csa.com/routenet/epan/inrgchsnIVb.html [Accessed 21 December 2002].

174. Van Swaaij, W.P.M. et al. (1969) Residence time distribution in the liquid phase of trickle flow in packed columns. *Chemical Engineering Science*, 24, 1083-1095.

175. Vogel, A.I. (1989) *Vogel's Textbook of Quantitative Chemical Analysis.* 5th Edition. Essex, Longman Scientific & Technical.

176. Warner, N.A. (1959a) Liquid metal irrigation of a packed bed. *Chemical Engineering Science*, 11(3), 149-160.

177. Warner, N. (1959b) The absorption of zinc vapour in molten lead. *Chemical Engineering Science*, 11, 161-182.

178. Warner, N.A. (1997) *Zinc-based clean technology for desulphurisation in advanced power generation.* COAL R127, UK DTI's Coal Research and Development Programme. Harwell, Energy Technology Support Unit.

179. Warner, N.A. (2000) Personal communication. *Theoretical Framework for Liquid Metal Based Coal Gasification (draft) – 23 February 2000.*

180. Warner, N.A. (2001) Personal communication. *Theoretical Framework for Liquid Metal Based Coal Gasification (draft) – 25 April 2001.*

181. Whalley, P.B. (1996) *Two-phase flow and heat transfer.* New York, Oxford University Press.

182. White, A.M. (1935) Pressure drop and loading velocities in packed towers. *Transactions American Institute of Chemical Engineers*, 31, 390-408.

183. Whitman, W.G. (1923) The two-film theory of gas absorption. *Chemical and Metallurgical Engineering*, 29(4), 146-148. Cited in: various sources.

184. Willfor, M. (2001) *Private communication.* AvestaPolarit AB, R&D Centre Avesta, High Temperature Materials.

185. Williams, B.C. and McMullan, J.T. (1998) *Hot gas chemical clean-up: current commercial and technological status.* COAL R139, UK DTI's Coal Research and Development Programme. Harwell, Energy Technology Support Unit.

186. Young, Th. (1805) Phil. Trans., I, 65,84. Cited in: Bikerman, J.J. (1970) *Physical Surfaces.* New York, Academic Press.

187. Zenz, F.A. (1993) Explore the potential of air-lift pumps and multiphase. *Chemical Engineering Progress*, 89(2), 51-56.

188. Zisman, W.A. (1964) Relation of equilibrium contact angle to liquid and solid constitution. *In:* Gould, R.F. (ed) *Contact angle, wettability and adhesion. Advances in Chemistry Series, 43.* Washington D.C., American Chemical Society.

Appendices

Appendix 1

Determination of Sulphur (and Chlorine) Content(s) in Fuel Sample

The High-Temperature Method for the simultaneous determination of sulphur and chlorine contents is outlined in BS 1016: Part 6: 1977 British Standard Methods for Analysis and Testing of Coal and Coke - Ultimate Analysis of Coal and Part 8: 1977: Chlorine in Coal and Coke. This method was followed, however with a modification to the titrimetric determination of the chlorine content in that the specified mercury II oxycyanide solution was not used due to its toxicity.

□ *Principle*

A known mass of fuel sample is burned in an oxygen stream at 1350°C. Aluminium oxide is added to facilitate decomposition of the sulphate and to prevent its retention in the ash. Oxides of sulphur as well as chlorine which are formed are absorbed into neutral hydrogen peroxide solution yielding HCl and H_2SO_4 acids:

$$SO_2 + H_2O_2 \rightarrow H_2SO_4 \tag{A1.1}$$

$$Cl_2 + H_2O_2 \rightarrow 2HCl + O_2 \tag{A1.2}$$
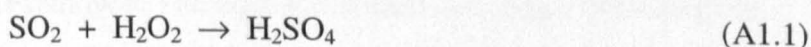
The total acidity due to HCl and H_2SO_4 acids formed is determined by titration with sodium borate solution. The Cl^- ion is determined by Mohr Titration. Knowing the chloride content, the sulphide hence the sulphur content can thus be determined.
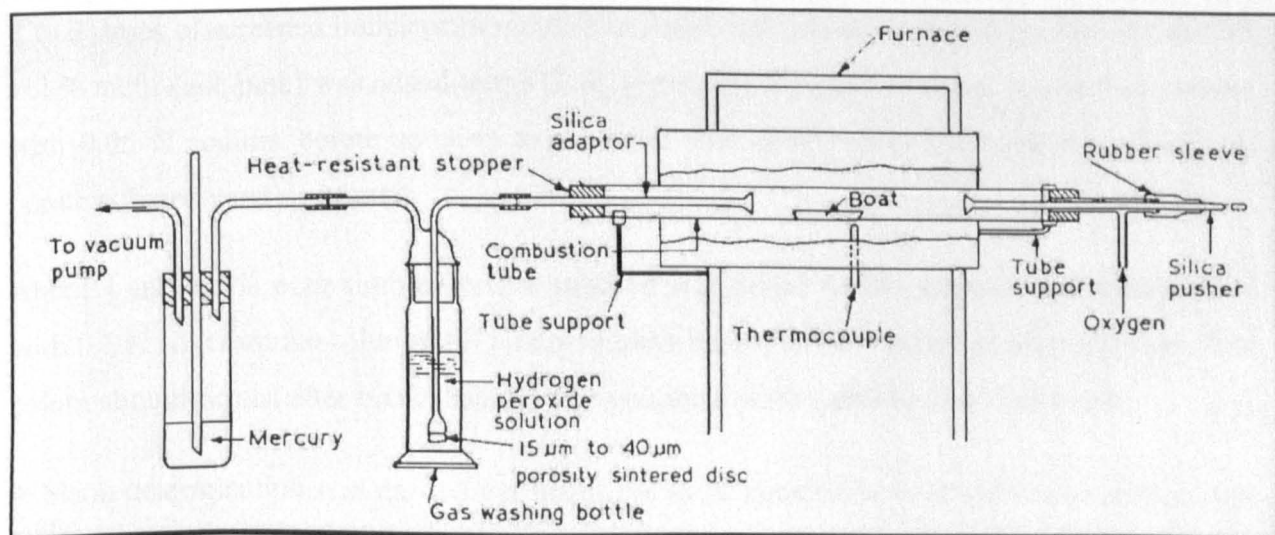

Figure A1.1 *High-Temperature Method: Absorption train and furnace for sulphur and chlorine determination (BS 1016: Part 6: 1977).*

292

❏ *Procedure*

The temperature of the furnace was raised to 1350°C and oxygen was passed through the combustion tube. Approximately 0.5 g of fuel sample was weighed to the nearest 0.1 mg, spread evenly in the boat and covered with 0.5 g of aluminium oxide. 100 ml of 3 vol.% hydrogen peroxide solution was measured into the absorption vessel. The apparatus was then assembled. The flow rate was adjusted using the vacuum pump and the seal depth in the mercury regulator to maintain a slight suction in the combustion tube with oxygen entering at 300 ml/min.

The rubber stopper carrying the silica pusher was removed and the charged boat was inserted into the combustion tube such that its centre was 240 mm from the centre of the hottest zone. With the silica pusher fully withdrawn, the rubber stopper was replaced and the flow of purified oxygen was continued at 300 ml/min. At the end of the first minute, the boat was pushed forward 40 mm. At the end of the next eight 1-minute intervals, the boat was pushed forward an extra 20 mm, withdrawing the silica pusher each time to prevent its distortion. After a further 1-minute interval (i.e. after 10 minutes) the boat was pushed forward 40 mm and allowed to remain in the hottest zone for a further 4 minutes. The absorption vessel was disconnected and the silica adaptor removed. The boat was withdrawn onto a refractory tile.

The silica adaptor was washed with water, the washings collected into a 250 ml flask. The content of the absorption vessel was transferred into the flask. The vessel was washed with water and the washings collected into the same flask. The total liquid should not exceed 150 ml.

2 to 3 drops of screened indicator (a mixture of equal volumes of 95 vol.% methyl red and 95 vol.% methylene blue) was added to the flask, producing a purple solution. It was then titrated with 0.05 N sodium borate solution to a neutral steel-grey colour. The volume of sodium borate solution used was noted.

About 1 ml of 5% potassium chromate solution was added to the solution and then titrated with 0.1 N silver nitrate solution till a faint reddish-brown colour end point was obtained. This colour should persist after brisk shaking. The volume of silver nitrate used was noted.

A blank determination was carried out under the same conditions as the actual determination but omitting the sample.

❑ *Analysis of Results*

The chlorine and total sulphur contents were calculated as follows:

$$\% \text{ Chlorine by weight} = \frac{0.3545}{m}[v_3 - v_4] \qquad (A1.3)$$

$$\% \text{ Total sulphur by weight} = \frac{0.0802}{m}[v_1 - v_2 - 2(v_3 - v_4)] \qquad (A1.4)$$

where m = Mass of sample taken (g)

v_1 = Volume of 0.05N sodium borate used in sample determination (ml)

v_2 = Volume of 0.05N sodium borate used in blank determination (ml)

v_3 = Volume of 0.1N silver nitrate used in sample determination (ml)

v_4 = Volume of 0.1N silver nitrate used in blank determination (ml)

The results were obtained as the mean of duplicate determinations as tabulated below. The sulphur content was reported to the nearest 0.1% while that of chlorine was reported to the nearest 0.01% as specified in BS 1016: Part 6 and Part 8: 1977.

Table A1.1   Determination of sulphur and chlorine contents.

	Test 1	Test 2	Test 3	Mean
m (g)	0.4713	0.4404	0.4815	-
v_1 (ml)	26.45	24.55	26.85	-
v_2 (ml)	0.15	0.15	0.15	-
v_3 (ml)	0.35	0.30	0.25	-
v_4 (ml)	0.15	0.15	0.15	-
Chlorine by wt. (%)	0.15	0.12	0.07	0.11
Sulphur by wt. (%)	4.4	4.4	4.4	4.4

Appendix 2

Tabulated Experimental Data from Cold Gas Scrubber Studies

(in accompanying compact disc)

Appendix 2.1 Experimental Data from Flooding Tests

Appendix 2.2 Experimental Data from Liquid Holdup Tests

Appendix 2.3 Experimental Data from Gas Lift Tests

Appendix 2.4 Experimental Data from Particulate Removal Tests

Appendix 2.5 Experimental Data from Gas Absorption Tests

Appendix 3
Analysis of Errors

Appendix 3.1 Propagation of Uncorrelated Errors (Lyons, 1992; Taylor, 1997)

❑ *Sums and Differences*

If the desired quantity f is a simple summation or subtraction of the measured quantities x and y:

$$f = x + y \quad or \quad f = x - y \tag{A3.1}$$

the absolute error on f (e_f) can then be derived from the absolute errors on x (e_x) and y (e_y) as follows with the condition that e_x and e_y are uncorrelated:

$$e_f^2 = e_x^2 + e_y^2 \tag{A3.2}$$

❑ *Products and Quotients*

If the desired quantity f is given in terms of the measured quantities x and y by:

$$f = x^a y^b \tag{A3.3}$$

where the powers a and b can be positive, negative or fractional. Hence this formula includes simple products, ratios, cubes, square roots, etc.

Provided x and y are uncorrelated, the fractional error on f is related to the fractional errors on x and y as follows:

$$\left(\frac{e_f}{f}\right)^2 = a^2 \left(\frac{e_x}{x}\right)^2 + b^2 \left(\frac{e_y}{y}\right)^2 \tag{A3.4}$$

Therefore for the simple functions:

$$f = xy \quad and \quad f = x/y \tag{A3.5}$$

the fractional error on f is:

$$\left(\frac{e_f}{f}\right)^2 = \left(\frac{e_x}{x}\right)^2 + \left(\frac{e_y}{y}\right)^2 \tag{A3.6}$$

❑ ***Measured Quantity Multiplied by Exact Number***

If *B* is an exact number and:

$$f = Bx \tag{A3.7}$$

then absolute error on *f* is $|B|$ times the absolute error on x:

$$e_f = |B| e_x \tag{A3.8}$$

and fractional error on *f* equals the fractional error on *x*:

$$\left(\frac{e_f}{f}\right) = \left(\frac{e_x}{x}\right) \tag{A3.9}$$

❑ ***General Case***

The following general equation defines the desired quantity *f* in terms of measured quantities x_i each with its own error e_{xi}. All errors on x_i are uncorrelated.

$$f = f(x_1, x_2, ..., x_n) \tag{A3.10}$$

The error e_f associated with the desired quantity *f* is then given by the following equation in terms of the known measurement errors e_{xi}:

$$e_f^2 = \sum_{i=1}^{n} \left(\frac{\partial f}{\partial x_i} e_{xi}\right)^2 \tag{A3.11}$$

Appendix 3.2 Statistical Analysis of Random Errors (Taylor, 1997)

For N measurements, x_1, x_2, ..., x_N of the same quantitity x, all using the same method and provided all errors are random and small:

❑ ***Mean***

The mean of these measurements represent the best estimate for x:

$$\bar{x} = \frac{1}{N} \sum_{i=1}^{N} x_i \tag{A3.12}$$

❑ *__Standard Deviation__*

The standard deviation gives the average error (uncertainty) of the individual measurements $x_1, x_2, ..., x_N$:

$$s_x = \sqrt{\frac{1}{N-1}\sum(x_i - \bar{x})^2}$$
(A3.13)

The significance of the standard deviation s_x is that approximately 68% of the measurements of x using the same method should fall within a distance s_x of the true value. Therefore s_x is identified as the error (uncertainty) in any one measurement of x:

$$e_x = s_x$$
(A3.14)

❑ *__Standard Deviation (or Standard Error) of The Mean__*

Where systematic errors are negligible, the error (uncertainty) in the best estimate of x (namely $\bar{x}$) is the standard deviation (or standard error) of the mean:

$$s(\bar{x}) = \frac{s_x}{\sqrt{N}}$$
(A3.15)

Hence the error in $\bar{x}$ is:

$$e_x = s(\bar{x})$$
(A3.16)

Appendix 3.3 Statistical Analysis of Correlation Errors

Average absolute relative error, AARE:

$$\frac{1}{N}\sum_{i=1}^{N}\left|\frac{x_{exp,i} - x_{pred,i}}{x_{exp,i}}\right|$$
(A3.17)

where   N   = number of data sets

$x_{exp,i}$ = experimental value

$x_{pred,i}$ = predicted value

Standard deviation of absolute relative error, s:

$$\sqrt{\sum_{i=1}^{N}\left[\left|\frac{x_{exp,i} - x_{pred,i}}{x_{exp,i}}\right| - AARE\right]^2 \bigg/ (N-1)}$$
(A3.18)

Appendix 4
Reference Tables
(in accompanying compact disc)

Table A4.1 Values of 1/H as a function of S = d_s/d_e (Niederhauser and Bartell, 1950).

Appendix 5
Publications
(in accompanying compact disc)

1. B.F.Chang *et al.* (2002) *Development of a Liquid Metal Based Fuel Gas Scrubbing System. Proceedings of the 5ᵗʰ International Symposium on Gas Cleaning at High Temperature, September 17-20, 2002, Morgantown, West Virginia, USA.* Morgantown, U.S. Department of Energy, National Energy Technology Laboratory.

2. B.F.Chang *et al.* (2002) A Non-Wetting Packed Bed Gas Scrubber.
    Submitted to the *Transactions of the Institution of Chemical Engineers: Part B: Process Safety and Environmental Protection.*